

Alma Mater Studiorum – Università di Bologna

DOTTORATO DI RICERCA IN

Scienze Chimiche

Ciclo XXIX

Settore Concorsuale di afferenza: 03/A2

Settore Scientifico disciplinare: CHIM/02

**MODELING SPECTRAL TUNABILITY AND PHOTOISOMERIZATION
MECHANISMS IN NATURAL AND ARTIFICIAL RETINAL SYSTEMS**

Presentata da: Mohsen Mamdouh Taha EL Tahawy

Coordinatore Dottorato

Prof. Aldo Roda

Relatore

Prof. Marco Garavelli

Co-Relatore

Dr. Artur Nenov

Esame finale anno 2017

DEDICATION

**I dedicate this thesis to
the memory of Dr. Artur
Nenov's Mother, may
ALLAH grant her his
highest paradise (Ameen).**

ACKNOWLEDGEMENT

In the name of ALLAH, the most Beneficent, the most Merciful, the most Compassionate.

First and foremost, all praise to **ALLAH, ALMIGHTY**, for giving courage, strength, and patience to complete this work.

I wish to express my sense of indebtedness and gratitude to **Prof. Marco Garavelli**, for giving me the chance to be a member of his group, his scholarly supervision, guidance and encouragement. He was always helpful and sympathetic to me. Working with him was indeed a wonderful and learning experience, which I thoroughly enjoyed.

I would like to express my deepest respect and most sincere gratitude to **Dr. Artur Nenov** for his guidance, encouragement at all stages of my work and stimulating discussion. I am lucky to have him as an advisor, mentor and also a friend. His constructive criticism and comments from the initial conception to the end of this work are highly appreciated and the motivation that I need to succeed in the future.

I would acknowledge the Erasmus Mundus Action 2 EUMETALIC Consortium for funding me within the EUMETALIC mobility scheme as a Ph.D. student at Bologna University

Also, I would like to express my pleasure of having many discussions and collaborations with other members of the group, which have contributed greatly to the work presented in this thesis so I would like to thank **Drs. I. Conti, I. Rivalta, J. Segarra-Marti, A. Giussani, A-J Pepino, S. F. Altavilla, B. Demoulin, F. Segatta and A. Bonvicini**.

I thank my family kept me going strong. Last but not least, I deeply thank my wife, **Amany**, for her productivity, her encouragement and for bringing happiness into my life. I could not have completed this thesis without her support and advice. Lastly, I dedicate this thesis to my lovely daughters **Hend** and **Shatha** who bring joyfulness and hope to my life.

Mohsen El Tahawy

Abstract

The photoinduced ultrafast isomerizations of the retinal chromophore in visual rhodopsins are characterized by high speed (ultrafast sub picosecond timescale processes) and efficiency (high quantum yields). This is due to a conical intersection between the excited and ground electronic states that drives its radiationless decay via an efficient internal conversion. The retinal chromophore displays also a cationic structure and the charge transfer character of its lowest excited bright state makes it sensitive to the environment, namely to the presence of an external electric field. This is in turn able to tune its absorption energy in order to cover the whole visible range (thus enabling color vision, for instance). All these properties call for the retinal chromophore as an ideal candidate for the design of fast, efficient and spectrally tunable molecular machines that work via reversible and controlled photo-induced reactions. The aim of this thesis is to investigate the mechanisms driving these reactions in different natural and artificial environments using high-level ab initio calculations and hybrid quantum mechanics / molecular mechanics methods. Eventually, the aim is to understand how these systems work and provide guidelines for the design of artificial photoactive retinal inspired systems that may mimic Nature.

Firstly, we investigate the effect of an homogeneous electric field on the spectral tunability, photoisomerization efficiency and selectivity of the native all-trans retinal protonated Schiff base (RPSB) chromophore. We have explored the possibility to tune the absorption wavelength of RPSB over the entire visible range by varying the electric field strength from -0.005 to $+0.004$ au. Moreover, we have proposed a tentative proportional correlation between the absorption energy modulated by the electric field and the corresponding ES lifetime. In addition to the isomerization rate control, it may become possible to selectively switch between different isomerization channels by adjusting the electric field to a specific value. Based on a large number of functionalized RPSB, hosting electron withdrawing and/or donating groups, and RPSB mimics, we have demonstrated that many of the characteristics/properties encountered for the native RPSB chromophore under the effect of an external homogeneous electric field are also observed for (and can be extended to) these systems. Furthermore, we explored the possibility to selectively switch on/off the isomerization by adjusting the electric field to a specific critical value via judicious substitutions/functionalizations of the chromophore. This would be a promising step toward

the design of bio-inspired photo-controlled molecular devices. The results are illustrated and discussed in chapters V and VI.

The second part of this thesis deals with the modeling of the isomerization mechanism of human melanopsin and invertebrate and vertebrate rhodopsins, and the prediction of the photoisomerization rates and quantum yields by means of semiclassical non-adiabatic molecular dynamics at the hybrid quantum mechanics (CASSCF)/molecular mechanics (QM/MM) level. Our results show that the Landau–Zener rule does not apply for visual pigments. Since the chromophore’s dynamics is essentially multi-dimensional (C11–C12, C10–C11–C12–C13 and HC11–C12H), the fate of the reaction depends on the phases of the reaction driving modes and their match with the electronic structure of the system. These results are reported in chapters VII and VIII.

In the last part of this thesis (chapter IX), we shed some light on the photoisomerization mechanism of the Siberian hamster ultraviolet (SHUV) visual pigment, a so far poorly investigated system. This pigment incorporates an unprotonated Schiff-base (USB) retinyl chromophore in the dark state, which becomes protonated after photoexcitation during the early stages of the photobleaching cycle. In such pigment, the photochemical relaxation processes is still unclear. We have investigated all the likely involved photoisomerization pathways, including singlet/triplet inter-system crossings as well as photoinduced proton transfers. The results suggest that the photoinduced proton transfer is a possible mechanism for the efficient photoisomerization and decay of the chromophore.

List of Publications

a. Already Published

6. El-Tahawy, M. M. T.; Nenov, A.; Garavelli, M. Photoelectrochromism in the Retinal Protonated Schiff Base Chromophore: Photoisomerization Speed and Selectivity under a Homogeneous Electric Field at Different Operational Regimes. J. Chem. Theory Comput., 12 (2016) 4460-4475.
5. Bonvicini, A.; Demoulin, B.; Altavilla, S. F.; Nenov, A.; El-Tahawy, M. M. T.; Segarra-Martí, J.; Giussani, A.; Batista, V. S.; Garavelli, M.; Rivalta, I., Ultraviolet vision: photophysical properties of the unprotonated retinyl Schiff base in the Siberian hamster cone pigment, Theo. Chem. Acc., 135 (2016) (4), 1-10.
4. Bonvicini, A.; El-Tahawy, M.M.T., Nenov, A., Garavelli, M.; Bahers, T., Intramolecular photo-induced charge transfer in visual retinal chromophore mimics: electron density-based indices at the TD-DFT and post-HF levels, Theo. Chem. Acc. 135 (2016) 1-10.
3. M.S. Masoud, M.K. Awad, Alaa E. Ali, M.M.T. El-Tahawy, Molecular structure of amino alcohols on aluminum surface, J. Mol. Struct., 1063, 24 (2014) 51–59.
2. M.K. Awad, M.S. Masoud, M.A. Shaker, Alaa E. Ali, M.M.T. El-Tahawy, MP2 and DFT Theoretical Studies of the Geometry, Vibrational and Electronic Absorption Spectra of 2-Aminopyrimidine, Res. Chem. Intermed., 39, 6 (2013) 2741-2761.
1. M. S. Masoud, M. K. Awad, M. A. Shaker, M.M.T. El-Tahawy, The role of structural chemistry in the inhibitive performance of some aminopyrimidines on the corrosion of steel. Corros. Sci., 52, 7, (2010) 2387-2396.

b. In Preparation

El-Tahawy, M. M. T.; Nenov, A.; Weingart, O, Olivucci, M, Garavelli, M. QM/MM study on the isomerization mechanisms of human melanopsin and invertebrate and vertebrate rhodopsins: going beyond the monodimensional Landau-Zener model.

El-Tahawy, M. M. T.; Nenov, A.; Garavelli, M. Functionalized Retinal Chromophore with Tailored Spectral and Photochemical Properties: Toward Bio-inspired Designer Molecules.

El-Tahawy, M. M. T.; Bonvicini, A.; Demoulin, B.; Nenov, A.; Rivalta, I.; Garavelli, M., The Siberian Hamster UV-light Cone Pigment: the Unusual Photochemistry and Photophysics of an Unprotonated Retinal Schiff-Base Chromophore

Contents

ACKNOWLEDGEMENT	i
Abstract.....	ii
List of Publications	iv
Contents	v
1 Introduction	1
1.1 Photoprocesses	1
1.2 Retinal proteins	2
1.3 Aims of the Study.....	2
2 Ab Initio Quantum Mechanics (QM), Molecular Mechanics (MM) and Hybrid QM/MM Methods	5
2.1 Quantum Mechanics.....	5
2.1.1 The Hartree-Fock Self-Consistent Field Method.....	8
2.1.2 Configuration Interaction.....	10
2.1.3 Multiconfigurational Self-Consistent Field	11
2.1.4 Multiconfigurational Second Order Perturbation Method.....	13
2.2 A Brief Introduction to Molecular Mechanics	14
2.2.1 Basic Theory	14
2.3 Hybrid Quantum Mechanics/Molecular Mechanics (QM/MM).....	15
2.3.1 COBRAMM as QM/MM Partitioning Scheme	16
3 Potential Energy Surfaces: Reaction Paths and Conical Intersections	20
3.1 Stationary Points	20
3.2 Geometry Optimizations	21
3.2.1 Constrained Optimizations.....	21
3.3 Conical Intersection.....	22
3.3.1 Conditions for the existence of conical intersections	22
3.3.2 On the “Physical Chemistry” of Conical Intersections.....	24
3.3.3 Conical Intersection Optimization	25
3.4 Locating Reaction Paths.....	26
4 Nonadiabatic Molecular Dynamics with Semiclassical Trajectories	27
4.1 Introduction	27
4.2 Mixed Quantum-Classical Dynamics.....	28
4.3 Surface Hopping Approach.....	29

4.3.1	Tully's Trajectory Surface Hopping	29
4.4	Equation of Motion: Integration.....	31
4.5	Sampling of Initial Conditions	32
5	Photoelectrochromism in the retinal protonated Schiff base chromophore: photoisomerization speed and selectivity under a homogeneous electric field at different operational regimes.....	34
5.1	Introduction	34
5.2	Computational Details.....	36
5.3	Results and Discussion.....	38
5.3.1	Effect of a Homogeneous Electric Field on the Absorption Energy	38
5.3.2	Effect of a Homogeneous Electric Field on the Ultrafast ES Dynamics	42
5.3.3	Correlation between Excited State Lifetime and Absorption Wavelength	49
5.3.4	Rationalization of the Results: The Extended Two-electron Two-Orbital Model 51	
5.3.5	An External Electric Field Affects the Topography of the CI Seam.	55
5.3.6	Electric Field Impeded Ultrafast Isomerization.....	59
5.3.7	Internal Fields Created by Polar Functional Groups: Transferability and Generalization of the Model.....	61
5.4	Conclusions	63
6	Functionalized Retinal Chromophore with Tailored Spectral and Photochemical Properties: Towards Bio-inspired Designer Molecules.....	65
6.1	Introduction	65
6.2	Computational Details.....	66
6.3	Results and Discussion.....	66
6.3.1	Influence of Functional Groups on the Absorption Energy.....	66
6.3.2	Influence of Functional Groups on Excited State Potential Energy Surface	70
6.3.3	Toward Applications.....	72
6.4	Conclusions	75
6.5	Additional Study	76
7	Photochemistry of Visual Pigments	78
7.1	Structure of Visual Pigments.....	78
7.2	Classification of the Vertebrate Visual Pigments	79
7.3	The Opsin Shift: Protein-Bound vs. Solution Environment.....	80
7.4	Melanopsins vs. Rhodopsins	81
7.5	UV-Visual Pigments	82

8	QM/MM Study on the Isomerization Mechanisms of Human Melanopsin and Invertebrate and Vertebrate Rhodopsins: Going Beyond the Monodimensional Landau-Zener Model	85
8.1	Introduction	85
8.2	Methodology and Benchmarking	87
8.2.1	Three Pigments Models	87
8.2.2	QM/MM Partitioning Scheme	87
8.2.3	Optimization and Single Point Calculations	88
8.2.4	Selecting the Active Space.....	88
8.2.5	MD Simulations	91
8.2.5.1	0K Trajectories	91
8.2.5.2	Trajectory Swarms	92
8.2.6	Time Scaling of the Excited-State Trajectory.....	92
8.3	Result and Discussion	94
8.3.1	Franck-Condon Geometries	94
8.3.2	Linear Absorption Spectra	96
8.3.3	Analysis of the Reference Trajectories	97
8.3.4	Rationalizing the Correlation between Excitation Wavelength and Isomerization Speed	98
8.3.5	Rationalization of the “Observed” Quantum Yields.....	101
8.3.6	Statistical Results	104
8.4	Conclusion.....	108
9	The Siberian Hamster UV-light Cone Pigment: the Unusual Photochemistry and Photophysics of an Unprotonated Retinal Schiff-Base Chromophore.....	110
9.1	Introduction	110
9.2	Computational Details.....	113
9.3	Results and Discussion.....	116
9.3.1	Populations of Singlet and Triplet States.....	116
9.3.1.1	Isomerization Profile of the Singlet Doubly Excited State dHL	117
9.3.1.2	Minima along the Triplet States T ₁ and T ₂	118
9.3.1.3	Spin Orbital coupling.....	120
9.3.1.4	Isomerization Energy Profiles of T ₂ and T ₁ Triplet States.	120
9.3.2	Photoinduced Proton Transfer (a comparison between models I & II)	123
9.3.2.1	Thermodynamics of Photoinduced Proton Transfer Process	126

9.3.2.2	Photoisomerization Energy Profile for model II SHUV-PSB.....	129
9.4	Conclusion.....	131
	Summary and Conclusions.....	133
	List of Abbreviations.....	137
	List of Figures.....	138
	References	146

1 Introduction

1.1 Photoprocesses

Photoprocesses are usually categorized into physical or chemical [1]. In both types of processes the molecule or the system absorbs or emits ultraviolet (wavelength from 100 to 400 nm), visible (400 – 750 nm) or infrared (750 – 2500 nm) radiation [2]. A classification for those processes as either photochemical or photophysical depends on the nature of the reaction occurring after the absorption or emission of light. For instance, a photochemical reaction is initiated by the absorption of energy, in the form of light, which leads to bond(s) breaking and/or forming in order to produce chemical species that differ from the original molecules: photoinduced fragmentation or polymerization reactions are typical examples of photochemical reactions. On the other hand, photophysical processes do not involve bond breaking or bond formation: the molecule absorbing light return back to their thermal equilibrium by simply emission of light, nonadiabatic decay and energy transfer phenomena, thereby dissipating the excess energy in the environment. Fluorescence and phosphorescence are examples of photophysical processes. It is worth to mention that the differentiation between both kinds of reactions might not be unambiguous. For instance, intramolecular photoinduced electron transfer reactions or photoisomerization reactions are examples of processes that might be classified as both photochemical and photophysical processes depending on whether one might define the photoproduct as a new chemical species or not..

Photoprocesses are common in biological systems such as proteins and they have a large impact in natural science. A well known example is the process of vision. Here, the cis to trans photoisomerization of the retinal protonated Schiff base chromophore, that is embedded in the visual protein, is the primary event in vision and a paradigm for fundamental studies of the molecular basis of vision [3-7]. The understanding of photoprocesses in nature as well as the description of photochemical properties of molecules in atomic scale requires accurate computational tools and physical models. Such theoretical tools should have the ability to describe both the ground and the photochemically relevant excited electronic states on the same footing and, desirably, with high accuracy. A key step in the description of photoinduced events lies in properly depicting radiationless non-adiabatic transitions which are coupled to atomic motions. Theoretical studies over the last decades, supported by experiments, have shown that internal conversion processes involve real crossing points between different electronic states, named conical intersections: this kind of transitions are “the rule rather than the exception” in photochemistry[3,8-10] and often determine the reaction rates and quantum yields. It is thus mandatory to select quantum mechanics (QM) methods [11] that are able to describe the electronic structure of these regions on the potential energy surface. Eventually, they should have the ability to describe the photoinduced the phenomena associated with population relaxation in the vicinity of such conical intersection which is the ultimate step necessary to model observable such as quantum yields and lifetimes, as well as transient spectroscopic signals.

Hybrid quantum mechanics/molecular mechanics (QM/MM) is a tool to model such processes in real/complex environments at the atomic level in real time. In this technique, the photoactive molecular region is studied at a suitable QM level [12-14], while all the rest of the system/environment surrounding that region is treated using classical molecular mechanics (MM) force field. This approach can be used to investigate large systems such as proteins. More details about QM/MM techniques, as well as the proper QM methods, will be presented later in this thesis.

1.2 Retinal proteins

Retinal proteins, also known as rhodopsins [15-17], achieve radiative into chemical energy transduction by an ultrafast internal conversion that involves the isomerization of the chromophore [18]. The speed and efficiency of this reaction is due to a conical intersection between the excited and ground electronic states that is responsible for both the lack of emission and the photochromism [3]. These properties are combined with the ability of rhodopsins to operate at different absorption wavelengths, a phenomenon known as spectral tuning [19,20]. Indeed, Nature has engineered the retinal chromophore such that it displays a cationic structure and a low lying bright transition with charge transfer character [21-24]. This property makes the system sensitive to the presence of an external electric field that may favour or hinder the intramolecular charge transfer process occurring upon absorption, thus resulting in energy gap modulation (see **Figure 1-1**). throughout the entire visible range. This wide operational spectral range observed in retinal proteins enables colour vision. In nature the energy gap modulation is achieved by via the non-uniform electric field of the opsin protein pocket embedding the retinal protonated Schiff base. The pronounced lighth-sensitivity of the retinal chromophore makes it an excellent candidate for the design of molecular machines capable of reversible photo-controlled reactions. Understanding the relation between chemical composition and photoinduced behavior in the retinal chromophore would allow to conceive devices with unprecedentedly high clock rates working without consuming any chemical reagent.

1.3 Aims of the Study

The first aim of this thesis is to explore the possibility to mimic the mechanism that is operative in rhodopsin proteins where photon energy transduction and colour vision is triggered by ultrafast and highly efficient cis-trans photoisomerization of the retinal chromophore embedded in the opsin pocket [3,25]. Changes in the protein allow the chromophore to operate over the whole visible spectrum [19]. Our study aims to artificially achieve analogous spectral modulation by applying an external electric field, to tune the colours (i.e., the absorption spectra) of retinal-inspired photoactive molecular materials and, ultimately, to control their photophysics and photochemistry. Indeed, the electric field can be used to induce even more radical modifications of the properties of retinal protonated Schiff-base chromophore (RPSB). Sufficiently high fields could in principle tune its energy gap so that the conical intersection becomes inaccessible and, as a consequence, the ultrafast photoisomerization is suppressed, thereby turning RPSB from an ultrafast photoswitcher into an efficient non-reactive light emitter (see **Figure 1-1**). In practice this could be facilitated

by designing synthetic RPSB analogs and pigments employing judicious substitutions which placed properly along the retinal polyene, will significantly affect (i.e., reduce) the light induced dipole of the chromophore **Figure 1-2** shows some examples of the retinal variants designed according to these principles, and displaying increased/decreased light induced dipole, according to the specific substitution considered. Their photophysical properties are modeled within/without a tunable electric field with different computational approaches. Eventually, such work may set solid guidelines for the design of ultrafast spectrally tunable molecular devices, based on judiciously modified RPSB or RPSB-mimics, whose polar substituents and groups may be employed as electric field generators to control their spectroscopic and photochemical properties and allow operation over a wide spectral range.

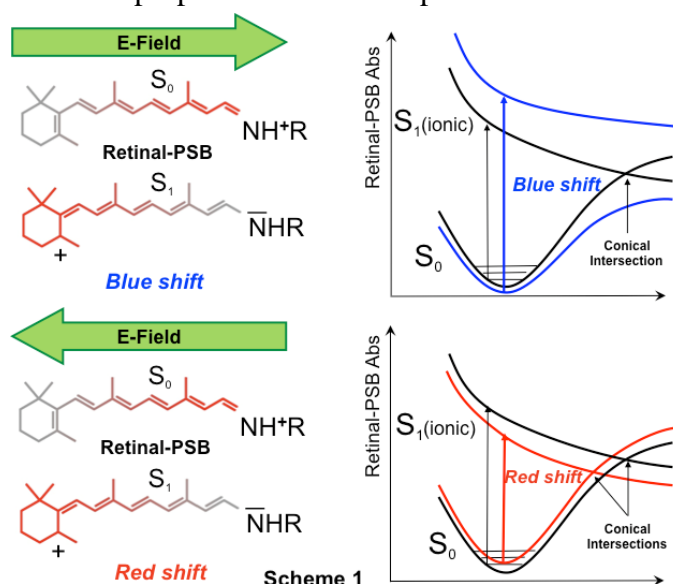


Figure 1-1. Visual rhodopsin (top). Mechanism of spectral tuning and conical intersection suppression in retinal.

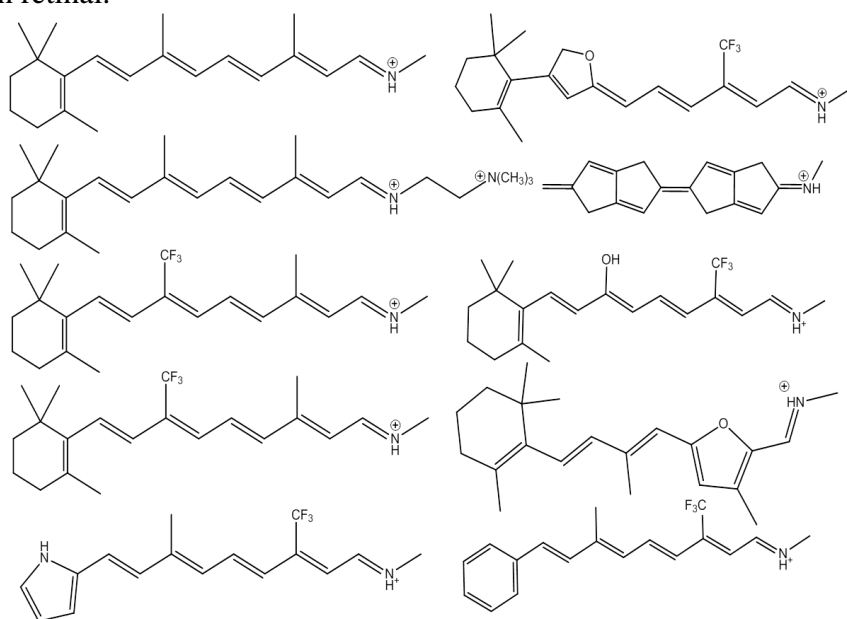


Figure 1-2. Proposals of retinal variants with potential electrochromic behavior.

The second aim of this thesis is the modeling of the isomerization mechanism of human melanopsin, invertebrate and vertebrate rhodopsins [26-28], and the prediction of the

photoisomerization rates and quantum yields by means of semiclassical non-adiabatic molecular dynamics at the quantum mechanics / molecular mechanics (QM/MM) level. The three visual pigments (bovine rhodopsin, Rh, squid rhodopsin, sqRh and human melanopsin, hMeRh) are absorbing at different wavelength (498, 476, and 462 nm) as a consequence of the different electric fields imposed by different environments around the same protonated retinal chromophore in their cavities [12,29-31]

A third aim of the thesis concerns the Siberian hamster ultraviolet (SHUV) visual pigment which incorporates an unprotonated Schiff-base (USB) retinyl chromophore in the dark state [32-35], which becomes protonated after photoexcitation during the early stages of the photobleaching cycle. In such pigment, the photochemical relaxation processes is poorly understood, and it is expected to show significant differences when compared to those of the protonated SB (PSB) chromophore in visual rhodopsin. The aim is to elucidate the photophysical/photochemical properties of SHUV-USB as compared to those of rhodopsin. Furthermore, we shed light on the SHUV-USB photoisomerization mechanism by investigating the viability of singlet/triplet inter-system crossings as well as photoinduced proton transfer. Multiconfigurational wavefunction methods coupled to multireference perturbative corrections within a hybrid quantum mechanics/molecular mechanics scheme, coupled to semiclassical non-adiabatic molecular dynamics, are employed for these studies. Comparisons of multireference and time-dependent density functional theory results are also presented.

It is apparent that understanding how the photoisomerization step works and can be tuned in those pigments could be very useful in designing mutants that fits our needs, for example absorbing light of the required wavelength or reacting with the desired rate and Quantum Yields. To achieve this goal, it is fundamental to understand each detail of the reaction mechanisms and the relation between chemical composition and topology of the potential energy surfaces of the photo-active states. Only after the reaction is carefully analyzed one can infer what can be done to change its course. Eventually, the aim of this thesis is to investigate, through high-level ab-initio QM/MM computations, the reaction mechanism underlying the photoreactivity of those systems and learn how to guide them so that those systems and processes can be successfully used in the design of bio-inspired photo-controlled molecular devices.

2 Ab Initio Quantum Mechanics (QM), Molecular Mechanics (MM) and Hybrid QM/MM Methods

2.1 Quantum Mechanics

Quantum mechanics (QM) is the body of scientific laws for the correct description of the behavior of electrons and thus of chemistry [36]. The use of molecular wave functions Ψ is the cornerstone of QM which provides an understanding of molecular structures, molecular energetics, and molecular dynamics. According to the QM, when the mathematical form of Ψ is known precisely for a certain system, it is possible, to compute the average value of any experimental observable property [37] (such as the energy, dipole moment, nuclear geometry, electron spin, transition probabilities, etc.) of a given state of a system for an assumed set of initial conditions and interactions in terms of a so-called *matrix element*.

$$\text{Observable Property } P = \langle \Psi/v/\Psi \rangle \quad (2.1)$$

where v is a mathematical operator containing the forces or interactions operating on Ψ to provide the property, P . If the property under investigation, P , is the energy, E , of the system, v is symbolized by \hat{H} and is known as the "Hamiltonian" operator or energy operator. According to the laws of QM mechanics, a wave function Ψ produced by solving the well-known Schrödinger wave equation [38]:

$$\hat{H}\Psi = E\Psi \quad (2.2)$$

mathematically, such equation is called an eigen equation. Ψ is then called the eigenfunction and E is an eigenvalue. The operator and eigenfunction could be a matrix and vector, respectively.

The Hamiltonian operator \hat{H} is, in general,

$$\hat{H} = - \sum_i^{\text{particles}} \frac{\nabla_i^2}{2m_i} + \sum_{i<j}^{\text{particles}} \frac{q_i q_j}{r_{ij}} \quad (2.3)$$

$$\nabla_i^2 = \frac{\partial^2}{\partial x^2} + \frac{\partial^2}{\partial y^2} + \frac{\partial^2}{\partial z^2} \quad (2.4)$$

where ∇_i^2 is the Laplacian operator acting on particle i (electrons and nuclei). m_i and q_i are the mass and charge of particle i , and r_{ij} is the distance between particles. The first term and the second term of the Hamiltonian give the kinetic energy of the particle and the energy due to Coulombic attraction or repulsion of particles, respectively. This formulation is the time-independent, nonrelativistic Schrödinger equation [36]. Further terms may appear in the Hamiltonian when the system is subjected to relativity or interactions with electromagnetic radiation or external electric fields. In fact, accurate wave functions many-particle molecular systems are extremely difficult to express because of the correlated motions of particles. Therefore the most important challenge is to find an expression for the wave function of a given molecular system in which the particles are in continuous movement and consequently

they interact with each other. In order to simplify the problem somewhat, some approximations would be used. One of the important approximations is the so-called Born-Oppenheimer approximation[39]; this assumption depends on the separation of the motion of both atomic nuclei and electrons in a given molecular system where the electrons move much faster than the nuclei. Mathematically, Born-Oppenheimer approximation allows the wave function of a molecule to be separated into its electronic Ψ_e and nuclear Ψ_n (vibrational, rotational) components where it simplifies the Hamiltonian expression by keeping the internuclear potential energy term as a constant and by eliminating the correlation terms in the electrons-to-nucleus potential energies[40]:

$$\Psi_{\text{Total}} = \Psi_e + \Psi_n \quad (2.5)$$

So,

$$(\mathbf{H}_e + \mathbf{V}_N) = \mathbf{E}_e \Psi_e \quad (2.6)$$

The last equation represents the electronic Schrödinger equation, where its eigenvalue is the electronic energy E_e . V_N is the nuclear-nuclear repulsion energy and it is a constant for a given set of fixed nuclear coordinates. In practice Eq. (2.6) is always solved without the inclusion of V_N in which case the eigenvalue is sometimes called the ‘pure electronic energy’, and one then adds V_N to this eigenvalue to obtain E_e .

Once the wave function has been determined, any property of the molecular system can be determined using Eq. (2.1) under the effect of the corresponding operator for that property. For instance, the energy is the expectation value of the value of the Hamiltonian operator given by

$$\langle E \rangle = \int \Psi^* \hat{H} \Psi \quad (2.7)$$

Such value is always greater than or equal to the exact energy so it is called the variational energy[41-43]. It is possible to determine different observable properties, such as the dipole moment or electron density if the corresponding operator is used. Properties other than the energy are not variational because only the Hamiltonian is used to obtain the wave function in the widely used computational chemistry methods. The best way to judge the quality of a wave function (in comparison to one another) is the evaluation of the energy eigenvalues associated with each. Where the one gives the lowest energy will be the most accurate and presumably the best one to use for computing other properties by the application of other operators. In particular, a wave function may be constructed as a guess of a linear combination of exact wave functions (the familiar hydrogenic atomic orbitals, 1s, 2s, 2p, 3s, 3p, 3d, etc.), so guess wave function ϕ constructed as a linear combination of atomic wave functions ϕ_i is given as:

$$\Phi = \sum_i^N c_i \phi_i \quad (2.8)$$

where the set of N functions ϕ_i is called the ‘basis set’ and each has associated with it some coefficient c_i . This construction is known as the *linear combination of atomic orbitals* (LCAO) approach[44,45].

One can evaluate the energy of the guess wave function [41-43].

$$\begin{aligned}
 E &= \frac{\int \phi_i H \phi_j dr}{\int \phi_i \phi_j dr} \\
 &= \frac{\sum_{ij} c_i c_j \int \phi_i H \phi_j dr}{\sum_{ij} c_i c_j \int \phi_i \phi_j dr} \\
 &= \frac{\sum_{ij} c_i c_j H_{ij}}{\sum_{ij} c_i c_j S_{ij}} \quad (2.9)
 \end{aligned}$$

where the matrix elements H_{ij} and S_{ij} are known as the ‘resonance integral’ and the ‘overlap integral’, respectively[40]. The overlap integral refers to the extent to which any two basis functions overlap in a phase-matched fashion in space. Orbitals which give rise to large overlap integrals will consequently give rise to large resonance integrals.

The coefficients c_i should be selected to the ones that minimize the energy for all possible linear combinations of the basis functions. Such condition is attained for a function (i.e., the energy) if its derivatives with respect to all of its free variables (i.e., the coefficients c_i) are zero. Accordingly, that is

$$\frac{\partial E}{\partial c_k} = 0 \quad (2.10)$$

where k refers to all orbital coefficients, applying this condition on Eq. (2.9) for all N variables, c_k gives rise to N equations which should be satisfied in order for Eq. (2.10) to hold true, so

$$\sum_{i=1}^N c_i (H_{ki} - E S_{ki}) = 0 \quad (2.11)$$

A non-trivial solution of the set of N equations in N unknowns is possible only if the determinant the unknown coefficients (i.e. $H_{ki} - E S_{ki}$) is equal to zero[40]. So,

$$\begin{vmatrix}
 H_{11} - ES_{11} & H_{12} - ES_{12} & \dots & H_{1N} - ES_{1N} \\
 H_{21} - ES_{21} & H_{22} - ES_{22} & \dots & H_{2N} - ES_{2N} \\
 & \vdots & \ddots & \vdots \\
 H_{N1} - ES_{N1} & H_{N2} - ES_{N2} & \dots & H_{NN} - ES_{NN}
 \end{vmatrix} = 0 \quad (2.12)$$

Solving this secular equation gives N roots corresponding eigenvalues E_j while by solving the set of linear Eqs. (2.11) will give rise to a different set of coefficients, c_{ij} , for each E_j . The coefficients then define an optimal wave function ϕ_j within the given basis set, i.e.,

$$\phi_j = \sum_{i=1}^N c_{ij} \phi_i \quad (2.13)$$

In a one-electron system, the lowest energy molecular orbital would thus define the ‘ground state’ of the system, and the higher energy orbitals would be ‘excited states’. One-electron system can be extended to a multi-electron system assuming that the energy of a

many-electron system as the sum of the energies of the occupied one-electron orbitals. Furthermore, the orbitals themselves are invariant to the number of electrons in the π system. Many attempts have been suggested to improve these models by taking a more sophisticated accounting of many-electron effects.

By considering only the one-electron kinetic energy and nuclear attraction terms, the Hamiltonian operator in Schrödinger may be expressed as following;

$$H = \sum_{i=1}^N h_i \quad (2.14)$$

where N is the total number of electrons and h_i is the one-electron Hamiltonian given by

$$h_i = -\frac{1}{2}\nabla_i^2 - \sum_{k=1}^M \frac{Z_k}{r_{ik}} \quad (2.15)$$

where M is the total number of nuclei and the corresponding one-electron Schrödinger equation for the one-electron Hamiltonian h_i is given as;

$$h_i\psi_i = \varepsilon_i\psi_i \quad (2.16)$$

The many-electron eigenfunctions for the Hamiltonian operator expressed by Eq. (2.14) can be constructed as products of one-electron eigenfunctions so;

$$\Psi_{HP} = \psi_1\psi_2 \dots \psi_N \quad (2.17)$$

where Ψ_{HP} is known as Hartree-product. By substitution Eqs. (2.14 & 2.17) in the electron Schrödinger equation, the eigenvalue of Ψ_{HP} is given as:

$$H\Psi_{HP} = H\psi_1\psi_2 \dots \psi_N \quad (2.18)$$

$$H\Psi_{HP} = \left(\sum_{i=1}^N \varepsilon_i \right) \Psi_{HP} \quad (2.19)$$

Eq. (2.19) proves that the energy eigenvalue of the many-electron wave function is simply the sum of the one-electron energy eigenvalues. Therefore, the Hartree-product wave functions are constructed from the individual ψ_i one-electron wave functions, which are actually not known, moreover, the electrons in HP assumption are not distinguishable and don't interact together. Therefore, a linear combination of the HP is required that is mathematically described using the Slater determinant [46] formalism as in the Hartree–Fock method.

2.1.1 The Hartree-Fock Self-Consistent Field Method

The Hartree–Fock method is built on the assumption states that a single Slater determinant of N spin-orbitals may express the exact N -body wave function of the system[47,48]. Using the variational method, it is possible to derive a set of N -Coupled equations for the N spin orbitals. The Hartree–Fock wave function and energy of the system is given by solving these equations as indicated in ref[40].

Self-Consistent field (SCF) method depends on an iteration process starting with a suitable initial-guess for the individual ψ_i one-electron wave functions with selecting an approximate h_i operators by solving the one-electron Schrödinger equation which then gives a new set of ψ_i . Such process is looped until the results converge [48,49]. According to the Pauli Exclusion Principle, any molecular orbital cannot be occupied with two electrons having the same spin quantum number [50]. Let α be the spin quantum number, a multi-electron wave function that satisfies Pauli exclusion principle can be expressed as a Slater determinant [46,51].

$$\Psi_{SD} = \frac{1}{\sqrt{N!}} \begin{vmatrix} \psi_1(1)\alpha(1) & \psi_1(1)\alpha(1) & \dots & \psi_N(1)\alpha(1) \\ \psi_1(2)\alpha(2) & \psi_2(2)\alpha(2) & \dots & \psi_N(2)\alpha(2) \\ \vdots & \vdots & \ddots & \vdots \\ \psi_1(N)\alpha(N) & \psi_2(N)\alpha(N) & \dots & \psi_N(N)\alpha(N) \end{vmatrix} \quad (2.20)$$

Considering the Coulomb interaction of each electron with the static field of all the other electrons, the individual HF MOs are given as the eigenfunctions of a set of one-electron operators [40]. The one-electron Fock operator is defined for each electron i as

$$f_i = \frac{1}{2} \nabla_i^2 - \sum_k^{\text{nuclei}} \frac{Z_k}{r_{ik}} + V_i^{\text{HF}} \{j\} \quad (2.21)$$

where the first term is related to the one-electron kinetic energy, the second term is the nuclear attraction contribution and V_i^{HF} is the Hartree-Fock potential and donated as $2J_i - K_j$ where J and K are the Coulomb and exchange operators.

$$\begin{vmatrix} F_{11} - ES_{11} & F_{12} - ES_{12} & \dots & F_{1N} - ES_{1N} \\ F_{21} - ES_{21} & F_{22} - ES_{22} & \dots & F_{2N} - ES_{2N} \\ \vdots & \vdots & \ddots & \vdots \\ F_{N1} - ES_{N1} & F_{N2} - ES_{N2} & \dots & F_{NN} - ES_{NN} \end{vmatrix} = \mathbf{0} \quad (2.22)$$

The S_{ij} elements are overlap integrals, similar to those previously given used in Eq. (2.9). The F elements depend on both the chosen basis set and the molecular orbitals. In order to determine the molecular orbitals, the method requires the availability of N basis functions and solving the secular Eq. (2.22) for E, the values of F_{ij} and S_{ij} being computed explicitly [52,53]. Given the couple of basis functions μ and ν , $F_{\mu\nu}$ is computed as[40]

$$F_{\mu\nu} = \left\langle \mu \left| -\frac{1}{2} \nabla^2 \right| \nu \right\rangle - \sum_k Z_k \left\langle \mu \left| -\frac{1}{r_k} \right| \nu \right\rangle + \sum_{\lambda\sigma} P_{\lambda\sigma} \left[(\mu\nu|\lambda\sigma) - \frac{1}{2} (\mu\lambda|\nu\sigma) \right] \quad (2.23)$$

The notation $\langle \mu | g | \nu \rangle$ implies an expression for the so-called one-electron integral of a basis function φ_ν where g is some operator.

$$\langle \mu | g | \nu \rangle = \int \varphi_\nu (g \varphi_\nu) d\mathbf{r} \quad (2.24)$$

The notation $(\mu\nu|\lambda\sigma)$ also implies a specific integration, in this case,

$$(\mu\nu|\lambda\sigma) = \iint \phi_\mu(1)\phi_\nu(1) \frac{1}{r_{12}} \phi_\lambda(2)\phi_\sigma(2) d\mathbf{r}(1)d\mathbf{r}(2) \quad (2.25)$$

where ϕ_μ , ϕ_ν , ϕ_λ and ϕ_σ are electron probability densities. The term $P_{\lambda\sigma}$ in Eq. (2.23) accounts for the contributions of base functions to a molecular orbital.

One of the defects of Hartree-Fock theory is due to the neglecting of the instantaneous interaction between the electrons, the so-called electron correlation. However, HF model is suitable for studying stable closed-shell molecules and other open-shell systems but it fails to give an accurate zeroth-order wave function in addressing systems in which the electron rearrangements is necessary[54]. Therefore, in those cases a more judicious treatment by including several electronic configurations in the wave function for better qualitative description. Many theories have been purposed to solve the problem of correlation energy. Some of them use the HF wave function as reference and then add a correction calculated using the variational principle such as configuration interaction (CI) or the perturbation theory such as Møller-Plesset (MP) as the natural extension of the Hartree-Fock method [11,55,56].

2.1.2 Configuration Interaction

Those methods play a central role in the studies of the electronic structure of molecules and chemical reaction mechanisms, especially in those concerned with electronic excited states.

In the CI method, the multi-electron wave functions are obtained from a linear combination of Slater determinants where the orbital coefficients are the HF coefficients. For instance, one can rewrite Eq. (2.6) for the ground state wave function as:

$$\Psi_I = \sum_L c_{LI} \Phi_L \quad (2.26)$$

Φ_L are the determinants of the ground state and all possible permutation of electrons among the available orbitals, then the corresponding Schrödinger equation is:

$$\sum_L c_{LI} \langle \Phi_K | \hat{H} | \Phi_L \rangle = E \sum_L c_{LI} \langle \Phi_K | \Phi_L \rangle \quad (2.27)$$

where $\langle \Phi_K | \hat{H} | \Phi_L \rangle$ is a general element of the Hamiltonian matrix and $\langle \Phi_K | \Phi_L \rangle$ is the overlap matrix element between Slater Determinants. The basis set constituted by the Slater determinants is an orthonormal set $\langle \Phi_K | \Phi_L \rangle = \delta_{KL}$, then one can rewrite Eq. (2.27) in this way:

$$HC_I = EC_I \quad (2.28)$$

where the eigenvector C_I collects all the coefficients weight contribution of each Slater determinant.

The full CI (FCI) refers the inclusion of all excitations in a given basis set. FCI calculations are too expensive and can only be performed for systems of a few atoms because the number of determinants increases rapidly with each order of excitation. However, since the method can in principle provide exact results, it is often used as a benchmark. In practice, approximations are required for the FCI method. For instance, the CIS method only includes singly excited determinants, while the CISD and CISDT methods include single and double excitations, and single, double, and triples excitations, respectively. In conclusion, the CIS method is quite fast, but not very accurate to describe electronic excitations since it can account only for single-excitation states. While the CISD is more accurate, but the

computational performance dramatically lowers down as the number of basis functions increases.

2.1.3 Multiconfigurational Self-Consistent Field

The multiconfigurational self-Consistent-field (MCSCF) method[57,58] is a general approach for describing chemical systems in which a single electron configuration is no longer an adequate description of the electronic structure. MCSCF methods are related to the CI method because they also use a multi-determinantal ansatz to describe the many-electron wave function. In other words, in the MCSCF method, one writes the wave function in CI form as a linear combination of Slater determinants, and the CI coefficients are determined variationally, as usual for CI wave functions. However, the orbitals are obtained to minimize the CI energy of the MCSCF wave function in contrasts to Hartree-Fock theory where the selected orbitals serve in decreasing the energy of a single Slater determinant, as in, [59]. Using this approach it is possible to get accurate results with a limited number of determinants. The mathematical methods to solve the MCSCF equations are very complicate and many different ways have been developed in this aspect. One way is depending on the optimization of the CI coefficients can be done by solving Eq. (2.28) without any difference from the normal CI procedure. The troublesome part is the orbitals optimization. The approach is based on a unitary transformation of the MO coefficients that leads to Newton-Raphson like equations.

Let Φ be an orthonormal basis set of orbitals and U the unitary transformation matrix that, applied to the basis set gives the transformed orbitals.

$$\Phi' = U\Phi \quad (2.29)$$

where U can be constructed as:

$$U = e^A = \begin{pmatrix} e^{A_{11}} & \dots & e^{A_{1n}} \\ \vdots & \ddots & \vdots \\ e^{A_{n1}} & \dots & e^{A_{nn}} \end{pmatrix} \quad (2.30)$$

that is based on a matrix (A) that is skew-symmetric ($A^T = -A$) in order to ensure that U is unitary. Therefore A can be expressed as a linear combination of E_{ij} matrices the elements of which are equal to 1 only at the $i - th$ row and $j - th$ column, whereas the other elements are zero. This allows rewriting Eq. (2.28) as:

$$U = e^{\sum_{ij} A_{ij} E_{ij}} \quad (2.31)$$

The wave functions have an analogous transformation as:

$$|\Psi'\rangle = e^A |\Psi\rangle \quad (2.32)$$

with an energy E' given by:

$$E' = \langle \Psi' | H | \Psi \rangle = \langle e^A \Psi | H | e^A \Psi \rangle \quad (2.33)$$

Such equation can be rewritten in the form of a Taylor expansion truncated to the second-order derivative term as following.

$$E' = E_0 + \sum_{ij} A_{ij} \left(\frac{\partial E}{\partial A_{ij}} \right)_0 + \frac{1}{2} \sum_{ijkl} A_{ij} A_{kl} \left(\frac{\partial^2 E}{\partial A_{ij} \partial A_{kl}} \right) \quad (2.34)$$

The same equation can, in turn, be expressed in matrix form, assuming that A is a column vector containing the parameters and defining F as a row vector containing the first order derivatives of the energies with respect to the skew-symmetric matrix elements, and defining G as the energy second order derivatives. According to such assumptions, Eq. (2.34) can be expressed as:

$$E' = E_0 + F_A + \frac{1}{2} A^T G A \quad (2.35)$$

The E' energy can be minimized if $\frac{\partial E \hat{a}}{\partial A} = 0$ that is true if $F + GA = 0$. That is:

$$A = -G^{-1}F \quad (2.36)$$

Since, according to equation 26, $U = e^A$ we can obtain U again as a Taylor expansion of the matrix exponential truncated to the second order term:

$$A = \mathbf{1} + A + \frac{1}{2} A^2 \quad (2.37)$$

The results of such sum of matrices, in the case A is skew-symmetric as this case, has the same form a rotation matrix has. This means that the orbitals optimization process is carried out by means of rotations which are iterated until convergence. Simulation softwares often implement the Complete Active Space Self-Consistent Field, CASSCF [54] or the Restricted Active Space Self-Consistent Field, RASSCF [60], both of them considering excitation as taking place only between a defined numbers of orbitals. According to such methods, the orbitals are subdivided into three groups: the core orbitals group, which is treated as a set of Hartree-Fock wave functions, the group of the occupied and empty active orbitals, where excitations are considered explicitly and eventually the virtual orbitals, treated as empty Hartree-Fock wave functions. These two methods display significant differences in the excitations that are introduced. In particular, in the CASSCF case, all the possible excitations are taken into account. On the contrary, in the RASSCF case, the excitations can be selected and the active space is further subdivided into three sections Section RAS1 contains occupied orbitals where only a defined number of the electrons can be excited. This is similar to a truncated CI. Section RAS2 contains both occupied and empty orbitals processed with CASSCF technique. Section RAS3 has the empty orbitals that can be occupied only by a defined number of electrons. The choice of the orbitals basis set for simulation has to be done taking into account the fact that the CPU usage dramatically increases with the number of the active orbitals introduced, so the use of the optimum basis set is not always viable. Therefore experience and intuition are an asset in the choice of a suitably limited set of active orbitals.

In conclusion, CASSCF method is commonly used nowadays because it has many attractive features[61]: (i) applicable to both the ground and excited state in single framework; (ii) size-Consistent; (iii) well defined on the whole potential energy surface if a suitable active space is chosen. On the other hand, CASSCF does not give accurate values in terms of energies such as the excitation energy (the error within several kcal/mol) the reason behind because it lacks to the dynamic correlation. Therefore, methods which consider account both the non-dynamic and dynamic correlations are required for better quantitative description. The multireference Møller – Plesset (MRMP) perturbation method [62,63], MCQDPT quasi-degenerate perturbation theory (QDPT) [64] with multiconfiguration self-consistent field reference functions (MC-QDPT) [65] and second order multireference perturbation theory (CASPT2) are perturbation methods of such a type. Using these

perturbation methods, it is possible to study the electronic structures of various systems since they are powerful tools for investigating excitation states and potential energy surfaces of chemical reactions. In the following sections, we introduce short summary about the CASPT2 methods.

2.1.4 Multiconfigurational Second Order Perturbation Method

The CASPT2 method is a post MCSCF method which allows computing the correlation energy of the rest of the system after the active part of the system has been treated with MCSCF. CASPT2 method [66,67] is based on correcting the wave functions applying the perturbation theory. Practically, The CASSCF wave function is followed by CASPT2 computations of the dynamic correlation energy of each state in order to get a more quantitative evaluation of the energies. Given a CASSCF wave function, the second order perturbation can be written on the basis of the $i - th$ perturbation Hamiltonians \hat{H}_i and the perturbation weight λ :

$$\hat{H} = \hat{H}_0 + \lambda \hat{H}_i \quad (2.38)$$

The energies can be expressed in a similar fashion:

$$\begin{aligned} E_0 &= \langle \Psi_0 | \hat{H}_0 | \Psi_0 \rangle \\ E_1 &= \langle \Psi_0 | \hat{H}_1 | \Psi_0 \rangle \\ E_2 &= \langle \Psi_0 | \hat{H}_1 | \Psi_1 \rangle \end{aligned} \quad (2.39)$$

In Eq. (2.36) the orthogonality is implied between the 0 - th order wave function and the perturbation. The \hat{H}_0 term is the \hat{F} Fock operator and since the CASSCF wave function is invariant with respect to rotations in the core, active and virtual orbitals, the Fock operator can be expressed as a superposition of diagonal subsets f_i :

$$\hat{H}_0 = \hat{F} = f_{cc} + f_{aa} + f_{vv} + f_{ac} + f_{vc} + f_{va} \quad (2.40)$$

in which the subscript c refers to core, a refers to active and v refers to virtual orbital spaces. The Hamiltonian of the perturbation is the difference between the whole Hamiltonian and \hat{H}_0 so that the wave function must be corrected by a term Ψ_1 that is the linear combination of the remaining configurations ϕ_μ in the CI space, i.e. except those of the active space. From a mathematical point of view:

$$\Psi_1 = \sum_{\mu} c_{\mu} \phi_{\mu} \quad (2.41)$$

where the C_{μ} is the linear combination coefficients:

$$c_{\mu} = \frac{\langle \phi_{\mu} | \hat{H}_1 | \phi_0 \rangle}{E_{\mu} - E_0} \quad (2.42)$$

From the CPU burden standpoint, the CASPT2 is very demanding.

2.2 A Brief Introduction to Molecular Mechanics

The most rigorous limitation of ab initio methods is the limited size of the molecule that can be handled on even the supercomputers. However Semiempirical calculations can be implied for large organic molecules, but are also too expensive for most biomolecular systems such as proteins. If a molecule is so big that a semiempirical treatment cannot be used effectively, the only possible way to model its behavior avoiding quantum mechanics totally by using molecular mechanics.

2.2.1 Basic Theory

Molecular mechanics is a simple "ball-and spring" model for molecular structure. Atoms (balls) are connected by springs (bonds), which can be stretched or compressed with a certain energy cost[51,68]. The energy expression effective potential for systems is expressed by a simple algebraic notation[69]:

$$E_{MM} = E_{bonds} + E_{angles} + E_{dihedrals} + E_{impropers} + E_{nonbonded} \quad (2.43)$$

where each term is a summation extended to all atoms involved in the system. Eq. (2.40) can be written in details as[70]:

$$\begin{aligned} E_{MM} = & \sum_{bonds} K_b (b - b_0)^2 + \sum_{angles} K_\theta (\theta - \theta_0)^2 + \sum_{dihedrals} K_x [1 + \cos(n\alpha - \delta)] \\ & + \sum_{impropers} K_\phi (\phi - \phi_0)^2 \\ & + \sum_{nonbonded} \left(\epsilon \left[\left(\frac{R_{min_{ij}}}{r_{ij}} \right)^{12} - 2 \left(\frac{R_{min_{ij}}}{r_{ij}} \right)^6 \right] + \frac{q_i q_j}{D r_{ij}} \right) \quad (2.44) \end{aligned}$$

The first term describes the bond-stretching term where K_b is the force constant of a covalent bond, b_0 is the bond's equilibrium length, and b is the bond's length; the second term describes bending of the angles between covalently bonded atoms where θ and θ_0 are the bond angle and its equilibrium value, and K_θ is the bending force constant; the third term describes torsion about the bond between the second and third of four sequential, covalently bonded atoms where the number of local energy minima is determined by n , and their corresponding internal dihedral angles α are determined by the offset δ . K_x is the associated force constant[71]. The fourth term, the improper dihedral, is used to keep atoms planar such as those which are sp² hybridized, and it is denoted by ϕ where K_ϕ is the respective force constant. The last term describes the Coulombic and van der Waals interactions where r_{ij} is the interatomic distance between atoms i and j . The depth of the Lennard-Jones well describing the van der Waals interaction is given by ϵ , and the location of its minimum is given by $R_{min_{ij}}$. The electrostatic interaction is represented by charges q_i , q_j the interaction of which is modified by an effective dielectric constant D .

The constants in this equation are determined empirically or from ab initio calculations that reproduce experimental data[72]. The fundamental assumption of the molecular mechanics method is the transferability of parameters. In other words, the energy penalty associated with a particular molecular motion such as the stretching of a carbon–Carbon

single bond will be the same from one molecule to the next. This gives a very simple calculation so MM methods are orders of magnitude cheaper from a computational point of view than quantum mechanical (QM) methods, and because of this, they have found a preferential position in a number of areas of computational chemistry such as molecular dynamics[6,12-14,30,73-79]. On the other hand electrons are not part of the MM description, and as a result, several chemical phenomena cannot be studied by this method. The accomplishment of MM technique is dependent on (i) the energy expression; (ii) the way by which the constant are parameterized; (iii) the method used to optimize constants from that data; and (iv) the user's skill to use the technique in a way consistent with its strengths and weaknesses.

2.3 Hybrid Quantum Mechanics/Molecular Mechanics (QM/MM)

However QM methods are able to compute many properties and model chemical reactions but they cannot be used to model large biomolecules (such as polypeptides, enzymes, nucleic acids, etc...). On the other hand molecular mechanics (MM) can model very large compounds quickly but they cannot model chemical reactions since the latter imply a change in the structure of the system. The hybrid QM/MM strategy originally introduced by Warshel and Levitt [80] opened the way to combine these two methods into one calculation which able to model a very large compound using molecular mechanics and the crucial portion of the molecule with quantum mechanics [14,73-75,77,81].

The QM/MM methods have the power to account for problems in which the electronic-structure calculations, including environmental effects, are essential or desirable. For instance it can be used for investigating structural and spectroscopic properties of complex biomolecular systems such as retinal proteins. Although there are a wide variety of QM/MM methods, the basic principle behind them is the same. Typically, the system under investigation is divided into two regions: a relatively small region of the system in which the chemical reactions occur is treated at a high level of theory (QM) and the remaining part is modeled with a low level of theory (MM force fields). Consequently, the hybrid QM/MM potential energy contains three types of interactions: (i) between atoms in the QM region, (ii) between atoms in the MM region, and (iii) between QM and MM atoms. Classes (i) and (ii) of interactions are relatively easily to describe at the QM and MM level, respectively. In the other hand the third kind of interaction between the two subsystems are more difficult to handle, and several approaches have been developed. These approaches can be categorized in schemes: subtractive and additive coupling schemes.

The total QM/MM energy of a system $E_{QM/MM}$ in *subtractive scheme* is calculated in the following steps. In the first step, the total energy of the system is computed at the MM level for both QM and MM atoms, $E_{MM}(MM + QM)$. Second, the QM energy of the isolated QM region is added, $E_{QM}(QM)$. Finally, the MM energy of the QM subsystem is computed, $E_{MM}(QM)$, and subtracted to correct for including the interactions within the QM subsystem twice:

$$E_{QM/MM} = E_{MM}(MM + QM) + E_{QM}(QM) - E_{MM}(QM) \quad (2.45)$$

The subtractive scheme is mostly used by the ONIOM method [82,83]. The main advantage of the subtractive scheme is that its implementation is relatively simple because the communication between the quantum chemistry and molecular mechanics routines is not required. On the other side, one of the drawbacks of this scheme is that a sufficiently

flexible force field is required for the QM region to account for the effect of any chemical change, this force field is not always available. A further disadvantage is that the QM electron densities do not polarize by the MM environment and this would be particularly problematic for modeling biological charge transfer processes, since these are usually mediated by the protein environment[84].

In additive schemes, the QM system is embedded within the larger MM system, and the energy for the whole system is a sum of MM energy terms, QM energy terms and QM/MM coupling terms[84]:

$$E_{QM/MM} = E_{QM}(QM) + E_{MM}(MM) + E_{QM-MM}(QM + MM) \quad (2.46)$$

In this scheme, no force field is required for the QM region where only the interactions within the MM region are described at the force field level, $E_{MM}(MM)$. Further, the interactions between the two QM and MM subsystems are treated explicitly: $E_{QM-MM}(QM + MM)$. These interactions can be described at various degrees of sophistication such as mechanical and electrostatic embeddings [76,85].

In the *mechanical embedding scheme*, the QM computations for the QM region is usually performed in the absence of the MM region, and the interactions between both regions are treated at the MM level. These interactions usually include both bonded (stretching, bending, and torsional) and non-bonded (electrostatic and van der Waals) interactions. While in an *electrostatic embedding scheme*, the QM computation for the QM is carried out in the presence of the MM by including terms that describe the electrostatic interaction between the QM and MM as one-electron operators that enter the QM Hamiltonian. The bonded and non-bonded van der Waals interactions between the QM and MM atoms are treated at the MM level[76].

2.3.1 COBRAMM as QM/MM Partitioning Scheme

COBRAMM software (Computational Bridge between Ab-initio and Molecular mechanic) has been developed at the Department of Chemistry at the University of Bologna to perform hybrid QM/MM calculations [77].

COBRAMM works as an interface combining several available codes which are working together thought exchanging data to deal with a specific problem. The most important feature of this approach is its ability to partition the system where QM/MM calculations are performed separately for the calculation of the energies and forces on one side and the projection of the new geometry on the other side this means that an independent QM and an MM calculation of the two regions are carried out to calculate the total QM/MM energy and the set of forces which finally give raise to a new geometry. During the last step the system is subdivided into two independent regions: the first one (Opt1) which is treated by a fast and rough algorithm such as Steepest Descents; the second is much smaller and it includes the QM part (Opt2/MD) where a sophisticated algorithm such as BFGS is used (Figure 2-2)[86]. There are two different cases, in the first the system is subdivided into two layers one known as high layer and is optimized at QM level with an accurate algorithms while the other is called low and it is handled by means of MM level using fast algorithm, such case appears if QM and Opt2/MD are identical. On the other hand, if the Opt2/MD is larger than QM, some other atoms are included together with the QM atoms, in the accurate geometry optimization or MD. Such approach shows a significant enhancement and it differs from the ONIOM-type methods [82,83] developed by Morokuma and co-workers where COMRAMM approach improves the simulation of the electrostatic interaction between the QM and MM regions

since the intermediate region is used to improve the reliability and efficiency in the optimization (or molecular dynamic) phase that allows the explicit treatment of large molecular motions around the reactive region without increasing the computational cost. In COBRAMM, the electrostatic influence of the surrounding MM region on the QM layer is taken into account by means of the electrostatic embedding approach[76,85].

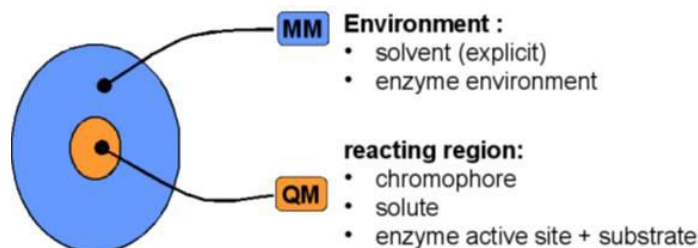


Figure 2-1. Schematic representation of the hybrid QM/MM approach.

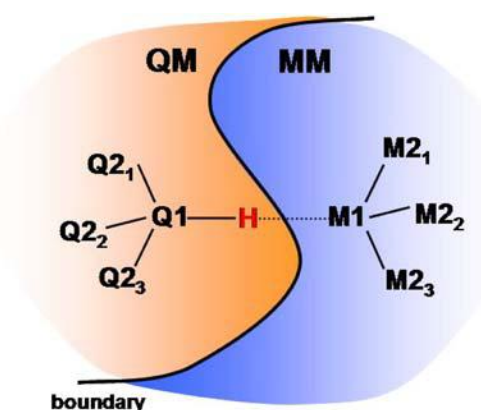


Figure 2-2. Boundary region crossing a covalent bond

There are several types of calculations implemented in COBRAMM depending on the combination among the three layers: High (H), Medium (M) and Low (L). For instance HML is a three layers level of calculation may be used to study the reaction mechanism of a photoisomerization processes in which the chromophore of is treated quantum mechanically (high layer), assigning the neighboring residues to the medium layer (MM) and leaving all the other residues of the protein in the low layer (Figure 2-4). Handling the boundary region between the QM and MM regions should be considered with a judicious manner to avoid unphysical results. There two different cases: the first is easy to handle where the QM layer is separated from the other layer through non-Covalent bond; the second in which the parceling between QM and MM regions scours via a covalent bond. The atom link approach [76,87-89] and the modified orbital methods [78,79,90,91] are two strategies have been proposed to account for the boundary region. In COBRAMM, the atom link approach is implied to handle the boundary region. Such approach is important in such cases where at least one covalent bond crosses the QM/MM boundary. Such cutting leaves the valence of the frontier QM atom (Q1 in Figure 2-2) remains unfilled (known as model). In this approach one hydrogen atom is added to the QM region as link-atom to form a bridge between the QM and the MM regions (model-H), furthermore the added H-atom compensates the valence. The atom-link approach is widely used and it gives realistic results however, the addition of artificial atoms that are not present in the original system, may cause problems in the total QM/MM energy value and in geometry optimizations. To avoid the problems due to the presence of such foreign H atoms, the position of those atoms is settled to be dependant at each step only on the line connecting Q1 and M1 atoms. Thus, removing two degrees while the last degree of

freedom can be simply eliminated by fixing the Q1-H distance for example at a fixed distance of 1.09 Å corresponding to the standard value for a C(sp³)-H.

QM calculation is implied to compute all the energy components of the high layer (QM region) while the bonded and non-bonded interactions within the medium and low layers (MM region) are computed at the MM level. The important challenge is the calculation of the electrostatic interactions between the QM and the MM region which is treated at QM level using an Electrostatic Embedding scheme in which QM computation are performed on model-H surrounded by the atomic point charges of the MM layers (i.e., the emb charges). The atomic point charges of the MM regions given by either pod or emb are identical (as given from the MM force field) except at the boundary region (**Figure 2-3**). In the emb scheme, the atomic point charge on the M1 atom near the hydrogen atom link (see **Figure 2-2**) is set to zero and its charge is spread on the neighbouring MM atoms (M2) such distribution of M1 charge will preserve the total charge of the system and avoid the unrealistic hyperpolarization of the wave function at the Q1-H bond.

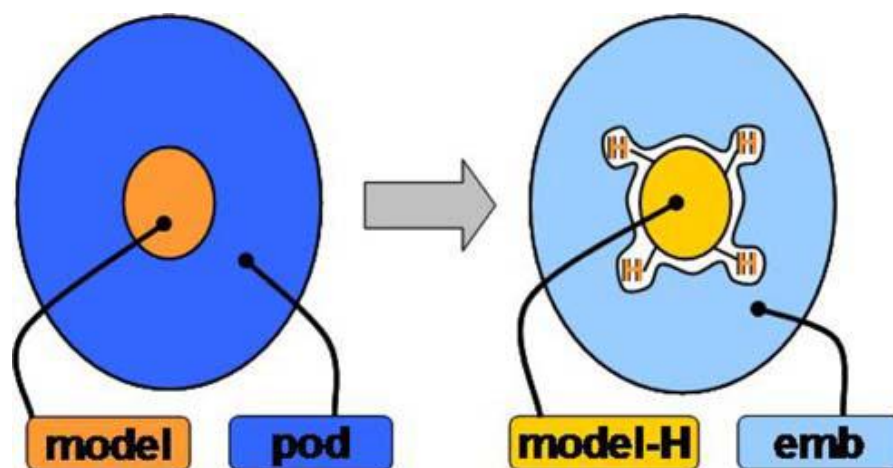


Figure 2-3. The atom-link approach implies a change in the original charges (pod) of the MM region to be introduced in the QM calculation, according to the electrostatic embedding scheme. The procedure to obtain the new set of charges (emb) is described in the text.

The total energy of the QM/MM system is given based according to the subtractive scheme as following [85]:

$$E^{tot} = E_{QM}^{model-H} + E_{MM}^{real} + E_{QM}^{el.model-H/emb} - E_{MM}^{el.model/pod} - E_{MM}^{model-H} \quad (2.47)$$

where the first term is the QM energy of the model-H in vacuum, and the third term describes the electrostatic interaction between the model-H and the emb subsystem. This allows the perturbation of the by the MM charges therefore the QM region is polarized by the MM environment. Both the first and third terms are computed are calculated together through a single QM computation on model-H in the bath of emb charges. The other terms of this equation represent the MM energies where they can be rewritten as:

$$E_{MM} = E_{MM}^{real} - E_{MM}^{el.model/pod} - E_{MM}^{model-H} = E_{MM}^{pod} - E_{MM}^{vdW.model/pod} - E_{MM}^{bond,bond,tors.model/pod} \quad (2.48)$$

where the first term involves only MM atoms, the second the third terms are cross contributions between the QM and MM atoms.

The atom-link scheme is a hydrogen link atom and the charges on M1 atoms are redistributed to its nearest-neighbors are two approximations are implied in this respect as previously described.

COBRAMM uses its own way to interface among series of standard commercial packages for QM and MM calculations including MOLCAS[92], GAUSSIAN03/09[93], MOLPRO[94], and others for the QM part; Amber [95,96] and Tinker [97] for the MM part.

The flowchart of the QM/MM interface implemented in COBRAMM is presented in **Figure 1-1**: in particular, points 2, 3, 4 and 5 do need external MM programs to calculate energies and forces, while point 6 uses a QM software to get the electrostatically embedded wave function and its energy and first derivatives. Point 7 merges all these results to give the total energy and gradient. Finally, in the ninth section, an external program for geometry optimization or molecular dynamics is used to generate the new geometry to restart the cycle. The calculation terminates when the convergence criteria are satisfied or when the time for a MD run is over.

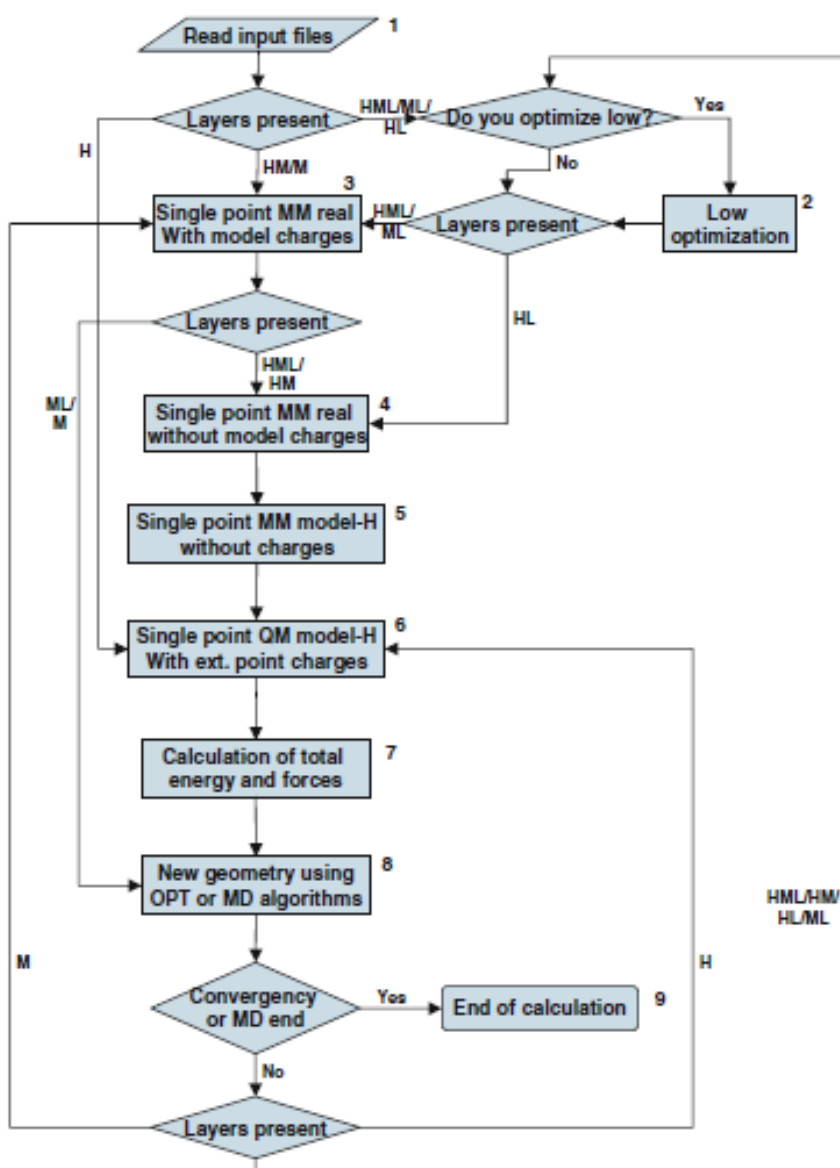


Figure 2-4. QM/MM implementation flowchart

3 Potential Energy Surfaces: Reaction Paths and Conical Intersections

The potential energy surface (PES) is a fundamental concept in computational chemistry. A PES is a mathematical or graphical relationship between the energy of a molecular system and its geometry [98-101]. PES is important in visualizing and understanding the relationship between potential energy and molecular geometry, and in understanding how computational chemistry programs locate and characterize structures under investigation. The most important aim of computational chemistry is to locate the structures and the corresponding energy along the PES: such “structures of interest” are Franck–Condon geometry, stationary points, transition states, and conical intersections between two states.

3.1 Stationary Points

A stationary point on a PES is a point at which the surface is flat where it occupies the lowest-energy point in its region of the PES, and any small change in the geometry increases the energy (**Figure 3-1a**).

The first and second derivatives of the energy with respect to the geometrical parameters can be used to construct a local quadratic approximation to the potential energy surface:

$$E(x) = E(x_0) + g_0 \Delta x + \frac{1}{2} \Delta x^T H_0 \Delta x \quad (3.1)$$

where g_0 is the gradient $(\frac{\partial E}{\partial x})$ at x_0 , H_0 is the Hessian $(\frac{\partial^2 E}{\partial x^2})$ at x_0 and $\Delta x = x - x_0$. The gradient and the Hessian can be used to confirm the minima and transition states characters.

Chemically, stationary points are minima or energy minima and they are corresponding to actual molecules with a finite lifetime, mathematically, at the stationary point, the first derivative of the potential energy with respect to each geometric parameter is zero i.e.

$$\frac{\partial E}{\partial x} = 0 \quad (3.2)$$

for all x , where x is a geometric parameter.

If the stationary point is the lowest-energy minimum on the whole PES it knows as global minimum, the relative minimum is a minimum compared only to nearby points on the surface. The lowest-energy pathway linking the two minima, the reaction coordinate or intrinsic reaction coordinate (IRC) is the path the molecule takes to pass from one minimum to another if it acquires enough energy to overcome the activation barrier, pass through a transition state (**Figure 3-1b**) [99]. The transition state linking the two minima displays a maximum along the direction of the IRC, but it is a minimum along all other directions. The Born–Oppenheimer approximation states that the nuclei in the molecule are essentially

stationary compared to the electrons. This is one of the cornerstones of computational chemistry because it makes the concept of molecular shape (geometry) meaningful, makes possible the concept of a PES, and simplifies the application of the Schrödinger equation to molecules by focusing on the electronic energy then adds in the nuclear repulsion energy later.

3.2 Geometry Optimizations

Due to the large number of internal coordinates of the molecule ($6N - 6$ where N is the number of atoms) and the failure of the algorithms in locating minima and/or transition states (TS), the identification of stationary points on the PES, which have a chemical meaning, remains a bothersome task[102,103]. The stationary point of interest might be a minimum, a transition state, or a higher-order saddle point.

Geometry optimization starts with an initial guess structure to find a stationary point (not necessarily the global minimum) on the PES. A special algorithm is usually required for transition state optimization, since it is more demanding than that required to find a minimum. Analytic first derivatives and (usually numerical) second derivatives are now used in optimization algorithms. Vibrational spectrum is usually carried out to investigate the type a stationary point (a minimum or a transition state). The algorithm for this depends on calculating an accurate Hessian (force constant matrix) and diagonalizing it to give a matrix with the “direction vectors” of the normal modes, and a diagonal matrix with the force constants of these modes. Real minimum has not any imaginary frequency, while a transition state has one imaginary vibration, corresponding to motion along the reaction coordinate. Moreover, vibrational frequencies calculation aids one to predict an IR spectrum and provides the zero-point energy (ZPE). The ZPE is needed for accurate comparisons of the energies of isomeric species as well as a starting structure for further computational investigations.

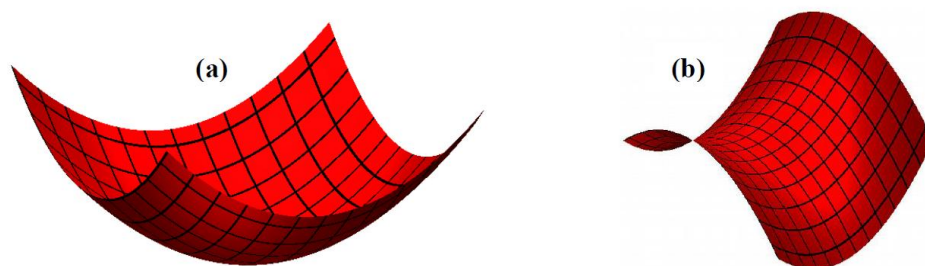


Figure 3-1. (a) Two dimensional minimum. (b) Two dimensional transition state.

3.2.1 Constrained Optimizations

Constrained geometry optimization is a general tool in finding transition states, exploring the energy as a function of specific internal coordinates, computing reactions paths (IRC), minimum energy paths (MEP), finding minimum energy cross point and searching for the conical intersections. For nonredundant coordinate systems and simple constraints, the coordinates under constrain can be easily deleted from the set of variables being optimized. different approaches have been developed to handle the constrain optimization such as Penalty functions, projection methods, and Lagrangian multipliers [104]. The penalty function method applies the constraints $C_i(x) = 0$ by adding an extra term, $\frac{1}{2} \sum \alpha_i C_i(x)^2$, to

the energy in Eq. (3.1) and the energy is minimized as usual. Where α_i should have a relatively large values so that the constraints are approximately attained at the minimum. The Lagrange multiplier method can solve optimization problems with equality constraints:

$$P\mathbf{g}_0 + PH_0P\Delta\mathbf{x} + \alpha(I - P) = \mathbf{0} \quad (3.3)$$

$$P = I - \sum_i \mathbf{c}_i \mathbf{c}_i^T / |\mathbf{c}_i|^2 \quad (3.4)$$

where the \mathbf{c}_i are a set of orthogonal constraint vectors and $\alpha > 0$. For redundant internal coordinates, the projector needs to remove the coordinate redundancies as well as the constraint directions[86].

3.3 Conical Intersection

Investigating the reactivity of excited molecular systems requires searching the decay point to the ground state, a numerous of computational and experimental studies have confirmed that the so-called conical intersections (CI) of PESs, predicted by von Neumann and Wigner in 1929 [105], are the rule rather than the exception in polyatomic molecules. In other words, the low-lying intersections (i.e. real crossings) between the reactive excited state and the ground state occur with a previously unsuspected frequency. The conical intersections play a critical mechanistic role in organic photochemistry. The location and characterization of conical intersections are therefore essential to the understanding of a wide range of excited state phenomena governed by non-adiabatic events, such as photoisomerization.

3.3.1 Conditions for the existence of conical intersections

In order to determine the crossing conditions for polyatomic molecules [106] one can suppose that the solution of the electronic wave function Schrödinger equation is known for all for functions except for ψ_1 and ψ_2 ones, those together with the found solutions, constitute a complete orthonormal set. The two missing solutions represent the two states (whose energy is E_1 and E_2) whose crossings is studied. Now is possible to express each of the two remaining electronic eigenfunctions as:

$$\Psi = c_1\psi_1 + c_2\psi_2 \quad (3.5)$$

The eigenstates and energies ε_1 and ε_2 in this basis are obtained by solving the secular problem:

$$\begin{bmatrix} H_{11} - E & H_{12} \\ H_{21} & H_{22} - E \end{bmatrix} \begin{bmatrix} c_1 \\ c_2 \end{bmatrix} = \mathbf{0} \quad (3.6)$$

where the matrix elements: $H_{ij} = \langle \psi_i | H | \psi_j \rangle$ and $H_{21} = H_{12}$. Solving Eq. (3.6) donates

$$E_{1/2} = \frac{H_{11} + H_{22} \pm \sqrt{(H_{11} - H_{22})^2 + 4H_{12}^2}}{2} \quad (3.7)$$

At the CI, $E_1 = E_2$, this means that the two energy solutions of Eq (3.8) do coincide and this occurs only if

$$H_{11} = H_{22} \text{ \& } H_{12} = H_{21} = 0 \quad (3.8)$$

For this condition to be satisfied, at least two independently variable nuclear coordinates are required. This explain why in diatomic molecule a real crossings can occur only between PES of two states if the states have a different (spatial or spin) symmetry, since there is only one variable nuclear coordinate (distance). This is not true the case of polyatomic systems [107] where two PES of a polyatomic molecule can in principle intersect even if their states have same symmetry and spin multiplicity. This means that for a polyatomic system two states (even with the same symmetry) will intersect along a $N - 2$ dimension hyperline as the energy is plotted against the N internal nuclear coordinates. In other words, there are $N - 2$ degrees of freedom along which the two electronic states preserve the degeneracy, while a displacement along the remaining two modes does separate the states. The vectors defining these two modes are called Derivative Coupling and Gradient and they define the so-called branching space[108,109].

If x_1 and x_2 are two independent coordinates satisfying Eq. (3.9) at their origin, then the secular equations can be written as:

$$\begin{bmatrix} W + h_1 x_1 - E & l x_2 \\ l x_2 & W + h_2 x_1 - E \end{bmatrix} \begin{bmatrix} c_1 \\ c_1 \end{bmatrix} = 0 \quad (3.9)$$

in another form

$$\begin{bmatrix} W + (m + k)x_1 - E & l x_2 \\ l x_2 & W + (m - k)x_1 - E \end{bmatrix} \begin{bmatrix} c_1 \\ c_1 \end{bmatrix} = 0 \quad (3.10)$$

where

$$m = \frac{1}{2}(h_1 + h_2), k = \frac{1}{2}(h_1 - h_2) \quad (3.11)$$

Then the eigenvalues are given as:

$$E = W + m x_1 \pm \sqrt{k^2 x_1^2 + l^2 x_2^2} \quad (3.12)$$

Eq. (3.13) is an equation of a double cone with vertex at the origin; this is the reason for calling such crossing points as conical intersections. Indeed, plotting the energies of the two intersecting states against the two internal coordinates x_1 and x_2 gives a double cone shape (Figure 3-2).

The physical meaning of the two conditions $H_{11} = H_{22}$ & $H_{12} = H_{21} = 0$ may be understood if we consider for ψ_1 and ψ_2 as the diabatic components of the adiabatic electronic eigenfunction, so the crossing condition (real or avoided) is fulfilled when the two diabatic components for ψ_1 and ψ_2 cross each other, and this occurs when $H_{11} = H_{22}$, i.e. the energy of the two diabatic potentials is the same.

At the crossing of the diabatic functions ($H_{11} = H_{22}$), the energies of the two real states is given by:

$$E_1 = H_{11} - H_{12}, E_2 = H_{11} + H_{12} \quad (3.13)$$

This means that an energy difference exists between the two states is:

$$\Delta\varepsilon = E_2 - E_1 = 2H_{12} \quad (3.14)$$

Apparently, if the exchange term $H_{12} = 0$, the two state energies are the same therefore the crossing takes place. On the other hand, if $H_{12} \neq 0$, the crossing will be avoided and the potential surfaces of the two real states will “diverge”, being one of the two energies slower and the other higher than the diabatic energy H_{11} . Moreover, the value of the exchange term H_{12} determines how deep the avoided crossing minimum is (small values will generate deep minima, big values shallow minima).

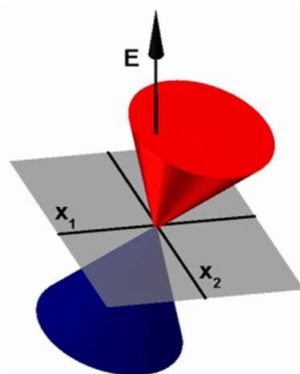


Figure 3-2. Double cone representation of a symmetric conical intersection within two-dimensional, which lifts the energetic degeneracy between the ground state (blue) and the excited state (red).

3.3.2 On the “Physical Chemistry” of Conical Intersections

In a thermal reaction, the TS forms a bottleneck that separates the reactant (R) and product energy wells along the reaction (P), **Figure 3-3a**. An accessible CI (**Figure 3-3b**) also forms a bottleneck that connects the excited state PES of the reaction path to the ground state one. The big difference between CIs and TSs is that, while the TS must lead to a single product via a single reaction path, an intersection is a “spike” on the ground state energy surface that connects the excited state reactant to the ground state via a branching reaction path that decay into several ground state relaxation channels giving two or more products (P and P’).

Mathematically, the double cone shape of the two intersecting potential energy surfaces can only be visualized by plotting the energies against as a function of the gradient difference vector x_1 and the gradient of the interstate coupling vector x_2 :

$$x_1 = \frac{\partial(E_1 - E_2)}{\partial q} \quad (3.15)$$

$$x_2 = \langle C_1 \frac{\partial \hat{H}}{\partial q} C_2 \rangle \quad (3.16)$$

C_1 and C_2 are the configuration interaction (CI) and \hat{H} is the CI Hamiltonian. The vector x_2 is parallel to the non-adiabatic coupling vector:

$$g_{(q)} = \langle \Psi_1 | \frac{\partial \Psi_2}{\partial q} \rangle \quad (3.17)$$

These geometric co-ordinates form the so called “branching space”. Where the degeneracy is preserved by moving from the apex of the cone along any of the remaining $n-2$ internal co-ordinates while moving away from the apex of the cone, the degeneracy is not available. The transition from the excited state to the ground state at the CI demonstrates a critical challenge because the non-adiabatic transition is rigorously quantum mechanically without a well-defined classical analogue. At a crude level of theory the probability of a surface hop is given as[110]:

$$P = e^{-\frac{\pi}{4}\zeta} \quad (3.18)$$

where the Massey parameter ζ is:

$$\zeta = \frac{\Delta E(q)}{\hbar |q| g(q)} \quad (3.19)$$

In words this means that an efficient radiationless transition is more likely to occur if the energy gap $\Delta E(q)$ is small as well as the product of the velocity vector and the non-adiabatic coupling $g(q)$ is large.

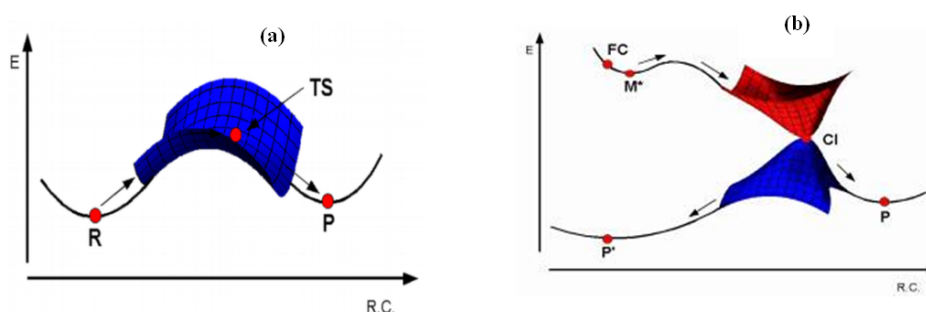


Figure 3-3. Schematic behavior of a thermal reaction. (b) Schematic behavior of a photochemical reaction.

3.3.3 Conical Intersection Optimization

Practically, the CI usually exists along a valley on the excited state PES. As the system moves down from the Franck–Condon (FC) region, it arrives to the excited state minimum M^* , this minimum may be connected to the CI trough a TS (**Figure 3-3b**). In some situations such TS connecting M^* to the intersection point or where an excited state intermediate on the upper energy surface does not exist. In such situations, mechanistic information must be obtained by locating the lowest lying intersection point along the $N - 2$ intersection space of the molecule.

Different approaches have been developed to optimize structures where two electronic states become degenerate. Such approaches are based on Lagrange-Newton methods [111-113] or projection methods [113-116]. The algorithms belonging Lagrange-Newton methods are generally very efficient since they are depending on the variations of the classical Lagrange multipliers method [117,118]. However these methods require higher

computational cost, furthermore they are difficult to be efficiently implemented and improved. One of the main challenge is related to the Lagrange Hessian, which is not positive definite, i.e., for each constraint a negative eigenvalue arises. Therefore efficient methods such as the Broyden- Fletcher-Goldfarb-Shanno (BFGS) scheme cannot be employed, and the overall algorithm may be affected in terms of efficiency and convergence rate [118-121]. In contrast, the projection methods establish the energy degeneracy by means of a displacement within the branching space, while optimizing simultaneously the energy of the excited state within the intersection space[122]. Bearpark et al. have developed an algorithm based on projection matrices, uses a gradient composed of two distinct parts [123]. One part represents the normalized gradient difference vector is responsible for minimizing the energy difference between the two crossing states. The other part of the gradient optimizes the excited-state energy within the intersection space. Therefore a critical point on the intersection hyperline can be located.

3.4 Locating Reaction Paths

The photochemical paths leading to the final photoproducts are computed in two steps. In the first step the MEP describing the excited state relaxation from the FC region is calculated. This MEP is unambiguously determined by using a methodology[124] to locate the Initial Relaxation Direction (IRD) from the starting point (i.e. the FC). Briefly, an IRD corresponds to a local steepest descent direction, in mass-weighted Cartesian coordinates, from a given starting point. The IRD is calculated by locating the energy minimum on a hyperspherical (i.e. $n-1$ dimensional) cross-section of the n dimensional PES centered on the starting point. We call this $n-1$ dimensional optimized structure "Hyperminimum". The radius of this hypersphere is usually chosen to be small (typically ca. 0.5-1.5 au. in mass-weighted Cartesian) in order to locate the steepest direction in the vicinity of the starting point (i.e. the hypersphere centre). The IRD is then defined as the vector joining the starting point to the Hyperminimum. Once the IRD has been determined, the MEP is computed as the steepest descent line in mass-weighted Cartesians (that is, the IRC) using the IRD vector to define the initial direction to follow. After the first point has been optimized by following the IRD direction, the IRC algorithm follows the forces acting along the reaction coordinate and optimizing the consecutive points at a distance which is proportional to the forces and to a chosen step size.

As stated above, by following downhill the MEP key structure like minima, CI and bifurcation points can be located. In the second step, the MEP describing the S_0 relaxation process from the S_1/S_0 CI determined in the first step is calculated with the same methodology and the paths leading to the various photoproducts are determined. In order to locate all the possible decay channels starting from a CI, all the chemically-Reasonable ways of re-Coupling the electrons and realistic molecular motions have to be systematically explored. Only when a decay channel cannot be found (or it starts at great distance from the CI), that reaction process can be ruled out.

4 Nonadiabatic Molecular Dynamics with Semiclassical Trajectories

4.1 Introduction

The molecular potential energy surface (PES) is a fundamental concept for the theoretical understanding of chemical reactivity [98-100]. PESs are described within the so-called Born-Oppenheimer approximation, which adiabatically separates the electronic and nuclear dynamics as a consequence of the large difference in mass for both nuclei and electrons [39]. Within the Born-Oppenheimer approximation, the time-independent electronic Schrödinger equation is usually solved for a given nuclear configuration, the gradient of the corresponding eigenvalues providing the quantum mechanical forces acting on the nuclei [125]. This approximation is usually suitable for the description of the molecular systems in their electronic ground state while it breaks down for a wide range of excited-state phenomena, particularly those where two or more electronic states are strongly coupled [126]. Well-known examples of this behavior would include processes like radiationless decay [127], energy and charge transfer [128], and photochemical reactions, their proper description requiring the inclusion of more accurate nonadiabatic molecular dynamics schemes to correctly describe phenomena beyond the Born-Oppenheimer approximation [39]. Ab initio nonadiabatic molecular dynamics schemes based on the mixed quantum/classical propagation of an ensemble of classical trajectories are the most prominent computational approaches that reproduce macroscopic observables such as quantum yields or fluorescence intensities. These approaches are usually implemented numerically with different electronic structure methods such as time-dependent version (TDDFT) [129-131] and Complete Active Space Self-Consistent Field (CASSCF) [132].

Tully's fewest switches trajectory surface hopping (TSH) [133,134] is probably the most widely used scheme for mixed nonadiabatic quantum/classical dynamics [135]. TSH does not require explicit propagation of the nuclear wave functions; instead, the nuclear wave packets are represented by a swarm of independent classical trajectories that follow different states along their PESs, while the hopping probability among the different surfaces depends on the nonadiabatic couplings and Tully's coefficients. Many other schemes have been adapted to handle the nonadiabatic dynamics of the nuclear degrees of freedom, such as linearized nonadiabatic dynamics (LAND-map) [136], correlated electron-ion dynamics [137], quantum/classical Liouville approaches [138,139], semiclassical approaches, extended surface hopping and hydrodynamic nonadiabatic dynamics methods [140] or direct quantum dynamics methods based on the Multiconfiguration Time-Dependent Hartree ansatz (MCTDH)[141]. Recently, the vMCG method has been developed depending on the full variational solution to the time-dependent electronic Schrödinger equation (TDSE) based on a time-dependent Gaussian wavepackets GWP basis [142]. This method is directly applicable to all types of problems related to both tunneling and non-adiabatic systems, with only a few GWPs capturing the major physics of these processes. Furthermore, this method is under development to be a general tool in developing quantum dynamics, especially in treatment large molecular systems.

4.2 Mixed Quantum–Classical Dynamics

For a molecular system treated with mixed quantum–Classical dynamics[134], where the electronic and nuclear degrees of freedom are separated, the nuclei are treated classically; the electrons evolve according to the time-dependent electronic Schrödinger equation (TDSE) that is given by:

$$i\hbar \frac{\partial}{\partial t} \Psi_{el}(r, R, t) = \hat{H}_{el}(r, R) \Psi_{el}(r, R, t) \quad (4.1)$$

where $\Psi_{el}(r, R, t)$ is the total wave function of the system, and r and R refer to the coordinates of the electrons and the nuclei, respectively.

The time-dependent electronic Hamiltonian may be split to different contributions as follows[143]

$$\hat{H}_{el}(r, R) = \hat{T}_{el} + \hat{V}_{ee} + \hat{V}_{en}(R) + \hat{V}_{nn}(R) + \hat{V}_{ext}(t) \quad (4.2)$$

where \hat{T}_{el} represents the kinetic energy of the electrons, \hat{V}_{ee} , $\hat{V}_{en}(R)$ and $\hat{V}_{nn}(R)$ are the columbic attraction and repulsions, and $\hat{V}_{ext}(t)$ is a time-dependent external potential.

By adding the operator of nuclear kinetic energy \hat{T}_n to $\hat{H}_{el}(r, R)$, the total Hamiltonian of any molecular system denote by

$$\hat{H}(r, R) = \hat{T}_n + \hat{T}_{el} + \hat{V}_{ee} + \hat{V}_{en}(R) + \hat{V}_{nn}(R) + \hat{V}_{ext}(t) \quad (4.3)$$

An exact expression for the total wave function $\Psi(r, R, t)$ is given by expanding to the complete basis set of electronic eigenfunctions $\hat{H}_{el}(r, R)$ [144-146];

$$\Psi(r, R, t) = \sum_i^{\infty} \Omega_i(R, t) \Phi_i(r; R) \quad (4.4)$$

The expansion “coefficients”, $\Omega_i(R, t)$ are functions of time and the nuclear coordinates, R . Replacing Eq. (4.4) into the Eq. (4.1), multiplying by $\Phi_j^*(r; R)$ and then integrating over r gives rise to the amplitude equation motion, $\Omega_j(R, t)$ [146]:

$$i\hbar \frac{\partial}{\partial t} \Omega_j(R, t) = \left[- \sum_{\gamma} \frac{\hbar^2}{2M_{\gamma}} \nabla_{\gamma}^2 + E_j^{el}(R) \right] \Omega_j(R, t) + \sum_i^{\infty} F_{ji}(R) \Omega_i(R, t) \quad (4.5)$$

$F_{ji}(R)$ represents the elements of the nonadiabatic coupling matrix between two different electronic states (*i.e.* $i \neq j$).

The BO approximation is given from Eq. (4.4) by neglecting all off-diagonal terms of $F_{ji}(R)$. Therefore each PES can be represented by a molecular wave function described as:

$$\Psi(r, R, t) = \Omega_j(R, t) \Phi_j(r; R) \quad (4.6)$$

The adiabatic BO approximation is calculated by neglecting the diagonal terms of $F_{ji}(R)$. The polar representation of $\Omega_j(R, t)$ is given by

$$\Omega_j(\mathbf{R}, t) = A_j(\mathbf{R}, t) \exp \left[\frac{i}{\hbar} S_j(\mathbf{R}, t) \right] \quad (4.7)$$

where both the amplitude, $A_j(\mathbf{R}, t)$, and the phase, $S_j(\mathbf{R}, t)$, are real. By inserting Eq. (4.7) into Eq. (4.5) one can get the so-called Hamilton-Jacobi equation of motion[146]:

$$\frac{\partial S_j(\mathbf{R}, t)}{\partial t} = -\frac{1}{2} M_\gamma^{-1} (\nabla_\gamma S_j(\mathbf{R}, t))^2 - E_j^{el}(\mathbf{R}) \quad (4.8)$$

where $S_j(\mathbf{R}, t)$ represents the classical Hamilton's principal function. From Eq. (4.8), we can obtain the Newtonian equation of motion for the nuclei:

$$F_j(t) = M_\gamma \ddot{R}_j^\gamma(t) = -\nabla_j E_j^{el}(\mathbf{R}(t)) \quad (4.9)$$

As the nuclei evolve on a given PES, the electrons adiabatically follow the nuclei along their classical trajectories. Thus, in the BO molecular dynamic method depends on an iteration process starts by solving TDSE to obtain the potential and the forces acting on the nuclei; these are then used to calculate the new nuclei coordinates at time step dt using Eq. (4.9), and the process is looped for certain time[146].

4.3 Surface Hopping Approach

As any trajectory evolves on a single adiabatic PES at each instance in time, the population probability of each state is non-zero according to Eq. (4.5). The force is then given by the gradient of a single surface

$$F_\alpha = -\nabla_\alpha E_j \quad (4.10)$$

At any time, the classical wavepacket is allowed to instantly switch from the surface it is evolving on to another surface, an event called a surface hop. The decision of hoping is taken stochastically by calculating the population on each state $a_{jj} = c_j^* c_j$ according to Eq. (4.5). There are several approaches to determine whether a hop should occur. The simplest way is to allow surface hop when the population of a certain state exceeds a certain threshold [147]. Another approach depends on the Landau-Zener transition probabilities[148,149]. Probably the most popular approach is the "fewest switches" developed by Tully [133,134], that will be discussed next.

4.3.1 Tully's Trajectory Surface Hopping

Tully's fewest switches surface hopping (FSSH) algorithm is one of the most popular approaches for nonadiabatic Surface Hopping [133,134]. The widespread popularity of FSSH is due to its extreme simplicity and computational efficiency[150]. In this approach, the nuclei are treated classically while quantum mechanical effects are accounted for the nonadiabatic transfer of "amplitude" between electronic states[146]. This is achieved by allowing the trajectories to hop from one surface to another according to nonadiabatic couplings the values of the state amplitudes, $C_i^{[\alpha]}(t)$ which is given from the description of the molecular wave function [134]

$$\Psi^{[\alpha]}(\mathbf{r}, \mathbf{R}, t) = \sum_i^{\alpha} C_i^{[\alpha]}(t) \Phi_i^{[\alpha]}(\mathbf{r}; \mathbf{R}) \quad (4.11)$$

Inserting the last equation into the TDSE, for a given trajectory α , one gets a set of coupled equations of motion for the complex nuclear state amplitudes, $C_i^{[\alpha]}(t)$:

$$i\hbar\dot{C}_i^{[\alpha]}(t) = \sum_i^{\alpha} C_i^{[\alpha]}(t) \left(E_i^{el}(\mathbf{R}^{[\alpha]})\delta_{ij} - i\hbar \sum_{\gamma}^{N_n} \mathbf{d}_{ji}^{\gamma}(\mathbf{R}^{[\alpha]}) \cdot \dot{\mathbf{R}}_{\gamma}^{[\alpha]} \right) \quad (4.12)$$

where $d_{ji}^{\gamma}(\mathbf{R})$ are the first-order nonadiabatic coupling given by

$$\mathbf{d}_{ji}^{\gamma}(\mathbf{R}) = \int d\mathbf{r} \Phi_j^*(\mathbf{r}; \mathbf{R}) \nabla_{\gamma} \Phi_i(\mathbf{r}; \mathbf{R}) \quad (4.13)$$

The probability for any classical trajectory α evolving adiabatically in a given electronic state, j to hop to another state i during the time interval $(t; t + dt)$ is given by solving Eqs. (4.12) [146]:

$$g_{ji}^{[\alpha]}(t, t + dt) = 2 \int_t^{t+dt} d\tau \frac{-\Re[C_i^{[\alpha]}(\tau)C_j^{[\alpha]*}(\tau)\Xi_{ij}^{[\alpha]*}(\tau)]}{C_j^{[\alpha]}(\tau)C_j^{[\alpha]*}(\tau)} \quad (4.14)$$

where

$$\Xi_{ij}^{[\alpha]}(\tau) = \sum_{\gamma}^{N_n} \mathbf{d}_{ij}^{\gamma}(\mathbf{R}^{[\alpha]}) \cdot \dot{\mathbf{R}}_{\gamma}^{[\alpha]} \quad (4.15)$$

A surface hop from j to i occurs when a randomly generated number, $\eta \in [0, 1]$ attains:

$$\sum_{k \leq i-1} g_{jk}^{[\alpha]} < \eta < \sum_{k \leq i} g_{jk}^{[\alpha]} \quad (4.16)$$

In other words, at any time step the change of population of a particular state j is expressed as[151]:

$$\Delta a_{jj} = - \sum_i p_{j \rightarrow i} a_{jj} + \sum_i p_{i \rightarrow j} a_{ii} \quad (4.17)$$

where $p_{j \rightarrow i}$ is the transition probability from state j to state i . According to Eq. (4.17) at every time step there is a non-zero probability for population transfer from j to i and backwards. Tully's ansatz looks for the fewest number of switches to set up the final population in all states at the end of the time step, for this reason, this approach is referred to as the "fewest switches algorithm". This can be attained by allowing the population transfer in only one direction[151]. For a two-state case the transition probability is given by the expression

$$p_{j \rightarrow i} = - \frac{\Delta a_{jj}}{a_{jj}} \quad (4.18)$$

By implying a short time step t , the change of the population Δa_{jj} can be approximated using a first order Taylor expansion

$$\Delta a_{jj} = \frac{\partial a_{jj}}{\partial t} \Delta t \quad (4.19)$$

and using Eq. (4.18) the fewest switches expression for transition probability is given as[151]

$$p_{j \rightarrow i} = -\frac{2\Re(a_{jj})\vec{F}_{ij} \cdot \vec{v}}{a_{jj}\Delta t} \quad (4.20)$$

This approach can be used to for more than two electronic states where the hop can occur at any time step if two conditions are fulfilled. First, if the transition probability from state to another is higher in magnitude than a randomly chosen threshold between the (0,1), and second, if the total energy of the system is conserved. The latter is attained by readjusting the velocity of the system to compensate the instant change in the potential energy. Such velocity adjustment can be performed in different ways; a common way is to perform it along the non-adiabatic vector \vec{F}_{ij} [152], alternative way is achieved by the adjustment along the energy difference gradient or along the velocity vector [151]. A hop to a higher PES is not allowed if the velocity reduction is higher than the component of the velocity in direction of \vec{F}_{ij} [153], although Eq. (4.5) suggests an electronic transition. These classically forbidden electronic transitions are the result of the deficiency of the classical description of a quantum mechanical property as the non-adiabaticity. The quality of the surface hopping approach is reflected in its ability to reproduce the averaged occupation $\bar{a}_{jj}(t)$ of state j at time t [151] (quantum mechanical quantity)

$$\bar{a}_{jj}(t) = \frac{\sum_j |N_j(t)|^2}{N_{tot}} \quad (4.21)$$

by the fraction of trajectories $N_j(t)$ evolving on state j (classical quantity)

$$f_j(t) = \frac{N_j(t)}{N_{tot}} \quad (4.22)$$

4.4 Equation of Motion: Integration

The molecular dynamics (MD) trajectories are usually performed using the Velocity Verlet algorithm [154] according to the classical Newton's equations which are solved numerically. At time (t) the algorithm requires coordinates, velocities and forces as input in each time step of a classical dynamics simulation. In the first step of the algorithm the coordinates for the new time step ($t + dt$) are determined:

$$\vec{r}(t + \Delta t) = \vec{r}(t) + \vec{v}(t) \cdot \Delta t + \frac{1}{2} \vec{F}(t) \cdot \Delta t^2 \quad (4.23)$$

where \vec{r} are the coordinates, $\vec{v}(t)$ the velocities and $\vec{F}(t)$ the force determined at time (t) from QM/MM calculation. The integration step Δt is the time step of the MD simulation. Also, the half-step velocities are computed:

$$\vec{v}\left(t + \frac{1}{2}\Delta t\right) = \vec{v}(t) + \frac{1}{2}\Delta t \cdot \vec{F}(t) \quad (4.24)$$

In the second step these velocities are used together with the new forces $\vec{F}(t + dt)$ to complete the integration and obtain the velocities for the next step using:

$$\vec{v}(t + \Delta t) = \vec{v}\left(t + \frac{1}{2}\Delta t\right) + \frac{1}{2}\vec{F}(t + \Delta t) \quad (4.25)$$

The velocity is needed for calculating the transition probability $p_{j \rightarrow i}$ (Eq. (4.19)) and for monitoring the conservation of total energy during surface switching. The Velocity Verlet algorithm has accuracy of the order of Δt^3 for positions and velocities[151].

The Velocity Verlet algorithm depends on iteration process based on Eqs. (4.23) and (4.25). In this process, for a given position r at time t , a first new position $r(t + \Delta t)$ is calculated using Eq. (4.23), then at $r(t + \Delta t)$ the new force is obtained using Eq. (4.10). It is then used to calculate the velocity at $r(t + \Delta t)$ through Eq. (4.25).

4.5 Sampling of Initial Conditions

One of the most important steps in mixed quantum/classical dynamics is the definition of the initial conditions for the swarm of trajectories. It is important to generate a swarm of trajectories that correctly account for the distribution of the GS wavepacket in phase space. Two common approaches exist in the literature have been proposed to generate the initial conditions: the first one depends on the zero-point level of the molecular system (known as the quantum or Q sampling) while in the second the molecular systems is considered in thermal equilibrium with the environment (known as thermal or T sampling)[155].

According to quantum sampling, Wigner's quasi-probability distribution [156] provides the probability distribution for a quantum mechanical wave function in phase space and encodes all expectation values. Phase space distribution is given by the Wigner distribution function[151]

$$P_w(\vec{q}, \vec{p}) = (2\pi\hbar)^{-1} \int \chi^*\left(\vec{q} + \frac{\vec{s}}{2}\right) \chi\left(\vec{q} - \frac{\vec{s}}{2}\right) \exp\left(\frac{i}{\hbar}\vec{s}\vec{p}\right) d\vec{s}. \quad (4.26)$$

This representation gives a correct expression for the probability of a quantum mechanical wave function in phase space. Assuming a quadratic approximation for the GS potential the GS wave function $\chi(\vec{q})$ can be spanned in the basis of eigenfunctions $\chi(\vec{q}_i)$ of the $3N - 6$ one-dimensional harmonic oscillators along the normal modes $q_1 \dots q_{3N - 6}$ with reduced masses μ_i and harmonic frequencies ω_i

$$\chi(\vec{q}_i) = \left(\frac{2\alpha}{\pi}\right)^{\frac{1}{4}} \exp\left(-\alpha\vec{q}_i^2 + \frac{i}{\hbar}\vec{p}_i\vec{q}_i + \frac{i}{\hbar}\gamma\right) \text{ with } \alpha = \frac{\mu_i\omega_i}{2\hbar} \quad (4.27)$$

Inserting the expression (Eq. 4.27) in the Wigner distribution (Eq. 4.26) and evaluating the integral gives

$$P_w(\vec{q}, \vec{p}) = (\pi\hbar)^{-1} \exp\left(-\frac{\mu_i\omega_i}{2\hbar}\vec{q}_i^2\right) \exp\left(-\frac{1}{\mu_i\omega_i\hbar}\vec{p}_i^2\right) \quad (4.28)$$

Eq. (4.28) gives the distribution of a quantum mechanical wavepacket in phase space. It can be utilized to sample the phase space and to reproduce the quantum dynamical distribution for quasiclassical trajectory runs.

An independent distribution sampling in coordinate space is performed for each mode. As GS vibrational wave functions are used, the maximal imposed displacement along a normal mode corresponds to a conversion of the zero-point energy $E_i^{ZVP} = \frac{1}{2\omega_i}$ into potential energy. Subsequently, the conjugated momentum is evaluated for each displacement and a stochastic algorithm decides on the sign of the momentum. Thereby, it is assured, that each trajectory has a total energy of E_{ZPE} such energy corresponding to the zero-point energy of the system and it is given by

$$E_{ZPE} = \frac{1}{2} \sum_i \omega_i \quad (4.29)$$

This procedure assures that the distribution of the quantum mechanical wave function is reproduced, assuming a sufficiently large number of initial conditions are generated. A large set of initial conditions is required to reproduce the quantum mechanical distribution in the GS. On the other hand the stochastic nature of the surface hopping routine makes a single trajectory physically meaningless and only a statistical average over all trajectories can be interpreted[151].

It is worse to mention that both Q and T samplings are not equivalent. While in the Q sampling each vibrational degree of freedom i has energy $\mathcal{E}_{vQ} = \frac{\hbar\omega_i}{2}$, in the T sampling each degree has $\mathcal{E}_{vT} = kT$. Such difference affects on the vibrational amplitude and consequently may be reflected as a difference on the simulation results based on one or other approach. The ratio between the amplitudes in the thermal and quantum samplings is given by[155]

$$\frac{Q^{aT}}{Q^{aQ}} = \left(\frac{2kT}{\hbar\omega_i} \right)^{\frac{1}{2}} \quad (4.30)$$

Q^a is the amplitude of a harmonic oscillator with energy \mathcal{E} and it is given by $Q^a = (2\mathcal{E}/\mu\omega^2)^{\frac{1}{2}}$.

Klaffki et. al. [157] have studied the difference between Q and T samplings on the excited-state dynamics simulations for a protonated Schiff base (PSB3). They assigned the use of T sampling as the preferred methodology because the Q sampling would provide “artificially high kinetic energies” and lower numerical stability so the use Q sampling showed a trend toward faster reactions; however the differences were really statistically non-significant. On the other hand Barbatti et al [155] favored the quantum sampling method to sample initial conditions for dynamics and spectrum furthermore they do not consider the high kinetic energies of the Q sampling as an artificial, but correspond to the kinetic energies expected for a quantum system. They concluded by studying the photodynamics and spectrum of Pyrrole that qualitatively, both T and Q samplings lead to similar results in the dynamics however quantitatively, dynamics is faster by few tens of femtoseconds in case of Q Sampling which performs better in terms of time constants and distribution of reaction pathways compared to the experimental results.

5 Photoelectrochromism in the retinal protonated Schiff base chromophore: photoisomerization speed and selectivity under a homogeneous electric field at different operational regimes

The spectral tunability, photoisomerization efficiency and selectivity, of the native all-trans retinal protonated Schiff-base (RPSB) chromophore driven by a homogeneous electric field is systematically investigated. By analyzing the absorption wavelength dependence, charge distribution, and PES profiles along selected torsional angles, as well as the electronic structure, energetics, and topography of the CI seam in the presence of strong positive and negative electric fields, we recognize the existence of qualitatively/fundamentally different photophysics and photochemistry with respect to the unperturbed (i.e., absence of an electric field) chromophore. We rationalize the findings within the scope of molecular orbital theory and deliver a unified picture of the photophysics of the RPSB chromophore over a wide, even beyond the usually observed, spectral regime, ranging from the near-infrared to the ultraviolet absorption energies. This work has a 3-fold impact: a) it accounts for, and extends, previous theoretical studies on the subject; b) it delivers a rationale for the ES lifetimes observed in retinal proteins, both archeal and visual rhodopsins, as well as in solvent; and c) the transferability of the discovered trends on RPSB mimics is demonstrated.

5.1 Introduction

Vertebrate vision is enabled by a family of retinidene proteins called opsins, found in the rods and cones of the retina which all contain the conjugated polyene chromophore retinal, covalently linked to the opsin backbone through a Schiff base linkage (that is protonated/unprotonated for visible/UV light absorbing pigments). Absorption of visible light, triggering population of the bright lowest excited state (ES) S_1 , induces an ultrafast photoisomerization of the RPSB, the first step in a complex signal transduction cascade[158,159] (often referred to as the primary visual event), that is driven by a barrierless path leading to a twisted conical intersection (CI) between the S_1 and S_0 [3,8,9]. The rigid scaffolds of the cone opsins (photopsins) and the polar protein-pocket residues and water molecules nearby the chromophore (including the primary counterion) create an electric field which, among other factors (e.g., structural effects involving different conformations of the retinal chromophore), tunes its maximum absorption wavelength throughout the whole visible spectrum (425–560 nm), thus enabling colour vision. The very same effects account also for the remarkably wide operational spectral range of archeal rhodopsins[4,160] (λ_{\max} from 480 to 590 nm), and have been recently exploited, very notably, to design artificial rhodopsin mimics further enlarging the natural absorption ability of retinal proteins (λ_{\max} from 425 to 644 nm)[161].

The spectral tunability of the cationic retinal chromophore driven by the electric field owes to the intramolecular charge transfer (ICT) nature of its bright lowest ES, which triggers a pronounced change in the dipole moment upon excitation, eventually resulting in a big solvatochromic effects, as evidenced by the so-called opsin-shift (i.e., the large change in absorption energy recorded on going from solvent to the protein). This ICT makes the photoactive ES highly sensitive to the charge distribution within the active site of the protein, eventually affecting not only the absorption wavelength but also the isomerization dynamics in terms of speed (ES lifetime), selectivity, and quantum yields[161-164].

A number of theoretical studies have addressed the sensitivity of the native RPSB and RPSB models to static electric fields created by counterions in specific positions nearby the chromophore, either in gas-phase[22,165-167], in solution[14,166,167] or in the protein[21,168-170]. In a series of papers, Garavelli and co-workers explored the effect of the position of a chloride and carboxylate anions on the minimum energy paths describing the photoisomerization of shorter RPSB models in vacuo, thereby reporting the following trends:

- if the counterion is placed closer to the C-tail of the RPSB the absorption maximum shifts to the red and the S_0 - S_1 energy gap at the twisted ES minimum grows with the proximity of the rotating double bond to the N-head;
- if the counterion is placed closer to the N-head of the RPSB the absorption maximum shifts to the blue and the S_0 - S_1 energy gap at the twisted ES minimum grows with the proximity of the rotating double bond to the C-tail.
- On the other hand, a recent computational study by Olivucci and co-workers suggests that the retinal chromophore inside three different visual proteins (rhodopsin, squidrhodopsin, melanopsin) photoisomerizes with a rate that is correlated to the size of the S_0 - S_1 energy gap at the Franck-Condon (FC) point, being higher the more blue-shifted the absorption[12], with a sub-100 fs photoisomerization time scale predicted for the more blue absorbing melanopsin pigment.

Other theoretical papers as well as numerous experimental works focus on scrutinizing the correlation between solvent's polarity and isomerization speed and selectivity. The commonly accepted view is that the ES lifetimes are 1-2 orders of magnitude longer in solution[171,172] than inside the protein pocket[5,173]. However, time-Resolved fluorescence studies in solvents of different polarity and viscosity could not establish a clear correlation between the absorption energy, the ES lifetimes, and the solvent properties[172,174-176]. Some researchers attribute therefore the isomerization slowdown in solution to purely steric effects[177]. others favor the view of a dynamic electrostatic barrier emerging as the solvent molecules need time to rearrange[14,171] and yet others suspect new pathways, e.g. the system exploring nonreactive regions of the ES potential energy surface (PES) which become reachable as a consequence of the external electric field (ionic/covalent mixing)[22,165] and/or of the less unconstrained environment and higher conformational freedom. On the other hand, and very notably, recent ultraresolved transient spectroscopic

data on substituted (methylated) RPSB chromophores in solution have revealed a subps decay, matching the one observed in the retinal proteins[178-180].

In the present study we systematically analyze the photophysics and photoisomerization ability of the all-trans RPSB chromophore in a homogeneous electric field as function of its strength and direction. Specifically, we examine in detail the operational regimes in strong fields: a) destabilizing the charge transfer (CT) state and inducing wave function mixing with the second ES of covalent nature and b) stabilizing the CT state and inducing an avoided crossing with the covalent ground-state. By referencing to the isomerization mechanism in the unperturbed gas-phase, we derive clear trends regarding the response of electronic states of essentially different nature (ionic and covalent) to geometrical deformations (bond relaxation and torsion) in the presence of the field, regarding the torsional bond selectivity, as well as regarding the relative positions of the reaction path and the CI seam, the latter having a direct implication for the ultrafast isomerization rates in retinal proteins. We rationalize the topography of the CI seam in the scope of the extended two-electron two-orbital theory, which explains the geometrical and electronic structure of CIs found in conjugated polyenes following the Woodward–Hoffmann (WH) rules[181,182]. This systematic analysis allows generalizing the behavior of retinal chromophores over a wide, even beyond the usually observed, spectral regime, from NIR to NUV, leading to a threefold impact. It provides a global unified view of electric field effects and an accurate model that accounts for previous theoretical studies on the subject, resolving pending contradictions and uncertainties. Within this unified picture we document a surprising correlation between the ES lifetimes recorded for some retinal proteins and their mutants (both archeal and visual rhodopsins) and the absorption wavelengths, reflecting protein-specific fields generated by the charge distribution inside the catalytic pocket. Furthermore, by studying the ES PES of two functionalized derivatives we demonstrate the transferability of the discovered trends on RPSB mimics. Eventually, this work sets solid guidelines for the design of ultrafast spectrally tunable molecular devices, based on judiciously modified RPSB or RPSB-mimics, whose polar substituents and groups may be employed as electric field generators to control their spectroscopic and photochemical properties and allow operation over a wide spectral range.

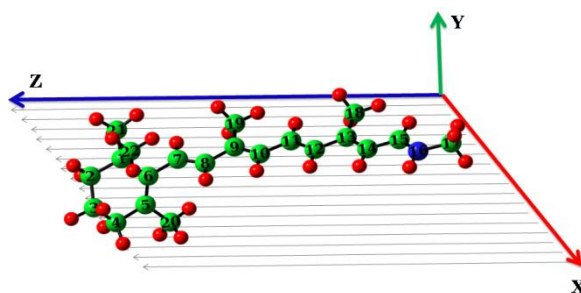


Figure 5-1. Retinal protonated Schiff base in an electric field.

5.2 Computational Details

All computations reported here were performed in vacuo with the 6-31G* basis set[183]. The ground-state geometry in the absence and in the presence of an electric field

was obtained via a single-Root unconstrained optimization using the complete active space self-Consistent field (CASSCF) level of theory[54]. Basis set dependence of the ground-state (GS) and ES properties was tested against the generally contracted atomic natural orbital (ANO) basis set[184] and is reported in the Supporting Information (SI). In all computations the active space consisted of the complete π -system consisting of 12 electrons distributed among 12 orbitals (**Figure 5-2**) A finite dipole electric field was applied along the long axis of the molecule parallel to the conjugated double bond chain (i.e., along the z-axis, **Figure 5-1**), and the dependence of the absorption energies and transition dipole moments (TDMs) on the sign and strength of the field varying from -0.005 to $+0.004$ au (i.e., from -25 to $+20$ MV/cm) were systematically studied. Computations in the presence of an electric field of the same strength along the other two axes did not result in a notable effect on the aforementioned observables and therefore are not further discussed.

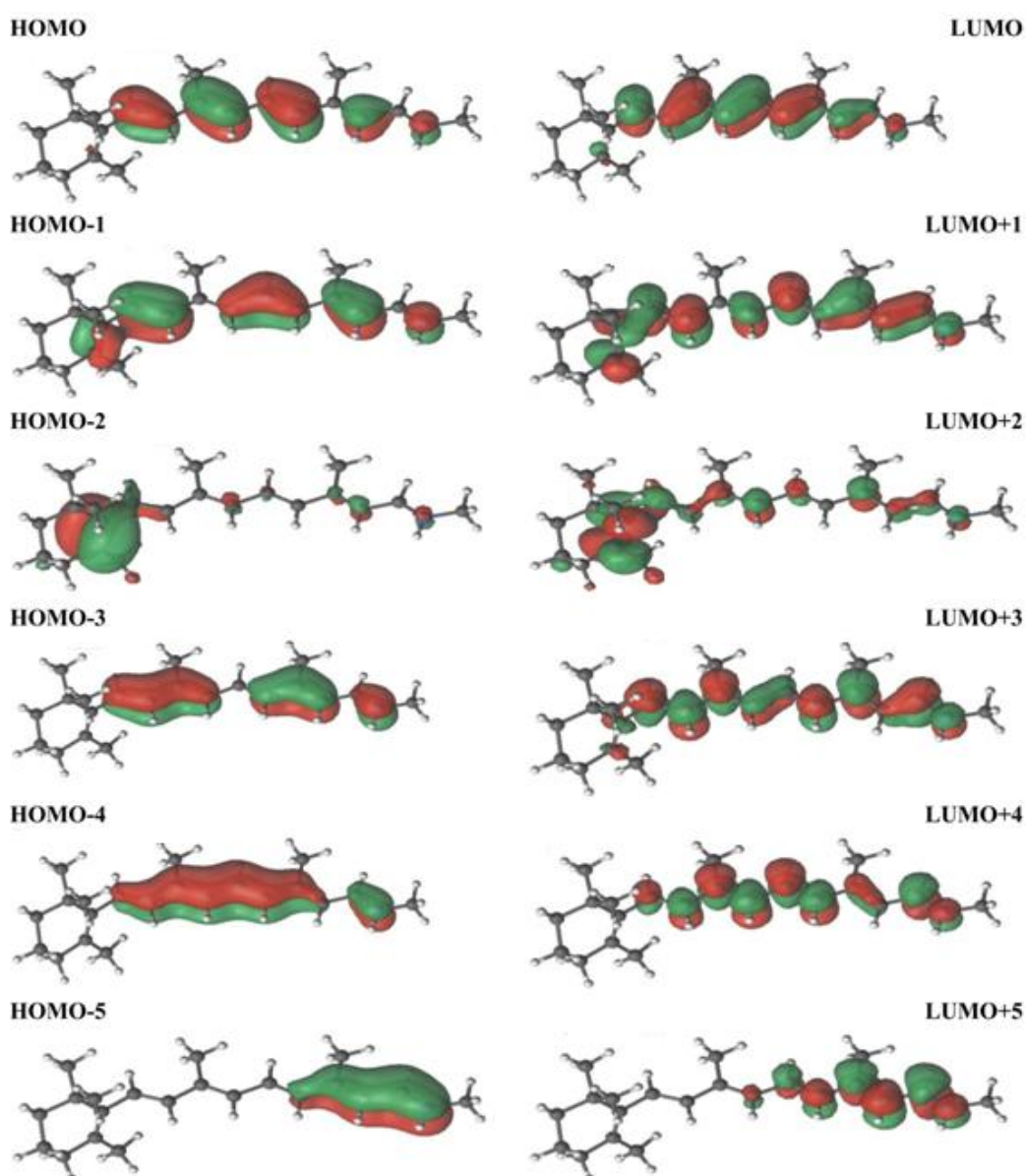


Figure 5-2. The complete active space molecular orbitals for the ground state optimized geometry of the RPSB chromophore calculated at CASSCF(12,12)/6-31G* level of theory in absence of the electric field.

Vertical excitation energies were computed applying the second order perturbation correction (CASPT2) in the single-state (SS)[66] and multistate (MS)[67] flavors, thereby using as a reference CASSCF wave functions averaged over three and four roots. An imaginary level-shift of 0.2 au was used to decrease the influence of weakly interacting intruder states in the CASPT2 calculations[185]. The ionization potential electron affinity parameter was set to 0.0 au[186], in accordance with previous studies of retinal in gas-phase and its protein environment[24,187-189]. TDMs were calculated at the CASSCF level and were used to compute oscillator strengths, which were corrected using the CASPT2 transition energies.

The ES profile of the first $\pi\pi^*$ state (with pronounced CT character) from the FC point to the CI in the presence of electric field strengths of -0.003 au and $+0.003$ au was recorded through relaxed scans along selected torsional coordinates with an increment of 10 degrees. The choice of torsional coordinate was done according to the bond lengths in the relaxed conjugated system, thereby choosing bonds with more pronounced single-bond character. The relaxed scans were carried out at the SA-CASSCF(12,12)/6-31G* level thereby averaging over two or three roots. The vertical transitions at the optimized points along the relaxed scan were corrected at the CASPT2 level. The ES profile of retinal in the absence of an electric field was also computed as a reference.

All calculations were carried out using Molcas 7.9[190], while the CI geometries were obtained with Molpro 2010[94] using the gradient projection method introduced by Bearpark et al.[123].

5.3 Results and Discussion

5.3.1 Effect of a Homogeneous Electric Field on the Absorption Energy

With electric fields applied parallel to the z-axis of the retinal chromophore the ground-state equilibrium geometries display following general features (6-31G* basis set):

- the planarity of the conjugated system is preserved in the presence of an external electric field;
- for electric field strengths in the range from -0.005 to $+0.004$ au all structures show the regular single-double bond alternation expected for the ground-state of a protonated Schiff's base, thereby localizing the positive charge in the proximity of the iminium moiety; the bond alternation is slightly perturbed in the presence of the electric field, with all bonds exhibiting an elongation reaching up to 0.06 Å towards positive electric fields;
- the β -ionone torsional angle with respect to the conjugated system increases by ca. 8° (i.e., from 60° to 68°) from negative to positive electric field.

The ANO-L (atomic natural orbital Widmark) basis set gives similar results with two distinctive differences:

- the β -ionone torsional angle exhibits a larger variation (i.e., from 50° to 75°);
- for strong negative electric fields (larger than -0.045 au) we observe bond inversion in the GS.

A comparison of the relevant geometrical parameters is provided in **Figure 5-3**.

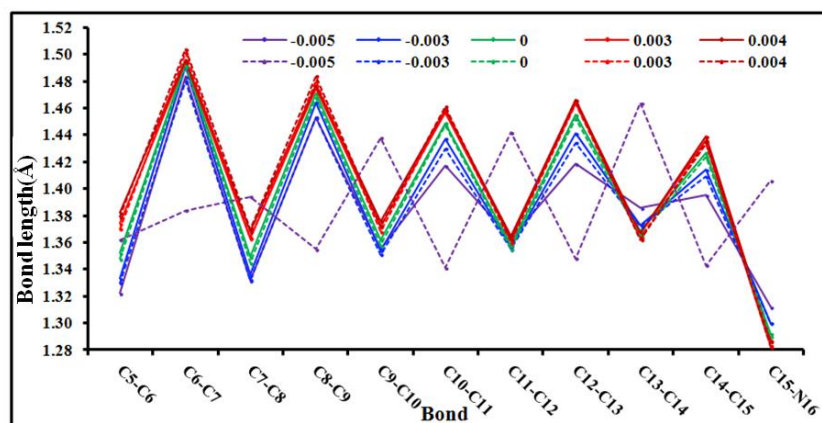


Figure 5-3. The geometry parameters of the ground state of the RPSB chromophore in electric field calculated at CASSCF(12,12) using 6-31G* (solid lines) and ANO-L (dashed lines) levels of theory.

Opposite to the relatively weak structural dependence on the electric field strength, retinal demonstrates a pronounced photoelectrochromism as demonstrated in **Figure 5-4** displaying the absorption wavelength (**Figure 5-4a**), charge distribution (**Figure 5-4b**), and TDM magnitude (**Figure 5-4c**) variation for the first three transitions at the relaxed ground-state geometries as a function of the electric field strength. The reported results were obtained at the SS-CASPT2//SA-3-CASSCF(12,12)/6-31G* level. An assessment of the effects of the basis set and the number of states averaged upon confirms the general trend (provided in **Figure 5-5**).

The apparent sensitivity to the electric field is a consequence of the different electronic nature of the ground-state and the bright first ES (essentially a HOMO (H) \rightarrow LUMO (L) transition, labeled with red squares in **Figure 5-4**), the former being a covalent state characterized by a concentration of the positive charge on the iminium moiety (from +0.9e to +0.5e, **Figure 5-4b**), the latter exhibiting a partial CT character, with +0.2 to +0.3e migrating to the ionone moiety. A positive electric field (for definition see **Figure 5-1**) works against the CT, thereby leading the overall destabilization of the first ES (i.e., a blue-shift of the absorption energy). In contrast, a negative electric field promotes the CT, and as a consequence the absorption energy of the first excited state exhibits a red-shift.

In the absence of an electric field the second (“dark”) ES is dominated by a double H \rightarrow L excitation (labeled with green triangles in **Figure 5-4**). This configuration shows a negligible response to the electric field in accordance with its pronounced covalent nature, revealed through the charge distribution in the second ES (**Figure 5-4b**). The different sensitivity of the CT and the covalent configurations leads to near degeneracy and eventually order inversion for positive electric fields (**Figure 5-4a**) above 0.002 au. In agreement with the increasing state mixing for field strengths between 0.000 au and +0.002 au the oscillator strength of the “dark” state increases at the expenses of the “bright” state (**Figure 5-4c**). Above +0.002 au the lowest charge on the iminium-group (**Figure 5-4b**) and the largest TDM

(Figure 5-4c) are observed for the second ES. Negative electric fields, on the other hand, stabilize higher lying CT configurations. A distinct CT configuration ($H \rightarrow L+1$, labeled with violet circles in Figure 5-4) with charge deposition of more than $+0.5e$ crosses the covalent configuration at electric field strengths around -0.001 au to become the second ES.

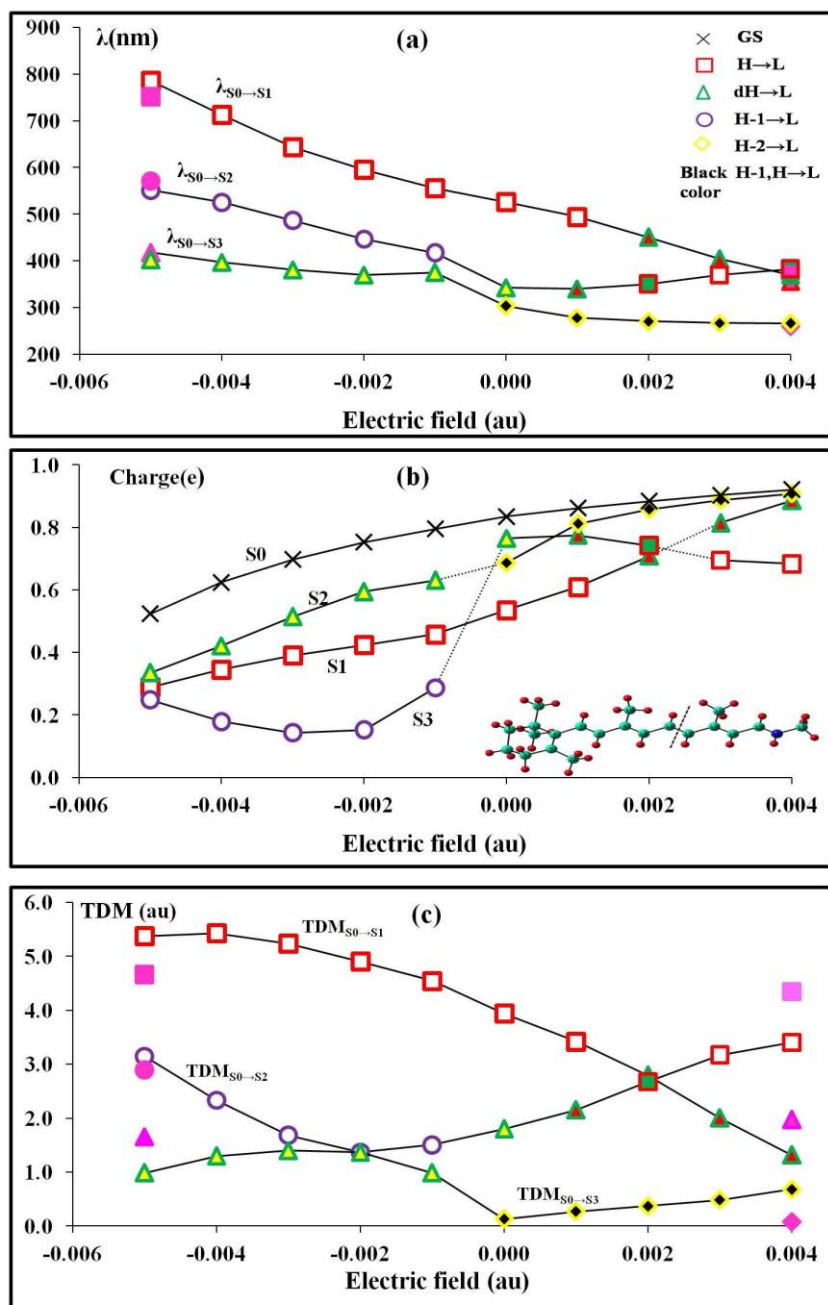


Figure 5-4. Dependence of a) the absorption energy; b) total Mulliken charge on the iminium moiety containing atoms C₁₂ through C₁₅ and the nitrogen (defined in the inset); c) TDM magnitude; on the electric field strength in the range -0.005 to $+0.004$ au. The dominant electronic configuration for each ES wave function is labeled through a coloured shape; in case of configuration mixing the second dominant configuration defines the inner colour of the shape. The strength of the external electric field is compared to the strength of an electric field created through a pair of point charges (shown in magenta for -0.005 au and $+0.004$ au field strengths), placed in 3 \AA distance to both ends of retinal chromophore, reminiscent for the situation in the reactive pocket of opsins.

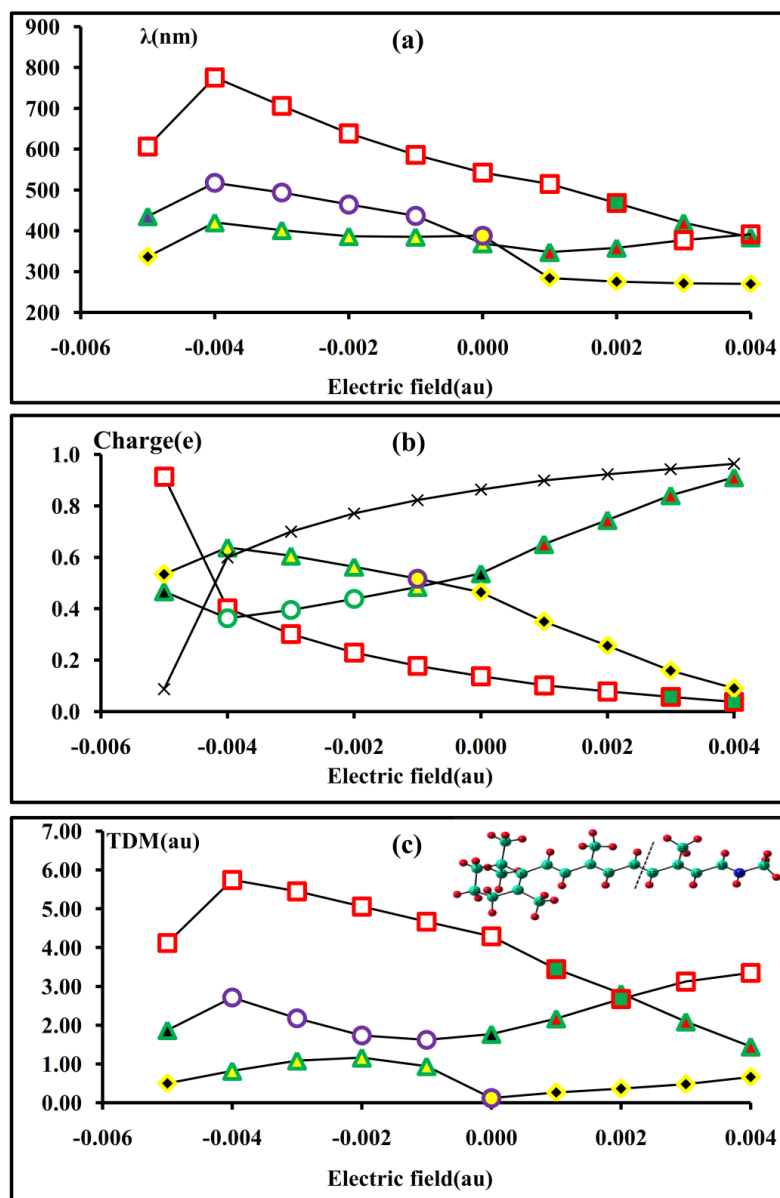


Figure 5-5. Dependence of a) the absorption energy; b) total Mulliken charge on the iminium moiety containing atoms C_{12} through C_{15} and the nitrogen (defined in the inset); c) TDM magnitude; on the electric field strength in the range -0.005 to $+0.004$ au. The calculation based on CASSCF(12,12)/ANO-L level of theory. The dominant electronic configuration for each ES wave function is labeled through a coloured shape; in case of configuration mixing the second dominant configuration defines the inner colour of the shape.

By varying the electric field strength from -0.005 au to $+0.004$ au one is able to manipulate the absorption wavelength of retinal over the entire visible range, i.e., 800–400 nm. In all fairness we note that the fields required for achieving a noticeable change of the molecular properties are approximately an order of magnitude larger than the technically available today (~ 1 MV/cm). Nevertheless, such electric fields are common in proteins as demonstrated by experimentally recorded electrostatic potential maps documenting electric field fluctuations in the range $+25$ MV/cm to -25 MV/cm (i.e., ± 0.005 au)[191,192]. In fact, photopsins, a light-sensitive family of proteins responsible for colour vision in vertebrates, utilize protein-specific and environment-induced electric fields of comparable strength in

their reactive sites allowing them to shift the absorption maximum of retinal between 560 and 425 nm. In order to correlate the required field strengths to the ones present in the binding pocket of the proteins we placed a pair of point charges in 3 Å distance to both ends of retinal chromophore and computed the vertical transitions, recognizing that this highly simplified approach cannot quantitatively reproduce the nonuniform electric field in the protein pocket. The absorption energies and TDMs obtained for charges $+0.5/-0.5e$ (labeled in magenta in **Figure 5-4**) resemble closely the one obtained for an electric field of -0.005 au and of $+0.004$ au; however the heterogeneous electric field imposed by such charges is changed dramatically from 0.016 au to 0.0028 au by moving from the N atom to the central of $C_{11}-C_{12}$ bond, respectively.

5.3.2 Effect of a Homogeneous Electric Field on the Ultrafast ES Dynamics

The pronounced photoelectrochromism of the retinal chromophore raises the question how its isomerization profile is affected in the presence of an electric field. To address this issue we computed the ES profile for field strengths of -0.003 au and $+0.003$ au by means of relaxed scans in the CT state along the rotation around three bonds (C_9-C_{10} , $C_{11}-C_{12}$ and $C_{13}-C_{14}$) from the conjugated π -system initiated out of the ES relaxed (planar) geometries. **Figure 5-6** summarizes the results. The profiles in the absence of an electric field are also reported as a reference and shall be used in the following to give a brief overview of the photoreactivity of retinal.

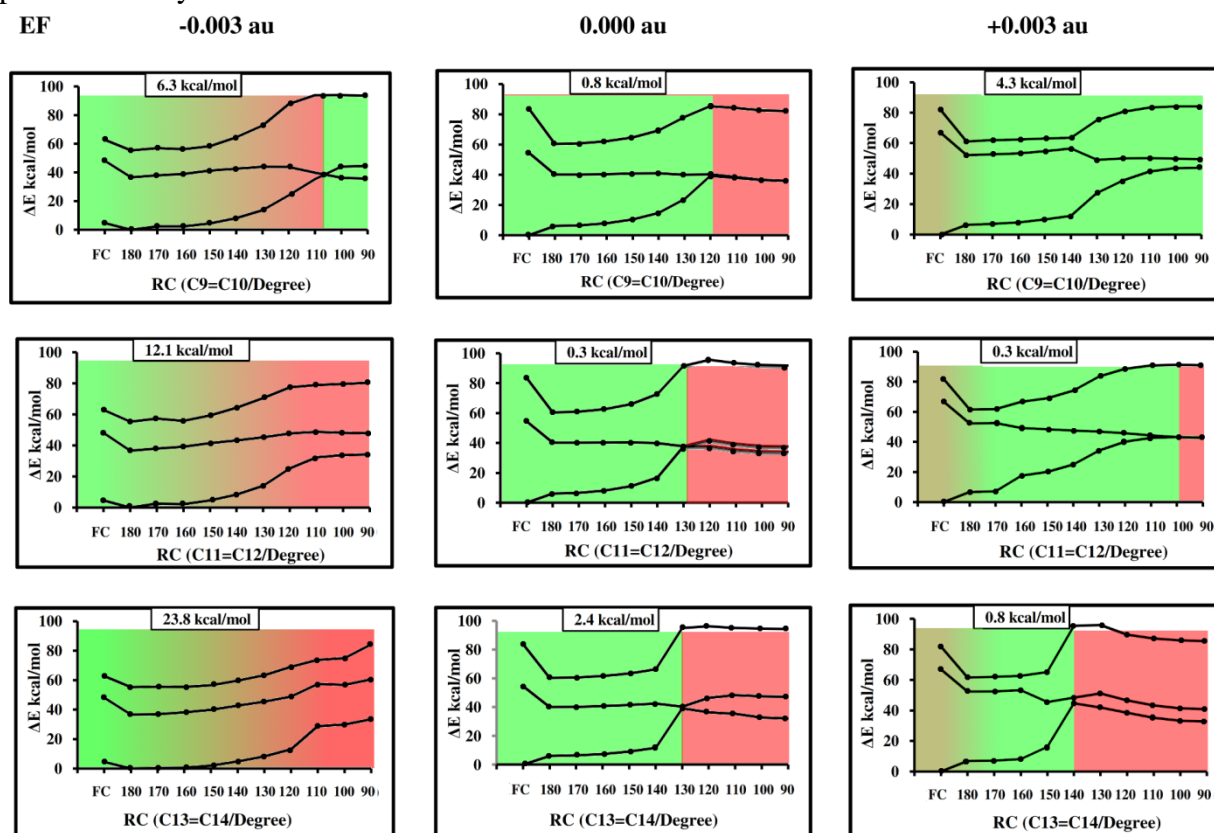


Figure 5-6. Profiles of RPSB along three torsion angles (around bonds C_9-C_{10} , $C_{11}-C_{12}$ and $C_{13}-C_{14}$) obtained from relaxed scans (relaxing the CT ES) in the presence of an electric field with strength -0.003 au (left column) and $+0.003$ au (right column). The profiles in the absence of an electric field are provided as a reference (middle column). The colour background denotes the character of the first ES along the optimized path being either covalent (red), CT (green), or mixed.

5.3.2.1 ES Profiles in the Absence of an Electric Field Indicate Fast De-Excitation with Little Selectivity

The initial ES relaxation is associated with double–single bond inversion in the conjugated system; as a consequence the bonds C₉–C₁₀ (1.471 Å), C₁₁–C₁₂ (1.465 Å) and C₁₃–C₁₄ (1.450 Å) adopt a pronounced single bond character (values in brackets, see also **Figure 5-7**). Remarkably, the bond relaxation leads to an energy stabilization of ~20 kcal/mol for both the ionic (S₁) and covalent state (S₂). Along the torsional coordinate around the single bonds the CT state characterizes through flat potentials with small barriers (with torsion around C₁₁–C₁₂ exhibiting the lowest barrier of 0.3 kcal/mol), while the covalent ground and second ESs increase substantially in energy, thereby showing similar slopes. A CI with the ground-state is encountered for all three scans early along the torsional coordinate, with a slight shift of the crossing point from 60° (torsion around C₉–C₁₀) to 50° (torsion around C₁₃–C₁₄). The occurrence of a CI at small torsional angles is accompanied by a hydrogen–out–of–plane (HOOP) deformation of the hydrogens attached to the rotating bond.

Although the torsion around C₁₁–C₁₂ appears to be slightly preferred, all scanned deformations allow for an ultrafast relaxation of the population back to the ground-state. In concordance, molecular dynamics simulations in gas-phase by Martinez and co-workers (30 trajectories) on a truncated all–cis retinal mimic with five double bonds report that only half of the molecules decay via isomerization of the central double bond (corresponding to C₁₁–C₁₂), furthermore confirming the low selectivity of the process through the participation of the C₉–C₁₀ and C₁₃–C₁₄ channels[14].

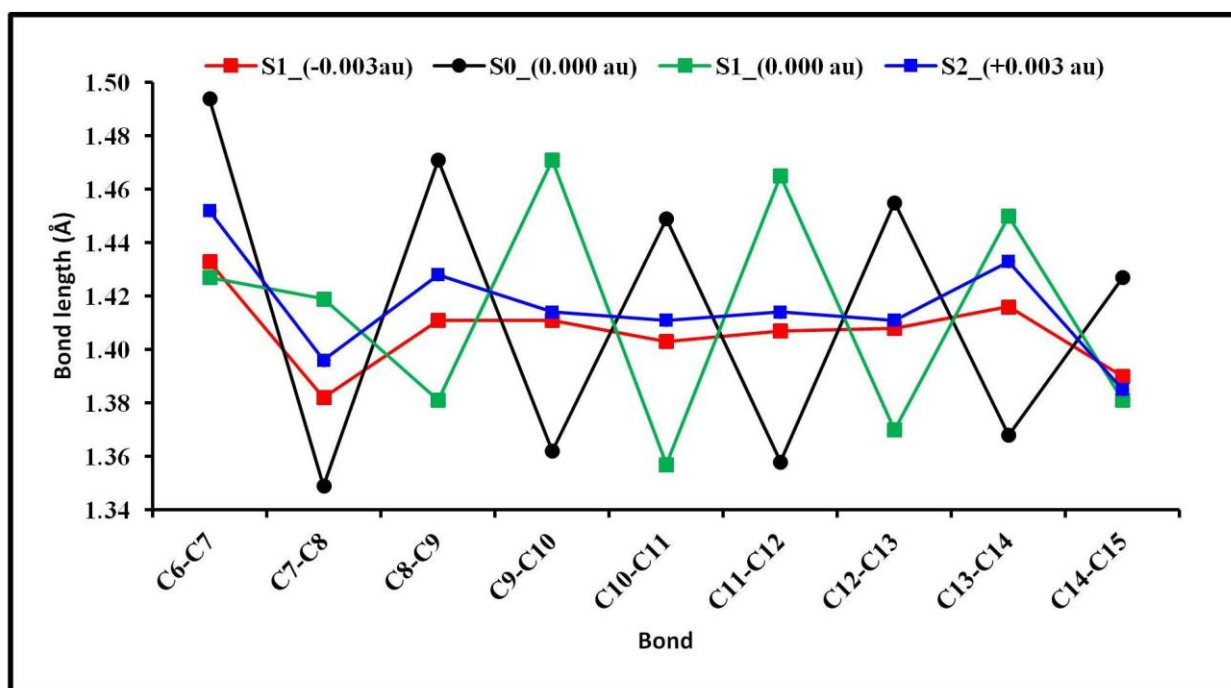


Figure 5-7. The bond lengths of optimized CT geometries of the RPSB for -0.003, 0.000 and +0.003 au versus the GS ones for 0.000 au.

5.3.2.2 Effects of Positive Electric Field

As elaborated in the previous section positive electric fields destabilize the CT state, so that for field strengths near +0.002 au (see **Figure 5-4**) it heavily mixes with the covalent ES making their discrimination ambiguous at the CASSCF level in the FC region. The S_1/S_2 state mixing is reflected in their dipole moments (**Figure 5-8**) which are nearly identical. Multistate (MS)–CASPT2 computations uncouple both states permitting to assign the CT character to the second ES[10], conclusion supported also by the charge distribution reported in **Figure 5-8**. For ionic states the σ – π correlation (i.e., the response of the σ -electron density to relocation of partial positive and negative charges in the π -electron density upon excitation) is significant. Due to the lack of this dynamic correlation effect at the CASSCF level when only π -orbitals are used to construct the active space geometry optimization (both using state–averaging of two and three states) relaxing the second root ends up in a planar minimum with covalent character and bond length equilibration (see **Figure 5-7**). Furthermore, this situation has been documented previously in studies on the counterion effects in RPSB chromophore models[22,165] and as a consequence it has been argued that the isomerization along S_1 acquires substantial barriers as activation energy is necessary to exit the covalent nonreactive trap into the ionic funnel to the CI region. However, we find that a computation averaging over the lowest three states, thereby relaxing the third root finds a minimum, energetically somewhat above the second root, characterized through a collapse of the wave function to a pronounced CT, accompanied by an increase of the magnitude of the TDM (and, consecutively a decrease for S_1). Subsequent SS–CASPT2 (**Figure 5-6**, right panel) and MS–CASPT2 (**Figure 5-9**) calculations demonstrate that this CT configuration is more stable than the covalent configuration upon bond length relaxation. Furthermore, while the covalent minimum (obtained by relaxing the second root) is ca. 0.5 eV more stable than the ionic one at the CASSCF level, we observe the opposite ordering at the SS–CASPT2 level with the ionic minimum being ca. 0.5 eV more stable. The present findings suggest that the collapse of the S_1 wave function to a covalent configuration observed in energy minimization on S_1 at the CASSCF level might be to a large degree an artifact of the tendency of CASSCF toward favoring covalent configurations, at least up to field strengths of 0.003 au. Furthermore, our computations indicate strongly that torsion around any double bond would instantaneously lead to unmixing as the ionic state is stabilized, while the energy of the covalent state would increase (see also **Figure 5-17a**). Similar observations were made recently by Dokukina et al. on the photoisomerization of the RPSB chromophore in the C1C2 channelrhodopsin which absorbs at 478 nm[193]. Although being the third excited state at the CASSCF level the CT state becomes the lowest ES after adding dynamic correlation via CASPT2. The work by Gozem et al. regarding the shape of the GS PES around the CI of a minimal rhodopsin chromophore model, thereby concluding that the dynamic correlation effects favor the CT region, provides a further example in this direction[194]. The immediate unmixing of the ionic and covalent states also agrees with the finding of Martinez and co-workers from QM/MM molecular dynamics simulations of RPSB in methanol that only a small portion of the population (< 5%) is transferred in the covalent state when the dynamics is initiated in the ionic state[14].

In contrast to the behavior in the absence of an electric field, the CT state exhibits a profile which becomes progressively steeper with the torsion shifting from bond C₉–C₁₀ to bond C₁₃–C₁₄ (5–10 to 20 kcal/mol). Correspondingly, barriers for torsion around C₁₁–C₁₂ or C₁₃–C₁₄ are practically nonexistent. CIs with the ground-state are found along all three torsional coordinates. In agreement with the progressive steepness of the CT potential, the CI is reached only at 90° for torsion around C₉–C₁₀, while it appears already at 40° for torsion around C₁₃–C₁₄. This trend corroborates the findings in refs[165] and[22] that a CI between the GS and the CT state is reached easier when the rotating bond is closer to the counterion. In conclusion, one may expect that in the native environment of the protein positive electric fields below a threshold (ca. +0.003 au) increase the steepness of the barrierless path to the CIs, thus allowing for a faster decay to the crossing region and, presumably, a decreased ES lifetime. Of course, this conclusion, drawn within the limited framework of a relaxed scan under far-from-realistic conditions (gas-phase, homogeneous electric field), demands verification through molecular dynamics studies in a realistic (protein) environment, which are outside the scope of the present work. For instance, it is well known that, even if the GS decay is always mediated through a 90° twisted CI, the isomerization mechanism inside the protein is a two-bond torsion (bicycle-pedal)[13] opposite to the one-bond torsion mechanism in gas-phase presented in **Figure 5-6**. Nevertheless, the relaxed scans demonstrate that any torsion around a bond with a pronounced single-bond character in the excited state would instantaneously lead to unmixing, thereby stabilizing the ionic state and destabilizing the covalent one. We expect that a combination of one-bond torsions, as it is essentially the bicycle-pedal, will not affect the universality of this observation, thus supporting the tentative transferability of the drawn conclusions to the protein environment.

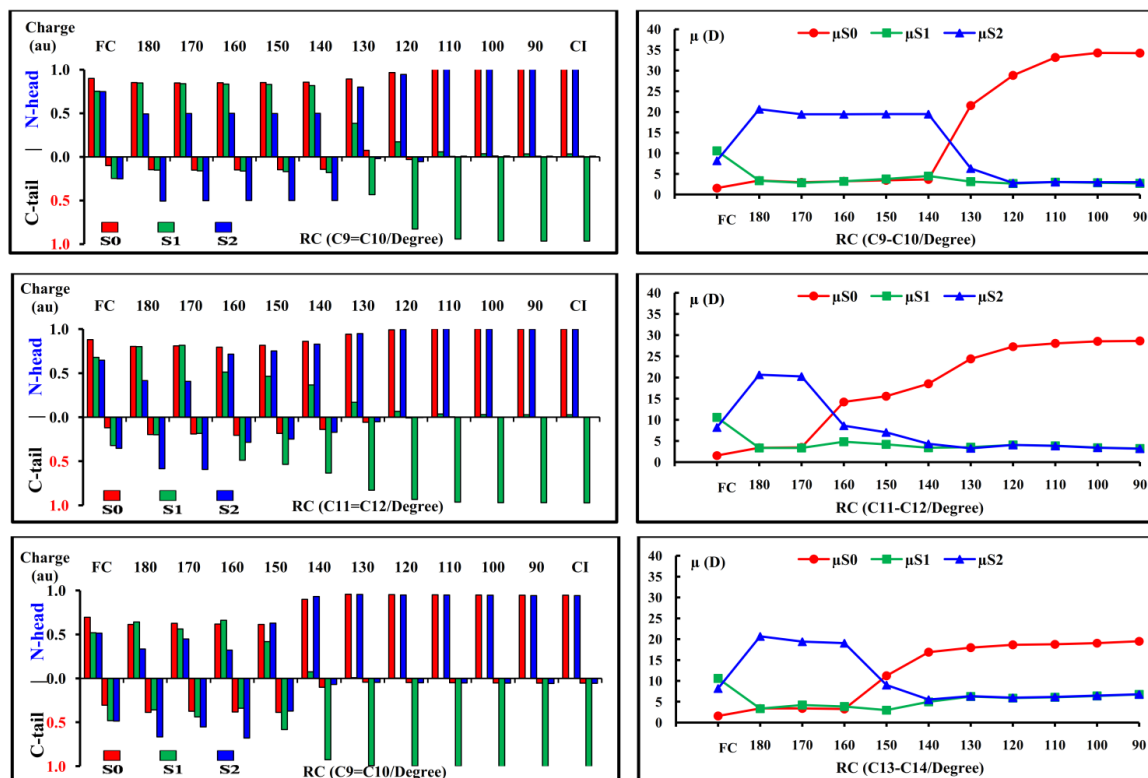


Figure 5-8. Mulliken charges (left column, N-head and C-tail refer to the charges for the right and left moieties from the central of rotating bond, respectively) and permanent dipole moments (right column) of RPSB chromophore for the relaxed scans around C₉–C₁₀, C₁₁–C₁₂ and C₁₃–C₁₄ in the presence of electric field with strength +0.003 au, calculated at SA3–CASSCF(12/12)/6-31G* level of theory.

The regions with covalent nature could also affect the isomerization dynamics under operational regimes of very strong positive electric fields. First of all, **Figure 5-4c** shows that the covalent state becomes accessible through borrowing oscillator strength from the CT state upon wave function mixing in the FC region. Second, provided the ionic configuration is strongly destabilized through the environment (see also **Figure 5-16a**), as can be extrapolated for electric fields above +0.003 au (such as the ones created by a counterion nearby the RPSB), the mixed ES S_1 could indeed collapse into a pure covalent configuration upon relaxation along the bond stretching coordinate, so that dynamics initiated in S_1 may indeed get trapped in a covalent well, in agreement with the outcome of the studies executed in the presence of a counterion close to the N-head of the RPSB in gas-phase[22,165]. We could reproduce the predicted behavior by attaching the positively charged trimethylamino-residue to the ionone ring of RPSB (**Figure 5-10**). This group strongly destabilizes the CT state causing a strong mixing with the second ES of covalent character and as a consequence both S_1 and S_2 exhibit large permanent and TDMs in the FC region. The equilibrated (i.e., covalent) and inverted (i.e., ionic) bond length minima found upon energy minimization are nearly isoenergetic upon addition of dynamic correlation (see **Figure 5-7**). In this same context, Olivucci and co-workers also reported the coexistence of two similar minima on S_1 for a rhodopsin mimic[195]. In fact, it seems that in the case of deprotonation of the RPSB the covalent configuration would become the only stable minimum on S_1 , as reported recently by Rivalta and co-workers for the ultraviolet visual pigment of the Siberian hamster[187]. In conclusion, it appears that positive electric fields above a threshold (ca. +0.003 au) open additional channels which slow down the photoisomerization by trapping the ES population and producing a barrier along the path to the twisted CIs that would increase the ES lifetime.

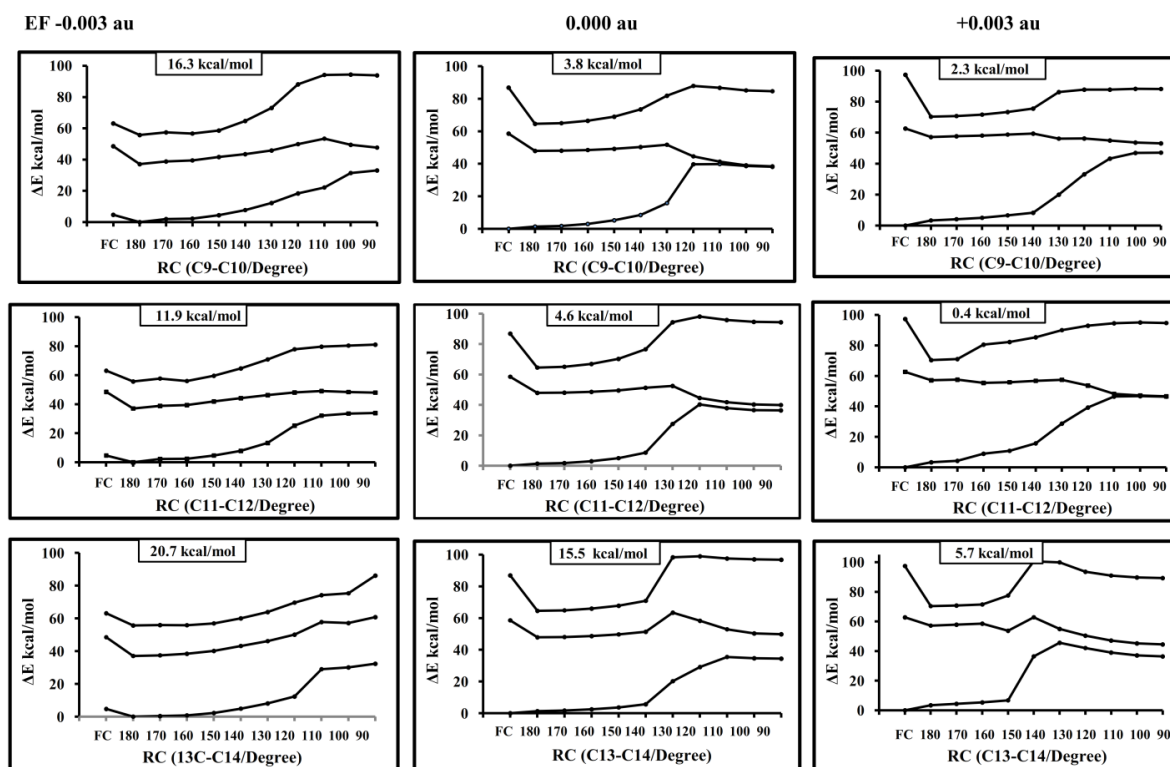


Figure 5-9. MS-3-CASPT2(12,12)/6-31G* on top of a SA-3-CASSCF computed adiabatic profiles of RPSB along three torsion angles (around bonds C_9-C_{10} , $C_{11}-C_{12}$ and $C_{13}-C_{14}$) obtained from relaxed scans (relaxing the CT excited state) in the presence of electric field with strength -0.003 au (left column) and +0.003 au (right column). The profiles in the absence of electric field are provided as a reference (middle column).

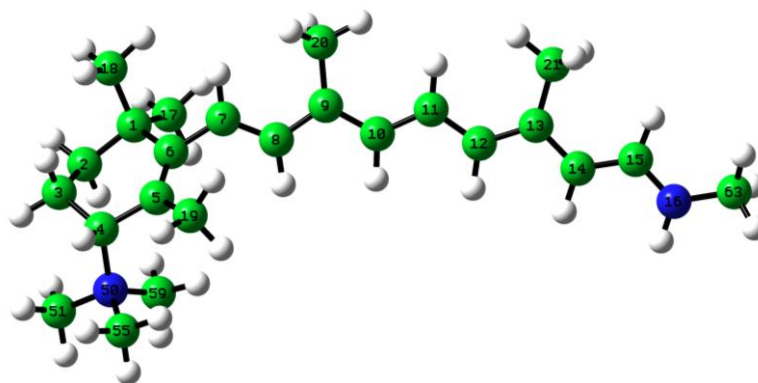


Figure 5-10. Structure of the RPSB chromophore functionalized with a $-\text{N}^+(\text{CH}_3)_3$ group at the ionone ring, which shows a blue-shifted linear absorption spectrum.

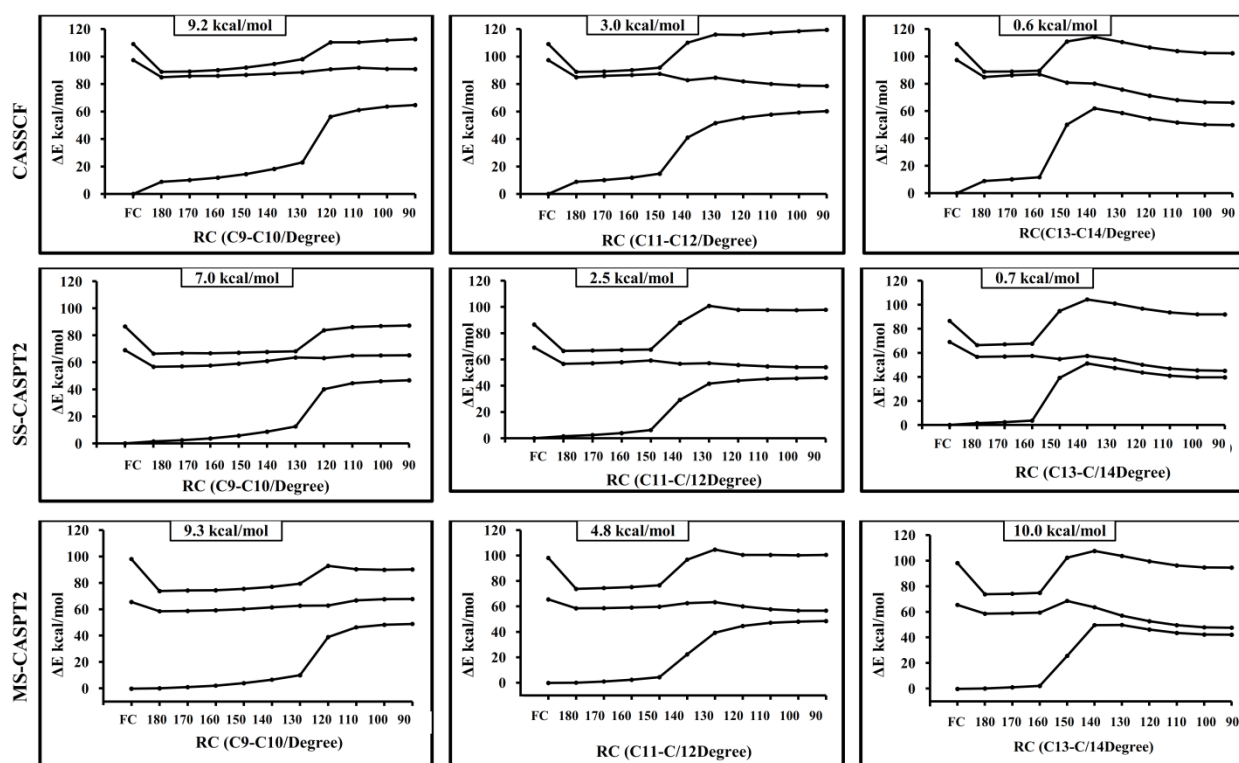


Figure 5-11. SA3-CASSCF(12,12)/6-31G* (top) and SS-CASPT2 (middle) and MS-3-CASPT2 on the top of CASSCF (bottom) adiabatic profiles of the blue shifted RPSB (**Figure 5-10**) along three torsion angles (around bonds C₉-C₁₀, C₁₁-C₁₂ and C₁₃-C₁₄) obtained from relaxed scans (relaxing the CT excited state) in the absence of electric field.

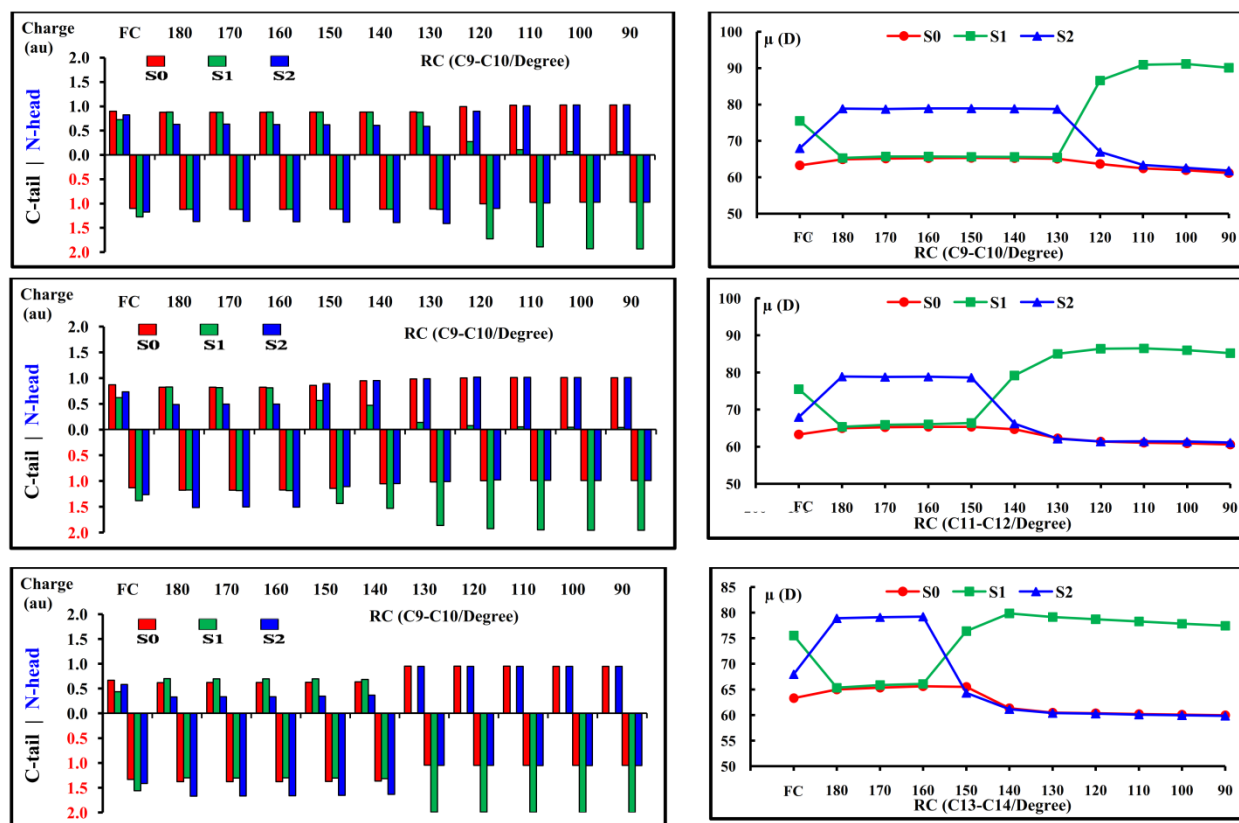


Figure 5-12. Mulliken charges (left column, N-head and C-tail refer to the charges for the right and left moieties from the central of rotating bond, respectively) and permanent dipole moments (right column) of the blue shifted RPSB (**Figure 5-10**) along C_9-C_{10} , $C_{11}-C_{12}$ and $C_{13}-C_{14}$ for the absence of electric field, calculated at SA3-CASSCF(12,12)/6-31G* level of theory.

5.3.2.3 Effects of Negative Electric Fields

Negative electric fields stabilize the CT state, though bond relaxation does not invoke single-double bond inversion as encountered for a zero electric field but rather leads to bond length equilibration (see **Figure 5-7**). Reference [165] documents identical behavior for a RPSB model with a counterion close to its C-tail, thereby reporting substantial barriers along the torsional coordinates C_9-C_{10} , $C_{11}-C_{12}$, and $C_{13}-C_{14}$. However, the absence of clear single bonds raises the question which is the preferable torsional angle. For the sake of comparison in **Figure 5-6** we present the profiles obtained by scanning around the same bonds C_9-C_{10} , $C_{11}-C_{12}$, and $C_{13}-C_{14}$ as for zero and positive electric fields, while the profiles for rotating around bonds C_8-C_9 , $C_{10}-C_{11}$, and $C_{12}-C_{13}$ are given in **Figure 5-13**. Significant barriers are evident for all torsional angles. Interestingly, for bonds C_9-C_{10} , $C_{11}-C_{12}$, and $C_{13}-C_{14}$ the barrier height and the S0-S1 energy gap at 90° torsion increase $C_{11}-C_{12}$ with the proximity of the rotating bond to the iminium moiety, while for bonds C_8-C_9 , $C_{10}-C_{11}$, and $C_{12}-C_{13}$ we observe the opposite trend. In the cases where a CI is not encountered along the relaxation path the CI seam is found to lie aside from the relaxed profile (implying a sloped CI topography), thereby requiring additional geometrical deformations. Overall, decay via torsion around bond $C_{10}-C_{11}$ seems most probable, though slowed down compared to zero and positive electric fields.

5.3.3 Correlation between Excited State Lifetime and Absorption Wavelength

The hitherto calculations demonstrate that the electric field direction and strength have a significant effect on the ES profiles and relative positions of isomerization paths and CI seam. On the basis of the observed trends we can tentatively postulate that the photoisomerization of the RPSB chromophores can be modulated, among many other factors (see discussion below), through the external field from a speed-up for positive fields below 0.003 au to a complete inhibition of the ultrafast decay for negative fields. Rather counter intuitively, strong energetic stabilization of the ionic state does not lead to an earlier crossing with the GS, a constellation believed to increase the speed of the cis-trans isomerization. In contrast, destabilization originates in a steeper slope and possibly a faster decay unless the applied electric field is too strong, which may eventually result again in slowing down the photoisomerization and increasing the ES lifetime, by producing a covalent trap on the S1 state. As stated earlier the conclusions have to be considered within the limited framework of relaxed scans under ideal conditions. Exemplarily, stronger fields would be required to achieve such effects in a realistic environment to overcome its shielding effect.

In the following we document a tentative qualitative correlation between the experimental lifetimes recorded for series of native and mutated proteins containing the RPSB chromophore and the maximum of the lowest electronic transition based on an extensive literature survey. We are aware that a comparison between a homogeneous electric field in vacuo and a heterogeneous field inside the catalytic center of a protein poses a great simplification, even if they are found to be of comparable strengths (i.e., +25 MV/cm to -25 MV/cm)[191,192]. Indeed, many factors exist, among them being also the electric field that is responsible for the detected lifetimes: cavity induced chromophore pretwisting, hydrogen-bonding network, temperature, pH, etc. The proposed correlation does not contradict the possible involvement of other factors from the listed above, and, in fact, an example will be presented where the correlation fails to fully rationalize the ES lifetimes. In the following, we briefly summarize some of these findings. We note that we compare only mutants of the same protein under the same external conditions in order to minimize the effect of factors like temperature and pH; however, we cannot exclude modifications of the catalytic cavity due to mutation, which may alter the hydrogen-bonding network or the embedding of the RPSB chromophore. Furthermore, in the case of multiexponential decays we always consider the decay component with the largest contribution to the ES absorption and stimulated emission decay as the ES decay rate (other rates come from GS cooling and product formation) chromospheres.

- mutations in bacteriorhodopsin (wt-bR, $\lambda_{\max} = 568$ nm) can tune its absorption maximum over a wide spectral range spreading from 608 to 543 nm: the most red-shifted mutant D85N, in which negatively charged residue Asp (D85) is replaced by a neutral amino acid Asn (N), displays 4-fold longer ES lifetime (2 ps) than that in wt-bR (0.45 ps); a slightly red-shifted mutant such as Y185F ($\lambda_{\max} = 578$ nm), where the non-hydrogen bonding residue Phe (F) replaces the H-bonding Tyr (Y185), shows a slight deceleration (0.55 ps)[162,196]; 55 blue- shifted Trp (W) mutants W182F ($\lambda_{\max} = 557$ nm) and W86F ($\lambda_{\max} = 443$ nm) show a decreasing order in the ES lifetimes compared to the wild type[197].
- the D100N mutant of rhodopsin in oxyrrhis exhibits a significantly red-shifted absorption maximum ($\lambda_{\max} = 562$ nm) compared to the wild type ($\lambda_{\max} = 520$ nm) at the same pH, the red-shift being accompanied by a slower isomerization rate[198].

- the D97N mutant of green proteorhodopsin GPR exhibits a significantly red-shifted absorption maximum ($\lambda_{\text{max}} = 550$ nm) compared to the wild type ($\lambda_{\text{max}} = 531$ nm) and again a slower ES decay rate has been documented for the mutant[199,200].
- most of the channelrhodopsin-2 (ChR2, $\lambda_{\text{max}} = 474$ nm) mutants, C128T ($\lambda_{\text{max}} = 480$ nm), E123D ($\lambda_{\text{max}} = 486$ nm) and E123T ($\lambda_{\text{max}} = 490$ nm), absorb slightly red-shifted compared to the wild type. Time-Resolved pump-probe spectra demonstrate that the ES in the wild type decays mono- exponentially with a rate of 0.4 ps. In all mutants on the other hand the ES decay is described by two lifetimes (i.e., biexponential decay), a subps (varying from 0.2 to 0.7 ps), and a few ps (varying from 1.8 to 4.8 ps) with ESA and SE contributing to both lifetimes. Consequently, it can be argued too that the wild type shows the shortest ES lifetime, in concordance with its absorption wavelength[201]. We draw the reader's attention to E123T and E123D which show different excited state lifetimes despite absorbing at nearly the same wavelength. This finding indicates that other factors besides the absorption energy are important for determining the lifetime of the ES such as structural deformations and hydrogen-network rearrangement in the binding pocket induced by the mutations.
- Notably, our predictions are a match also with a recent computational study by Olivucci and co-workers. By means of mixed quantum-Classical simulations, they showed that the retinal chromophore inside three different visual proteins (rhodopsin, squidrhodopsin, melanopsin) photoisomerizes with a rate that is higher than the more blue-shifted absorption (498, 476, and 462 nm, leading to 90, 60, and 40 fs ES lifetimes, respectively)[12].

The behavior predicted with very strong positive ($>+0.003$ au) electric fields, and discussed in the section before, can be expected in solution. Polar solvents, like methanol[14,166,177,202] or dichloromethane[166], shield the counterion and, in turn, do strongly stabilize (destabilize) the covalent states (CT state), as their molecular dipoles, which are in equilibrium with the electronic density of the covalent GS, are oriented favorably (unfavorably) with respect to the GS (CT ES) density. The same effect on covalent and CT states is also expected in nonpolar solvents where tight bound ion pairs between the cationic RPSB chromophore and its negative counterion exist[172,175]. Remarkably, this would explain why no correlation between the polarity of the solvent and the ES lifetime is found in time-Resolved fluorescence measurements. As stated by Chergui and co-workers "The various decay channels show little or no dependence with respect to the viscosity or dielectric constant of the solvents." [174] and further "There is no clear trend of the fluorescence decay times with solvent properties." [175]. In general, longer lifetimes are observed in solution (in the order of few picoseconds compared to 100 fs in rhodopsin[5,173]) independent of the solvent polarity. These longer lifetimes have been controversially disputed over the years[172,174-176,203] and are here believed to be caused by trapping the population in a covalent well on the S1 surface due to the dramatic stabilization/destabilization of the covalent/CT states operated by the solvent polarization and/or the counterion that produce a local very strong positive field ($>+0.003$ au). On the other hand, subtle changes in the electronic structure of the retinal chromophore, such as the ones caused by substitutions along the chain, may restore the stability of the inverted (i.e., ionic) photoactive bond length minimum on S₁, thus speeding up the decay and photoisomerization reaction as recently observed in substituted RPSBs[178-180]. Studies in explicit solvent to validate this scenario are currently in progress.

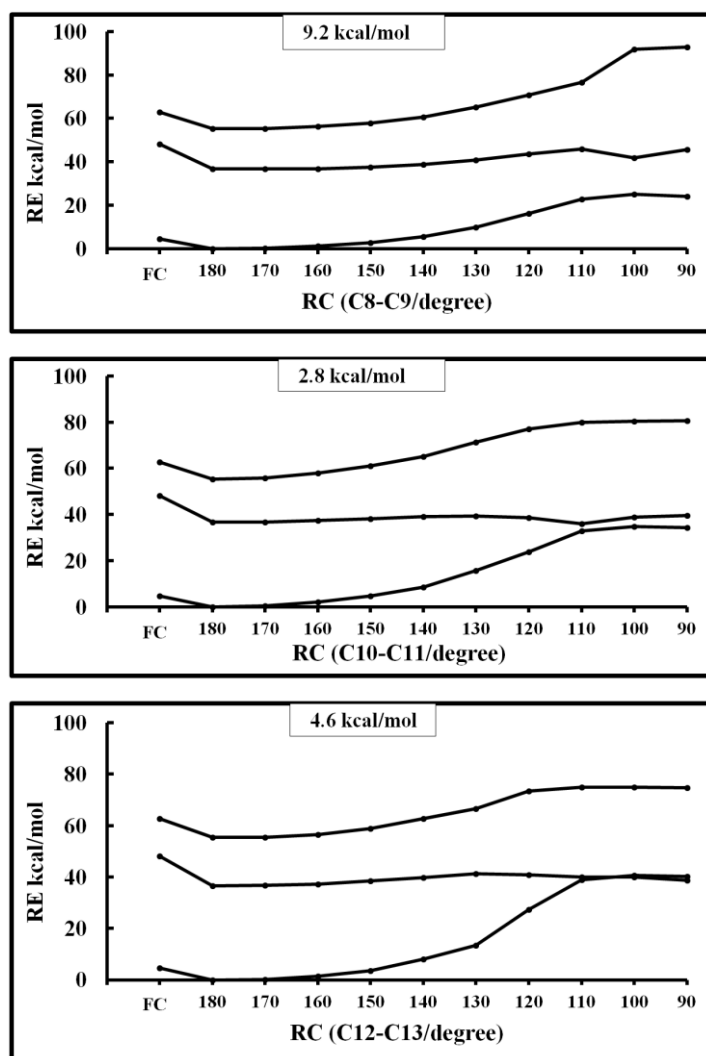


Figure 5-13. Profiles of RPSB along three torsion angles (around bonds C₈–C₉, C₁₀–C₁₁ and C₁₂–C₁₃) obtained from relaxed scans (relaxing the CT ES) in the presence of an electric field with strength -0.003 au.

5.3.4 Rationalization of the Results: The Extended Two-electron Two-Orbital Model

In the following, we will elucidate the observations outlined in the previous section in the scope of the two-electron two-orbital theory originally introduced by Michl and Bonacic-Koutecky to explain the geometrical and electronic structure of one-bond-flip CIs found in strongly polar conjugated polyenes[204], and which was later generalized to predict the topography and energetics of the CI seam in both polar and nonpolar polyenes whose initial ES dynamics follow the Woodward–Hoffmann rules[181,182]. According to the “extended” two-electron two-orbital theory which treats interactions of two “active” electrons in two noninteracting (i.e., not sharing common atomic centers) “active” orbitals, two conditions must be fulfilled in order to reach a CI out of the FC point, the resonance condition

$$h_{AB} \approx 0 \quad (5.1)$$

and the heterosymmetry condition

$$J_{AA} - J_{AB} = \varepsilon_B - \varepsilon_A \quad (5.2)$$

The individual terms in Eqs. (5.1) and (5.2) are the one-electron resonance integral h_{AB} , the Coulomb repulsion integrals J_{AA}/J_{AB} and the one-electron energies $\varepsilon_{A/B}$ of the two non-interacting orbitals A and B, subject to Coulombic repulsion and exchange interaction with the remaining electrons in the system. Distinct motions that cancel the resonance term, and hence fulfill the resonance condition, can be identified by the Woodward–Hoffmann (WH) rules depending on the number of π -electrons involved. For two π -electrons, the motion is a 90° torsion around a double bond (one-bond-flip), for $4i\pi$ – and for $(4i + 2)\pi$ – electrons a disrotatory and conrotatory ring closure/opening rotations, respectively. Thus, one can view ethylene, 1,3-butadiene (cyclobutene), and 1,3,5-hexatriene (2,4-Cyclohexadiene) as the basic units which allow for dynamics driven by the (WH) rules. Fulfillment of the resonance condition in the basic unit leads to a homosymmetric biradical with energetically degenerate active orbitals (**Figure 5-14**). The GS is a (singlet) biradical (denoted as $|A \bullet B \bullet\rangle$ in **Figure 5-14**), while the first ES is a linear combination of closed shell configurations ($|A^2\rangle, |B^2\rangle$), referred to as a zwitterionic, i.e., $|A^2\rangle - |B^2\rangle$. The energy difference of the two states is given by the difference in the Coulombic terms $J_{AA} - J_{AB}$, thus, the higher energy of the zwitterionic state arises from the stronger repulsion of both active electrons occupying the confined space of the same localized orbital. To reach degeneracy the heterosymmetry condition of Eq. (5.2) can be fulfilled by adjusting the one-electron energies $\varepsilon_{A/B}$. This can be realized by asymmetric geometrical deformations, orthogonal to the WH deformation and/or by electronic effects induced through asymmetric functionalization.

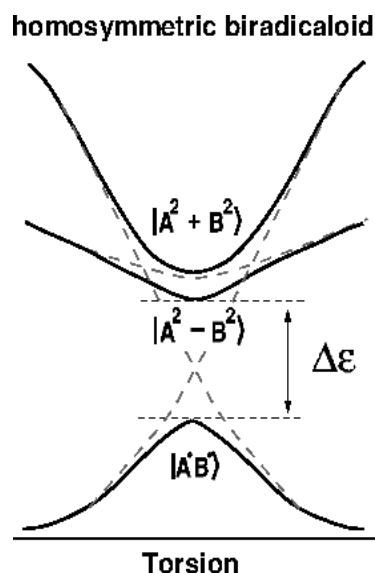


Figure 5-14. Two-electron / two-orbital model, introduced via a correlation diagram for the π^2 , $\pi\pi^*$, and π^{*2} configurations for the torsional deformation along a double bond. In the region around 90° a noninteracting (not sharing common atomic centers) orbital basis (A,B) provides a more comprehensive description of the emerging covalent ($|A \bullet B \bullet\rangle$) and zwitterionic ($|A^2\rangle, |B^2\rangle$) configurations. Absent or symmetric functionalization at both sides of the twisted double bond implies equivalence of the noninteracting orbitals A and B, a constellation known as a homosymmetric biradical.

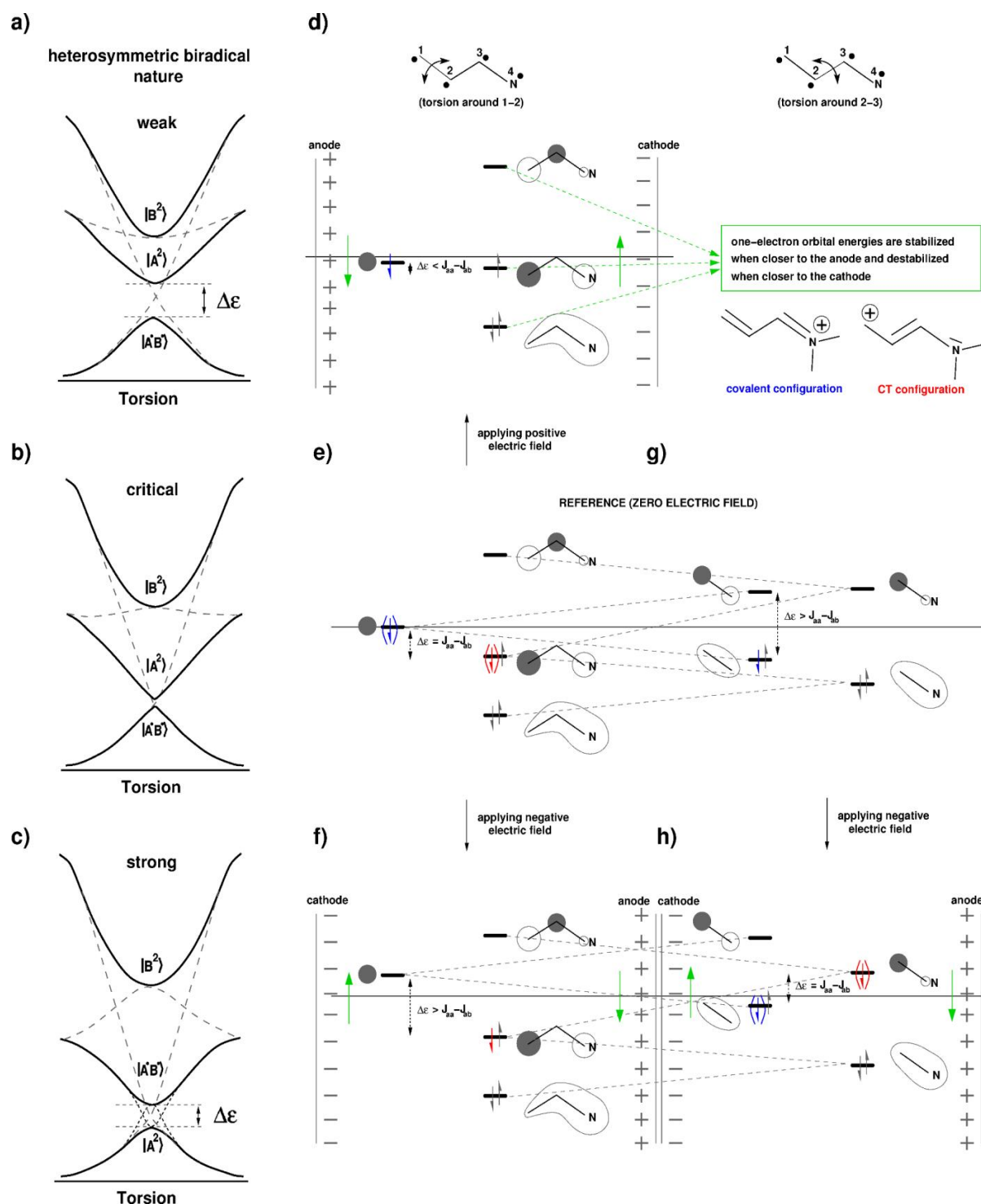


Figure 5-15. a–c) Asymmetric geometrical or electronic (functionalization / substitution) deformation alters the electron affinity on both sides of the twisted double bond; depending on the strength of the deformation the systems can be categorized as weak (a), critical (b), and strong (c) heterosymmetric biradicaloids. An external electric field can alter the nature of the biradicaloid. Frontier orbitals and electronic structure of the GS and first ES resulting from occupying these orbitals at the geometry twisted by 90° around the C₁₁–C₁₂ (d–f) and C₁₂–C₁₃ (g–h) bonds of a minimal RPSB model consisting of two double bonds under the influence of a uniform external electric field.

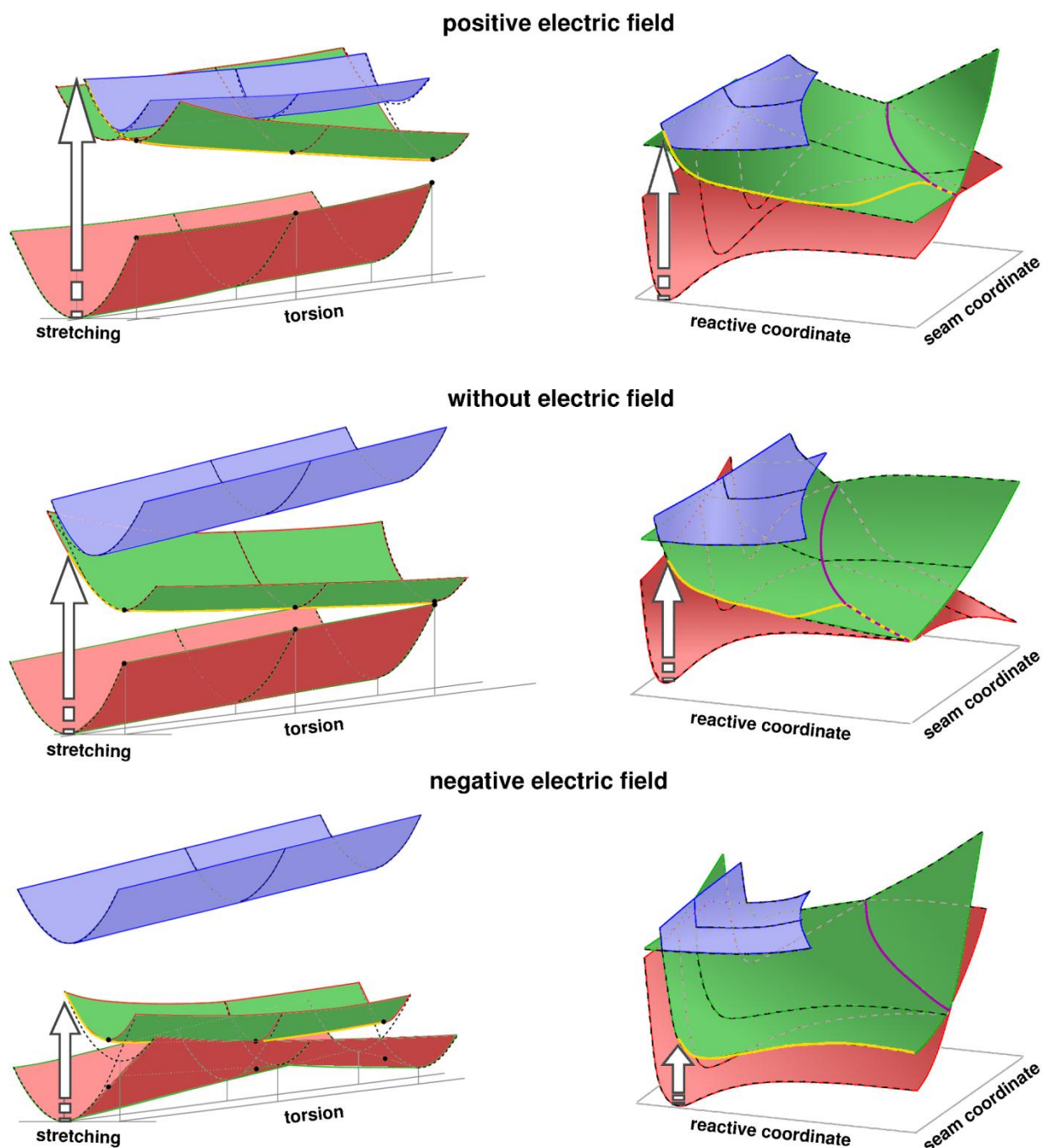


Figure 5-16. a)–C) Sketches of the potential energy surfaces of the ground (red), first (green), and second (blue) adiabatic ESs in the subspace of stretching and torsion for different electric field strengths; d)–f) sketches of the potential energy surfaces of the ground, first, and second ESs representing the relative position of the reactive coordinate (yellow) and the CI seam (magenta) for different electric field strengths. Dashed lines follow the diabatic character (covalent or ionic).

In the particular case of protonated Schiff's bases the basic unit is ethylene, and torsion around any double bond fulfills the resonance condition. Exchange of a carbon atom at one side of the rotating bond with the isoelectronic positively charged nitrogen introduces an asymmetric deformation of the electronic structure of the biradical, turning it into a heterosymmetric biradicaloid ($\epsilon_B \neq \epsilon_A$, **Figure 5-15**). The induced energetic splitting of the

one-electron orbitals suffices to overcome the excessive electron repulsion in the zwitterionic configuration $|A^2\rangle$, thus, allowing to reach a CI without an additional geometrical deformation (critically heterosymmetric biradicaloid, **Figure 5-15**). **Figure 5-15 6e** depicting this situation for a minimal RPSB model consisting of two double bonds rationalizes the photochemistry of retinal in the absence of an electric field (**Figure 5-6**, middle column). Torsion around any double bond would stabilize the ionic state and will lead to a CI with the covalent GS as shown schematically in **Figure 5-16b**. The early encounters of crossings evident in the ES profiles in the absence of an electric field (i.e., before reaching twisting of 90°) do not contradict the above statements. In fact, the hydrogen-out-of-plane (HOOP) deformation (**Figure 5-17b**) ensures that the resonance conditions are fulfilled also for smaller twisting angles by keeping the resonance term h_{AB} close to zero. As the degree of HOOP deformation must increase with decreasing torsional angle to ensure the fulfillment of the resonance condition the CI seam becomes energetically less favorable (i.e., sloped) below 50° and shifts away from the minimum energy profile as demonstrated schematically in **Figure 5-16e**.

The position of the torsional angle within the conjugated system has a quantifiable, albeit minor effect on the energetic profile of the CT state. Torsion along a bond closer to the iminium-group allows delocalizing the positive charge in the ES state over a more extended conjugated region, effectively contributing to the stabilization of the CT state. As a consequence the GS/ES crossing shifts to slightly smaller torsional angles (from 60° to 50° , **Figure 5-6**, middle column).

5.3.5 An External Electric Field Affects the Topography of the CI Seam.

Already Michl and Bonancic-Koutecky demonstrated that an external electric field, simulated through point charges in the vicinity of the twisted double bond of ethylene has an effect identical to asymmetrically distorting the active orbitals and is capable of lifting the degeneracy of the one-electron orbital energies $\varepsilon_{A/B}$: the orbitals closer to the positive charge (i.e., the anode) are stabilized, while the orbitals closer to the negative charge (i.e., the cathode) are destabilized (**Figure 5-15d**). The effect is comparable to the one exerted by the internal field created via asymmetric functionalization through push-pull groups, which have been shown to introduce a CI along the electrocyclic isomerization (WH) coordinate of cyclohexadiene-based molecular switches[182,205], while the parent compound exhibits the CI aside from the WH coordinate.

Following the above consideration a positive electric field (according to the definition in **Figure 5-1**) applied to the protonated Schiff's base reduces the energy gap between the frontier orbitals A and B, thereby turning the critically heterosymmetric biradicaloid into a weakly heterosymmetric one (**Figure 5-15a**). The fulfillment of the heterosymmetry condition requires more pronounced geometrical deformations as compared to the zero field reference. In gas-phase this is achieved by elongation of the C_{15} -N bond from 1.32 Å to 1.38 Å, accompanied by the pyramidalization of the iminium-group (**Figure 5-17c**) which effectively stabilizes the CT state through shielding the lone pair of the nitrogen. A study on a

solvated RPSB model with five double bonds in methanol showed that the same effect can be achieved by deploying solvent molecules close to the C-terminus[202]. The stabilization of the ES (through the additional geometrical deformations or solvent effects) in the CI region opposite to its blue-shift in the FC region introduces a steeper slope on the bright state, thereby completely suppressing any barriers (**Figure 5-6** lower right window, see also **Figure 5-16a**). However, torsion around double bonds closer to the β -ionone ring (e.g., around the C₉-C₁₀ bond, **Figure 5-6** upper right window) are expected to destabilize the CT so much as to shift the CI seam completely aside from the minimum energy path, thereby altering its slope as shown schematically in **Figure 5-16d**. The impeded access to the CI seam and the time required to either redistribute vibrational energy into the iminimum modes or to rearrange the first solvent shell could potentially increase the lifetimes in strongly polar solvents independent of the predicted steeper slope, thus offering a further explanation for the longer ES lifetimes observed in solution beside the already discussed population trapping in nonreactive channels.

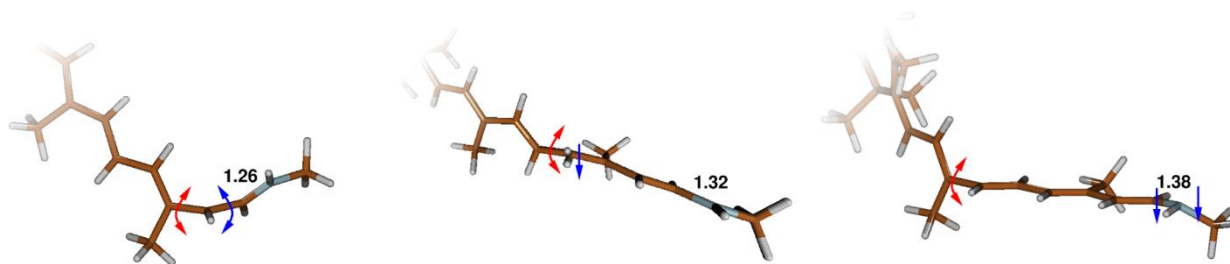


Figure 5-17. CIs of RPSB for torsional angle 90° for negative (left) and positive (right) electric field of strength 0.003 au, as well as the CI for 50° torsion in the absence of electric field (middle). The bonds around which the torsion occurs, as well as the additional deformations, necessary to reach the CI are highlighted.

A Negative electric field increases the energy gap between the frontier orbitals A and B, thereby creating an inversion of the energetic order of the biradical $|A \bullet B \bullet\rangle$ and the zwitterionic $|A^2\rangle$ configurations along the torsional deformation (**Figure 5-15f**). This situation is known as a strong heterosymmetric biradicaloid (**Figure 5-15c**). The observed configuration inversion in the absence of a CI along the path suggests the participation of an avoided crossing as schematically shown in **Figure 5-16c**. This hypothesis is verified by inspecting the charge distribution and permanent dipole moment along the reaction coordinate (**Figure 5-18** and **Figure 5-19**). While for zero and positive electric fields the ES characterize by primarily (in the CI exclusively) localizing the positive charge closer to the β -ionone moiety (**Figure 5-20**), we encounter the opposite situation for negative electric fields. For field strength beyond 0.001 au the covalent configuration becomes dominant already at the relaxed planar ES geometry and as a consequence does not exhibit the expected bond inversion. Eventually, for field strengths around -0.003 au all bonds become equilibrated. The avoided crossing along the torsional coordinate introduces a finite S0/S1 gap along the entire reaction coordinate (**Figure 5-16c**), which must be overcome in gas-phase through additional geometrical deformations. Our computations demonstrate that again the iminium-group is mainly involved through shortening of the C₁₅-N bond length from 1.32 to 1.26, aiming to destabilize the CT configuration, now dominating the ground-state (**Figure 5-17a**). The cooperative effect of a negative electric field and torsion closer to the iminium-group

(e.g., around the C₁₃–C₁₄ bond, **Figure 5-6** lower left window) shifts the CI seam completely aside from the minimum energy path hardly reachable even for 90° torsion (**Figure 5-16f**).

As shown earlier (**Figure 5-13**) the bond length equilibration at the ES minimum in the case of strong negative fields opens new deactivation channels involving torsion around bonds C₈–C₉, C₁₀–C₁₁ and C₁₂–C₁₃ (with single bond character in the GS). **Figure 5-15f,h** correlates the two sets of isomerization coordinates. While for zero and weak electric fields the isomerization along a single bond preserves a large HOMO–LUMO gap even for a 90° twisting angle (**Figure 5-15f**), for strong negative field the covalent closed shell configuration becomes destabilized and degenerates with a biradical CT configuration (**Figure 5-15h**), contrary to the situation discussed above, where the CT state was described through a closed shell configuration (**Figure 5-15e**). For sufficiently large negative electric fields the isomerization along C₈–C₉, C₁₀–C₁₁, and C₁₂–C₁₃ will become more favorable (compare barriers in **Figure 5-13** and **Figure 5-6**, left column). Departing from the electronic structure in the vicinity of CI we trace back to the FC point where both “active” orbitals A and B couple, thus creating bonding and antibonding delocalized orbitals HOMO and LUMO provided they are energetically close in energy which is fulfilled for stronger negative fields. We recognize that the HOMO and LUMO have a different nodal structure than in the absence of an electric field. The GS is characterized by a partial positive charge at the C-tail, resembling the shift of the electron density toward the anode. Upon excitation a full CT to the N-tail occurs, coded in the strong increase of the dipole moment. However, and most noticeably, due to the different nodal structure of the frontier orbitals participating in the transition the relaxation of the CT configuration is not accompanied by bond–order inversion, thus favoring isomerization around C₈–C₉, C₁₀–C₁₁, and C₁₂–C₁₃.

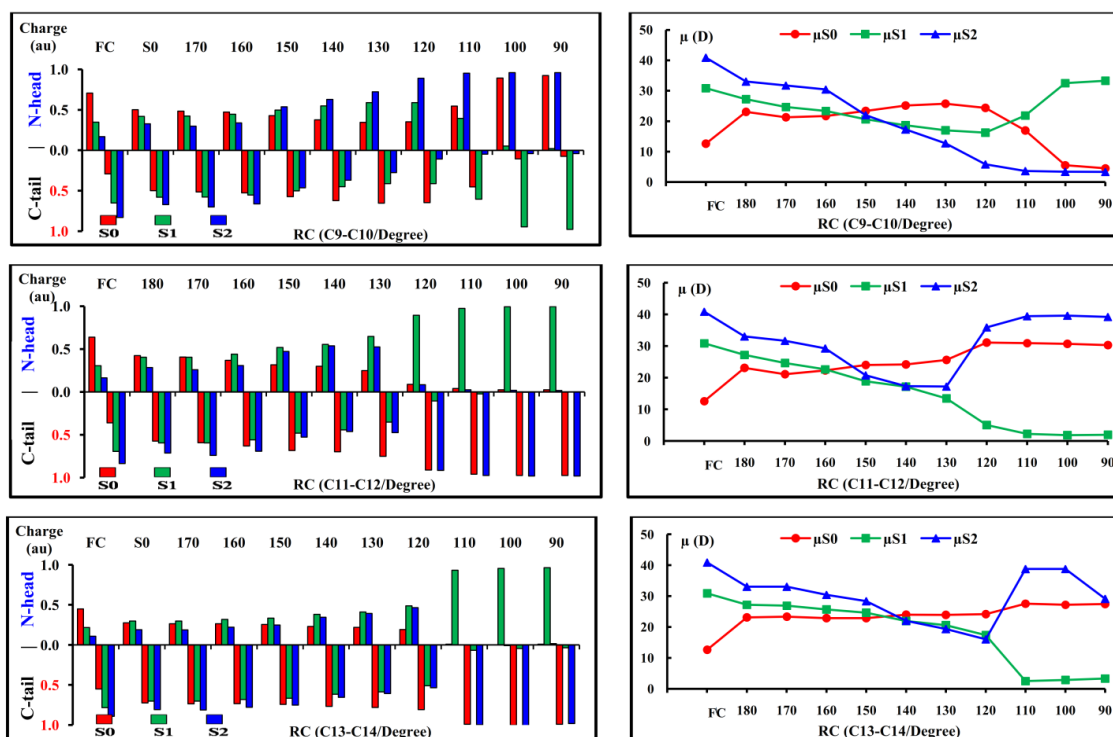


Figure 5-18. Mulliken charges (left column, N-head and C-tail refer to the charges for the right and left moieties from the central of rotating bond, respectively) and permanent dipole moments (right column) of RPSB chromophore for the relaxed scans around C₉–C₁₀, C₁₁–C₁₂ and C₁₃–C₁₄ in the presence of electric field with strength -0.003 au, calculated at SA3–CASSCF(12/12)/6-31G* level of theory.

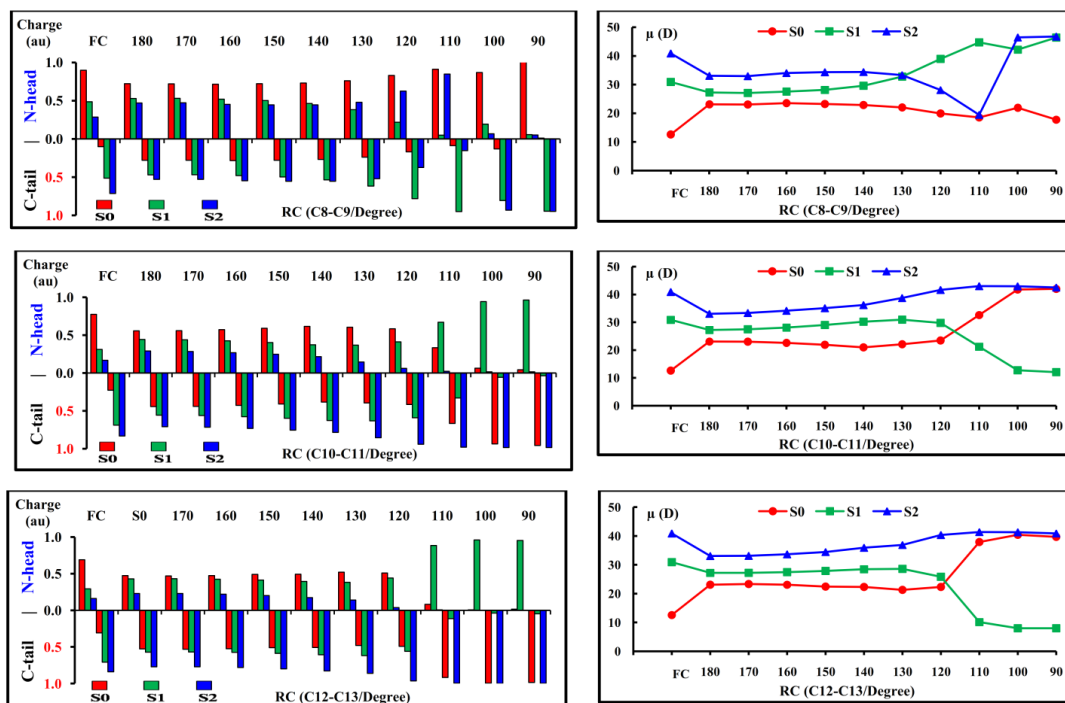


Figure 5-19. Mulliken charges (left column, N-head and C-tail refer to the charges for the right and left moieties from the central of rotating bond, respectively) and permanent dipole moments (right column) of RPSB chromophore for the relaxed scans around C₈-C₉, C₁₀-C₁₁ and C₁₂-C₁₃ in the presence of electric field with strength -0.003 au, calculated at SA3-CASSCF(12/12)/6-31G* level of theory.

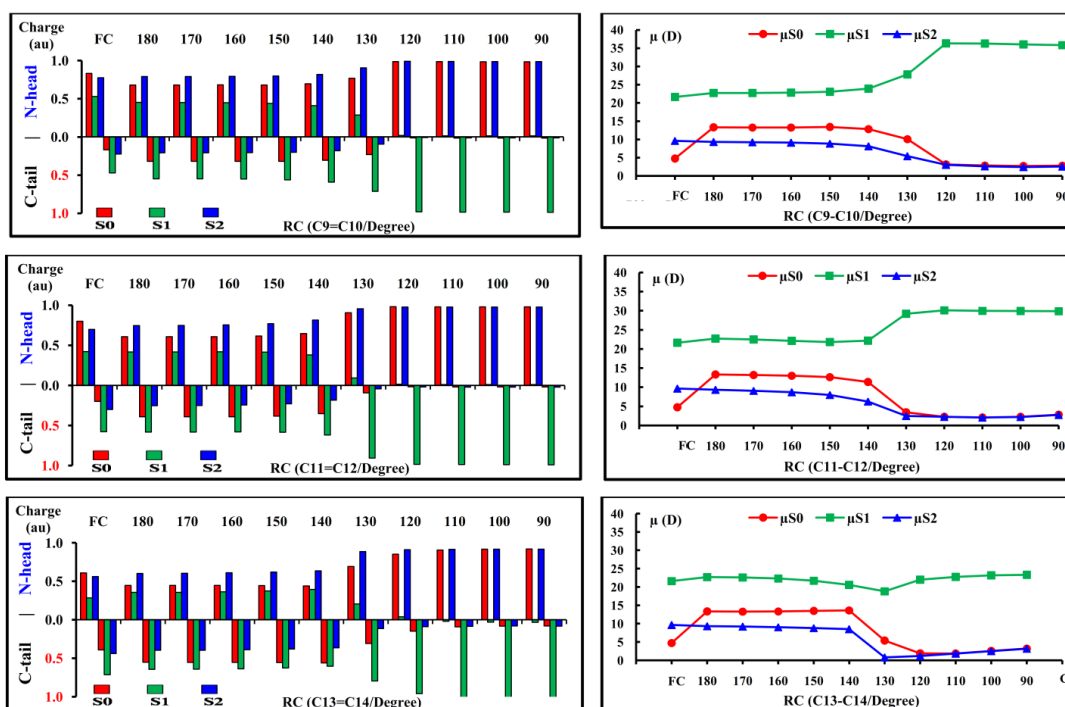


Figure 5-20. Mulliken charges (left column, N-head and C-tail refer to the charges for the right and left moieties from the central of rotating bond, respectively) and permanent dipole moments (right column) of RPSB chromophore for the relaxed scans around C₉-C₁₀, C₁₁-C₁₂ and C₁₃-C₁₄ in the absence of electric field, calculated at SA3-CASSCF(12/12)/6-31G* level of theory.

5.3.6 Electric Field Impeded Ultrafast Isomerization.

Unlike the mechanism of CT destabilization in polar solvents and in certain protein environments, which has been studied extensively in the literature, the mechanism of configuration inversion upon CT stabilization has not been documented thoroughly. From a practical point of view one could ask what is the optimal electric field which would cause bond equilibration in the ES and, hence, would introduce a substantial barrier along any torsional coordinate, thereby inhibiting or at least severely slowing down the ES deactivation. If such a window can be found, RPSB mimics, where the electric field effect would be achieved through suitable functionalization bare the potential to be utilized as photoswitchable fluorescent dyes.

To answer this question we performed a fine scan of the electric field strength between -0.0015 au and -0.0040 au in steps of 0.0001 au, thereby relaxing the planar geometry in the ES. The result is documented in **Figure 5-21**. Due to the coexistence of two electronic configurations (a CT accompanied by single–double bond inversion and a CT which preserves the bond order, both strongly mixing with the corresponding covalent configuration) for strong negative electric fields we observe two stable bond configurations in the window between -0.0018 and -0.0033 au (solid and dashed lines). Below -0.0022 au, the CT configuration accompanied by single–double bond inversion (solid line) is more stable, while above -0.0022 au, the CT configuration preserving the bond order (dashed line) becomes more stable. The energetic differences are rather small (<1 kcal/mol) suggesting a flat potential connecting both geometries and confirmed by linear interpolation for three electric field strengths (-0.0018 , -0.0025 and -0.0032 , see **Figure 5-21b** and **Figure 5-22**); therefore, at room temperature both structures will be populated. A clear trend of bond inversion is observed for both sets when varying the electric field strength: C_9-C_{10} , $C_{11}-C_{12}$, and $C_{13}-C_{14}$ having a more pronounced single bond character for weak electric fields, while adopting a double bond character for strong fields. Correspondingly, bonds C_8-C_9 , $C_{10}-C_{11}$, and $C_{12}-C_{13}$ behave the other way around. What is attracting the attention is the window between -0.0026 and -0.0028 au in which all bond lengths are comparably short. In fact, there is no bond longer than 1.42 Å, compared to 1.47 Å for a zero electric field. The presented example of constrained scans for -0.003 au (**Figure 5-6**, left column) lies very close to this window (with a maximal bond length of 1.43 Å), which explains the lower but non-negligible barriers for rotations around bonds C_8-C_9 , $C_{10}-C_{11}$, and $C_{12}-C_{13}$ (**Figure 5-13**).

We could speculate that the encountered behavior in a strong negative electric field accounts for the lack of retinal proteins absorbing into the red above 590 nm[**206-209**], as this is exactly the absorption energy window caused by an electric field of -0.0025 to -0.0030 au which leads to bond length equilibration in the ES. This situation would be incompatible with the requirement of ultrafast decay and photoisomerization necessary to facilitate light transduction. In any case it would be interesting to study the dynamic behavior of retinal under these conditions.

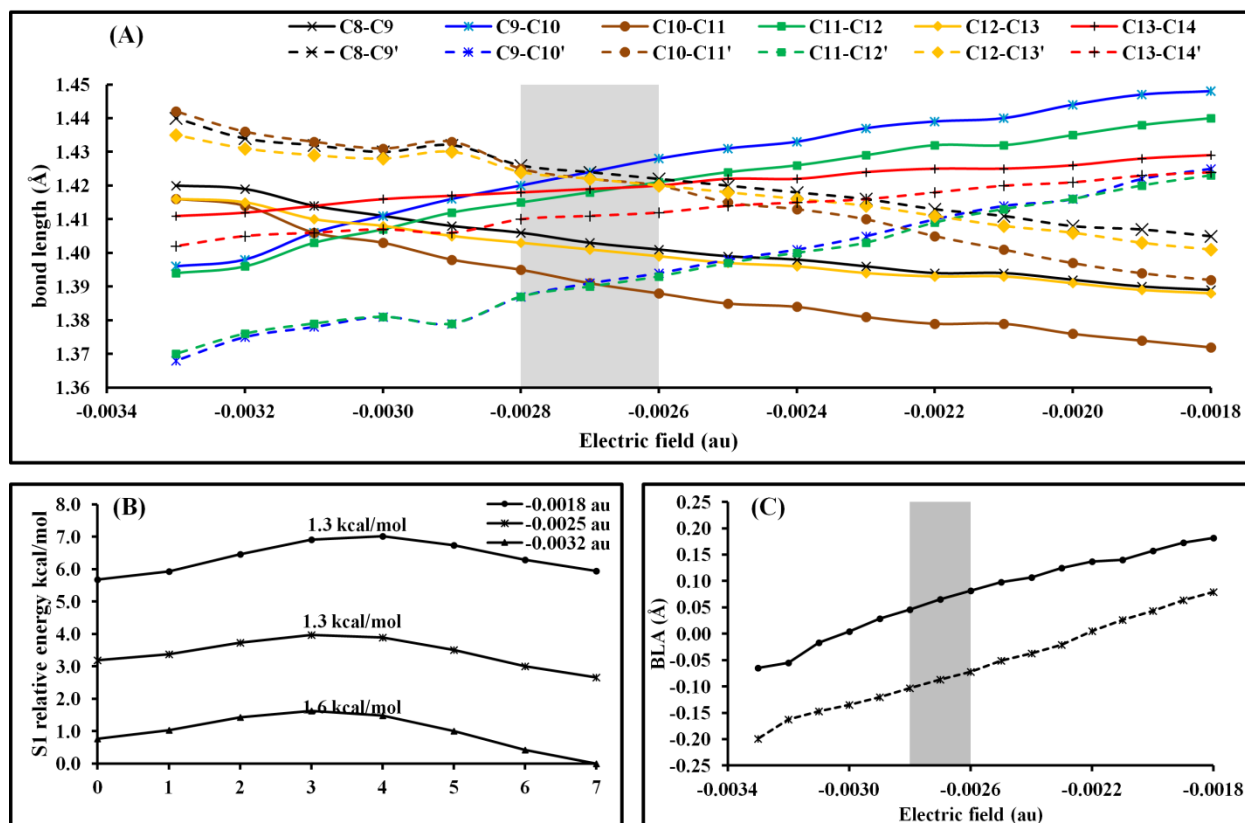


Figure 5-21. (A) Bond lengths at the equilibrated ES geometry of the parent molecule for different strengths of the electric field (between -0.0018 au and -0.0033 au). (B) SS-CASPT2 S_1 energy profiles obtained through linear interpolation between both minima coexisting in the electric field range -0.0018 au : -0.0032 au at the SA-2-CASSCF level. Profiles for three electric field strengths, -0.0018 , -0.0025 and -0.0032 au, are shown. (C) Bond length alternation ($BLA = \sum_{i=7,9,11,13} d_{C_i-C_{i+1}} - \sum_{i=8,10,12,14} d_{C_i-C_{i+1}}$, d is the bond length) of both minima at different strengths of the electric field shown in part A.

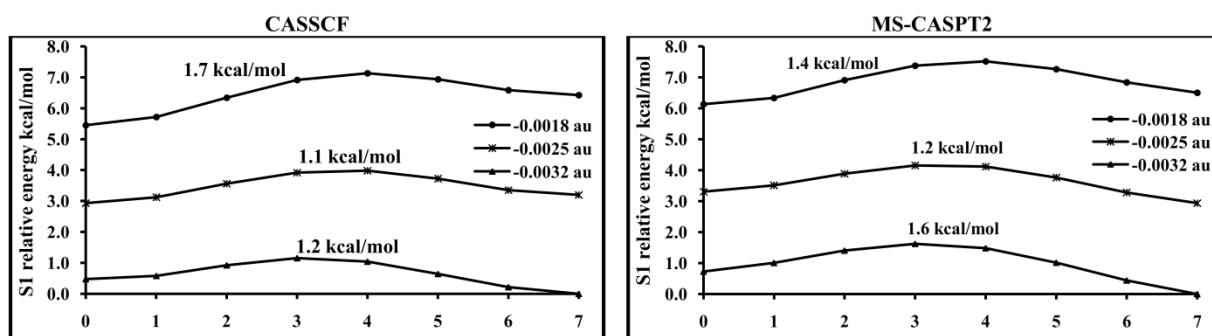


Figure 5-22. CASSCF and MS-CASPT2 S_1 energy profiles of the RPSB chromophore obtained through linear interpolation between both minima co-existing in the electric field range -0.0018 au : -0.0032 au at SA-2-CASSCF level. Profile for three electric field strengths, -0.0018 , -0.0025 and -0.0032 au, are shown.

5.3.7 Internal Fields Created by Polar Functional Groups: Transferability and Generalization of the Model.

The heterosymmetry condition (Eq. 5.2) has a great importance for generalizing the described trends to functionalized RPSB chromophores. It states that the effect of an external electric field, namely to vary the gap between the “active” orbitals, can be achieved also through selective functionalization with electron donating / withdrawing groups which induce an intramolecular electric field. It is therefore justified to ask to what extent the trends derived for the parent RPSB compound are transferable to functionalized systems. We demonstrated earlier that introducing a pair of 0.5e charges with opposite signs in the immediate vicinity of the retinal chromophore (see **Figure 5-4**) has a comparable effect on the FC transition energies as applying an electric field of ± 0.004 au. Furthermore, we discussed that attaching a positively charged trimethylamino group to the C-terminus side of the RPSB destabilizes the CT state, thus opening a new population trapping channel involving the covalent ES. In the following paragraph we demonstrate that the photophysics of push/pull-functionalized RPSB derivatives can be also forecast based on what we have learned from the parent compound. For this purpose we functionalized the RPSB asymmetrically with a σ -electron withdrawing trifluoromethyl-group (CF_3^-) closer to the ionone ring and a π -electron rich methoxy-group (MeO^-) closer to the iminium-group (see **Figure 5-23** right) and vice versa (see **Figure 5-23** left) and computed the profiles of the three lowest states along the torsion around the central double bond involving C11 and C12. Thereby the MeO-group was confined in a five-membered ring to the conjugated double bond chain in order to prevent twisting and utilize the mesomeric effect of the oxygen lone pair. The electron withdrawing and donating groups can be regarded as having partial positive and negative charges, respectively, thus a nonuniform intramolecular electric field is generated upon functionalization.

The positive intramolecular electric field, created via attaching the CF_3 -group to C₉ and enclosing the MeO-fragment in the ring comprising C₁₁, C₁₂, and C₁₃, induces the expected blue-shift of the absorption energy of the CT state. Wave function analysis shows that the S2 state, placed at 2.89 eV (428 nm) above the ground-state in the FC point, has a more pronounced CT character than the S1 state of covalent nature at 2.50 eV (496 nm), however the state mixing is encoded in the nearly equal magnitude of the dipole moments (14.2 D vs 12.2 D, see **Figure 5-24**). The absorption energy of the CT state puts the functionalized species on a level with positive electric field strengths of ca. +0.0025 au. However, it should be noted that the covalent state is significantly more red-shifted than in the parent compound at comparable field strengths. As in the parent compound, exposed to an electric field of strength +0.003 au (**Figure 5-6**, right column), upon ES relaxation the wave function of the S2 state collapses to a pure CT configuration, which equilibrates at a much lower energy at CASPT2 level than the relaxed covalent configuration (see **Figure 5-23** right). Consequently, already upon 10° torsion full single–double bond inversion takes place. Thus, once more, we demonstrate that ionic–covalent mixing is confined to a very limited coordinate space and either bond relaxation or torsion lead to instantaneous collapsing of the S₁ wave function into a pure CT. Further similarity with the parent compound is the impeded accessibility of the CI seam which is reached only at angles close to 90° due to the additional deformations necessary to stabilize the CT state. As in the parent compound the CT stabilization in gas-phase is achieved through utilizing iminium modes (pyramidalization and C–N bond elongation, see **Figure 5-17**). It attracts our attention that the ES does not exhibit the characteristic steep profile observed for the parent molecule in positive electric fields (**Figure 5-6**, right column). We believe that in order to shed light into this discrepancy one needs to

scrutinize the ES potential energy surfaces of a broad selection of functionalized RPSB, a work currently in progress.

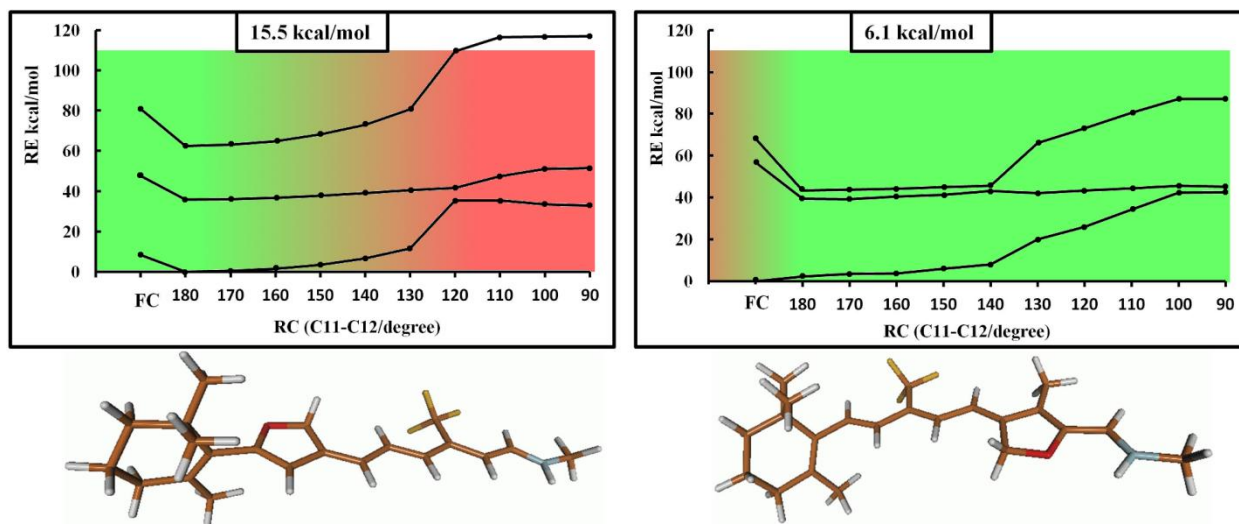


Figure 5-23. Profiles of red-shifted (left) and blue-shifted (right) RPSB derivatives along the torsion angle $C_{11}-C_{12}$ obtained from relaxed scans (relaxing the CT ES) in the absence of an electric field. The colour background denotes the character of the first ES along the optimized path being either covalent (red), CT (green) or mixed.

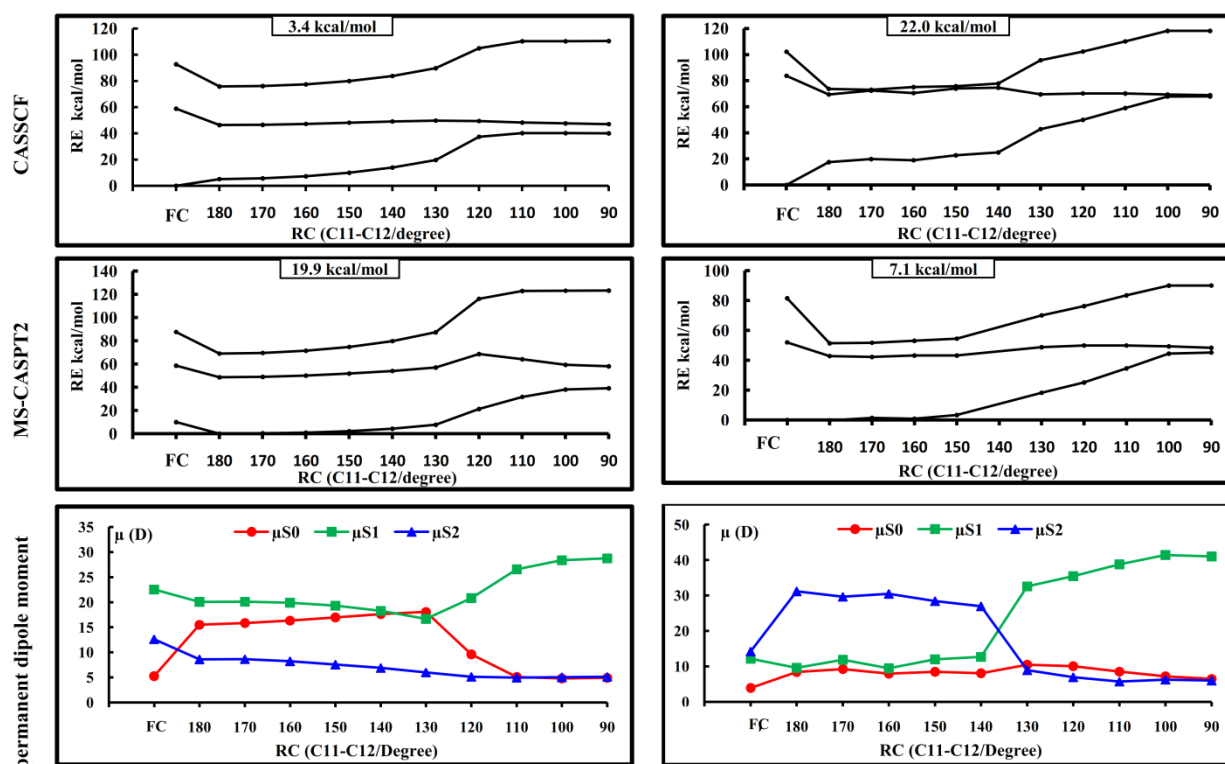


Figure 5-24. SA3-CASSCF(12,12/6-31G* (top), MS-3-CASPT2(12,12/6-31G* on the top of CASSCF calculations (middle) and CASSCF permanent dipole moments (down) profiles of the blue-shifted RPSB (**Figure 5-23**, right) (right column) and red-shifted RPSB (**Figure 5-23**, left) (left column) along the torsion around $C_{11}-C_{12}$ bond calculated from relaxed scans (relaxing the CT excited state) in the absence of electric field at CASSCF(12,12)/6-31G* level of theory.

The negative intramolecular electric field, created via attaching the CF₃-group to C₁₃ and enclosing the MeO-fragment in the ring comprising C₅, C₆, and C₇, induces the expected red-shift of the absorption energy of the CT state down to 1.70 eV (730 nm) which reproduces the effect of electric field strengths of -0.003 au. Torsion around the central double bond, which, as in the parent compound exposed to a -0.003 au electric field, does not show the characteristic bond inversion, leads to a progressive energy increase of both S₀ and S₁ and does not encounter a CI (see **Figure 5-23** left). Inspection of the permanent dipole moments, however, clearly points at an avoided crossing around 120°.

In conclusion, the effect of an inhomogeneous electric field generated via functionalization can be very well reproduced by studying the effect of an externally applied homogeneous electric field whose strength can be estimated in relation to its effect on the absorption energy at the FC point.

5.4 Conclusions

In the present contribution we report the results of a systematic computational study on the dependence of the absorption energies and photoisomerization ability of the RPSB chromophore on the strength and direction of a uniform external electric field. A systematic linear shift of the absorption energy throughout the whole visible spectrum as a function of the field strength is observed. Specifically, fields between -25 MV/cm and $+20$ MV/cm shift the absorption energy from 800 to 400 nm. While external fields of such a strength are technologically not accessible, yet, comparable fields can be locally achieved by nearby charges and polar groups (such as the ones found in the retinal binding pocket of opsins) as well as charged/polar functional groups introduced in the vicinity of the RPSB chromophore.

The photoisomerization paths revealed clear trends in the topography of the ES energy profiles that can be related to the interplay of the ionic and covalent configurations and their response to the geometrical deformations (bond relaxation and torsion) in the conjugated system. The strong ionic/covalent wave function mixing observed at the edges of the two (positive and negative) operational regimes, i.e., mixing between S₁/S₂ for positive and between S₀/S₁ for negative electric fields, rapidly collapses upon bond relaxation and torsion as covalent (ionic) configurations are destabilized (stabilized). Consequently, in the case of positive electric fields, S₁ adopts a pure CT configuration, which eventually relaxes barrierlessly to a CI with the ground-state, while in the case of negative electric fields S₁ becomes covalent (and S₀ ionic) and this introduces a barrier along the decay profile, eventually turning the chromophore from a nonfluorescent ultrafast photoisomerizing device into a fluorescent dye. This behavior could explain why there are no retinal proteins absorbing in the far red above 590 nm. At the same time we could resolve the formation of another CT electronic configuration in the presence of strong positive fields characterized through a different nodal structure of the frontier orbitals participating in the CT excitation which largely preserves the GS bond-order, thus opening new isomerization channels. The existence of two distinct CT configurations may open the possibility for designing molecular devices that can be reversibly switched between a nonfluorescent ultrafast photochromism (i.e., photoisomerization) and a fluorescent state by applying electric fields already achievable by nowadays technology.

Interestingly, a simple correlation between the absorption energy decrease (increase) and the corresponding increase (decrease) of the ES lifetime that is tentatively based on our

calculations is supported by time-Resolved data recorded for native and mutated retinal proteins. Eventually, we expect that blue-shifting the absorption energy of the RPSB chromophore would speed-up its photoisomerization, unless very strong positive fields, as the ones present in solution, are used. If this is the case, our simple model suggests that isomerization would slow-down due to a) the observed shift of the CI seam away from the minimum energy path and b) the state inversion (i.e., first ES adopts covalent character) and potential trapping of the ES population in a covalent excited minimum. Notably, this correlates with the general decrease in photoisomerization and decay rates observed in solution.

Not only the isomerization rate but also its selectivity seems to be largely affected by the electric field, thereby making it possible to conceive controlling schemes involving switching between isomerization channels. Positive fields favor torsion around bonds closer to the iminium-group, while negative fields favor torsion around bonds closer to the ionone rings. More complex controlling schemes are imaginable when considering that for negative electric fields beyond -20 MV/cm new isomerization channels become accessible.

We also explored the possibility of utilizing a homogeneous electric field for understanding the effects of functionalization with electron withdrawing and donating groups, which can be seen as generators of local electric fields. We demonstrated that many of the characteristics encountered in the reference system exposed to an external field can be recovered also in the two functionalized retinal PBS chromophores investigated here, one absorbing in the red-side and the other in the blue-side of the spectral window explored.

Further research on the field would involve as a first step a study of a large variety of functionalized RPSB chromophores in order to scrutinize the correlation between homogeneous external fields and local fields created through functional groups. As a second step, molecular dynamics on the parent and selected systems in the presence of “quasi-homogeneous” external fields (as generated by a capacitor) in a realistic environment treated at the QM/MM level can be envisioned. Those studies may become the cornerstone toward defining the prerequisites for designing ultrafast spectrally tunable molecular devices, whose functional groups work as electric field generators to tailor specific properties.

6 Functionalized Retinal Chromophore with Tailored Spectral and Photochemical Properties: Towards Bio-inspired Designer Molecules

6.1 Introduction

In the previous section it was demonstrated how a homogeneous electric field can be utilized to tune the absorption wavelength of the retinal protonated Schiff-base (RPSB) chromophore throughout the entire visible range and to steer the isomerization. In the following section we argue that a similar effect can be anticipated by introducing electron withdrawing and/or donating functional groups along the backbone of the RPSB chromophore as generators of non-uniform strong electric fields. It will be demonstrated how this intervention affects directly the electronic and, as a consequence, the geometrical structure of the chromophore which translates into variations of the absorption and emission features. Moreover, quantifying the effects and understanding how each functional group modulates the potential energy surfaces will allow to utilize them as tools for fine-tuning and, thus, controlling isomerization rate, efficiency and selectivity of the photo-process [210,211] without the necessity to apply external fields in the 25 MV/cm range, anyway out of technical reach nowadays.

It is well documented that the reaction mechanism of PRSB is characterized by a barrierless photoisomerization path on the spectroscopic state S_1 (that has a CT character, i.e. a positive charge transfer occurs from the N-head to the C-tail of the chromophore) and the system is ballistically driven into a conical intersection (CI) between S_1 and S_0 that has the form of a twisted intramolecular CT (TICT) state. From a static point of view, two reaction coordinates are involved in this mechanism. The first describes the relaxation out of the FC region to the S_1 minimum and involves a bond order inversions. The second coordinate is dominated by twisting around one of the double bonds which leads to the CI. Using the example of RPSB chromophore R_{30} (see **Figure 6-2**, called parent compound thereafter) in the previous section we discussed how electric fields affect absorption, emission and the topology of the potential energy surface and established a direct connection to the environment-induced electrostatic effects inside the reactive pockets of RPSB embedding proteins and in solution. The main results are summarized below:

- Positive electric fields (for definition of see **Figure 5-1**) available for example in the cavities of blue-opsins or in polar solvents destabilize the bright CT state in the FC region with respect to the covalent ground and S_2 states (blue-shift of the absorption). For weak fields a steeper S_1 PES towards the CI region is observed with an avoided crossing formation along the torsional coordinate with increasing electric field strength, implying that torsion alone is insufficient to stabilize the CT to reach a CI with the GS. The system needs to redistribute the kinetic energy into other vibrational

modes in order to reach a sloped CI away from the minimum energy path. For stronger fields population trapping in the FC region may be expected due to the preferable stabilization of the covalent S_2 state. This can effectively lead to an inversion of the order of the excited states, resulting into a covalent S_1 minimum that would be connected to the twisted CI region via a finite barrier. Thus, the isomerization along S_1 would require activation energy.

- Negative electric fields stabilize the bright CT state in the FC region with respect to the covalent ground and S_2 states (red-shift of the absorption), thereby inducing an adiabatic ionic/covalent character inversion along the S_1 potential energy surface towards the CI. For medium-strength fields this transition may happen already in the FC region thus introducing a finite barrier on S_1 state. Strong fields induce the ionic/covalent inversion already at the GS equilibrium, thus preventing bond inversion in the first place.

In the above mentioned principle study we made first efforts towards replicating the above mentioned electric field effects by functionalizing the parent compound with: (i) push-pull groups; (ii) electronegative groups which act along the sigma-backbone; (iii) charged groups. In the following proof-of-concept study we present a thorough, systematic, in-depth study covering a large variety of functionalized RPSB chromophores to explore their photophysical and photochemical properties and thus, understanding their abilities and limitations of functional groups to mimic eclectic fields.

6.2 Computational Details

See the computational details described in chapter 5. All computations have been performed in gas-phase. The only difference is the active space that can comprise up to 14 electrons in 14 π -orbitals if the system contains more than 6 π -bonds. Moreover, a state average CASSCF over 4 roots was used for single point calculations. A variety of functional groups were used to modify the RPSB chemosphere **Figure 6-2**.

6.3 Results and Discussion

6.3.1 Influence of Functional Groups on the Absorption Energy

The parent compound R_{30} displays an absorption energy of ca. 2.36 eV associated with the bright $H \rightarrow L$ transition. The absorption is modulated between 1.58 eV (382 nm) and 3.24 eV (786 nm) under the effect of electric fields in the range +0.004 au to -0.005 au **Figure 6-1** shows that a gradual modulation of the absorption can be instead achieved by functionalizing the parent compound with one or more chemical groups (compounds 1 through 44, see **Figure 6-2** for their chemical composition). The shift in absorption energy depends on two factors: the electronic nature of the functional groups and their positions in RPSB system, i.e. a group may promote or retard the positive charge transfer from N-head to C-tail depending on its electronic nature and position, eventually resulting in a red- or blue-shift of the absorption energy, respectively. Clearly, functional groups that cause blue shifts would destabilize the ionic S_1 state and stabilize the covalent (S_0 and S_2) states. As the CT absorption blue shifts, the covalent states red-shifts, consequently the ionic and covalent become close to each other and do mix in the FC region. On the other hand, red-shifted

functional groups stabilize the ionic S_1 state toward the covalent S_0 state, again inducing state mixing in the FC region.

Here we summarize the effect of individual groups:

- i- Inductive effects (CF_3 vs. CH_3):** replacing the methyl group by a CF_3 group at positions closer to the N-tail such as C_{13} (R_{18}) and at positions closer to the C-tail such as C_9 (R_{34}) causes a red- and blue-shift of ca. 0.3 eV with respect to the parent compound R_{30} , respectively. Consequently, interchanging the positions of CH_3 and CF_3 modulates the absorption energy by entire 0.6 eV, this can be realized by comparing the absorption energies of both R_{18} (2.05 eV) and R_{34} (2.64 eV). Generally, a similar shift was also observed by replacing the CH_3 in R_5 , R_{20} , R_{22} and R_{23} with CF_3 , thus, giving R_1 , R_6 , R_{10} and R_9 systems. CF_3 is an electron-withdrawing group with a pronounced inductive effect while the CH_3 group has a weaker electron releasing inductive effect. For instance, CF_3 in R_{18} stabilizes the CT transition since C_{13} is expected to host more positive charge (as evident from the different resonant Kekule contributions to the S_0 and S_1 , see **Figure 6-3**) in the ground state than in the excited state. In R_{34} , the situation is completely reversed, where in the excited state the positive charge that migrates from N-head to the C-terminal is located at C_9 in one of the main resonant contributions to S_1 so that an electron withdrawing group placed there blue-shifts the CT transition. It is worth mentioning that the exchange of a CH_3 for CF_3 in the pair R_{22}/R_{26} shows a smaller (compared with the same exchange between R_{30} and R_{34}) blue-shift of ca. 0.1 eV, this is a consequence of the different conjugated systems.

- ii- Mesomeric effects** (e.g. O- and N- containing groups constrained in non-aromatic rings in order to prevent rotation and to orient their lone pair to the conjugated plane): introducing such mesomeric group close to N-head side (C_{14}) results in a blue shift of 0.25 for R_{37} (O-Containing) and 0.4 eV for R_{38} (N-Containing). On the other hand, putting these groups at the other side (C_7) decreases the energy gap by 0.35 eV (R_3 and R_4). A similar red shift (ca. 0.37) is observed by modified R_{19} though a MeO at R_7 . The observed blue and red shifts are attributed to the positive mesomeric effect of those groups which overcomes their negative inductive effect (**Figure 6-3**). Moreover, the relative effect of the position of those groups may be estimated by comparing the interchange of CH_3/MeO or CH_3/MeN in R_3/R_{13} and R_4/R_{15} , respectively, where upon this interchange the energy gap is modified by 0.3 eV. On the other hand, the use unconstrained mesomeric groups, i.e. exchanging of the methyl at C_9 with NH_2 , OH or OCH_3 displays negligible effect on the absorption energies as shown in R_{14} , R_{16} and R_{17} compared to the bare R_{18} .

- iii- Shielding of the charge:** (OX or NHX with X being either H or CH_3). As the computations are performed in gas-phase and those groups are not constrained in a ring, it was found that, when placed close to the N-head (i.e. at C_{14}), they prefer to orient their lone pair towards the nearby imine upon GS structure optimization in order to effectively shield the positive charge in protonated Schiff-base. Such effect is

will be observed for compounds R_{39} – R_{41} and R_{43} with a particularly strong CT destabilizing effect of 0.60–0.65 eV.

- iv- **Variation of the length of the conjugated system:** Comparison between R_{30} and R_{23} shows that the absorption energy is red-shifted by ca. 0.2 eV by increasing the length of the conjugated π -system by an additional double bond in the β -ionone ring. Most remarkably the ground state structures of the β -ionone containing RPSB compounds show highly twisted dihedral angle C_5 – C_6 – C_7 – C_8 (around 60° – 70°), thus resulting in a substantial deconjugation of the β -ionone ring from the conjugated system. The effect of this deconjugation is demonstrated by removing the β -ionone ring yielding a fully planar structure (R_{28}) with small red shift (0.1 eV). On the other hand, the effect of the cyclic constraints in R_7 and R_{19} was revealed by studying the absorption of the R_{19} analogous R_{25} where a blue shift of ca. 0.15 eV is observed.

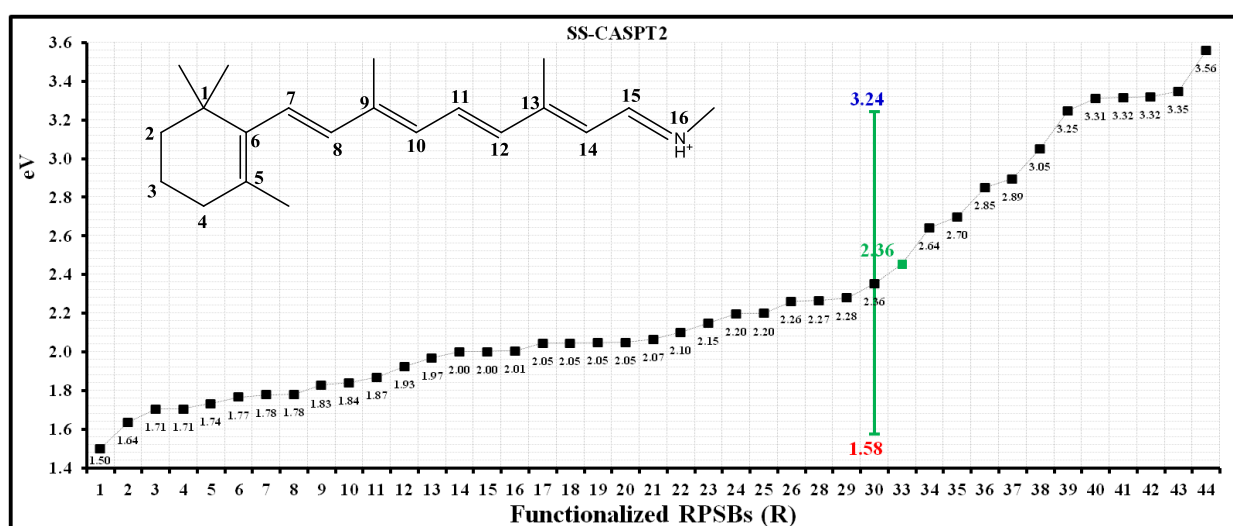


Figure 6-1. Dependence of the absorption energy on the electronic natures and positions of the functional groups along the backbone of the RPSB. The vertical green line shows the shift in absorption energy by applying electric field of +0.004 and -0.005 au.

- v- **Charged groups such as $(-\text{CH}_2)_x\text{N}^+(\text{CH}_3)_3$:** As expected, introducing the charged groups is the most intuitive and straightforward way to shift the absorption energy in both directions, which most closely reproduces the effects of a homogeneous external field. A positively charged group like $-\text{N}^+(\text{CH}_3)_3$ in the C-terminal (as in R_{36} , R_{42} and R_{44}) retards the CT from N-head to the C-terminal and a blue shift is observed, while the same groups in the N-head side will enhance the CT causing a red shift (as in R_{12}).
- vi- **Aromatic heteroatomic five- and six-membered rings:** generally replacing the β -ionone ring with a heterocyclic ring decreases the absorption energy due to increasing number of π -bonds and restoring the complete planarity along the whole conjugated system. The estimated replacement effect β -ionone ring by one of electron rich aromatic rings furan (R_6 vs. R_{18} or R_{20} vs. R_{30}), pyrrole (R_1 vs. R_{18} or R_5 vs. R_{30}) and 1,4-dihydropyridine (R_2 vs. R_{30}) rings are ca. 0.3 eV, 0.6 eV and 0.6 eV. Thereby N-Containing rings have a more pronounced effect in agreement their strong mesomeric effect compared to O-Containing ones. Such effect is not pronounced for

R₂₉ functionalized with electron-poor aromatic ring (pyridine) where the red shift associated with the increase of the conjugated system is eliminated by the electron withdrawing hetero ring retards the CT to C-terminus. On the other hand a small red shift (0.15 eV) is observed through replacement the β-ionone ring with a benzene ring (R₂₂ and R₁₀).

In conclusion, it seems possible to reach strong red- or blue-shifts (i.e. above 0.3 eV) by employing different scenarios: (i) through charged groups (ii) a combination of two or more additive functional group effects and (iii) electron rich heterocyclic rings such as pyridine.

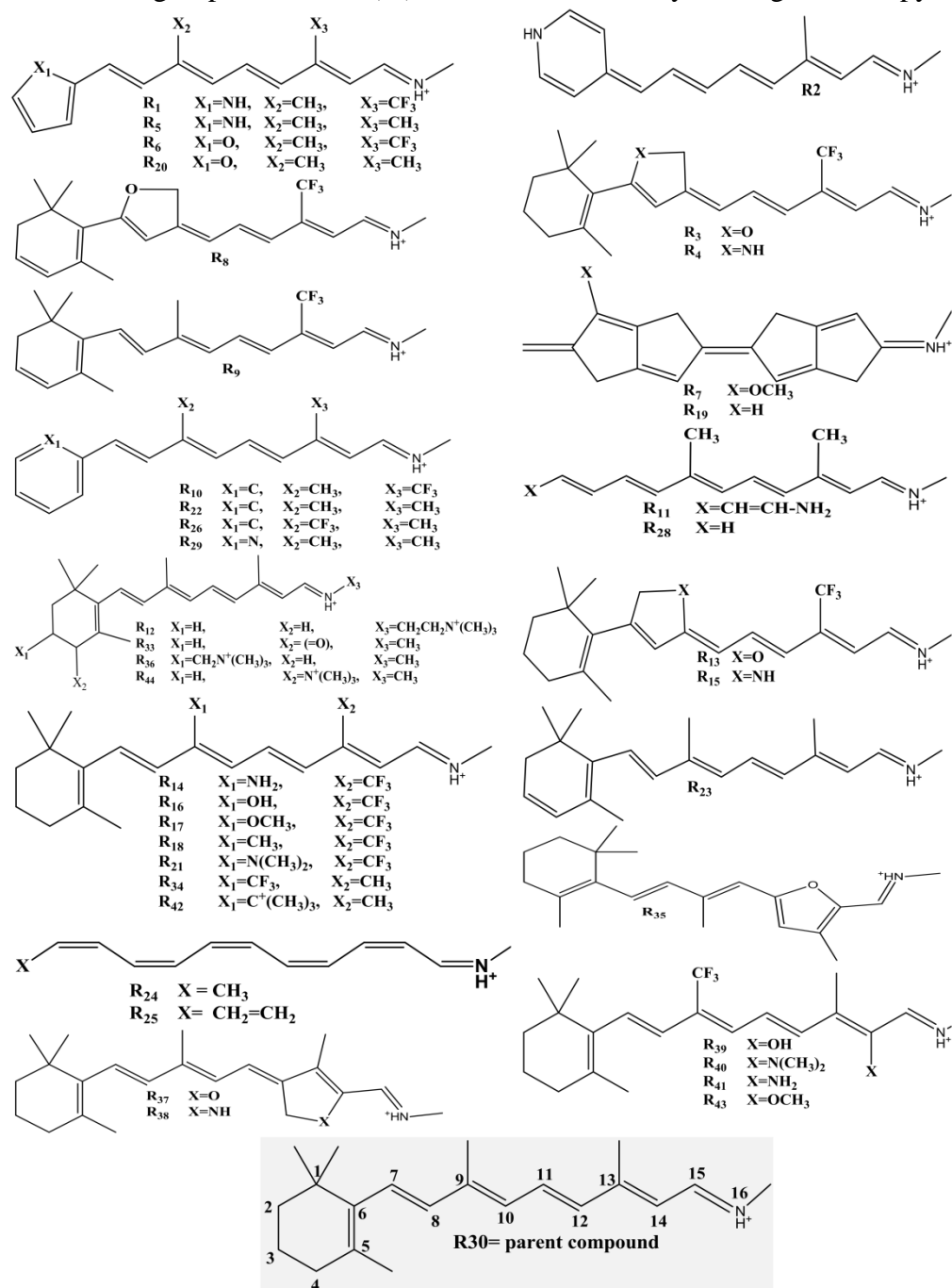


Figure 6-2. Functionalized retinal protonated Schiff bases (R₁→44). The numeration is shown in R₃₀, the same descending order, starts at protonated SB which takes the number (16), will be used for the other systems.

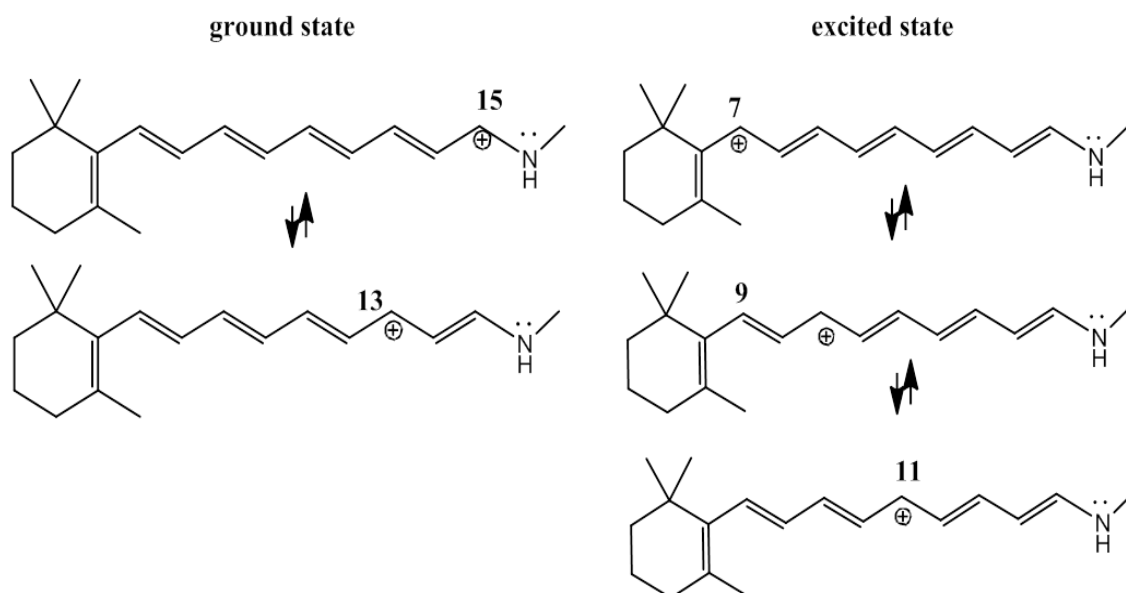


Figure 6-3. The most important mesomeric structures in ground and excited state of RPSBs.

6.3.2 Influence of Functional Groups on Excited State Potential Energy Surface

In the previous section we have demonstrated that through modification of the PRSB backbone with certain functional groups, it becomes possible to fine-tune the absorption energy over the whole visible range in a similar way to what can be achieved by applying a homogenous external electric field. In this section we go one step further and investigate the effect of the functionalization on the excited state profile. As established on the parent compound [3] external electric fields have opposite effects on the CT S_1 state and the pair of covalent states S_0 and S_2 . Thus, at certain field strengths, i.e. medium-strength positive (ca. 0.003 au) and negative (ca. -0.003 au) which cause a blue- and a red-shift of the CT, respectively, we observe ionic/covalent state-mixing in the bright excited state. The mixed WF nature of the ES is reflected in the bond order in the conjugated chain of the relaxed S_1 as elucidated in the seminal study on the parent compound [3]. In this spirit we used the sensitivity of bond lengths to the electronic nature of the ES to categorize the functionalized systems in 5 different groups. As quantitative criteria we utilize the bond length alternation (BLA) at the relaxed ES geometry and correlate it to the absorption energy:

- I- Normal BLA region: a wide variety of functionalized systems (R17–R35) with absorption energies within 2.00-2.70 eV, i.e. +/- 0.3 eV from the parent compound absorbing at 2.36 eV. This group exhibits a clear CT character in the ES (ca. 60% weight in the WF) and a fairly large gap to either S_0 or S_2 . Consequently, ES relaxation reaches a minimum characterized with the classical inverted single-double bond order established for the R₃₀. The same behavior was shown for the parent compound under the effect of the electric field of -0.0025 – 0.0020 au. These systems are expected to have an ES profile similar to that of the bare RPSB.
- II- Blue-shifted intermediate BLA region: systems belonging to the spectral region of

2.70-2.90 eV (R₃₅, R₃₆ and R₃₇) characterize with an S₁ WF which shows partial ionic/covalent mixing (still prevalently ionic, though) causing a less pronounced bond length alternation. This is equivalent to the effect observed for the parent compound in intermediate field strengths of 0.0020 – 0.0025 au. Such effect can be achieved through modification with a positive charge at in the β-ionone ring (R₃₆), combination of CF₃ (C₉) with the mesomeric effect of OCH₃ at C₁₄ (R₃₇), and also a combined mesomeric effect at C₁₂ and C₁₄ through furan ring (R₃₅). We note that the effect of WF mixing is observed at the CASSCF level. Knowing that non-Correlated methods favor covalent states we expect that the intermediate region is accessed at higher absorption energies, i.e. the normal BLA region extends beyond 2.70 eV.

- III- Blue-shifted BLA equilibrium region: systems functionalized with a CF₃ group close to the β-ionone ring and twisted MeO/NH₂ in the N-terminus (R₃₈–R₄₄) display absorption energy above 2.90 eV which corresponds to an electric field > 0.0025 eV. In those systems, the CT actually becomes the second ES at CASSCF level. CASPT2 energetics at the relaxed S₁ and S₂ geometries, being predominantly covalent and ionic, respectively, show that they are iso-energetic.
- IV- Red-shifted intermediate BLA region: the excited state relaxed geometries of compounds R₁₃, R₁₄ and R₁₆, functionalized by a CF₃ group at N-head in addition to MeO or NH₂ at the C-tail, show intermediate BLA values. Their absorption energy of these compounds falls in the range 1.90-2.00 eV corresponds to an electric field of -0.0030 to -0.0025 au. Considering dynamic correlation effects, not present at CASSCF level, which decrease the S₀/S₁ gap, we can anticipate the WF ionic/covalent WF mixing to set in at higher energy, i.e. already in the yellow/orange part of the visible spectrum.
- V- Red-shifted BLA equilibrium region: systems R₂, R₃, R₄, R₇, R₁₂ and R₁₅ absorbing below 1.90 eV display full equilibration upon S₁ relaxation where an inversion of the ionic/covalent character of the ES is detected. This effect consistent with the effect reported for R₃₀ by applying negative electric fields stronger than -0.0030 au.

As show from **Figure 6-4**, the majority of the systems can be classified based on their BLA and their absorption energies. However, in the course of the study we encountered also outliers to the expected behavior (R₁, R₅, R₆, R₁₀, R₁₅ and R₃₈). Compounds R₁, R₅, R₆ and R₁₀ are found to exhibit high values for the BLA (> 0.02) although their absorption energies would put them in group V with BLA around 0.01. R₁₅ and R₃₈, on the other side, show more equilibrated bond lengths then expected according to their absorption energies. This odd behavior may be attributed to different factors. It should be noted that the majority of outliers R₁, R₅, R₁₅ and R₃₈ contain a nitrogen introducing further stable resonance configurations to the ones given in **Figure 6-4**. Consecutively, geometry optimization in the GS and ES of the red-shifted compounds encountered more than a single local minimum with very different bond order. A clear explanation for this deviation still an open question which

requires further investigations to scrutinize the ES potential energy surfaces and/or employing other approaches such as MS-CASPT2 flavor.

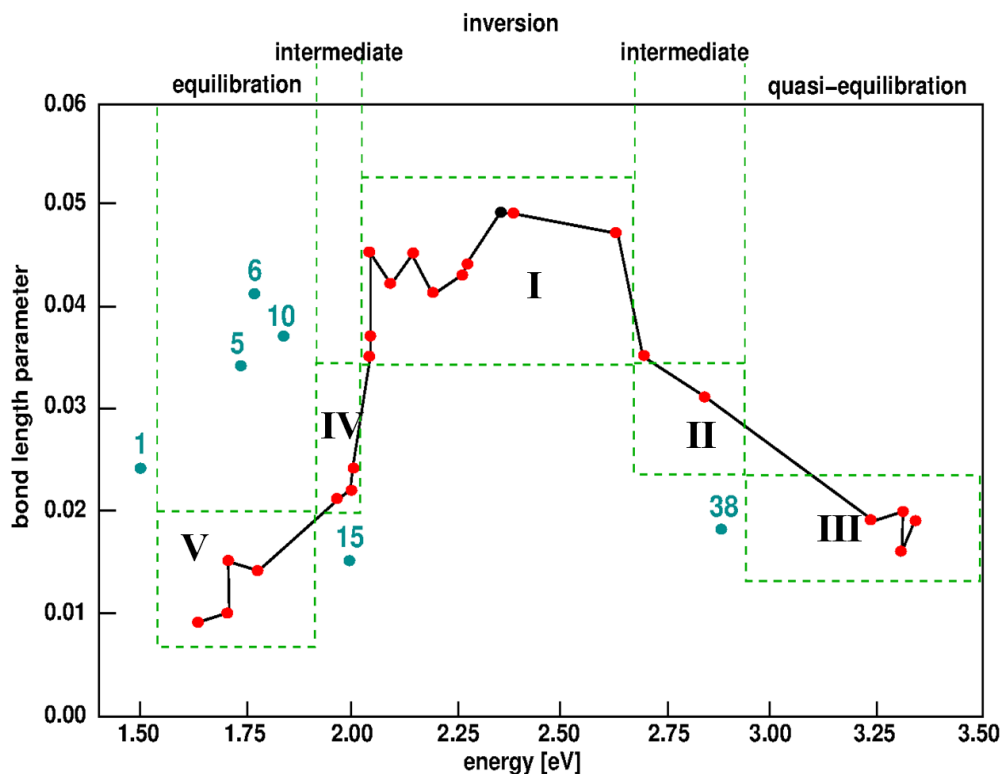


Figure 6-4. Correlation between the absorption energy and BLA of the relaxed geometries. Where $BLA = \sum_{i=7}^{14} |d_{C_i-C_{i+1}} - 1.41| / 8$, with $d_{C_i-C_{i+1}}$ the bond length between carbon atoms I and $i+1$ from the conjugated chain labeling according to **Figure 6-2** R30, C_5-C_6 and C_6-C_7 are excluded for better comparison with systems without β -ionone ring.

6.3.3 Toward Applications

Our study on the application of electric field to the parent RPSB R₃₀ reveals that bond length equilibration in the relaxed S_1 state is achieved in gas-phase for values of the field strength between -0.0024 au and -0.0031 au with an optimal value at -0.0027 au for which the BLA is 0.016. Such an electric field red-shifts the absorption energy of the parent compound to 1.95 eV with respect to the field-free case (2.36 eV). As can be seen in **Figure 6-4** using functional groups instead of electric fields categorizes transition energies in the range 1.90-2.00 eV in the red-shifted intermediate region IV with similar BLA values around 0.02-0.03 of the relaxed ES geometries. This region is particularly intriguing as it lies between the normal BLA and the equilibrated BLA regions. Thus, by applying external electric fields in the order of few MV/cm to compounds belonging to this window we anticipate to be able to shift their absorption energy in the neighboring BLA region, where based on the gathered knowledge regarding the potential energy profiles of the parent compound for different electric field strengths we expect to observe a markedly different behavior. In particular we expect to see a barrierless surface connecting the FC and the CI regions when the system's absorption energy is blue-shifted in the inverted BLA region, while

we expect to see a sloped path towards an energetically higher lying CI when the system's absorption energy is red-shifted in the equilibrated BLA region. Hence, within the approximations of the current theoretical set up functionalized RPSB from the red-shifted intermediate BLA region bare the potential for selective switch on/off of their ultra-fast isomerization behavior.

In order to test the idea we selected R₁₉ (**Figure 6-5**), a planar all-trans RPSB with seven double bonds constrained in two ring formations. Although, its absorption energy is located rather at the border between inverted and intermediate BLA (~2.05 eV) with a rather large BLA of 0.035 R₁₉ is particularly tempting for control purposes as it offers a single free double bond (C₉=C₁₀) for photoisomerization. **Figure 6-6** shows a relaxed scan around the central double bond in the absence of an external electric field. Evidently, a steep ES profile is encountered to drive the system towards a 90° twisted CI. This is in agreement with the bond inversion of the central bond found to be 1.47 Å in the relaxed S₁ geometry and also in agreement with the place of R₁₉ in group I. Astonishingly, application of a homogeneous external field of just -0.001 au which red-shifts the absorption energy by ca. 0.1 eV to 1.92 eV lowers dramatically the BLA to 0.17. Notably, the central double bond becomes 1.40 Å at the relaxed S₁ geometry which is now found to be a local minimum connected with a barrier of 3.3 kcal/mol to the CI region (**Figure 6-6**).

Table 6-1. Bond length lengths for S₀ and S₁ states of R₉ and R₇ in electric field of 0.000, -0.001 and +0.001 au strengths.

System	R19				R7						
	EF	0.000		0.001		0.001		0.000		+0.001	
		S ₀	S ₁								
C ₅ -C ₆		1.349	1.372	1.340	1.370	1.346	1.391	1.351	1.387	1.347	1.390
C ₆ -C ₇		1.452	1.415	1.451	1.410	1.450	1.399	1.453	1.402	1.453	1.399
C ₇ -C ₈		1.352	1.392	1.345	1.391	1.346	1.398	1.351	1.404	1.353	1.428
C ₈ -C ₉		1.471	1.417	1.465	1.416	1.466	1.414	1.468	1.411	1.469	1.393
C ₉ -C ₁₀		1.353	1.405	1.350	1.404	1.350	1.403	1.353	1.411	1.354	1.447
C ₁₀ -C ₁₁		1.466	1.427	1.455	1.426	1.459	1.427	1.465	1.422	1.461	1.392
C ₁₁ -C ₁₂		1.352	1.408	1.352	1.413	1.352	1.407	1.353	1.411	1.354	1.445
C ₁₂ -C ₁₃		1.442	1.395	1.429	1.387	1.434	1.391	1.442	1.394	1.436	1.374
C ₁₃ -C ₁₄		1.360	1.424	1.368	1.431	1.366	1.424	1.361	1.420	1.365	1.435
C ₁₄ -C ₁₅		1.443	1.392	1.422	1.371	1.428	1.376	1.442	1.395	1.430	1.377
C ₁₅ -N ₁₆		1.294	1.346	1.300	1.340	1.297	1.336	1.294	1.341	1.294	1.334
C ₃ -C ₄		1.342	1.351	1.333	1.348	1.334	1.340	1.340	1.345	1.342	1.351
C ₄ -C ₅		1.477	1.452	1.477	1.445	1.475	1.460	1.477	1.462	1.475	1.462
BLA		0.051	0.012	0.045	0.017	0.047	0.014	0.050	0.008	0.046	0.027

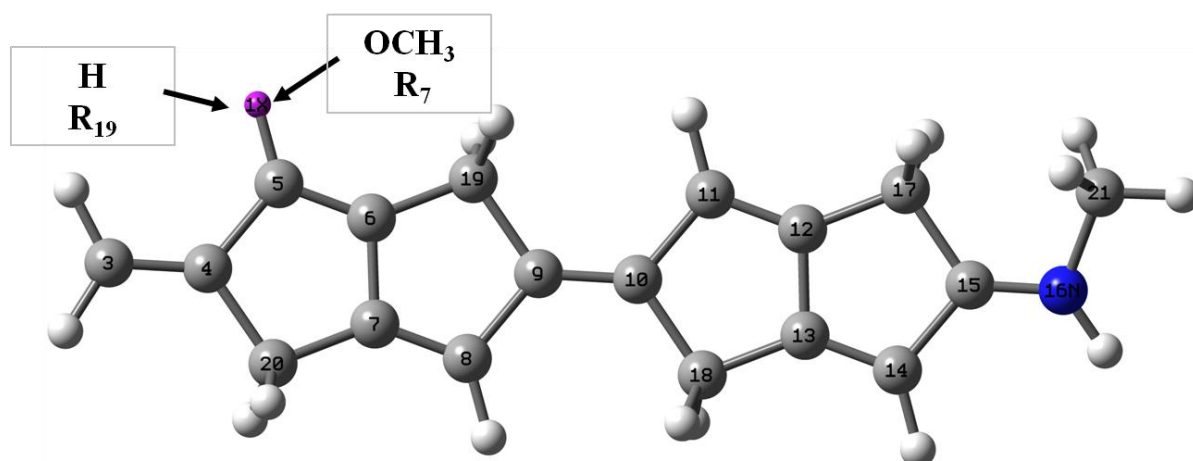


Figure 6-5. Molecular structures of R₇ and R₁₉.

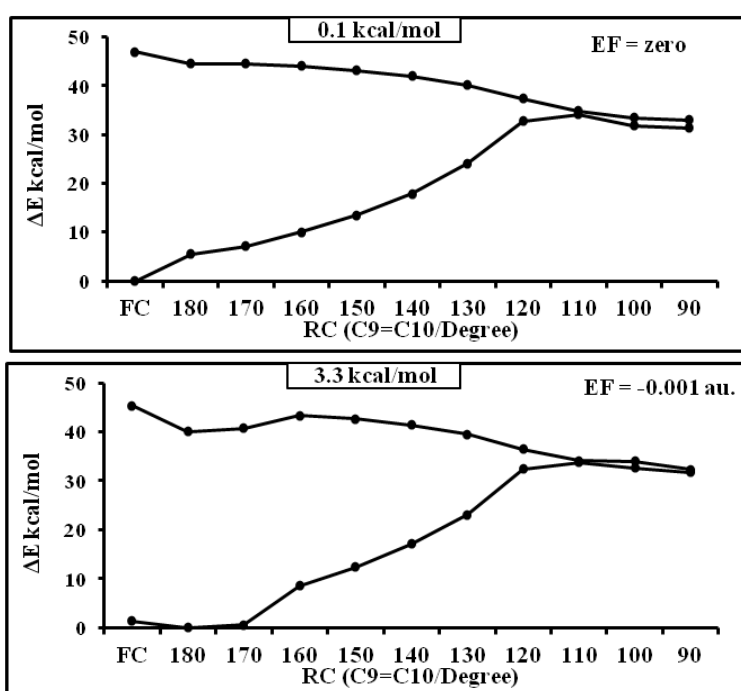


Figure 6-6. CASSPT2/SA2-CASSCF/(12,12/6-31G* profile along relaxed scans (relaxing the CT excited state) around C₉-C₁₀ torsion bond of R₁₉ calculated in the absence (top) and in presence of EF of -0.001 au (bottom).

Although the above example is a neat proof of concept the functionality of R₁₉ can be further improved. In particular we want to make use of the possibility to apply an available electric field in both directions, thus doubling its energy modulation range. However, we recognize that applying a positive electric field to R₁₉ is of no avail as already in the absence of a field there is no ES barrier to surmount. A finite barrier along S₁ in the absence of electric field is desired which can be then overcome by applying a positive field. Above we demonstrated that negative electric fields (Figure 6-6 bottom) introduce such a barrier by placing R₁₉ deeper in the red-shifted intermediate region (i.e. reducing notably its BLA). Relying on the equivalence between electric field and functionalization we have modified system R₁₉ with a MeO group close to the C-tail to enforce a small red-shift (Figure 6-5)). Since only positions C₅ and C₁₄ are directly available, position C₅ was selected for this

purpose giving compound R7. As expected, the functionalization with the weak mesomeric MeO group leads to a 0.2 eV red-shift of the absorption energy accompanied by a near equilibration of all bond lengths upon S₁ relaxation, thus placing the system at the border between the intermediate and equilibrated BLA regions. **Figure 6-7** shows the ES profiles of this tailored compound in the absence of external field (middle), as well as for negative (top) and positive (bottom) fields. In contrast to R₁₉ in the absence of an external EF R₇ exhibits a finite barrier along the torsional coordinate of 2.2 kcal/mol peaking around 35°. Applying a positive EF of +0.001 au decreases the barrier to 1.0 kcal/mol, thereby shifting the TS towards the FC region to 20°. On the other hand, applying a negative electric field of -0.001 au seemingly completely blocks the isomerization due to a sloped S₁ profile and a missing real crossing.

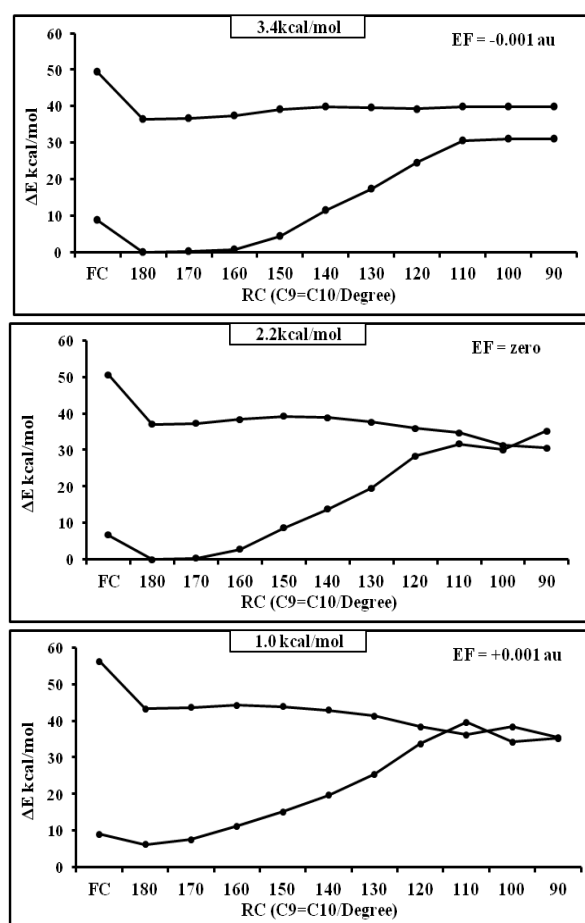


Figure 6-7. CASSPT2/SA2–CASSCF/(12,12/6-31G* profile along relaxed scans (relaxing the CT excited state) around C₉–C₁₀ torsion bond of R7 calculated in EF of -0.003 au (top), 0.000 (middle) +0.001 au (bottom).

6.4 Conclusions

In conclusion, it is possible to fine-tune the absorption energy of RPSB throughout the entire visible specter with designer molecular systems. Beyond this, we demonstrate that for a variety of compounds there is a correlation between the absorption energy and the topology of the ES profile, which can be employed to synthesize systems with desired photophysical

and photochemical properties. On the example of a modified all-trans RPSB we showed how the photo-isomerization can be selectively switched on/off by combining chemical rationale and weak external electric fields. This marks a promising step toward the design of bio-inspired photo-controlled molecular devices.

6.5 Additional Study

Some of the aforementioned RPSBs mimics were further used (in cooperation with Baptiste Demoulin and Tangui Le Bahers [24]) to study the intramolecular photoinduced charge transfer via calculating electron density-based indices.

In this study, the first bright transition of a series of ten retinal-based dyes (R₁₂, R₁₈, R₁₉, R₃₀, R₃₄, R₃₃, R₃₅, R₃₆, R₄₂ and R₄₄) was simulated using TD-DFT, with several hybrid functionals, and with several post-Hartree-Fock methods. The CASPT2 results were used as reference to compare the results. The comparisons were not only based on the transition energies, that is generally the case for such works, but were also based on the variation of the electron density from the ground to the excited along with several density-based indices recently developed. Among all the results obtained, it clearly appears that the PT2 correction to the CASSCF wave function is increasing with the increase in the charge transfer character of the transition. As already highlighted in the literature, TD-DFT poorly reproduces transition energies of this family of molecules whatever the functional. This work also confirms this observation for the variation of the electron density that is different between TD-DFT and CASPT2. Nevertheless, some functionals give better results than others. It appears that functionals having a fraction of 40–50 % of exact exchange give a better description of the electron density variation than the other functionals. Moreover, the best functional to compute the transition energies is not the best to simulate excited electron density that confirms an observation done in the literature on a different family of molecules.

The use of the variation of the electron density maps and the related indices offers a new perspective in comparing excited states calculations with several methods. The retinal chromophore and mimics investigated here are known to be a really severe test case for TDDFT as compared to multireference perturbative (CASPT2) approaches, regardless the specific functional employed. In particular, the following conclusions can be drawn:

The CIS method, frequently used by the TD-DFT community as a reference to characterize the nature of a transition, is not reliable for retinal dyes. From a general point of view, CIS reference must be used with caution. These indices allow quantifying the influence of the PT2 correction on other properties than only the transition energies. As a matter of fact, these tools highlighted that the PT2 correction on the electron density is larger for long-Range charge transfer. Nevertheless, generally, CASSCF is found to give density-based indices similar to the one of CASPT2 that is expected since CASPT2 is a correction of the CASSCF wave function. This result shows that dynamical correlation has a larger influence on the transition energies than on the electron density reorganization. Compared to CIS, the CASSCF method offers a much better description of the nature of a transition, very close to the CASPT2 level but with a much lower computational cost.

TD-DFT globally fails to reproduce the nature of the transitions in retinal-based dyes although offering a better description of the transition energies than CASSCF. Even recent and sophisticated functionals, like the meta-GGA range-separated hybrid M11 functional, are still far from the CASPT2 reference. The discrepancy could come from the double excitations that are involved in the CAS wave functions but not in the TD-DFT wave functions. Nevertheless, it can be observed that some functionals perform better to reproduce the density-based indices. These functionals (M06-2X and the range-separated ones having an intermediate fraction of HF exact exchange) are recent ones, confirming that the development of new functionals is still a useful work. Finally, it appears that a relatively large amount of exact exchange (40–50 %) is the best ratio to get closer to the CASPT2 reference explaining the failure of PBE0 functional (25 % of HF exchange), yet a very appropriate functional to compute electronic transitions in organic molecules[212]. The conclusion was also drawn by Valsson et al.[213] based on the simulation of the photo-isomerization of a series of four protonated Schiff's base.

It is known that the environment has a strong influence on the characteristics of a charge transfer transition, especially the transition energy and especially for retinal-based dyes[214-216]. Consequently, it must be stated again that the results presented here are obtained in gas phase and can be notably modified in another environment.

From the point of view of the indices developed to analyse electronic transitions (based on the electron density or not), this work highlights their importance and usefulness in quantitatively comparing methods beyond the transition energies only. These indices are now fully available in the toolbox of theoretical chemists as diagnostic, analysis and development tools and should be used in concert with traditional checks for validating computational approaches.

7 Photochemistry of Visual Pigments

The vision process is one of the extremely interesting natural phenomena induced by light and one of the most extensively studied. This phenomenon is a photo-transduction process where the light energy from an optical stimulus is converted into an electrical impulse in the form of a neural signal to the brain. In the human eye, the pigments are manufactured and stored in photoreceptor cells known as the rod and cone cells [217]. The cones are responsible for colour vision (as they contain three different photoreceptors able to absorb at blue, green and red light respectively) and daylight, while the rods are more sensitive than cones and therefore they allow night vision but they do not distinguish colours (as they contain a single photoreceptor called rhodopsin). Both rod and cone pigments have the same basic structure: a transmembrane protein called opsin that comprises a 11-Cis retinal chromophore bound through a protonated Schiff base linkage. Although they have different functions, rods and cones have a whole similar operational mechanisms relying on the same triggering process (the so called primary event of vision): the ultrafast photoisomerization of the retinal chromophore. Recently, some studies have referred to the discovery of a third type of photoreceptor cells that regulate nonvisual photoresponses [218] known as intrinsically photosensitive retinal ganglion cells (ipRGCs). ipRGCs express an atypical opsin-like protein named melanopsin[28,219,220] which plays a role in the regulation of unconscious visual reflexes and in the synchronization of endogenous physiological responses to the dawn/dusk cycle (circadian rhythms)[26,27].

7.1 Structure of Visual Pigments

Visual pigments[221,222] are the light-absorbing molecules that mediate vision. The visual pigments constitute a family of membrane bound receptors to which the chromophore, the 11-Cis-isomer of retinal, is covalently bound. The opsin of vertebrates have a common tertiary structure from a single polypeptide chain containing a number between 340 and 370 amino acids that feature an up-down bundle architecture of seven transmembrane α -helices which constitute the binding pocket around the chromophore, see **Figure** 7-1. The biochemical events that occur following the absorption of a photon have been best worked out for the bovine rod photoreceptor and its pigment rhodopsin. When a photon strikes a rhodopsin protein and is absorbed by retinal, the chromophore undergoes a fast and efficient photoisomerization driving 11-Cis to all-trans formation, (**Figure** 7-2). Such isomerization is a space-saving mechanism involving the unidirectional, counterclockwise twisting of the $=C_{11}H-C_{12}H=$ moiety with respect to its Lys340-linked frame as proposed by Warshel for visual pigments [6]. The isomerization leads to a change in the conformation of the protein, presumably as a result of a shift in the position of helices, which make up the retinal binding pocket, which is in turn the result of the build-up of new steric interactions between the all-trans photoproduct and the opsin binding pocket. Consequently, this conformational change allows the protein switch from an inactive to an active form on the binding of a ligand. The

activated receptor can trigger an intracellular signal cascade that eventually delivers the signal to the brain as an electrical impulse.

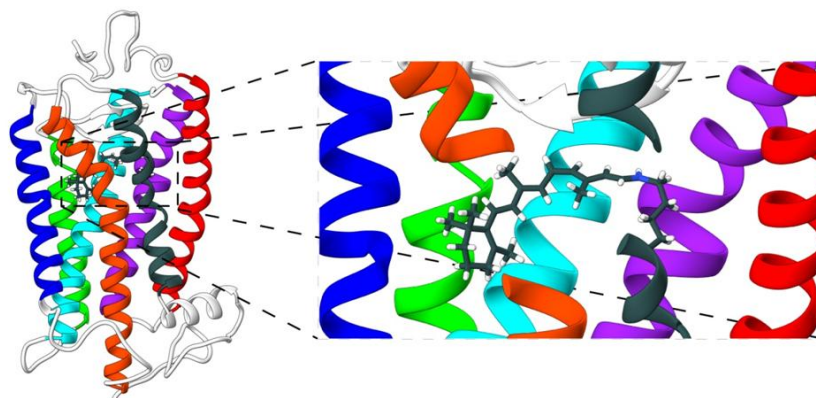


Figure 7-1. Bovine rhodopsin structure resolved at 2.2 Å of resolution (pdb code 1U19). a) The tertiary structure of the protein where the seven transmembrane α -helices are highlighted with different colours. b) A magnification of the binding pocket around the chromophore (RET, in dark gray) showing the link of Schiff base with a Lys296 through the C15 N bond..

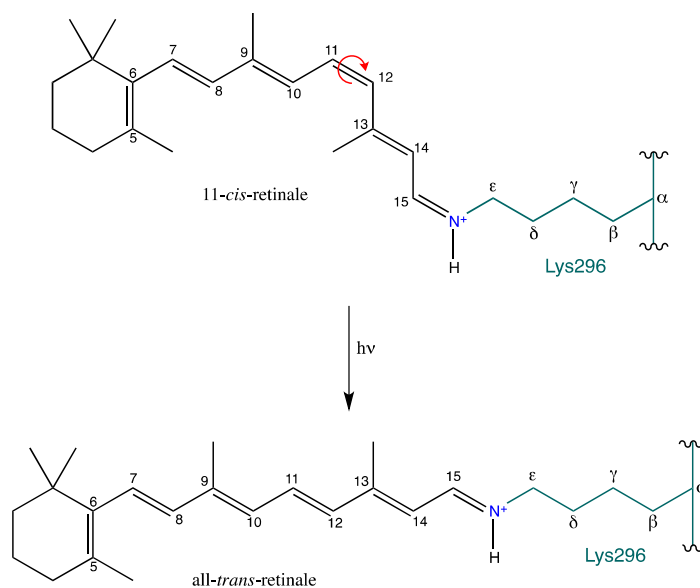


Figure 7-2. Diagram of the photoisomerization process of 11-Cis-Retinal to form all-trans-Retinal Schiff base (the double bond C₁₅-N is protonated). The Greek letters refer to the nomenclature of the carbon atoms of the lysine residue 296 belonging to the protein.

7.2 Classification of the Vertebrate Visual Pigments

In nature, an enormous number of visual pigments have been discovered, all of them display the same basic structure (seven transmembrane helices) but they do differ in their absorption spectroscopic properties as a result of different sequence and number of amino acids around the chromophore. The major finding on studying the visual pigments is that all retinal visual pigments seem to fall into one of five distinct families[223].

The five classes of vertebrate visual pigments are designated:

- **M/LWS (Mid and Long Wavelength Sensitive):** visual pigment in this family contains both the human red and green cone pigments. Their amino acid sequences are quite similar to each other, as well as to the long wavelength cone pigments of most other species which have been investigated. The spread of the known absorption maxima is from 521 to 575nm.
- **SWS1 (Short Wavelength Sensitive1) family:** which contains mostly pigments whose absorption maxima are in the ultraviolet, but it also has the human blue cone pigment, shifted further to the red than most other members of this family (absorption maxima fall in the range from 358 to 425 nm)
- **SWS2 (Short Wavelength Sensitive2),** those pigments have not been found in mammals, but are present in many bird, fish, reptile, and amphibian retinas. Their known absorption maxima range from 437 to 455 nm.
- **RH1:** this class contains most if not all of the standard rod pigments, the rhodopsins. Their absorption maxima at ca. 470-490 nm [224].
- **RH2:** related to the rhodopsins, containing pigments that mostly absorb around 500nm. They range from 466 to 511 nm. They are found in both morphological rods and cones.

7.3 The Opsin Shift: Protein-Bound vs. Solution Environment

The retinal chromophore is attached via a Schiff base linkage to Lys 296 in the opsin sequence of rhodopsin. Since covalent retinal binding is obligatory for visual pigment function, all opsins indeed have such a lysine. This Schiff base has been shown to be protonated [225-227], the carboxylate of a glutamic group (e.g., 113 Glu in rhodopsin) serving as a negative counterion and formal proton donor. Protein-bound retinals and the corresponding free- retinal PSI3 (in organic solvents) have a very different timescales, selectivity and Quantum Yields (QYs) in photoisomerizations (see chapter 5). The protein environment plays important role (electrostatically and sterically) in determining the wavelength of chromophore absorption. For instance, it can shift the wavelength of the chromophore from that of a protonated Schiff base in solution (440 nm) to 420, 498 and 565 nm for the blue cone, rod rhodopsin and red cone, respectively. This shift is known as the “opsin shift” and buried/shielded counterions have been proposed to explain the spectral shift in bovine rhodopsin [228]. Generally, the substitution of specific amino acids along the polypeptide chain can affect the opsin-shift through several mechanisms [229]:

- by changing the electrostatic interaction between the protonated Schiff base and its primary counterion;
- by modulating the electrostatic interaction between the chromophore and groups (amino acids) of the polar binding pocket;
- by influencing the conformation of the chromophore itself, due to steric interactions with adjacent amino acids.

There are some other factors that may affect the opsin shift: (i) in some vertebrates the spectral shift is due to the replacement of the chromophore 11-Cis-Retinal with the 11-Cis-3,4-dehydroretinal (i.e. the extension of π -conjugated system) which red shifts the absorption up to 20 nm [73]. This red-shift is essentially due to an intrinsic property of the chromophore (i.e., the extension of π -Conjugation) and not due to any particular residue-based mechanism [73]. (ii) the different dispersion stabilization of the excited states in protein and in solution, and (iii) the protein electrostatic bath in general, that adds up to the primary electrostatic effect of the nearby counterion(s). Of course a major role is played by the counterion which balances the RPSB positive charge (the Glu-113 in Rh). However, another major factor with a strong influence on the absorption spectra of the visual pigments is the protonation state of the Schiff base (SB) bond between the chromophore and the lysine residue of the protein: all proteins incorporating protonated Schiff base (PSB) chromophores show a λ_{\max} that falls in the visible, while the ones with unprotonated Schiff base (PSB) chromophores show λ_{\max} that falls off the visible spectrum and absorb in the UV (members of the SWS1 class).

7.4 Melanopsins vs. Rhodopsins

As mentioned earlier, in addition to rods and cones, the human retina contains photoreceptor system based on a subset of melanopsin expressing photosensitive retinal ganglion cells (pRGCs) [220]. While melanopsins belong to vertebrate photoreceptors, their amino acid sequence resemble more the invertebrate ones than vertebrate rhodopsin [230,231]. Moreover, melanopsins are bistable similar to invertebrate and in contrast to vertebrate rhodopsins [232]. Similar to rhodopsins, hMeOp share the same general architecture of seven transmembrane α -helices with the same chromophore (PSB11) as a covalently bound protonated Schiff base which photo-isomerizes to its all-trans isomer (PSBAT) causing an opsin conformational change that, ultimately, activates the receptor and signaling cascade[7,233]. Melanopsins use an intrinsic light-driven chromophore regeneration function via RPSBAT back-isomerization, i.e. melanopsins share some of the key characteristics of an invertebrate-like signal transduction cascade[234], in contrast to vertebrate rhodopsins where they regenerate RPSB11 through a retinoid cycle[235].

Melanopsins modulate several physiological processes including photoentrainment, pineal melatonin suppression, pupil constriction and the modulation of arousal states and sleep induction, in other words they adjust the circadian rhythm[236,237]. The different studies carried out so far on melanopsin light sensitivity do not lead to consistent results. The melanopsin density in the membrane is 104-fold lower than that of rhodopsins, however they display high light sensitivity relative to other visual pigments. Moreover, the receptor is not confined in a dedicated cellular domain such as the outer segment of rods and cones, resulting in a very low photon catch and a phototransducing role only in relatively bright light [238]. Despite the many studies carried out since its discovery, many things remain unknown and more studies are required to shed light on the molecular mechanism of melanopsin activation. In Chapter X, we present the results of a modeling study on the isomerization mechanisms of human melanopsin and invertebrate and vertebrate rhodopsins[26-28], in order to predict the

photoisomerization mechanisms, rates and the quantum yields by means of semiclassical non-adiabatic molecular dynamics at the quantum mechanics (CASSCF)/molecular mechanics (QM/MM) level. The three visual pigments (bovine rhodopsin, Rh, squid rhodopsin, sqRh and human melanopsin, hMeRh) are absorbing at different wavelength (498, 476, and 462 nm) as a consequence of the different electric fields imposed by different protein environments around the same (PSB11) protonated retinal chromophore [12,29-31]. This may result in different operational regimes and/or mechanism for the three pigments.

Unlike hMeRh, the isomerization mechanism of RPSB11 in vertebrate rhodopsins has been extensively investigated. Such photoisomerization reaction of retinal constitutes the primary step of vision and is known as one of the fastest reactions observed so far in nature (occurring within 200 fs) [3,5,73,239,240]. The observation of coherent vibrational motion of the photoproduct indicates that the primary step in vision is a vibrationally coherent process and that the high efficiency of the isomerization reaction in rhodopsin is a consequence of the extreme speed of the excited-state passing through a conical intersection (CI) [3,173,241,242].

7.5 UV-Visual Pigments

Those kind of visual pigments are belonging the SWS1 class. It has been shown experimentally that they absorb in the UV-Region (359 nm)[243] due to the presence of a deprotonated form of the Schiff base (USB) in the dark state, **Figure 7-3**.

The study of such UV pigments is important for two main reasons:

- very few computational studies exist so far on these UV pigments, whose photoactivated mechanism is essential unknown [34].
- A distinct aspect of UV-sensitive pigments, when compared to visual rhodopsin, is that the chromophore is bound to the protein by an unprotonated Schiff-base (USB) linkage in the dark state[32,35]. An extensive network of hydrogen bonds and/or the presence of water molecules in the binding pocket seem to play important role in controlling the protonation state of the Schiff. Therefore, understanding how the conditions of the surroundings determine the protonation state and consequently the photophysical properties of retinal can provide useful information for biomimetic UV photochromic switches[244-247].

Chapters IX of this thesis will focus on the study of the primary photochemical events that characterize a sensitive UV visual pigment; specifically, it has been studied the UV-pigment present in the photoreceptor of the cones Siberian hamster (Siberian hamster). This UV-pigment consists of 348 amino acid residues and binds the chromophore 11-Cis-Retinal, as in rhodopsin, through the conserved lysine residue 296, see **Figure 7-3**.

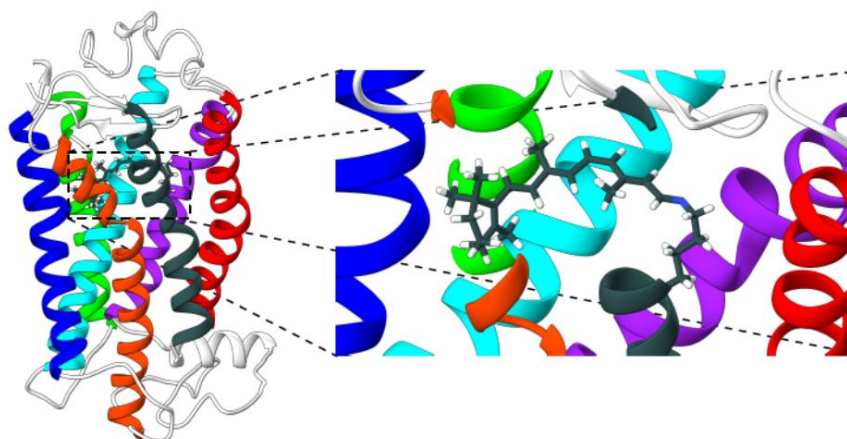


Figure 7-3. Tertiary structure of the UV-pigment. To the left is shown the overall structure of the protein, and are highlighted with different colours the seven transmembrane α -helices. Zoom into the right focus the area around the chromophore (note the deprotonated Schiff base).

Although in the literature there are several studies, both experimental and theoretical, which aim to clarify the mechanism of photoisomerization and the subsequent photochemical events that characterize the UV-pigment, a clear understanding of this mechanism has not yet been reached.

Unfortunately, accurate time-Resolved spectroscopic studies, that may clearly probe the primary events (that is, all those events that follow the photon absorption), are lacking as their temporal resolution is not high enough to characterize the first intermediate(s) of the ultraviolet vision process [32]. Time-Resolved absorbance measurements for UV-pigment shows a photoactivation characterized by several changes in the protonation of the Schiff base where the first photo-intermediate, called batho-like because it is similar to the bathorhodopsin photo-intermediate already observed in the photoactivation cycle of rhodopsin, is protonated and it appears after the photoisomerization of the chromophore. This intermediate has been detected after 300 ns of the photoexcitation. It also rebalances very quickly with the deprotonated form, in a scale much shorter than the experimental time resolution. This observation implies the existence of various events of proton transfer in the early stages that characterize the phototransduction of the UV- pigment; this indicates that the photoactivation mechanism is distinctly different from that of bovine rhodopsin where the chromophore remains protonated up to the formation of the meta II photocycle intermediate, i.e. substantially up to the higher conformational changes of the transmembrane helices that allow transmission of the signal to the cytoplasm and the start of the subsequent transduction of biochemical processes.

In the study of the primary events following UV-light absorption in the UV-pigments, one cannot exclude the possibility that the photoisomerization may involve the unprotonated species up to the primary photoproduct formation (that gets then protonated afterwards in the ground state). However, alternatively, a fast protonation of the Schiff base immediately following UV-photon absorption (photoinduced proton-transfer) represents also a distinct

possibility: the Schiff base basicity (i.e., its proton accepting ability) is expected to increase in the excited state and hence a proton-transfer may occur from the nearby carboxylic residue and the Schiff base. This would lead to the formation of a protonated Schiff base in the excited state, thus possibly favoring an efficient and fast isomerization of the chromophore as already observed and modeled in rhodopsin where the chromophore is indeed protonated: Rh photoisomerization is carried out within 200 fs, which is about six orders of magnitude than the experimental time resolution (100 ns) employed to track the “first” protonated photo-intermediate in the UV-pigment[32].

8 QM/MM Study on the Isomerization Mechanisms of Human Melanopsin and Invertebrate and Vertebrate Rhodopsins: Going Beyond the Monodimensional Landau-Zener Model

8.1 Introduction

The ultrafast isomerization of retinal protonated Schiff base (RPSB) chromophore in opsins is a textbook example of excited state (ES) ultrafast photoreactivity. Its photoisomerization in Rh is the primary event in the process of vision and a cornerstone for molecular fundamental studies of vision in vertebrates[13]. As a consequence, the understanding of the intrinsic photophysical and photochemical properties of RPSBs within different environmental effects of the surroundings (proteins, solvent, etc.) is critical for the design of tailored and high performance photo-sensitive bimolecular devices. The ultrafast isomerization of RPSBs in the chiral protein environment characterizes with an electrostatic control showing tunability of absorption spectra, sub-100fs lifetime, high quantum yield, long living coherences even after decay to the ground state (GS)[173,248]. All these characteristics are in agreement with a ballistic ES motion funneled to the GS through a peaked CI placed along the reaction coordinate. The RPSB decay has been thus regarded as a common example of the Landau Zener model [149], i.e. the high velocity RPSB has in the C₁₀-C₁₁-C₁₂-C₁₃ (CCCC) mode upon reaching the CI seam leads to a highly effective population transfer to the GS with a high QY.

With the time science has acquired more in-depth knowledge into RPSB dynamics, thereby revealing a way more complicated mechanism / relationships:

- While the photoisomerization reactions of RPSBs in rhodopsins are extremely fast (sub ps) and photo selective with high quantum yield (QY ca. 67%) [5,249,250], in solution the reaction is much slower (2–3 ps) and poorly selective with low QY (ca. 25%)[14,166,171,172,177,202,251]. The different behaviors of RPSBs in proteins and in solution are attributed to a lot of factors including structural and electrostatic interactions. The protein environments have a significant counterion shielding effect (and thus red shifted absorptions, in general); on the other hand, in solution, a tight bound ion pairs between the cationic RPSB and its negative counterion exist and, in turn, the covalent ionic S₁ states is destabilized with respect to the covalent (S₀ and S₂) states due to the different charge distributions and this may explain the slow RPSB isomerization in solution. Therefore, the intrinsic (photophysical and photochemical) properties of RPSBs are highly regulated through the electrostatics

effects. While in Rh proteins, the S_1 and S_2 state are well separated from each other and thus, two-state single-mode model could account for the photoisomerization of the RPSBs[5,13,189,252,253], the three-state model[13,254-256], involving the interaction between the ionic S_1 and the covalent S_2 states, represents the photoisomerization process when both states become close to each as found in solution. However, a similar situation was also reported for the photoisomerization of the RPSB in the C1C2 channelrhodopsin [193] [26] in which S_1 and S_2 states are close in energy and their interplay in the photoconversion dynamics cannot be excluded.

- The photoisomerization of RPSB in Rh is governed not only by the isomerizing double bond (CCCC) but rather by the faster moving hydrogens attached to the reactive center [257], which is related to the hydrogen out-of-plane (HOOP) mode at this bond. As a consequence, the molecules may re-cross the CI region many times before decaying back to the GS. Eventually, it has been argued that an efficient product generation relies in the phase matching between H-C₁₁-C₁₂-H (HCCH) and CCCC when the molecules decay to the GS.
- The decision of photo-product formation is taken at hopping time if biracial configuration is established, otherwise the system roams in the CI region until this condition is established [258].

Although the last two findings suggest that the 1D Landau-Zener model might be oversimplified, its intuitive nature and simplicity make it very attractive and it is still applied for making predictions or designing artificial pigments. Recently, Olivucci and co-workers presented theoretical investigation on the light sensitivity of three pigments, Rh, sqRh and hMeOp, which suggests a correlation between absorption wavelength and ES lifetime, i.e. the more blue-shifted the absorption, the faster the isomerization. Based on this fact, and following the Landau Zener model, they anticipated that hMeOp which was shown to have the steepest ES potential energy surface and to reach the conical intersection seam with the ground states the earliest should exhibit the highest QY[12].

In the following, we argue, based on semi-classical trajectory simulations on the three aforementioned pigments that the Landau-Zener rule does not apply for visual pigments. The reason is that opsin dynamics is essentially multi-dimensional (C₁₁C₁₂, CCCC and HCCH) and although an efficient ultrafast decay to the GS is observed, the reaction outcome (and hence QY) depends on the phases of the reaction driving coordinate HCCH and the torsion CCCC and the electronic structure of the system. The hybrid quantum mechanics/molecular mechanics (QM/MM) approach has been extensively used for modeling RPSBs in solution and in proteins[12,14,73,74,76,77]. The QM/MM approaches are able to handle the electrostatic effects of the environments and, in turn, give better understanding of the photoisomerization mechanism at atomistic details.

8.2 Methodology and Benchmarking

8.2.1 Three Pigments Models

One of the prerequisites of our computational study is the construction of a computer model starting from the crystal structure of the three pigments. In contrast to both Rh and sqRh, there is no available crystallographic data for hMeOp. Therefore, Rinaldi et. al. have exploited the high sequence similarity between sqRh, whose crystal structure is available (PDB code: 2Z73) [259], and hMeOp (40%) to construct an atomistic structural model of hMeOp (**Figure 8-1**). Here we employ the same models used in the study of Rinaldi et al. for the three pigments [12]. Briefly, the QM/MM models of Rh and sqRh were prepared utilizing only one unit of the dimeric of the crystallographic structures in which all the crystallographic water molecules were included while the membrane lipids at the protein surface were excluded (for Rh: PDB code 1U19 [260], resolution 2.2 Å; for sqRh: PDB code 2Z73 [259], resolution 2.5 Å). On the other hand, the QM/MM model of hMeOp was constructed by homology modeling, i.e. starting from the comparative modeling structure using the crystallographic structure of sqRh as a template in which the retinal chromophore coordinates were kept fixed as in sqRh. Such protocol of the comparative modeling was validated by reproducing the observed absorption maximum for the human rhodopsin built using the crystallographic structure of Rh as a template.

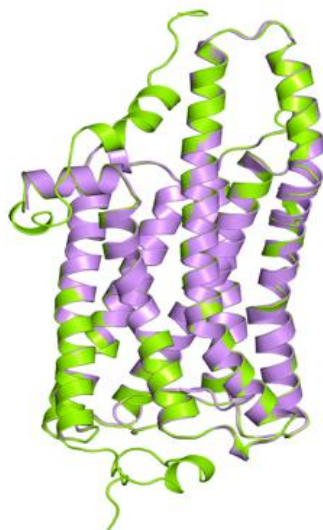


Figure 8-1. Comparative model (violet) of hMeOp superimposed on top of sqRh crystallographic structure used as template (green), this **Figure** taken from ref [12].

8.2.2 QM/MM Partitioning Scheme

The QM/MM boundary was placed on the Lys C δ –C ϵ bond and the link–atom approach was used to model the frontier (**Figure 8-2**)[54,261,262]. The whole PRSB chromophore is treated quantum mechanically (54 atoms including the link atom) keeping the protein environments fixed at their crystal structure atomic positions except the closest 9 atoms of the lysine side–chain connected to the PRSB were free to move (i.e., as M layer). The protein environments were described by a modified AMBER96 force field. Electrostatic embedding was used to describe the interaction between MM and QM systems [74].

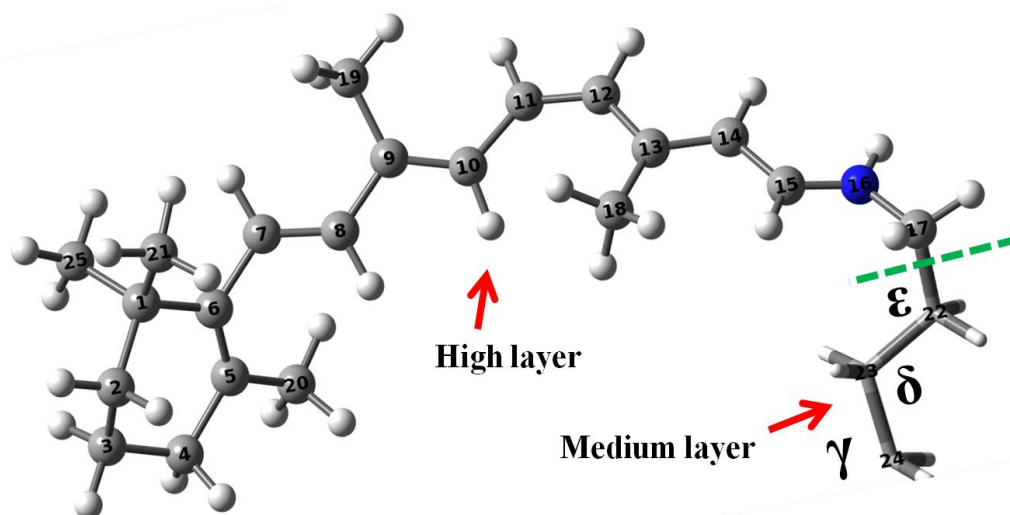


Figure 8-2. Schematic representation for high and medium layers, the green dashed line show the cut between the H and M layers. The atoms in ball and stick are belonging to QM region while atoms represented in tube belong to medium layer. The low layer includes the rest of the protein not shown in the **Figure**.

8.2.3 Optimization and Single Point Calculations

The ground state structures of the three pigments were optimized at the complete active space self-consistent field CASSCF/6-31G*/AMBER level employing two different active spaces (see next section). The CASSCF wave function was followed by subsequent multiconfigurational second-order perturbation theory (CASPT2) computations to estimate the dynamic correlation energy of each state in order to get a more quantitative evaluation of the excitation energies [66]. This combined CASPT2//CASSCF approach has been shown to return experimentally accurate energies with errors within 0.2-0.3 eV. An imaginary level-shift of 0.2 au was used to decrease the influence of weakly interacting intruder states in the CASPT2 calculations [185]. The ionization potential and electron affinity parameter was set to 0.0 au [186], in accordance with previous studies of retinal in gas-phase and its protein environment [24,187-189].

8.2.4 Selecting the Active Space

The complete active space CAS(12,12) of RPSB comprises twelve electrons in twelve π -orbitals (**Figure 8-3**), yet such large active space maybe practically used for optimization but it is not practical for frequency calculations and extensive dynamics simulations. A possible way to overcome this problem is to reduce the active space to ten electrons in ten π -orbitals CAS(10,10) by rejecting one occupied and one virtual π -orbitals from the full π -system. In order to select the two orbitals that have the least pronounced effect on the results we have computed for each pigment a single adiabatic trajectory with zero initial velocity (i.e. 0K reference trajectory) employing both the full- π CAS(12,12) and the a reduced active space CAS(10,10). For that purpose many trials have been performed, each time excluding a couple of π/π^* -orbitals (i.e. one occupied and one virtual). Eventually, the

reduced active space that most accurately reproduced the reference CAS(12,12) trajectories was selected for running systematic dynamical studies (see **Figure 8-4**).

We found out that the trajectories computed with a CAS(10,10), thereby excluding the pair of bonding and non-bonding π -orbitals localized on the β -ionone ring (**Figure 8-3**) reproduced perfectly both the energy profiles and the structural features shown using the full- π CAS(12,12) active space along the whole photoisomerization path, see **Figure 8-4** and **Figure 8-5**.

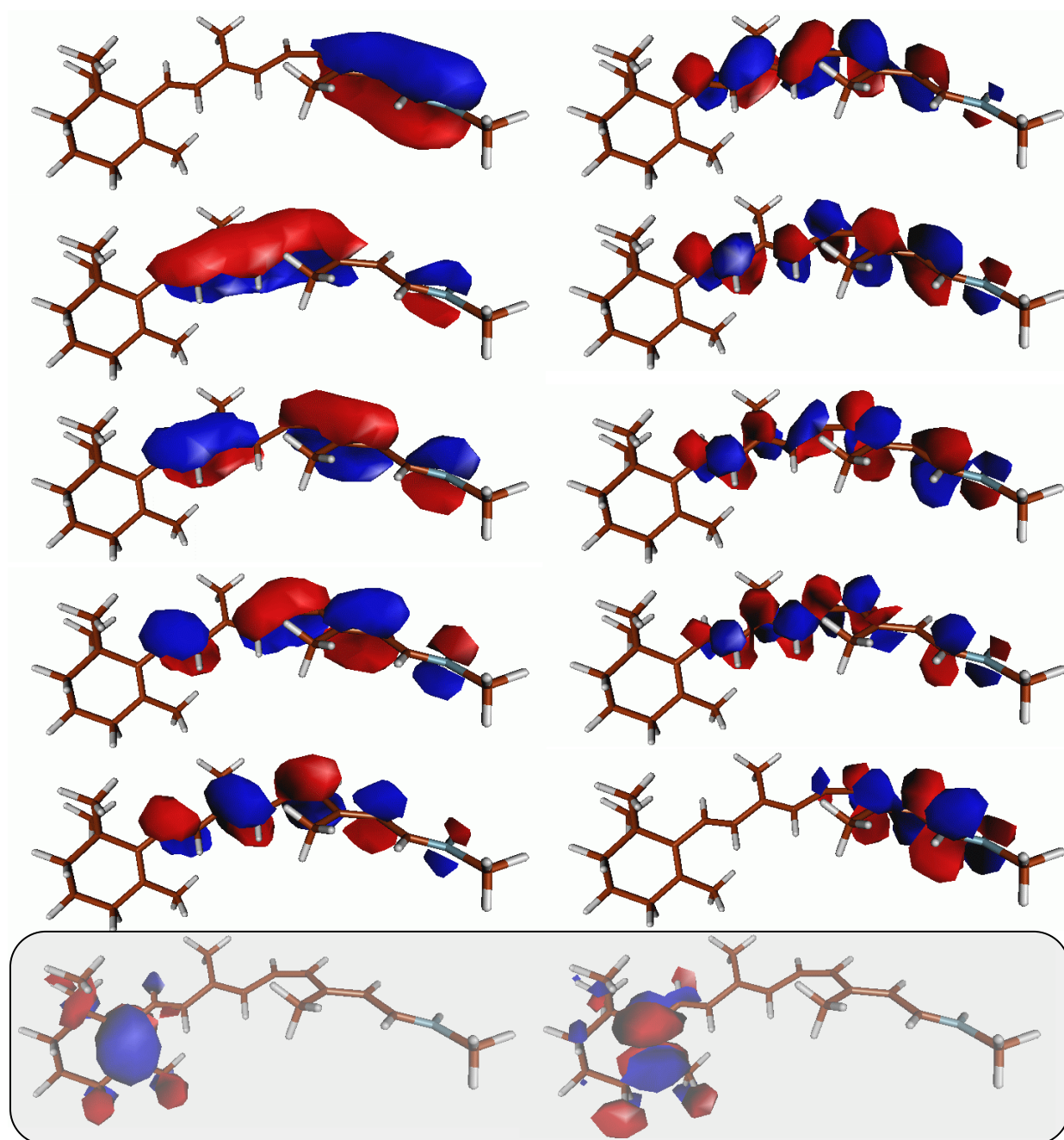


Figure 8-3. The molecular orbitals comprising the full active space CAS(12,12). Highlighted in gray is the pair of bonding and anti-bonding orbitals resulting in the reduced CAS(10,10) which best reproduces the energy profiles and the structural features obtained using the full- π active space.

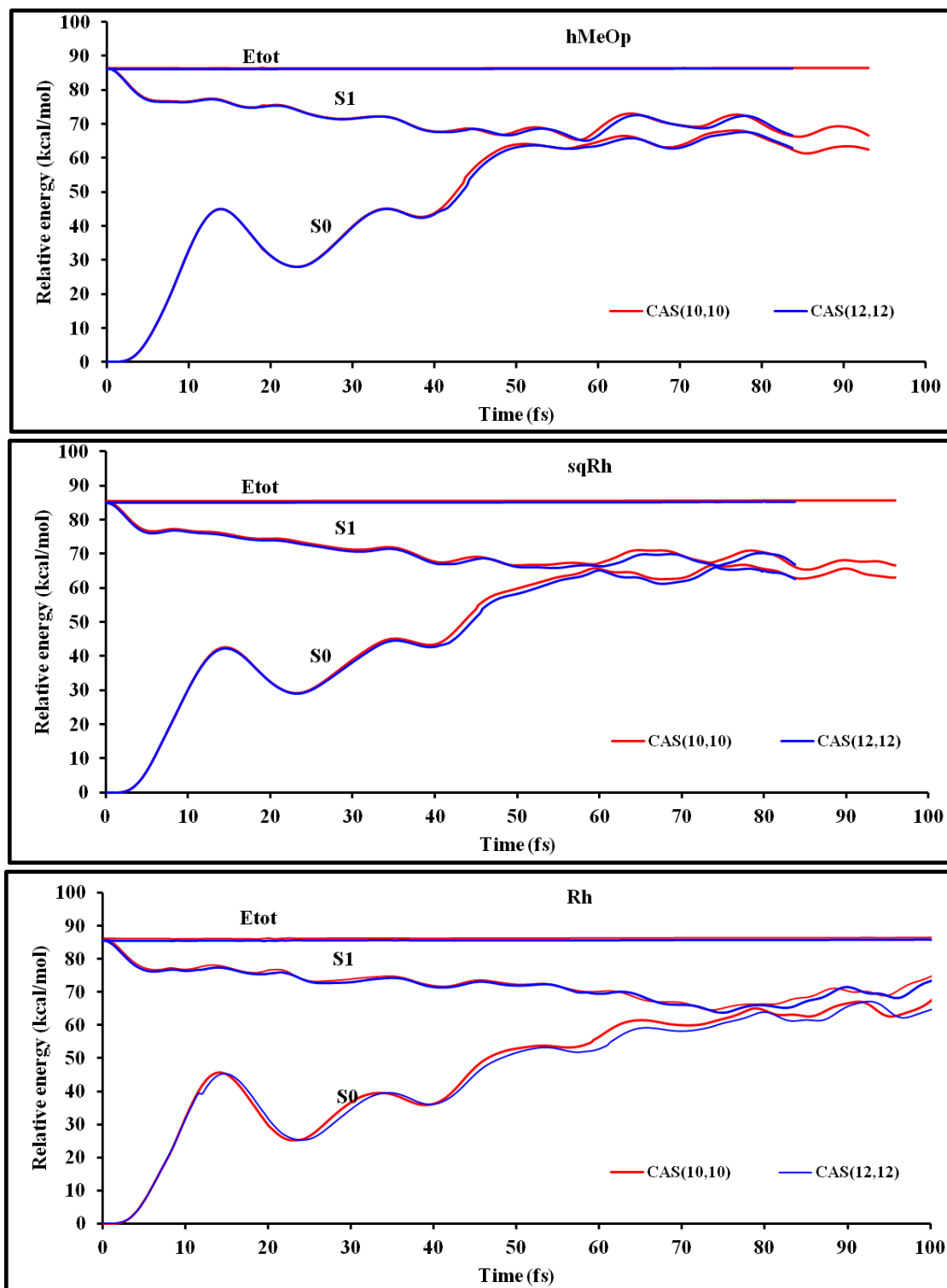


Figure 8-4. Overlay of S_1 and S_0 and total energies in pigment trajectories computed with CAS(10,10) and CAS(12,12) active spaces shown in red and blue colours, respectively. The overlays show, that CAS space and time step have virtually no influence on the excited state dynamics.

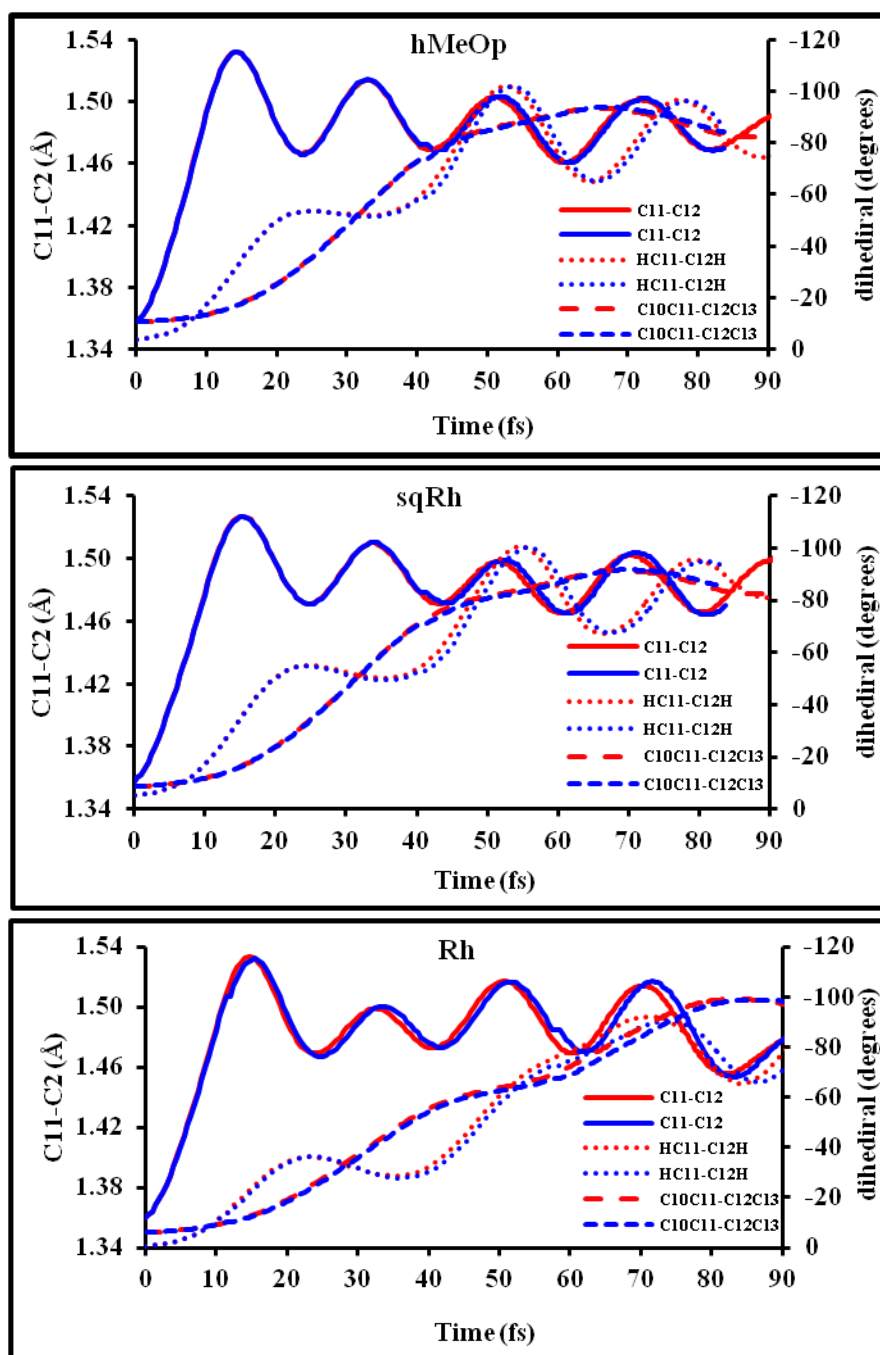


Figure 8-5. Overlays of $C_{11}-C_{12}$ bond length, $C_{10}-C_{11}-C_{12}-C_{13}$ and $H-C_{11}-C_{12}-H$ dihedrals in 0K trajectories computed with CAS(10,10) (red colours) and CAS(12,12) (blue colours) active spaces.

8.2.5 MD Simulations

8.2.5.1 0K Trajectories

The reference trajectories were started, without any initial kinetic energies, for the three pigments from the corresponding FC geometries optimized using CASSCF/6-31G*/AMBER with single root. Each trajectory was calculated at the same level of theory, used for ground

state optimization, but with State-Averaged, NRoot=2, (weights: 0.5, 0.5) employing both a time step of 0.5 and 1.0 fs, which was reduced to 0.25 fs in the vicinity of the crossing between S_0 and S_1 (i.e. $\Delta E_{S_1-S_0} < 15$ kcal/mol); surface hopping was switched off (**Figure 8-4** and **Figure 8-5**).

8.2.5.2 Trajectory Swarms

For each pigment, a set of 60 geometries with their associated velocities were created using Wigner's quasi-probability distribution [156] through ground state sampling utilizing their normal modes (computed by numerical frequency calculations operated through COBRAMM on the top the re-optimized ground state using CASSCF/6-31G* level with single root employing the selected CAS(10,10) active space.). Such set of initial conditions is intended to mimic the wave packet nature of the quantum-mechanical system. The molecular dynamics simulations were started in the bright excited state (S_1) employing a two root state averaged with CAS(10,10)/6-31G* and time step of 0.5 fs, which was reduced to 0.25 fs in the vicinity of a crossing (i.e. $\Delta E_{S_1-S_0} < 15$ kcal/mol). A velocity Verlet algorithm has been used in order to propagate trajectories at constant energy. The surface hop between S_1 and S_0 potential energy surfaces was activated: a Tully's fewest switches surface hopping algorithm with decoherence correction ($d = 0.1$ au) [263] was used for this purpose. Back hopping is switched off during the simulation. Trajectories were computed up to the formation of clear photoproducts through tracking the evolution of the $C_{10}-C_{11}-C_{12}-C_{13}$ torsion angle. The molecular orbitals calculated using MOLCAS were transformed to MOLPRO in order to calculate the non-adiabtic coupling vectors. All QM/MM single point, geometry optimizations, numerical frequency and molecular dynamic calculations have been performed using COBRAMM, a QM/MM program interfacing various QM and MM codes [77,92,94,190].

8.2.6 Time Scaling of the Excited-State Trajectory

The relation between the CASPT2 energy and the corresponding CASSCF value is given by the following relation [241]:

$$\alpha E_{CASSCF}(x) = E_{CASPT2}(x) \quad (8.1)$$

where α is the proportional factor. This means that in the excited state there is proportionality between the CASSCF gradient and the CASPT2 one along the PES. Since the molecular dynamics explores a region of the PES that is close to the reaction path, one may assume that this relation is also valid along any computed trajectory. Another way to scale the CASSCF gradient to CASPT2 one during the MD is to scale the time of CASSCF simulation according to the following equation

$$t_{scaled} = t_{unscaled} \alpha^{\frac{1}{2}} \quad (8.2)$$

where $t_{unscaled}$ is the unphysical CASSCF time, and t_{scaled} is the physical CASPT2 time.

In order to determine α , we have calculated the CASPT2 and CASSCF excited-state energies along the reaction path by means of relaxed scan around C11=C12 torsional coordinate with 10° increment. The values of α then was obtained by linear fitting of the corresponding energies of S₀, S₁ and ΔE (Figure 8-6 and Table 8-1). The linear fitting between CASSCF and CASPT2 energies of S₁ state for all three pigments is consistent with the previously reported to Rh (0.795)[241].

Table 8-1. α values according the linear fitting between CASSCF and CASPT2 of S₀, S₁ and ΔE energies

	S ₀	S ₁	ΔE	Average
hMeOp	0.8341	0.7837	0.8161	0.811
sqRh	0.8943	0.7913	0.8117	0.832
Rh	0.9251	0.6233	0.8461	0.798

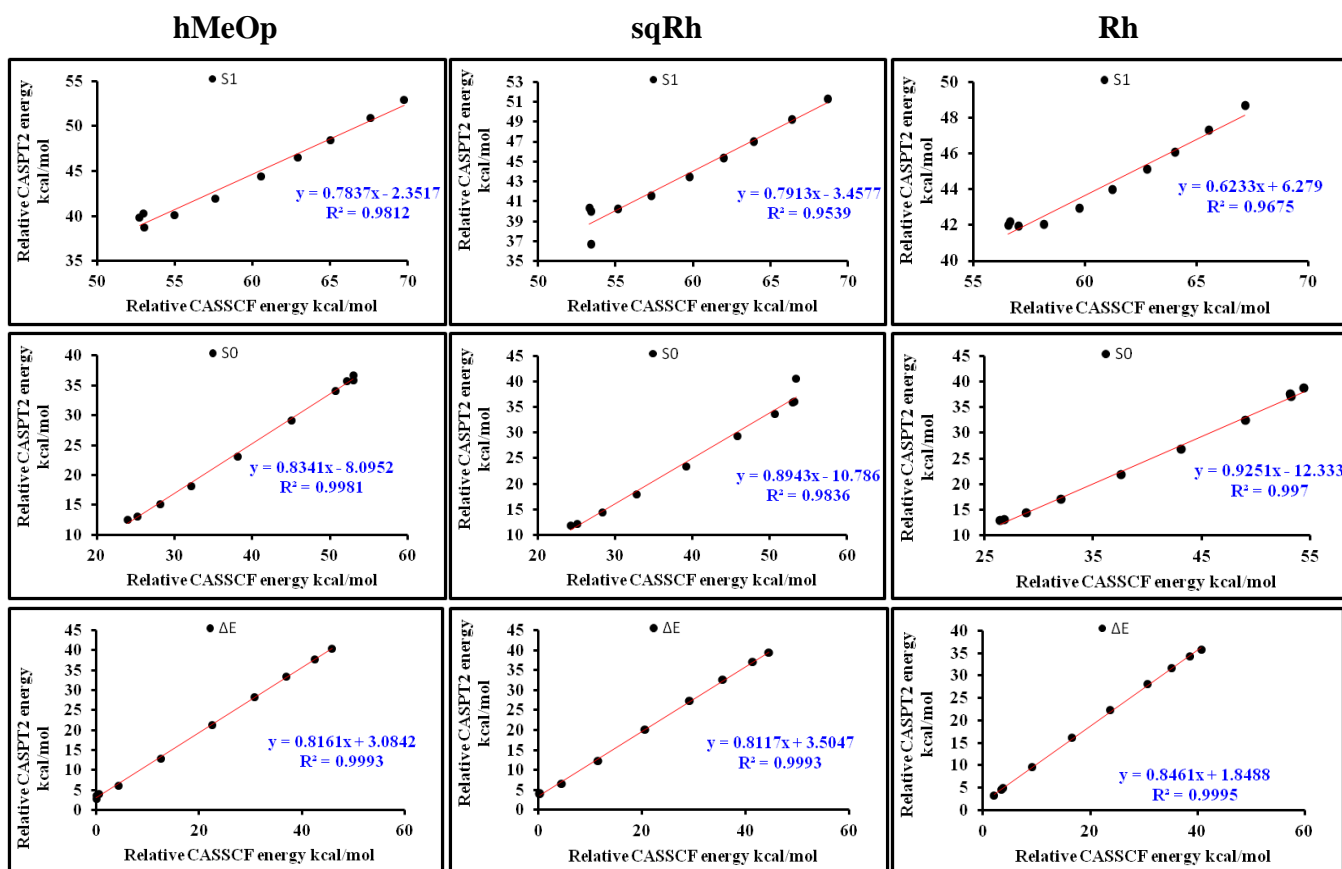


Figure 8-6. Linear fit of relative energies (referred to the ground-state minimum) calculated at CASPT2 and CASSCF level of theory along the computed CASSCF reaction path.

8.3 Result and Discussion

8.3.1 Franck–Condon Geometries

The three pigments incorporate in their cavities the very same chromophore (11-cis-retinal). Upon relaxation, the ground state structures show a clear single/double bond alternation with nearly the same Bond Length Alternation (BLA) of ca. 0.12 Å (BLA is defined as the average of the bond lengths of single bonds minus that of double bonds of the retinal polyenic chain). Moreover, the β -ionone ring in Rh is slightly less twisted (by ca. 5°) compared to the one of sqRh and hMeOp; the other dihedral angles distributed over the conjugated π chain show smaller distortions which are more pronounced in hMeOp than for sqRh or Rh (Table 8-2).

Table 8-3 reports the SS-CASPT2 as well as MS-CASPT2 vertical excitation energies as well as the corresponding predicted oscillator strengths for the RPSB in the pocket of the three proteins. Calculated values for the oscillator strengths show that the first excitation corresponds to the bright state with a larger ionic character (larger dipole moment) than the second dark excited state (possessing a covalent character and a smaller dipole moment). We also calculated the corresponding absorption energy of the isolated optimized geometries of RPSB (after removing the protein environment) to separate the contribution of the protein environment in the excitation energies from the effect of the geometrical distortion. Furthermore, the excitation energies of the RPSB freely optimized in the gas phase are also reported.

Theoretical calculations of the absorption maximum based on SS-CAPT2 reproduced the experimental absorption maximum for the three pigments within ca. 2–3 kcal/mol. The three pigment are absorbing at increasing wavelength where hMeOp is the most blue shifted while Rh is the most red shifted. In Rh, the 40% of the charge originally located on the –NH=CH.C₁₁ moiety shifts toward the β -ionone ring upon H→L vertical excitation. Such charge migration is slightly enhanced to 42% in case of hMeOp. By considering the vertical excitation of the isolated RPSB as a reference, one can observe that the structural deformation imposes a red-shift in all three pigments, whereas it is most pronounced in Rh (i.e. 1.8 kcal/mol) while negligible in hMeOp. Thus, it is apparent that the spectral properties are mainly attributed to the electrostatic interactions of the RPSB with the surrounding protein residues, that pushes in an opposite direction eventually resulting into a blue opsin shift of ca. 8.0, 7.6 and 7.2 kcal/mol for hMeOp, sqRh and Rh, respectively. Our findings are in match with the recent theoretical study reported by Rinaldi et al. [12]. Rinaldi et al. have extensively investigated the effect of individual amino acid residues surrounding the chromophore where they found that in hMeOp and in sqRh the largest blue shift effect is caused by E215 and E172 (showing a change of ca. 5.4 and 8.5 kcal/mol, respectively). E215 and E172 are homologous to the E181 counterion in Rh, that shows a small effect, the largest contribution depending by the E113 primary counterion (ca. 17.6 kcal/mol), which is located closer to the Schiff base than the corresponding residues (E172 and E215) in the other two pigments.

Table 8-2. The ground state geometrical parameters optimized using CAS(12,12) and CAS(10,10)

Parameter Model	CAS(12,12)				CAS(10,10)		
	Rh	sqRh	hMeOp	gas	Rh	sqRh	hMeOp
C ₅ -C ₆	1.352	1.351	1.354	1.353	1.332	1.332	1.334
C ₆ -C ₇	1.493	1.491	1.494	1.493	1.494	1.491	1.495
C ₇ -C ₈	1.352	1.346	1.348	1.349	1.351	1.347	1.348
C ₈ -C ₉	1.474	1.469	1.471	1.471	1.474	1.470	1.472
C ₉ -C ₁₀	1.361	1.359	1.360	1.364	1.361	1.359	1.360
C ₁₀ -C ₁₁	1.464	1.459	1.459	1.451	1.465	1.459	1.459
C ₁₁ -C ₁₂	1.360	1.358	1.357	1.363	1.360	1.358	1.357
C ₁₂ -C ₁₃	1.466	1.471	1.467	1.460	1.466	1.471	1.467
C ₁₃ -C ₁₄	1.370	1.364	1.365	1.370	1.370	1.364	1.365
C ₁₄ -C ₁₅	1.434	1.425	1.429	1.428	1.435	1.425	1.429
C ₁₅ -N ₁₆	1.292	1.294	1.293	1.292	1.292	1.294	1.293
C ₅ -C ₆ -C ₇ -C ₈	-54.9	-61.6	-60.7	-65.7	-55.4	-62.8	-61.9
C ₆ -C ₇ -C ₈ -C ₉	179.3	-177.6	178.7	-178.6	179.3	-177.4	178.8
C ₇ -C ₈ -C ₉ -C ₁₀	-173.5	176.0	171.2	179.5	-172.4	176.3	171.2
C ₈ -C ₉ -C ₁₀ -C ₁₁	173.9	177.9	178.0	179.9	173.8	178.0	178.0
C ₉ -C ₁₀ -C ₁₁ -C ₁₂	163.1	165.1	164.6	176.4	163.3	165.0	164.5
C ₁₀ -C ₁₁ -C ₁₂ -C ₁₃	-6.0	-8.8	-10.6	-2.7	-6.0	-8.7	-10.5
C ₁₁ -C ₁₂ -C ₁₃ -C ₁₄	163.0	156.6	161.0	175.7	163.1	156.5	160.9
C ₁₂ -C ₁₃ -C ₁₄ -C ₁₅	-178.3	179.0	172.8	-179.8	-178.3	179.1	172.8
C ₁₃ -C ₁₄ -C ₁₅ -N	168.4	168.0	169.1	179.1	168.4	167.8	169.2
H-C ₁₁ -C ₁₂ -H	-0.7	-5.3	-3.8	-1.1	-0.7	-5.3	-3.8
C ₈ -C ₉ -C ₁₀ -H	-1.9	0.4	0.6	0.1	-1.9	0.5	0.6
C ₁₄ -C ₁₅ -N-H	-1.0	-0.3	-3.7	0.0	-0.9	-0.4	-3.7
C ₇ -C ₉ -C ₁₀ -H	177.2	179.1	-179.6	179.8	177.3	179.1	-179.6
BLA	0.12	0.12	0.12	0.11	0.12	0.12	0.12

Table 8-3. SS-CASPT2 and MS-CASPT2//CASSCF(12,12)and(10,10)/6-31G*/AMBER, NRroot=3, State-Averaged (weights: 1/3, 1/3, 1/3) absorption maxima (λ_{max} , nm) and the corresponding oscillator strengths f, calculated on the top of the corresponding S₀ minima employing.

	Model	CAS (12,12)								exp. λ_1								
		SS-PT2				MS-PT2												
		λ_1	λ_2	f1	f2	λ_1	λ_2	f1	f2									
protein	hMeOp	468	326	0.64	0.3	452	313	1.2	0.1	463	325	0.7	0.3	449	312	1.2	0.1	467-480
	SqRh	477	329	0.58	0.3	463	316	1.1	0.1	469	328	0.6	0.3	458	314	1.1	0.1	489
	Rh	486	332	0.59	0.3	469	313	1.3	0.1	475	329	0.6	0.3	462	310	1.3	0.1	498
isolated	hMeOp	538	340	0.65	0.3	505	331	1.2	0.2	526	337	0.7	0.3	497	328	1.2	0.2	
	SqRh	545	344	0.62	0.3	513	335	1.1	0.3	531	339	0.6	0.3	502	330	1.1	0.2	
	Rh	554	349	0.67	0.3	518	340	1.2	0.3	530	339	0.7	0.3	499	330	1.3	0.2	
	free	535	347	0.82	0.2	495	334	1.5	0.2									

8.3.2 Linear Absorption Spectra

Table 8-4 and **Figure 8-7** report the linear absorption (LA) as computed on top of the 60 snapshots employed for the dynamic simulations of each pigment. Both SS-CASPT2 and MS-CASPT2 calculations, employing the complete active space CASS(12,12) are reported. Interestingly, SS-CASPT2 calculations better reproduce the experimental absorption energies for both Rh and sqRh, while it overestimates the absorption maximum in case of hMeOp. In this case, MS-CASPT2 leads to a computed excitation energy in match with the experimental value. This happens because in the FC region the ionic S₁ and covalent S₂ states are more close to each other (and mixed) in hMeOp than in the other two pigments, thus calling for a multi-state approach to better model excitation energies. Generally, the absorption maximum of the three pigments are in line with those computed at the FC point, just slightly red shifted as expected when the absorption energy is averaged out an ensemble of points. As readily seen from **Table 8-4**, the SS-CASPT2 spectroscopic features are similar for both Rh and sqRh where the vertical low-lying electronic transitions (to S₁ and S₂) are displaying oscillator strengths of ca. 0.5 and 0.3 while hMeOp displays slightly higher value for electronic transition to S₁ state (0.6) and slightly lower for transition S₂ state (0.2). In the three pigments, especially with MS-CASPT2 treatment, the S₁ state shows a large contribution of the HOMO-LUMO while the second excited state is dominated by the H→L double excitation and H-1→L single excitation, and holds a small, but non-negligible, oscillator strength. The agreement of the computed absorption energies with the experimental values supports the reliability of the sampling procedure and of the ensemble employed for molecular dynamic simulations.

Table 8-4. SS-CASPT2 and MS-CASPT2//CASSCF(12,12)/6-31G*/AMBER, NR_{root}=3, State-Averaged (weights: 1/3, 1/3, 1/3) calculation of the averaged absorption maxima (λ_{\max} , nm), vertical excitation energies ΔE (kcal/mol), oscillator strength f , over all the 60 starting geometries of each pigment ensemble.

Model	SS-CASPT2						MS-CASPT2					
	λ_1	λ_2	ΔE_1	ΔE_2	f_1	f_1	λ_1	λ_2	ΔE_1	ΔE_2	f_1	f_1
hMeOp	496	351	57.8	81.9	0.59	0.24	478	331	60.0	86.8	1.14	0.10
SqRh	488	354	58.9	81.7	0.49	0.31	481	328	59.8	87.6	1.04	0.13
Rh	497	355	57.9	81.6	0.48	0.34	488	321	59.0	89.5	1.17	0.12

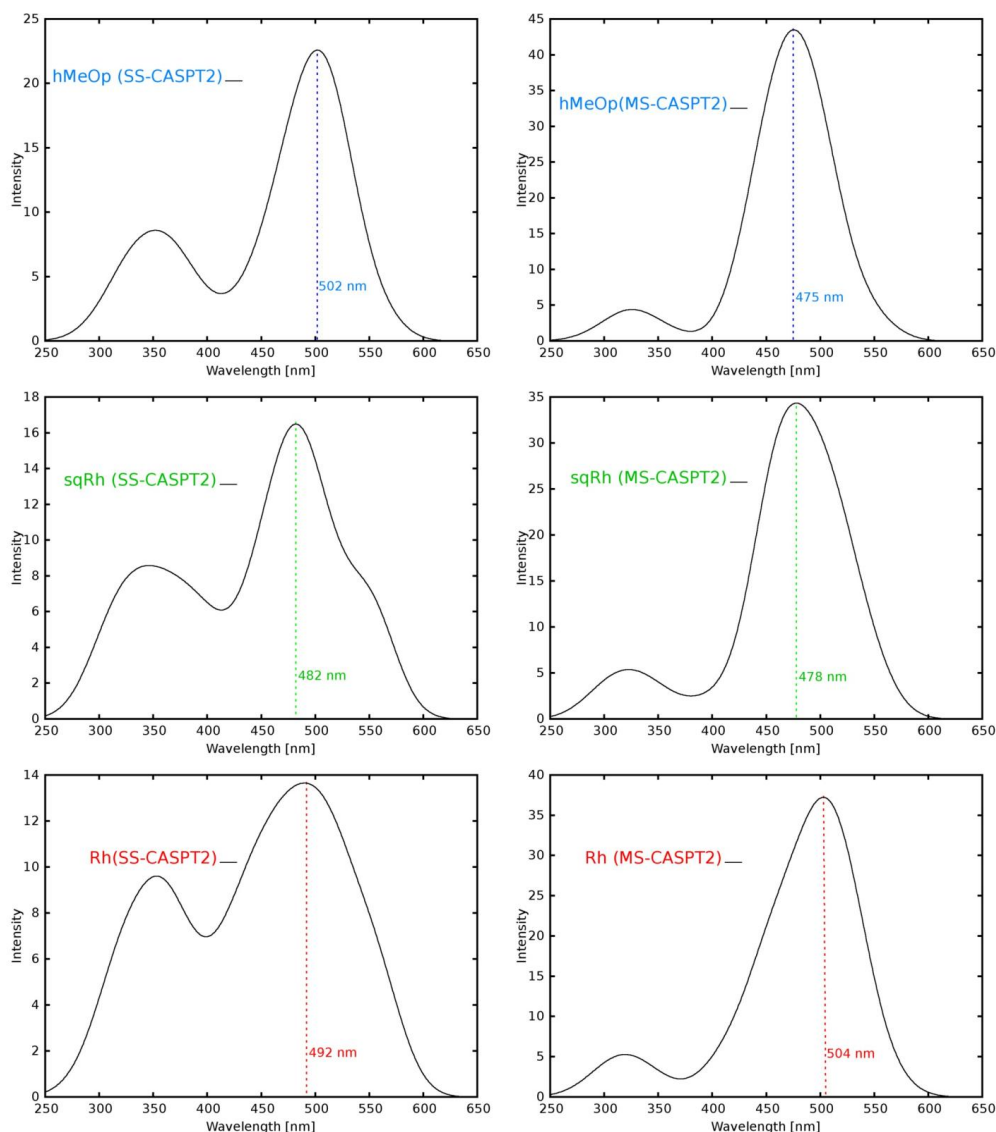


Figure 8-7. LA of the three pigments obtained from averaging over 60 calculated corrected with SS-CASPT2 (left) and MS-CASPT2 (right) after SA3-CASSCF(12, 12) calculations.

8.3.3 Analysis of the Reference Trajectories

As discussed in the section 8.2.5.1 the reference QM/MM semiclassical OK trajectories for the three pigments were calculated starting at the corresponding FC points on the S_1 energy surface with zero initial velocities and propagated until reaching the S_1/S_0 crossing seam. Usually, such zero velocity trajectories represent an averaged evolution of the excited state population generated after photoexcitation and therefore they may be used to have a qualitative behavior for the photoinduced dynamics of the investigated system (**Figure 8-4**). **Figure 8-4** shows that hMeOp, sqRh, and Rh all reach the CI region at progressively longer times (50, 60 and 78 fs respectively). This order is in agreement with the steepness of the PESs of the three models as evident from the relaxed scan around the $C_{10}-C_{11}=C_{12}-C_{13}$ torsional angle shown in **Figure 8-8**: hMeOp shows a steeper PES than Rh and therefore reaches CI earlier along the torsional coordinate.

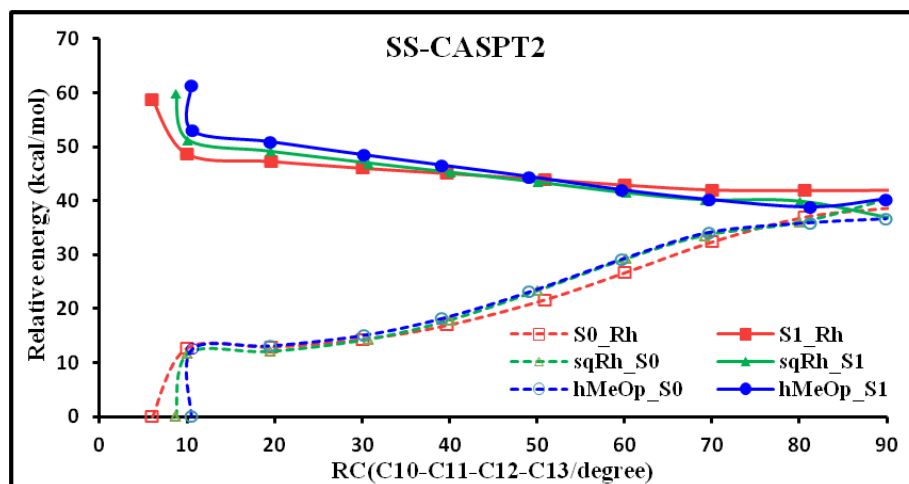


Figure 8-8. CASPT2//SA2-CASSCF(12,12)/6-31G*/AMBER energy profiles along the torsion angle $C_{10}-C_{11}-C_{12}-C_{13}$ obtained from constrained relaxed scan with 10° increment.

8.3.4 Rationalizing the Correlation between Excitation Wavelength and Isomerization Speed

The following sections deal with the analysis of the swarms of trajectories, run for each pigment. All three pigments show an ultra-fast behavior with the entire population having decayed down to the GS within 150 fs. As evident from **Figure 8-9**, though, hMeOp (55 fs) and sqRh (58 fs) swarms hit the CI seam notably earlier than Rh (80 fs). The three swarms of trajectories exhibit average ES lifetimes in the same order observed for the reference trajectories, i.e. Rh (78 fs) \rightarrow sqRh (60 fs) \rightarrow hMeOp (50 fs), **Figure 8-4**. Furthermore, it is worth mentioning that the crossing region in hMeOp and sqRh is reached in a confined time-window of about 30 fs, whereas in Rh hopping events occur in a time span of nearly 50 fs, thus, suggesting a more ballistic dynamics in hMeOp and sqRh. This is further corroborated by the distribution of hopping events in the three systems (**Figure 8-10**). A clear Gaussian distribution, peaking at the average lifetime is evident for hMeOp and sqRh, while in Rh the hopping events are distributed evenly.

The driving force in the ES of RPSB is the double bond alternation. While in gas-phase, where RPSB is planar, this involves only bond length rearrangement, inside the protein RPSB is heavily distorted around the pseudo-single bonds in the GS (C_8-C_9 , $C_{10}-C_{11}$, $C_{12}-C_{13}$, $C_{14}-C_{15}$). Therefore, the double bond rearrangement triggered after excitation is accompanied by an out-of-plane motion of the hydrogens (Hs), towards the formation of planar double bond fragments in the ES. Following this line, in all three pigments, the very first geometrical deformation upon excitation is the out-of-plane (clockwise) motion of H12 required for the formation of the planar $C_{12}=C_{13}$ double bond fragments in the ES.

Due to the structure of the protein cavity at their equilibria, sqRh and hMeOp are more pronouncedly bent at the C-terminus (β -ionone ring) than Rh. This affects the central fragment as the angles $C_{10}-C_{11}-C_{12}$ and $C_{11}-C_{12}-C_{13}$ are both $\sim 4-5^\circ$ smaller for sqRh and

hMeOp compared to Rh (see **Figure 8-11**). As a consequence H₁₀ and the methyl group at C₁₃ come closer leading to a more pronounced steric repulsion between them. As an immediate consequence we note an increase of the C₁₀-C₁₁=C₁₂-C₁₃ dihedral angle in the series Rh (-6°) → sqRh (-9°) → hMeOp (10.5°). Moreover, the CH₃ group (C_m in **Figure 8**) at C₁₃ is stronger twisted out of the plane defined by C₁₃-C₁₂-C₁₁ in sqRh and hMeOp, implying a more pronounced torsion around the C₁₂-C₁₃ pseudo single-bond. Hence, both systems gain a higher momentum along the H₁₂ out-of-plane coordinate already in the first 10–15 fs of the MD simulation compared to Rh (note that the C_m itself is inert as it is much heavier so all the momentum is concentrated in the H₁₂ motion). This can be appreciated by looking at the temporal evolution of the H₁₂-C₁₂-C₁₃-C_m dihedral (**Figure 8-11**). Due to the momentum gained by H₁₂ the HCCH of the RPSB in sqRh and hMeOp reaches values of 50° already after 20 fs whereas the same value for Rh is only about 30°.

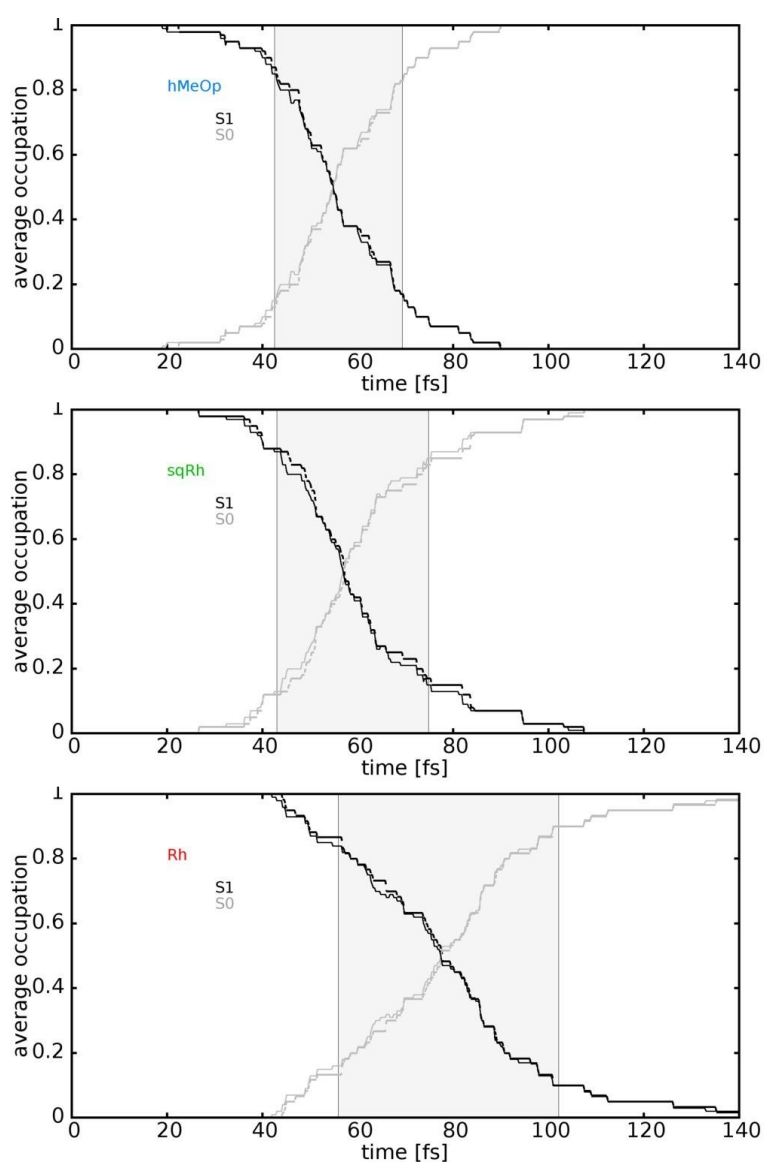


Figure 8-9. Population transfer dynamics for the three pigments, quantum mechanical and classical quantities are shown in solid and dashed lines, respectively. Hopping zones highlighted in gray.

Following the initial H₁₂ out-of-plane motion the torsion around the central bond kicks in through counter-clockwise motion of the H₁₀-C₁₀-C₁₁-H₁₁ fragment. This second step of the isomerization is accelerated in sqRh and hMeOp again due to the stronger repulsion between H₁₀ and the methyl group at C₁₃. This can be appreciated by looking at the temporal evolution of the distance between H₁₀ and the closest hydrogen H_{ma} from the methyl group (Figure 8-11). At the FC point the H₁₀-H_{ma} distance in sqRh and hMeOp is ~ 2.25 Å, while it is ~ 2.45 Å in Rh. After initial shortening (due to planarization of the C₁₀-C₁₁ fragment) this distance quickly starts to grow in sqRh and hMeOp, notably ~ 5fs earlier than in Rh (Figure 8-11 and Figure 8-9).

Consequently, the stronger bending of the RPSB chromophore inside the reactive pockets of sqRh and hMeOp leads to a more pronounced steric repulsion between the neighboring groups of the central double bond (C₁₁=C₁₂). Immediate consequences are: a) accumulation of momentum in the out-of-plane motion of H₁₂ early in the dynamics (0–20fs) and in the torsion around the C₁₁=C₁₂ bond at later times (20–50fs); b) the increased dihedral angle (–6° → –9° → –10.5°). The former leads to a steeper potential energy surface, while the latter reduces the conjugation strength and causes a blue-shift of the absorption wavelength in the series Rh (–6°) → sqRh (–9°) → hMeOp (10.5°). As a consequence sqRh and hMeOp reach the CI region substantially faster than Rh.

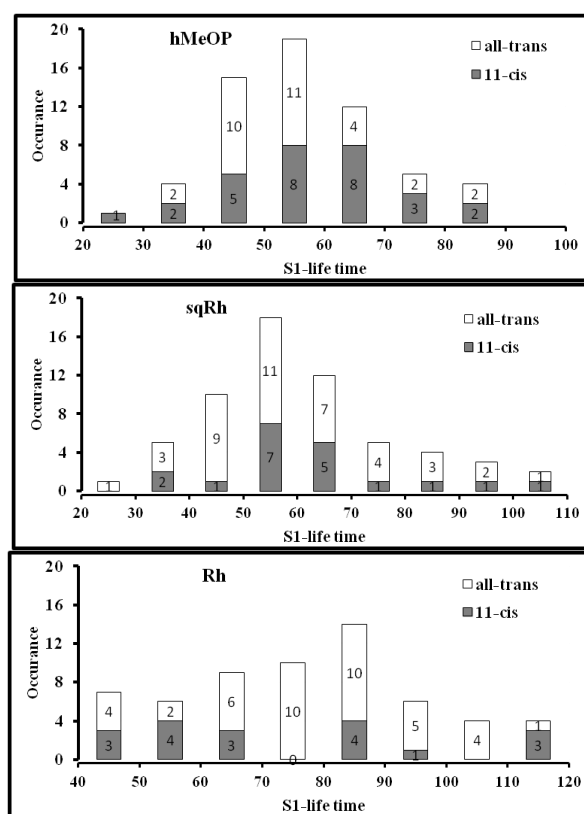


Figure 8-10: Distribution of hopping events as a function of the S₁ lifetimes for hMeOp (top), sqRh (middle) and Rh (bottom). The height of the bar graphs corresponds to the number of trans (nofill) and cis (gray) photoproducts of individual trajectories.

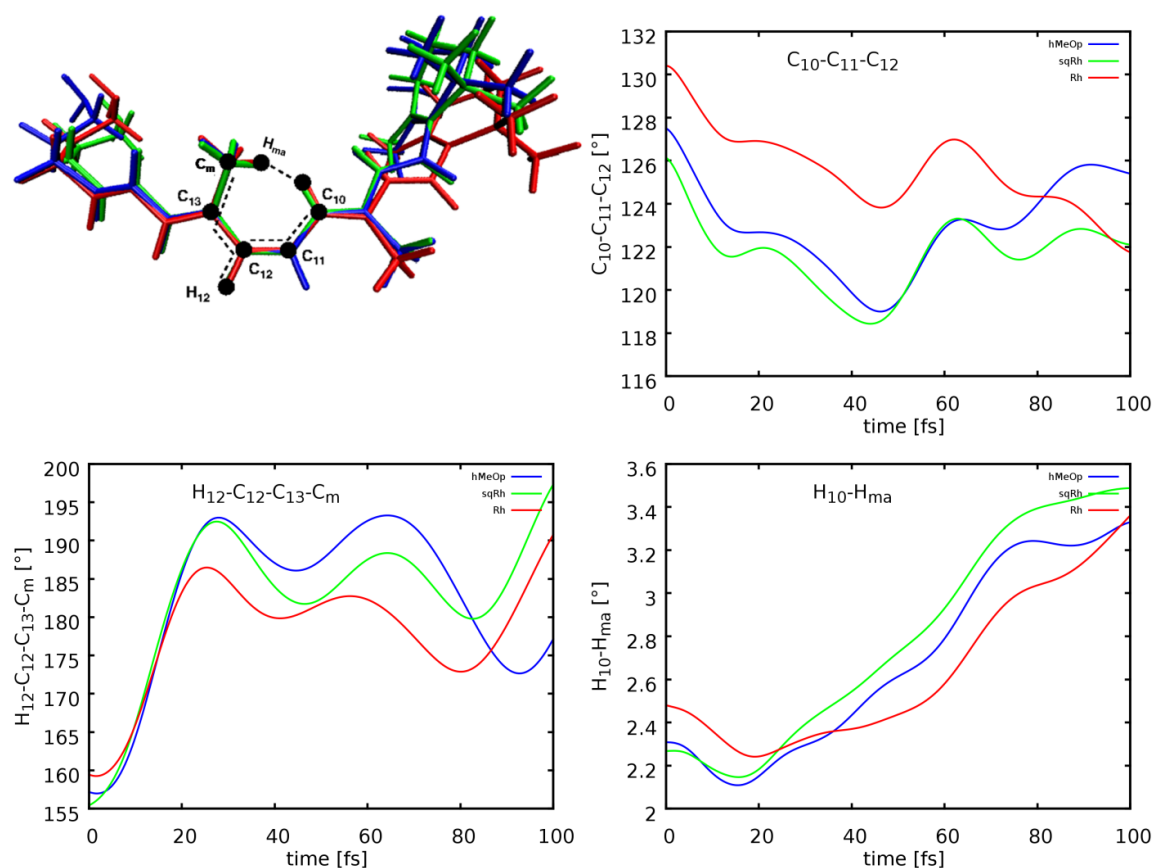


Figure 8-11. Characteristic geometrical parameters in the three pigments and their temporal evolution.

8.3.5 Rationalization of the “Observed” Quantum Yields

Figure 8-12 shows two-dimensional correlation plots of the hopping events in hMeOp (left), sqRh (middle) and Rh (right) in the subspace of the backbone torsion (CCCC) and hydrogen out-of-plane (HOOP) deformation. These plots demonstrate clearly that the direction of the CCCC dihedral (the reaction coordinate) *is not* the decisive mode for the outcome of the isomerization. In particular, when the hopping event occurs at earlier times (as the case for sqRh and hMeOp) the CCCC is found to increase at the moment of hopping, hence, all events appear almost exclusively in the lower part of the plots.

It has been recognized that the driving mode of the isomerization is the out-of-phase motion of the hydrogens, which has been described by either looking directly at the HCCH angle or at the difference between HCCH and CCCC, the so called hydrogen-out-of-plane (HOOP) mode. Applying these criteria to predict the outcome of the photoisomerization we obtain the QYs listed in the second column of **Table 8-5**. A very good agreement with the observed QY is achieved, with deviations within 10%.

As evident from **Figure 8-12** and rather counter-intuitively the pigments hMeOp (left) and sqRh (middle) that reach the CI seam earlier (i.e. being subject to a more ballistic-like dynamics) and decay to the GS faster compared to Rh exhibit a larger number of samples in which the HCCH dihedral decreases at the moment of hopping, thus favoring the recovery of

the reactant according to the rule of thumb introduced above. Based on the (limited) statistics one can expect ~15–20% lower QY for sqRh and hMeOp. *This observation contradicts predictions made on the basis of the Landau–Zener model*, that suggests a higher QY for hMeOp and sqRh. The presented results demonstrate neatly that the light–sensitivity of opsins *cannot* be described within the limits of the 1D Landau–Zener model. Rather, it is a multi–dimensional process driven by bond stretching, hydrogen out of plane motion and torsion. This makes possible for a CCCC/HCCH phase mismatch to occur, i.e. the driving mode HCCH could surpass the 90° region and reach a turning point before the CCCC mode reaches the 90°. This is most easily appreciated by turning back to the 0K trajectories and plot the evolution of the CCCC and HCCH dihedrals (**Figure 8-13**). When HCCH reaches 90° for the first time in hMeOp (49 fs) and sqRh (51 fs) the CCCC is still around 80°. CCCC reaches 90° about 10 fs later (58 fs and 64 fs, respectively) when HCCH is has already reached a turning point and is decreasing. In Rh, on the other side, HCCH and CCCC reach the CI region at the same time (72 fs), i.e. Rh appears as the system where CCCC and HCCH move in phase.

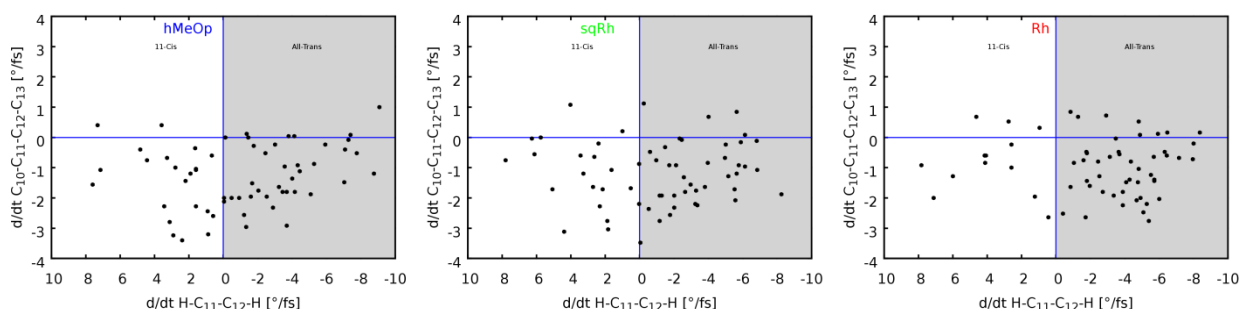


Figure 8-12. Distribution of the hopping events in the space of the HCCH and CCCC coordinates.

Table 8-5. The observed quantum yield vs. the predicted ones based on the HCCH direction at both the hopping decision times.

Model	QY for...	observed	prediction using HCCH direction at...	
			hopping time	switching to biradical WF
Rh	<u><i>all-trans</i></u>	70	78 (+8%)	71 (+1%)
	<u><i>11-cis</i></u>	30	22 (–8%)	29 (–1%)
sqRh	<u><i>all-trans</i></u>	68	65 (–3%)	63 (–5%)
	<u><i>11-cis</i></u>	32	35 (+3%)	37 (+5%)
hMeOp	<u><i>all-trans</i></u>	52	61 (+9%)	55 (+3%)
	<u><i>11-cis</i></u>	48	39 (–9%)	45 (–3%)

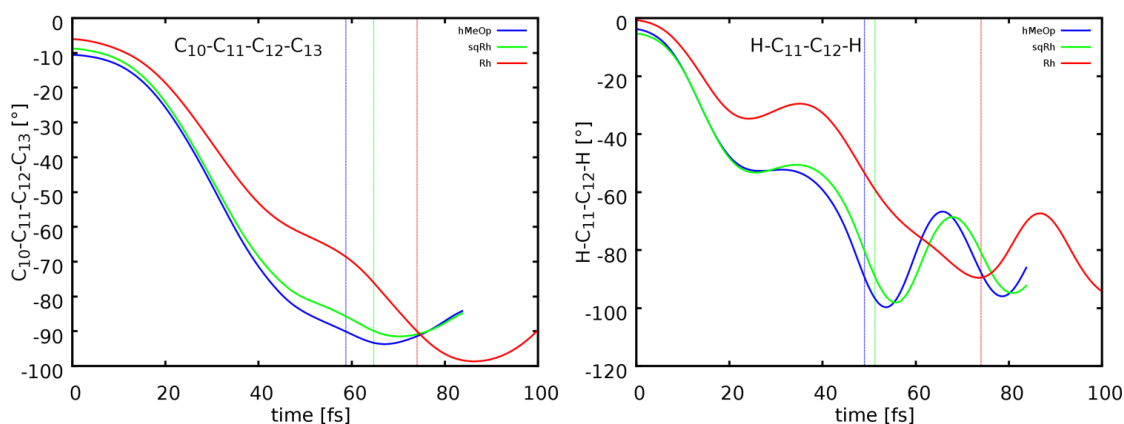


Figure 8-13. Temporal evolution of CCCC and HCCH the 0K trajectories

As argued above the direction of the HCCH mode at the moment of hopping can be used as an easy-to-apply tool for predicting the outcome of the isomerization in opsins. Nevertheless, we recognize that sqRh exhibits a QY nearly identical to that of Rh, which is not in line with the above claim that sqRh and hMeOp should exhibit a substantial QY decrease due to CCCC/HCCH phase mismatch. Is there an additional parameter that influences the decision besides the direction of the HCCH at the hopping time? Shapiro and co-workers argued recently [258] that the decision about the outcome is not always taken at the moment of hopping. In fact, if after hopping the S_0 WF has a charge transfer character the system would roam in the CI region until it accesses a region of biradical nature. Only then the system would exhibit a force to form again a C_{11} – C_{12} double bond. They demonstrated the concept on a few 0K trajectories in Rh and bathRh.

Plotting the decision events based on this modification we observe an even better agreement with the experimental QYs with errors for Rh and hMeOp of below 2% and somewhat bigger error of 5% for sqRh (3rd column in **Table 8-5**). We find that about half of the trajectories end up in a CT state after hopping to the GS and the CT region is left on average between 5 fs (Rh) and 9 fs (sqRh). While this time window is relatively short it allows for a minority of trajectories to change the direction of the HCCH dihedral (corresponding to a trajectory moving between quadrants along the left \leftrightarrow right axis in **Figure 8-14**), which leads to the modulation of the QYs. At the same time **Figure 8-14** shows that changes in the direction of the CCCC dihedral (corresponding to a trajectory moving between quadrants along the up \leftrightarrow down axis) does not change the final outcome of the reaction, once more highlighting the leading role of the HCCH mode.

Despite the remarkable agreement in all three cases we recognize that the faster the relaxation the more outliers to the rule we find. In fact, in Rh there are 5 trajectories which do not follow the rules of thumb, i.e. the HCCH exhibits a turning point after the biradical WF region is reached. In sqRh and hMeOp, the numbers of such trajectories are 9 and 11. Effectively, the faster the decay through the ES/GS funnel, the more kinetic energy RPSB has accumulated and the more often the product formation is decided randomly instead of according to the derived rules.

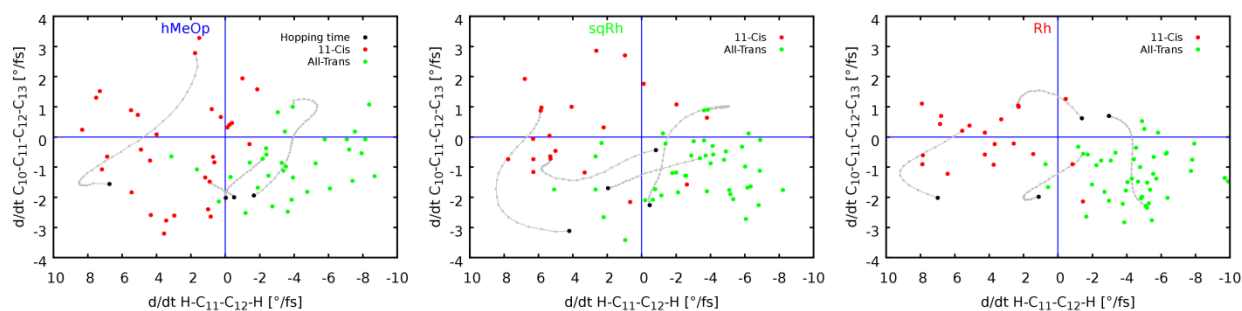


Figure 8-14. Distribution of the "switching to a biradical WF" events in the space of the HCCH and CCCC coordinates.

8.3.6 Statistical Results

The distribution of S_1/S_0 energy gaps at the decay points shows that non negligible percentage of the ensemble decays while the S_1/S_0 gas is relatively large however, most of the trajectories are decaying to the ground state close to the crossing, then the number of decay events decreases with the increase of the S_0/S_1 energy gap (**Figure 8-15**). **Figure 8-16** depicts the distribution of hopping events as a function of the value of the torsion CCCC exhibiting a typical Gaussian like shape centered around $80-90^\circ$ as also show from the calculated averaged coordinates at the decay points overall ensemble, **Table 8-6**.

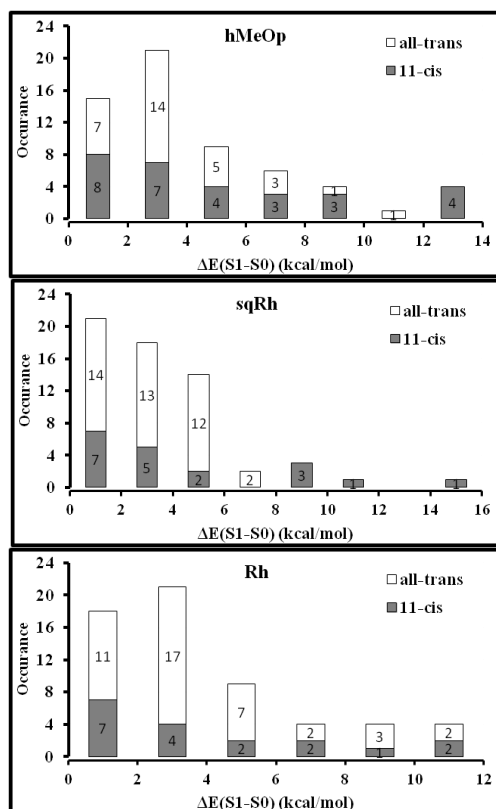


Figure 8-15. Distribution of hopping events as a function of the CASSCF energy differences $\Delta E(S_1-S_0)$ for hMeOp (top), sqRh (middle) and Rh (bottom). The height of the bar graphs corresponds to the number of trans (nofill) and cis (gray) photoproducts of individual trajectories.

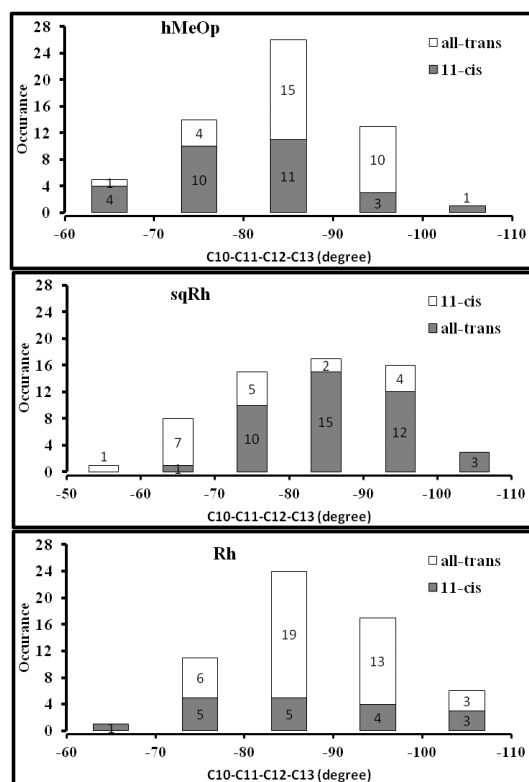


Figure 8-16. Distribution of hopping events as a function of the torsion $C_{10}-C_{11}=C_{12}-C_{13}$ for hMeOp (top), sqRh (middle) and Rh (bottom). The height of the bar graphs corresponds to the number of trans (nofill) and cis (gray) photoproducts of individual trajectories.

Table 8-6. The averaged geometry parameters of the three pigments at hopping point.

Parameter	hMeOp	sqRh	Rh
C_5-C_6	1.339	1.333	1.345
C_6-C_7	1.482	1.478	1.489
C_7-C_8	1.380	1.375	1.373
C_8-C_9	1.445	1.436	1.427
C_9-C_{10}	1.421	1.438	1.450
$C_{10}-C_{11}$	1.388	1.382	1.381
$C_{11}-C_{12}$	1.492	1.481	1.482
$C_{12}-C_{13}$	1.373	1.378	1.370
$C_{13}-C_{14}$	1.453	1.468	1.466
$C_{14}-C_{15}$	1.369	1.369	1.366
$C_{15}-N$	1.375	1.384	1.365
$C_8-C_9-C_{10}-C_{11}$	143.3	143.3	149.1
$C_{10}-C_{11}-C_{12}-C_{13}$	84.0	83.4	88.1
$C_{12}-C_{13}-C_{14}-C_{15}$	167.7	165.4	166.3
$C_8-C_9-C_{10}-H$	23.7	25.2	24.3
$H-C_{11}-C_{12}-C_{13}$	90.1	89.7	87.6
$C_{10}-C_{11}-C_{12}-H$	97.6	96.6	99.6
$C_{12}-C_{13}-C_{17}-H$	15.4	15.7	14.7
$H-C_{15}-N-H$	165.5	165.4	167.1
$H-C_{11}-C_{12}-H$	88.3	90.2	84.8

Table 8-7. Statistical of the individual trajectories of *Rh* shown the hopping and decision time, the photoproduct distribution and the mode govern the reaction.

Traj	hopping time	Product formation follows ...			leading mode	decision time	Product formation follows ...			leading mode	Observed Product		Expected Product at decision time		Expected Product at hopping time		
		H-C11-C12-H at hopping time	HOOP at hopping time	C-C11-C12-C at hopping time			H-C11-C12-H at decision	HOOP at decision time	C-C11-C12-C at decision		Trans	Cis	Trans	Cis	Trans	Cis	
		01	88.5	F			F	F	N/A		90.0	T	T	F	HCCH		√
02	49.5	F	F	N/A	N/A	68.0	T	T	N/A	HCCH		√		√			
03	62.5	T	T	N/A	HCCH	62.5	T	T	N/A	HCCH	√		√		√		
04	83.5	T	T	N/A	HCCH	85.0	T	T	N/A	HCCH		√		√		√	
05	108.8	T	T	N/A	HCCH	108.8	T	T	N/A	HCCH	√		√		√		
06	77.3	T	F	T	CCCC	95.0	T	T	N/A	HCCH	√		√		√		
07	68.0	T	F	T	CCCC	68.0	T	F	T	CCCC	√		√		√		
08	91.8	T	T	T	HCCH	91.8	T	T	T	HCCH	√		√		√		
09	107.8	T	T	F	HCCH	117.0	T	T	T	HCCH	√		√		√		
10	76.5	T	T	N/A	HCCH	76.5	T	T	N/A	HCCH	√		√		√		
11	126.0	T	T	T	HCCH	126.0	T	T	T	HCCH	√		√		√		
12	97.8	T	T	T	HCCH	97.8	T	T	T	HCCH		√		√		√	
13	89.0	T	N/A	T	CCCC	110.0	T	T	T	HCCH	√		√		√		
14	75.3	F	F	T	CCCC	88.0	T	T	N/A	HCCH	√		√		√		
15	172.3	T	T	T	HCCH	180.0	T	T	T	HCCH		√		√		√	
16	49.3	T	T	F	HCCH	68.0	T	T	T	HCCH	√		√		√		
17	112.3	N/A	N/A	T	CCCC	120.0	N/A	F	T	CCCC		√		√		√	
18	50.3	T	T	T	HCCH	60.0	T	T	T	HCCH	√		√		√		
19	85.5	T	T	T	HCCH	85.5	T	T	T	HCCH	√		√		√		
20	56.5	T	T	F	HCCH	68.0	T	T	F	HCCH		√		√		√	
21	81.5	N/A	F	T	CCCC	92.0	T	T	T	HCCH	√		√		√		
22	59.8	F	F	N/A	N/A	73.0	T	T	T	HCCH		√		√		√	
23	97.5	T	T	T	HCCH	97.5	T	T	T	HCCH	√		√		√		
24	82.3	T	T	N/A	HCCH	82.3	T	T	N/A	HCCH	√		√		√		
25	77.5	T	T	T	HCCH	77.5	T	T	T	HCCH	√		√		√		
26	82.8	T	T	F	HCCH	90.0	T	T	T	HCCH		√		√		√	
27	44.8	F	F	F	N/A	55.0	T	T	F	HCCH		√		√		√	
28	61.5	T	T	T	HCCH	61.5	T	T	T	HCCH	√		√		√		
29	58.3	T	T	F	HCCH	58.3	T	T	F	HCCH		√		√		√	
30	69.8	T	T	T	HCCH	69.8	T	T	T	HCCH	√		√		√		
31	75.8	T	T	N/A	HCCH	92.0	T	T	N/A	HCCH	√		√		√		
32	63.0	T	T	F	HCCH	63.0	T	T	F	HCCH		√		√		√	
33	86.3	T	T	F	HCCH	86.3	T	T	F	HCCH		√		√		√	
34	44.0	T	T	T	HCCH	44.0	T	T	T	HCCH	√		√		√		
35	80.0	T	T	T	HCCH	80.0	T	T	T	HCCH	√		√		√		
36	48.8	T	T	T	HCCH	48.8	T	T	T	HCCH	√		√		√		
37	90.5	T	T	N/A	HCCH	90.5	T	T	N/A	HCCH	√		√		√		
38	83.3	T	T	T	HCCH	83.3	T	T	T	HCCH	√		√		√		
39	44.5	T	T	T	N/A	60.0	T	T	F	HCCH	√		√		√		
40	100.8	T	T	T	HCCH	100.8	T	T	T	HCCH	√		√		√		
41	85.3	T	T	T	HCCH	85.3	T	T	T	HCCH	√		√		√		
42	85.5	T	T	F	HCCH	85.5	T	T	F	HCCH	√		√		√		
43	73.8	T	T	N/A	HCCH	73.8	T	T	N/A	HCCH	√		√		√		
44	76.3	T	T	T	HCCH	76.3	T	T	T	HCCH	√		√		√		
45	77.5	T	T	T	HCCH	88.0	T	T	T	HCCH	√		√		√		
46	74.0	T	T	T	HCCH	82.0	T	T	T	HCCH	√		√		√		
47	100.8	T	T	T	HCCH	112.0	T	T	T	HCCH	√		√		√		
48	85.8	T	N/A	T	HCCH/CCCC	85.8	T	N/A	T	HCCH/CCCC	√		√		√		
49	69.5	T	T	F	HCCH	69.5	T	T	F	HCCH		√		√		√	
50	65.8	T	T	T	HCCH	65.8	T	T	T	HCCH	√		√		√		
51	96.0	T	T	N/A	HCCH	110.0	F	F	T	CCCC	√		√		√		
52	69.0	T	F	F	N/A	80.0	T	T	F	HCCH		√		√		√	
53	65.8	T	T	T	HCCH	65.8	T	T	T	HCCH	√		√		√		
54	57.0	T	T	T	HCCH	68.0	T	T	T	HCCH/CCCC	√		√		√		
55	88.5	T	T	F	HCCH	102.0	T	T	T	HCCH	√		√		√		
56	135.0	T	T	N/A	HCCH/N/A	135.0	T	T	N/A	HCCH/N/A		√		√		√	
57	90.3	T	T	T	HCCH	90.3	T	T	T	HCCH	√		√		√		
58	56.5	T	T	F	HCCH	65.0	T	N/A	T	CCCC		√		√		√	
59	46.8	F	F	N/A	N/A	60.0	T	T	T	HCCH		√		√		√	
60	79.3	T	T	T	HCCH	93.0	T	T	T	HCCH	√		√		√		
average	79.0					84.4					number	42	18	41	17	45	13
											%	70	30	69	29	78	22
28 hop into CT or into BiRad in order to return to CT immediately				HCCH (HOOP works)	45				HCCH	53-55							
				CCCC	7				CCCC	4-6							
				N/A	8				N/A	1							
				HOOP breaks	13				HOOP breaks	5							
				HCCH breaks	8				HCCH breaks (or N/A)	3							

Table 8-8. Statistical of the individual trajectories of *sqRh* shown the hopping and decision time, the photoproduct distribution and the mode govern the reaction.

Traj	hopping time	Product formation follows ...			leading mode	decision time	Product formation follows ...			leading mode	Observed Product		Expected Product at decision time		Expected Product at hopping time		
		H-C11-C12-H at hopping time	HOOP at hopping time	C-C11-C12-C at hopping time			H-C11-C12-H at decision time	HOOP at decision time	C-C11-C12-C at decision time		Trans	Cis	Trans	Cis	Trans	Cis	
01	53.0	T	T	F	HCCH	63.0	T	T	F	HCCH	√	√	√	√	√	√	
02	50.0	T	N/A	T	CCCC	63.0	T	T	T	HCCH/CCCC	√	√	√	√	√	√	
03	58.5	T	F	T	CCCC	58.5	T	F	T	CCCC	√	√	√	√	√	√	
04	54.0	T	T	T	HCCH	54.0	T	T	T	HCCH	√	√	√	√	√	√	
05	59.0	T	T	F	HCCH	72.0	T	T	N/A	HCCH	√	√	√	√	√	√	
06	36.0	F	F	T	N/A	49.0	T	T	N/A	HCCH	√	√	√	√	√	√	
07	40.0	T	T	T	HCCH	55.0	T	T	N/A	HCCH	√	√	√	√	√	√	
08	52.5	T	T	T	HCCH	65.0	T	T	T	CCCC	√	√	√	√	√	√	
09	63.5	T	T	N/A	HCCH	78.0	T	F	T	CCCC	√	√	√	√	√	√	
10	50.8	T	T	T	HCCH	62.0	T	T	T	HCCH	√	√	√	√	√	√	
11	63.8	F	F	T	N/A	63.8	F	F	T	N/A	√	√	√	√	√	√	
12	81.8	T	T	F	HCCH	95.0	T	N/A	T	CCCC	√	√	√	√	√	√	
13	44.8	F	F	N/A	N/A	60.0	T	T	N/A	HCCH	√	√	√	√	√	√	
14	44.0	T	T	N/A	HCCH	55.0	T	T	N/A	HCCH	√	√	√	√	√	√	
15	62.5	F	F	T	N/A	62.5	F	F	T	N/A	√	√	√	√	√	√	
16	63.5	T	T	N/A	HCCH	75.0	T	F	T	CCCC	√	√	√	√	√	√	
17	103.0	T	T	F	HCCH	115.0	N/A	F	T	CCCC	√	√	√	√	√	√	
18	32.3	F	T	F	N/A	35.0	T	T	F	HCCH	√	√	√	√	√	√	
19	56.8	N/A	F	T	CCCC	70.0	T	T	T	HCCH	√	√	√	√	√	√	
20	66.3	F	F	T	N/A	66.3	F	F	T	N/A	√	√	√	√	√	√	
21	39.8	T	T	F	HCCH	52.0	T	T	T	HCCH	√	√	√	√	√	√	
22	83.5	T	T	N/A	HCCH	83.5	T	T	N/A	HCCH	√	√	√	√	√	√	
23	72.3	N/A	N/A	T	CCCC	87.0	T	T	T	HCCH	√	√	√	√	√	√	
24	60.8	T	T	T	HCCH	60.8	T	T	T	HCCH	√	√	√	√	√	√	
25	38.8	T	F	T	CCCC	75.0	T	F	T	CCCC	√	√	√	√	√	√	
26	51.3	T	T	T	HCCH	56.0	T	T	T	HCCH	√	√	√	√	√	√	
27	55.3	F	F	T	CCCC	65.0	T	T	T	HCCH	√	√	√	√	√	√	
28	48.0	T	T	T	HCCH	48.0	T	T	T	HCCH	√	√	√	√	√	√	
29	49.0	F	F	N/A	N/A	49.0	F	F	N/A	N/A	√	√	√	√	√	√	
30	48.8	T	T	T	HCCH	62.0	T	T	T	HCCH	√	√	√	√	√	√	
31	57.0	T	T	N/A	HCCH	57.0	T	T	N/A	HCCH	√	√	√	√	√	√	
32	43.8	T	T	N/A	HCCH	43.8	T	T	N/A	HCCH	√	√	√	√	√	√	
33	75.3	F	F	N/A	N/A	115.0	T	T	T	HCCH	√	√	√	√	√	√	
34	56.8	F	T	F	HCCH	70.0	T	T	N/A	HCCH	√	√	√	√	√	√	
35	26.5	F	F	T	CCCC	50.0	T	T	T	HCCH	√	√	√	√	√	√	
36	72.5	T	T	T	HCCH	83.0	T	T	T	HCCH	√	√	√	√	√	√	
37	62.5	T	T	F	HCCH	62.5	T	T	F	HCCH	√	√	√	√	√	√	
38	56.3	F	F	T	N/A	56.3	F	F	T	N/A	√	√	√	√	√	√	
39	74.3	T	F	T	CCCC	95.0	T	T	T	HCCH	√	√	√	√	√	√	
40	58.3	T	T	F	N/A	82.0	F	F	T	N/A	√	√	√	√	√	√	
41	107.3	T	T	F	HCCH	130.0	T	F	T	HCCH/CCCC	√	√	√	√	√	√	
42	60.8	T	F	T	CCCC	60.8	T	F	T	CCCC	√	√	√	√	√	√	
43	51.0	T	T	T	HCCH	51.0	T	T	T	HCCH	√	√	√	√	√	√	
44	37.5	T	T	T	HCCH	48.0	T	T	T	HCCH	√	√	√	√	√	√	
45	49.8	N/A	F	T	HCCH	50.0	T	T	T	HCCH	√	√	√	√	√	√	
46	73.5	T	T	N/A	HCCH	80.0	T	T	N/A	HCCH	√	√	√	√	√	√	
47	94.5	T	T	F	HCCH	94.5	T	T	F	HCCH	√	√	√	√	√	√	
48	60.5	N/A	T	T	HCCH	75.0	T	T	T	HCCH	√	√	√	√	√	√	
49	58.0	T	T	F	HCCH	58.0	T	T	F	HCCH	√	√	√	√	√	√	
50	62.5	T	T	T	HCCH	62.5	T	T	T	HCCH	√	√	√	√	√	√	
51	65.8	T	T	N/A	HCCH	65.8	T	T	N/A	HCCH	√	√	√	√	√	√	
52	81.8	T	T	T	HCCH	95.0	T	T	T	HCCH	√	√	√	√	√	√	
53	56.0	T	T	T	HCCH	68.0	T	T	T	HCCH	√	√	√	√	√	√	
54	69.3	F	F	T	N/A	69.3	F	F	T	N/A	√	√	√	√	√	√	
55	85.8	T	T	T	HCCH	85.8	T	T	T	HCCH	√	√	√	√	√	√	
56	45.8	T	T	T	HCCH	54.0	T	T	T	HCCH	√	√	√	√	√	√	
57	57.0	T	T	T	HCCH	70.0	N/A	N/A	T	CCCC	√	√	√	√	√	√	
58	45.3	T	T	T	HCCH	45.3	T	T	T	HCCH	√	√	√	√	√	√	
59	57.0	F	F	N/A	N/A	74.0	T	T	N/A	HCCH	√	√	√	√	√	√	
60	50.0	T	T	T	HCCH	50.0	T	T	T	HCCH	√	√	√	√	√	√	
average	58.9					67.6					number	41	19	37	21	37	20
		time shift from hopping to decision time = 8.7									%	68	32	64	36	65	35
36 hop into CT or into BiRad in order to return to CT immediately		HCCH (HOOP works)			39		HCCH (HOOP works)			44-46							
		CCCC			9		CCCC			7-9							
		N/A			12		N/A			7							
		HOOP breaks			19		HOOP breaks			16							
	HCCH breaks			15		HCCH breaks (or N/A)			9								

QY indicates that these random events lead to a 50/50 population distribution between trans and 11-cis.

Based on these findings we expect to find a reduced QY for pigments which decay to the GS on a time-scale below 60–65 fs for two reasons: a) HCCH/CCCC phase mismatch; b) an increase of random events in the GS. On the contrary, it would be intriguing to investigate the efficiency of slower isomerizer (with ES lifetimes around and beyond 100 fs). Rh has taught us that when the hydrogen out-of-plane mode *does not* acquire large momentum (which could be accomplished for example through weaker steric repulsion in the backbone or through H-bonds to nearby residues from the cavity), CCCC and HCCH are likely to be still in phase when the CI seam is reached, thus leading to higher QY.

9 The Siberian Hamster UV-light Cone Pigment: the Unusual Photochemistry and Photophysics of an Unprotonated Retinal Schiff-Base Chromophore

The Siberian hamster ultraviolet (SHUV) visual pigment has an unprotonated Schiff-base (SB) retinyl chromophore in the dark state, which becomes protonated after photoexcitation during the early stages of the photobleaching cycle. While the photochemical relaxation processes of the SHUV remain poorly understood, they are expected to show significant differences when compared to those of the protonated SB (PSB) chromophore in visual rhodopsin. We [187] have performed a preliminary study of the photophysical properties of the SHUV unprotonated SB (SHUV-USB), based on multiconfigurational and multireference perturbative methods within a hybrid quantum mechanics/molecular mechanics scheme. We have employed both multireference and time-dependent density functional theory techniques, showing that both methodologies predict a bright (Homo \rightarrow Lumo, HL) ionic excited state similar to the RPSB of rhodopsin, although its minimum has even bond-lengths in the central region of the retinyl polyene chain. Moreover, the wave function analysis of the excited-state manifold at the Franck–Condon region and at the S_1 minimum indicates that the skeletal relaxation initiated in the S_1 surface is likely to involve an adiabatic change of the wave function from HL to Homo² \rightarrow Lumo², (dHL). In this chapter, we explore the possible photoisomerization mechanisms, going beyond the characterization of the photophysical properties of the SHUV-USB pigment provided initially by Bonvicini et al. [187].

9.1 Introduction

Visual perception is one of the most fascinating and extensively studied natural light-induced processes, in which a phototransduction process occurs where radiative energy is converted into chemical energy (that is stored as steric strains after a phototriggered configurational change – photoisomerization – has occurred). This triggers a cascade of reactions, eventually resulting in an electric signal to the brain. As we elucidated in the previous chapter, the UV-sensitive pigments are different opsin prototype with respect to the widely studied visual rhodopsins, since they incorporate an *unprotonated* Schiff base (USB) linkage in the dark-state [32,35], while rhodopsins, the visual pigment of rod cells, embeds a protonated 11-*Cis*-Retinal chromophore, absorbing visible light ($\lambda_{\text{MAX}}=498\text{nm}$ in bovine Rh) and triggering an ultrafast 11-*Cis* \rightarrow all-trans photoisomerization as the primary photochemical event in vision (Figure 9-1).[260].

Unlike rhodopsins which were extensively studied, very few computational/experimental studies exist so far on the UV pigments, whose photoactivated mechanism is essential

unknown [34]. It is worth to further stress that a distinct aspect of UV-sensitive pigments, when compared to visual rhodopsin, is that the chromophore is bound to the protein by an USB linkage in the dark state [32,35]. Recently [32], the existence of multiple changes in the protonation state of the SB linkage during the photoactivation of SHUV has been confirmed, by means of time-Resolved spectroscopy (Figure 9-1). The dark-adapted state is deprotonated. An intermediate (all-trans protonated) analogous to the bathorhodopsin intermediate of Rh has been detected by spectroscopic fingerprints after 300 ns of the photoexcitation. This protonated batho-like intermediate of the SHUV pigment is equilibrates very quickly (ca. 7 ns) with a deprotonated blue-shifted intermediate (BSI). This observation suggests different phototransduction mechanism for SHUV from what happen in Rh, this mechanism depends on the occurrence of proton-transfer process during the early stages of photoactivation, while in bovine Rh, in fact, the protonated form of the SB is remaining up to the meta II state, i.e., up to large conformational changes of the transmembrane protein helices that transmit the signal to the cytoplasmatic surface [264].

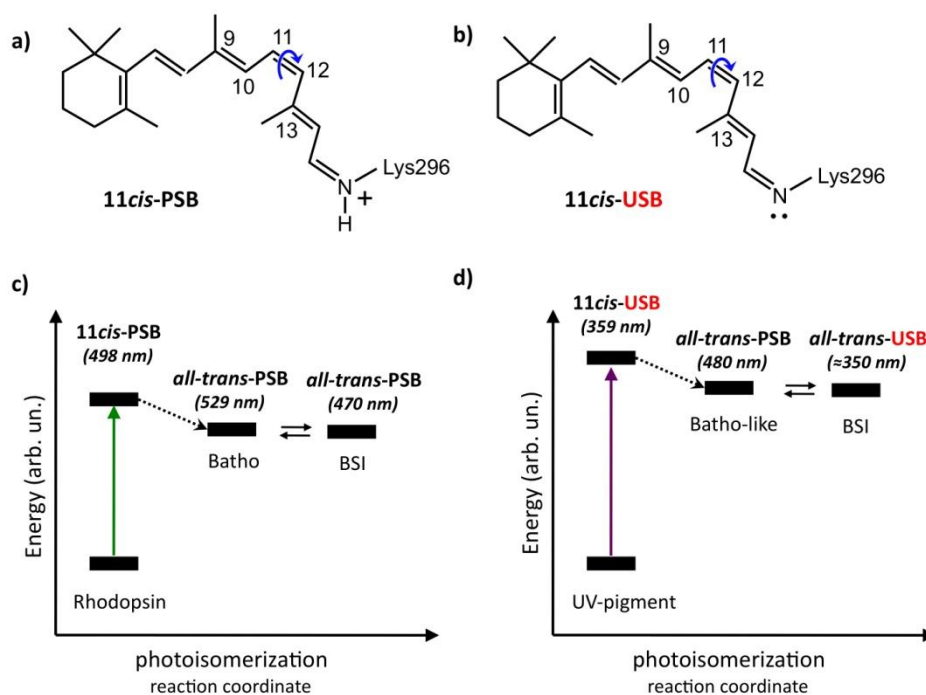


Figure 9-1. Schematic representation of the 11-Cis protonated (PSB) and unprotonated (USB) Schiff bases found in the dark state of (a) rhodopsin and (b) Siberian hamster UV pigment. Early photointermediates detected experimentally in (c) rhodopsin (batho and BSI) and (d) UV pigment (Batho-like and BSI) showing the preservation of the RPSB in rhodopsin and the multiple changes of the protonation state in the UV pigment. The photorhodopsin intermediate in rhodopsin is omitted for clarity. Absorption λ_{MAX} reported in parentheses are taken from Refs. [32,264]

An extensive network of hydrogen bonds and/or the presence of water molecules in the binding pocket seem to play an important role in controlling the protonation state of the Schiff base. Therefore, a better understanding of the environment local conditions,

determining the protonation state and, consequently, the photophysical properties of the retinal Schiff base chromophore, is mandatory for the study of this process [244-247].

In our preliminary study [187] we used a hybrid QM/MM computational approach to elucidate the photophysical properties of a specific UV-pigment belonging to the Siberian hamster (*Phodopus sungorus*). Multireference calculations were used in conjunction with time-dependent density functional calculations, addressing the ionic nature of the bright initially populated HL excited state (S_1), analogous to the rhodopsin case.

The main findings of this initial study may be summarized as follows:

- There is a good agreement between the experimental vertical excitation absorption ($\lambda_{\text{MAX}}=359\text{nm}$) and the computed CASPT2 one ($\lambda_{\text{MAX}}=340\text{nm}$), thus validating the computational QM/MM model employed for SHUV-USB;
- The bright HL state minimum doesn't establish bond-order inversion along the retinal polyene chain, suggesting a higher barrier for the photoisomerization path on the HL state. This finding contrasts with what is found in rhodopsin, where the photoisomerization path is barrierless and triggered by an HL excited state minimum featuring a full bond-order inverted structure (i.e., showing single $C_{11}-C_{12}$ bond).
- The photoinduced proton transfer from the E113 counterion to the USB chromophore is unlikely to occur either in the ground or in the excited states. In the FC point (ground state minimum), the deprotonated chromophore is more stable than the protonated by ca. 22.5 and 11.5 kcal/mol for ground and excited states, respectively. However, interestingly, the destabilization energies of the protonated chromophore are changed drastically in the region of HL minimum to ca 25.0 and 3.5 kcal for the ground and excited states, respectively.
- A conical intersection (CI) between the bright HL and the dark dHL excited states is established during the initial barrierless/ultrafast relaxation (skeletal relaxation) out of the FC region along the bright state HL, a feature analogous to what happens in neutral polyenes in which a real crossing between the HL state, with symmetry Bu, and dHL state, with symmetry Ag, exists during the initial relaxation pathway out of the FC region of the bright Bu state. This causes a swap in state ordering between the HL and dHL state that becomes S_1 at the HL minimum geometry.

We extended this work by addressing the following points:

- The presence of a S_1/S_2 excited-state surface crossing during the initial skeletal relaxation on the S_1 potential energy surface, suggests that the two-electron excitation associated with the covalent dHL S_2 state (at FC) may play an important role in the photoisomerization mechanism of SHUV-USB.
- The role played by singlet/triplet inter-system crossings in the photoisomerization mechanism.
- While our preliminary study rules out the possibility of a photoinduced proton transfer, it must be stressed that this conclusion was based on calculations performed on a model that did not include waters nearby the SB. On the other hand, time-Resolved absorbance measurements for UV-pigment show the existence of

various events of proton transfer in the early stages that characterize the phototransduction of the UV-pigment. Thus, while we cannot rule out the possibility that the photoisomerization may involve the unprotonated species up to the primary photoproduct formation (that gets then protonated afterwards in the ground state), a fast protonation of the Schiff base immediately following UV-photon absorption (photoinduced proton-transfer) represents also a distinct possibility. This would lead to the formation of a protonated Schiff base in the excited state, thus possibly favoring an efficient and fast isomerization of the chromophore as already observed and modeled in rhodopsin. One cannot exclude the role played by water molecules in promoting this process. Therefore, we explored the effects that nearby water molecules (like the ones found in Rh) may play in the photoinduced proton transfer and photoisomerization mechanism.

The following study was performed together with *Baptiste Demoulin*, a PhD candidate at Ens de Lyon, CNRS, Université Lyon, who investigated the triplet deactivation channels.

9.2 Computational Details

Two models are used in this study; we will refer to them as model I and model II. Model I and Model II were obtained employing homology modeling based on the bovine rhodopsin crystal structure resolved at 2.2 Å [260] after DFT-QM/MM and MM/MM structure optimizations, respectively[35]. Moreover, models I and II differ in the number of water molecules within the protein pocket, where in model II all the crystal waters of bovine rhodopsin are preserved (26 molecules), while model I has only two water molecules. Our preliminary tests on model I show that there are no significant effects on the vertical excitation when adding up more water molecules to the two ones originally considered. Another difference is related to the positions of E113 relative to the SB: E113 in model I is closer to the SB than in model II, where both the distances NC and NH (NC and NH stand for the distances between nitrogen of the SB and both the carboxyl carbon and hydrogen of E113, respectively) are 3.85/2.44 and 4.22/2.54 Å for NC and NH in models I and II, respectively(see **Figure 9-2**). For better comparison between Rh and SHUV, the Rh structure residue numbering is used, however the SHUV-pigment primary sequence has a 5-Residue shift in the N terminus (i.e., rhodopsin residue numbers are 5 greater than those of SHUV).

QM/MM calculations (geometry optimizations and subsequent single points) were carried out using three different HML schemes in COBRAMM [77] (we will call them as HML1, HML2 and HML3). In HML1, the high (H) layer includes only the full retinal chromophore, while the neighboring 9 atoms of the lysine residue ($-\text{CH}_2-\text{CH}_2-\text{CH}_2-$) and 10 atoms of the E113 counterion ($-\text{CH}_2-\text{CH}_2-\text{COOH}$) were included in the mobile medium (M) region, keeping frozen the rest of the system in the low (L) layer. The cut between the QM region and the MM region was located at the N-C ϵ (K296) bond where a hydrogen atom link scheme is used to attain the saturation at C ϵ [75] (**Figure 9-3a**). HML2 scheme is slightly modified from HML1 where one water molecule was added to the M layer (**Figure 9-3b**). The

third scheme HML3 was designed to be suitable for studying the photoinduced proton transfer, in which the QM region was extended to comprise, in addition to the retinal chromophore, the E113 counterion ($-\text{CH}_2-\text{COOH}$) as well as one water molecule. The medium layer was reduced in this scheme to include 9 atoms of lysine residue and only 3 atoms of E113, the rest of the protein kept fixed in the low layer (**Figure 9-3c**). In all schemes, the High layer was treated at the QM level of theory using Molcas 8.1 [92,265,266] as implemented in the COBRAM interface [77], while both M and L layers were treated at the MM level with the Amber99ffSB[95]. As a result, during geometry optimizations only the atoms in high and medium regions are free to move (following the gradient) while all the rest (belonging to the Low layer) are fixed at their starting geometry.

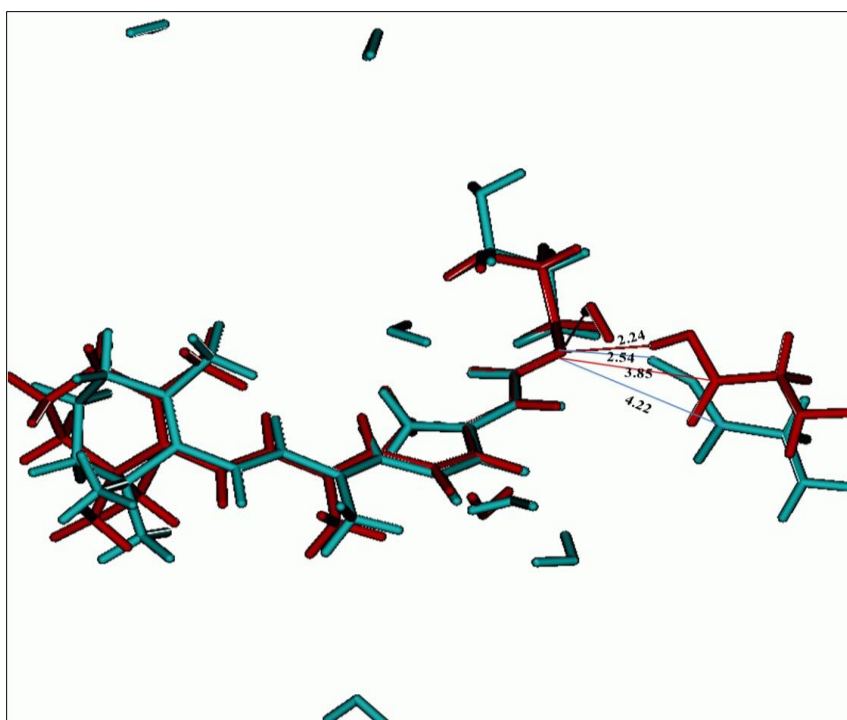


Figure 9-2: Superimposed of the initial geometries of model I (pale blue) and II (brown) showing the retinal chromophore, E113 and water molecules, only few water molecules of model I are shown. The distance values shown are in Å.

The 6-31G* basis set[183] was employed to carry out all calculations reported in this chapter. The ground-state geometries were optimized via a single-Root unconstrained optimization using the complete active space self-Consistent field (CASSCF) level of theory[54] while the geometries of any other state were obtained through state average CASSCF calculations (SA)-CASSCF, employing the minimum number of roots required to catch the desired configuration. The need to use different state averages is due to the fact that the position of the CASSCF root corresponding to a specific spectroscopic state is highly sensitive to the geometry. The second order perturbation correction (CASPT2) in the single-state (SS)[66] and multistate (MS)[67] flavors were used on top of the reference SAx-CASSCF wave functions (where x refers to the number of CASSCF states included) to calculate energies and vertical excitations. An imaginary level-shift of 0.2 au was used to decrease the influence of weakly interacting intruder states in the CASPT2 calculations[185].

The ionization potential electron affinity parameter was set to 0.0 au[186], in accordance with previous studies of retinal in gas-phase and its protein environment[24,187-189]. TDMs were calculated at the CASSCF level and were used to compute oscillator strengths, which were corrected using the CASPT2 transition energies. The CASSCF active space includes the entire π system of the chromophore, i.e., CASSCF(12,12), except for the calculations of the $n\pi^*$ states, where a CASSCF(14,13) was used.

The excited state photoisomerization profiles on the HL, dHL, the first triplet (T_1), and the second triplet (T_2) states were performed via relaxed scans along selected torsional coordinates with an increment of 10 degrees per step. The relaxed scans were carried out at the SAx-CASSCF(12,12)/6-31G* level thereby averaging over x roots. Energies at the optimized points along the relaxed scan were corrected by CASPT2 calculations.

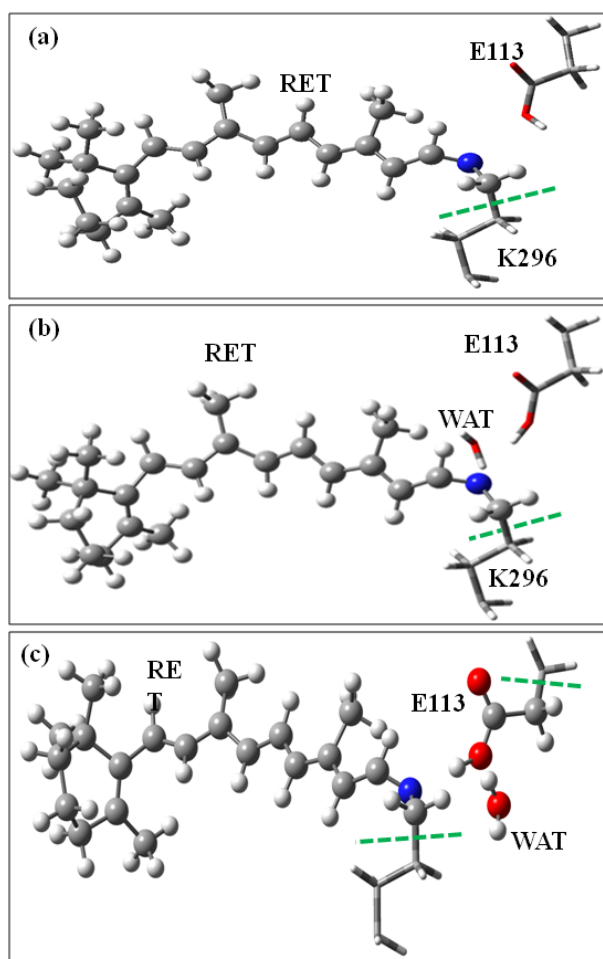


Figure 9-3. Schematic representation for high and medium layers for (a) HML1 (b) HML2 (c) HML2 schemes, the green dashed line show the cut between the H and M layers. The atoms in ball and stick are belonging to QM region while atoms represented in tube belong to medium layer. The low layer includes the rest of the protein and is not shown in the **Figures**.

9.3 Results and Discussion

9.3.1 Populations of Singlet and Triplet States

All the results reported in this section have been performed on Model I employing the HML1 scheme. We initially showed [187] a S_1/S_2 surface crossing between the HL bright and the dark dHL excited states where the dHL excitation is highly stabilized going from FC geometry to the HL minima (see **Figure 9-4**). Opposite to the situation at FC point, where HL is the first singlet excited state exists on S_1 and dHL corresponds to S_2 , HL becomes on S_2 at the HL minimum geometry, dHL getting lower (S_1) in energy. Moreover, the GS state minimum displays the classical single-double bond alternation common in the ground-state of a protonated Schiff's base while for the HL minimum, the inversion in single-double bonds is not shown, instead it displays an equalized bond lengths within the range 1.40 to 1.41 Å, especially for the central of the polyene chain (i.e. bonds between C_9 and C_{13}). This is not the case for rhodopsin where, the single and double bonds alternation shown in the ground state geometry is completely reversed in the HL minimum. Moreover, the charge transfer state remains the lowest excited state S_1 along the whole photoisomerization path, starting from the Frank–Condon region, passing through the relaxed HL minimum, till to the twisted conical intersection with the ground state [3]. In conclusion, due to higher energy of the HL state in the unprotonated Schiff base, and the absence of clear single bond characters of the C_{11} – C_{12} bond at the HL minimum, together with the fact that dHL crosses HL and gets lower in energy, the photoisomerization of the SHUV-USB on the HL PES is unlikely to occur and an efficient ultrafast HL→dHL internal conversion is expected. Moreover, at dHL minimum, the HL state (S_2) is further destabilized while dHL (S_1) is largely stabilized (by ~18.5 kcal/mol at SS–CASPT2/SA10–CASSCF) and becomes degenerate with the second triplet state (**Figure 9-4**). On the other hand, the $n\pi^*$ state is almost unperturbed by the skeletal deformations along the S_1 relaxation pathway and it remains well separated from the low lying excited state; consequently, one can exclude its role in the photoisomerization. However, other photochemical mechanisms exist and could be considered for the photoisomerization of the SHUV-USB, including (allowed or avoided) surface crossing among singlet excited-state surfaces or inter-system crossing between surfaces with different spin multiplicities. Unlike the HL minimum, the ES relaxation to dHL minimum is associated with double–single bond inversion in the conjugated system where the C_{11} – C_{12} (1.45 Å) displays a clear single bond and the C_{10} – C_{11} – C_{12} – C_{13} torsion angle is largely distorted (~ – 25°). As a consequence one should study the isomerization energy profile on the singlet dHL S_1 state by means of relaxed constrained scan around the C_{10} – C_{11} – C_{12} – C_{13} torsion angle with 10° incremental steps.

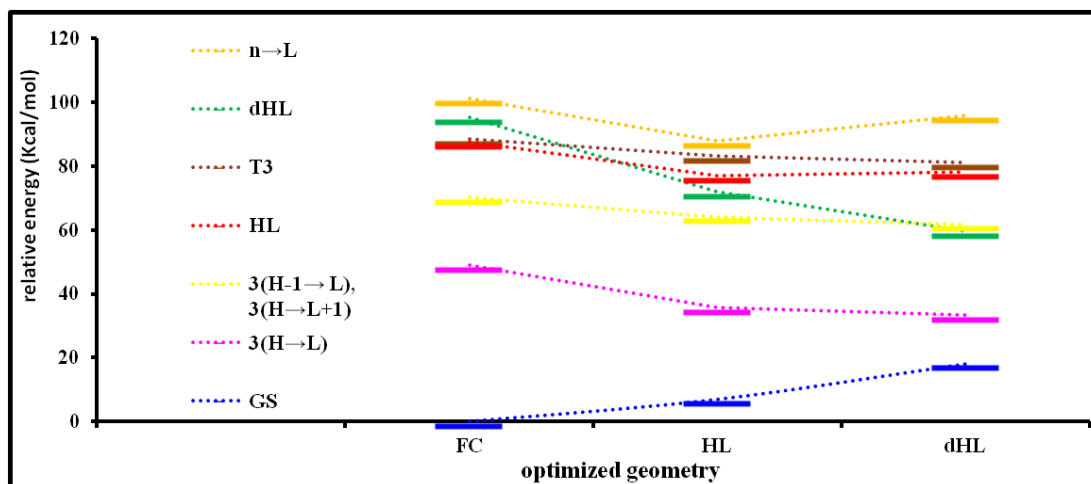


Figure 9-4. Evolution of energy levels of the low laying singlet and triplet excited states of the SHUV-USB along at FC, HL and dHL minima calculated at CASPT2/SA5-CASSCF(12,12)/6-31G* level, the active space was extended to (14,13) to locate the $n \rightarrow L$ state, the **Figure** modified from ref [187].

9.3.1.1 Isomerization Profile of the Singlet Doubly Excited State dHL

Initial bond relaxation from the FC to the dHL leads to an energy stabilization of ~ 36 kcal/mol for the covalent state (dHL). However, along the torsional coordinate around the $C_{11}-C_{12}$ bond, the dHL state shows an uphill potential with a barrier that increases gradually up to ~ 17.5 kcal/mol for a 90° tension. At this point, a large energy gap between GS and dHL still exists (~ 33 kcal/mol). Thus, the presence of a CI between S_0/S_1 is not established along the torsional coordinate; instead, a very high energy sloped CI was found associated with high distortion in the conjugated chain and the bond lengths. The characteristic wave functions and the positions of the other states (low laying singlet and triplet states) are depicted in **Figure 9-5**. The first triplet state T_1 (${}^3H \rightarrow L$) exhibits a barrier of ~ 15 kcal/mol to reach the 90° twisted point where a crossing with the S_0 exists. This suggests that intersystem crossing from T_1 to the GS is a barrier controlled process. Moreover, T_1 cannot be populated through the documented isomerization path, since it is always well separated from all the other higher excited states.

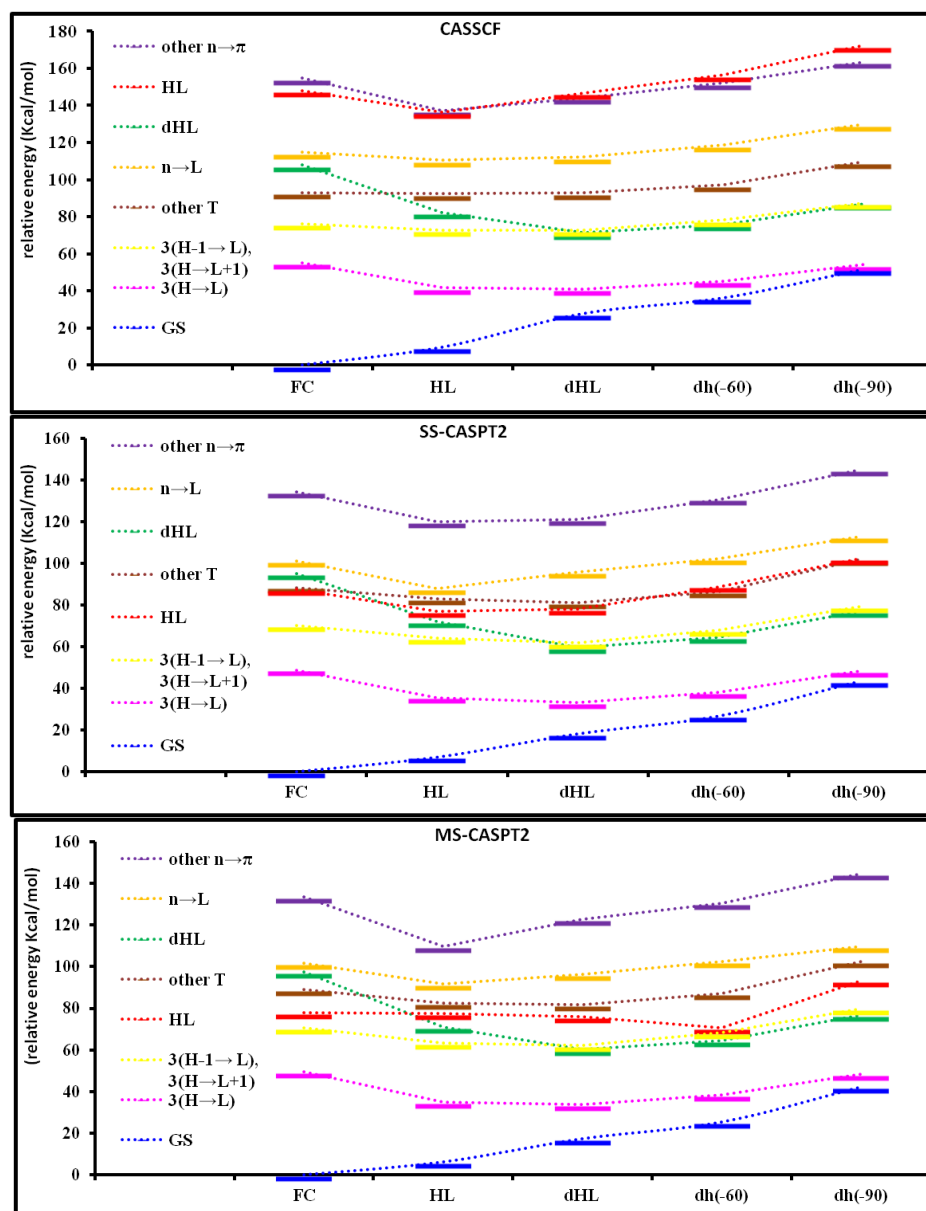


Figure 9-5. Evolution of the most important singlet and triplet states along the constrained scan on dHL state at different selected geometries (FC, dHL, dh(-60) and dh(-90)). The energies were calculated at SA10-CASSCF(12,12)/6-31G*, then corrected with SS-CASPT2 and MS-CASPT2. The active space was extended to (14,13) to locate the $n \rightarrow \pi$ transitions. For triplet state only SA5 was used, the order of the states at FC geometries is the same as they appear in the legend of each **Figure**.

9.3.1.2 Minima along the Triplet States T1 and T2

At the dHL relaxed geometry (dHL minimum, called dHL thereafter), both the dHL state and the second triplet state T2 (${}^3\text{H-1} \rightarrow \text{L}$, ${}^3\text{H} \rightarrow \text{L+1}$) are nearly degenerate (less than 1kcal/mol energy gap). Notably, this degeneracy is preserved along the whole scan (**Figure 9-5**). Assuming a not negligible spin-orbit coupling between these two states, the system could then hop from dHL to the triplet state T₂ along this path. Consequently, starting from the dHL geometry, we optimized the minimum on the T₂ state. On top of this minimum, we

then performed an optimization for the T_1 state, resulting in the T_1 structure shown in **Figure 9-6**. The geometrical parameters of those minima are shown in **Figure 9-7**. While dHL triggers an inversion of the bond lengths with respect to the ground state geometries, T_2 shows bond lengths closer to FC for the β -ionone side and even bond lengths at the Schiff base side. In particular, the elongation of ($C_{11}-C_{12}$) is reduced to 1.40 Å. T_1 on the contrary shows more even inverted pattern, especially for the $C_{11}-C_{12}$ bond (1.48 Å). This indicates that an isomerization is more likely to occur on this state than in the others. In the next section we will examine the possible isomerization paths on the T_1 and T_2 PESs

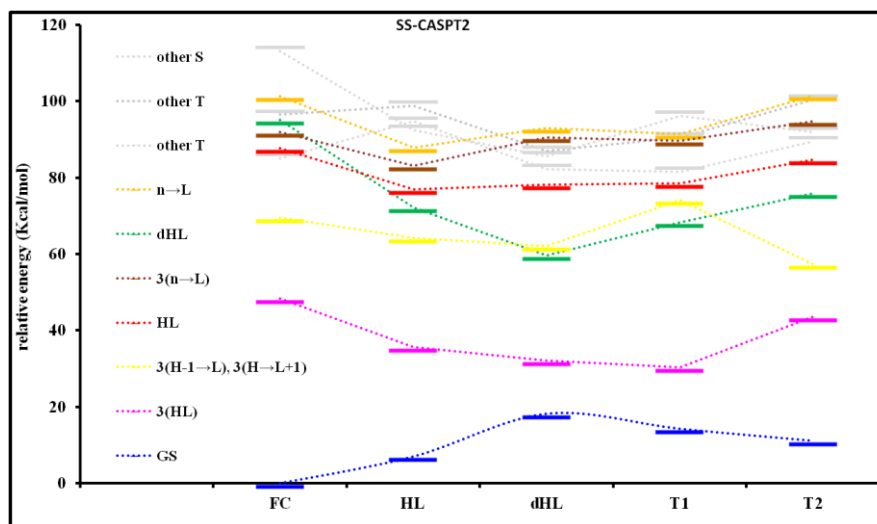


Figure 9-6. Evolution of the excited state manifold spectroscopic states on FC, HL, dHL, T_1 and T_2 regions. The energies were calculated at SS-CASPT2/CASSCF using in case singlet states SA10, SA8 and SA9 for FC and dHL, T_1 and T_2 minima, respectively, for the triplet states SA6 was used for T_1 minimum while SA5 was used for the other geometries. The active space was expanded to (14,13) to locate the $n \rightarrow \pi$ transitions. The order of the states at FC geometry is the same as they appear in the legend of the **Figure**.

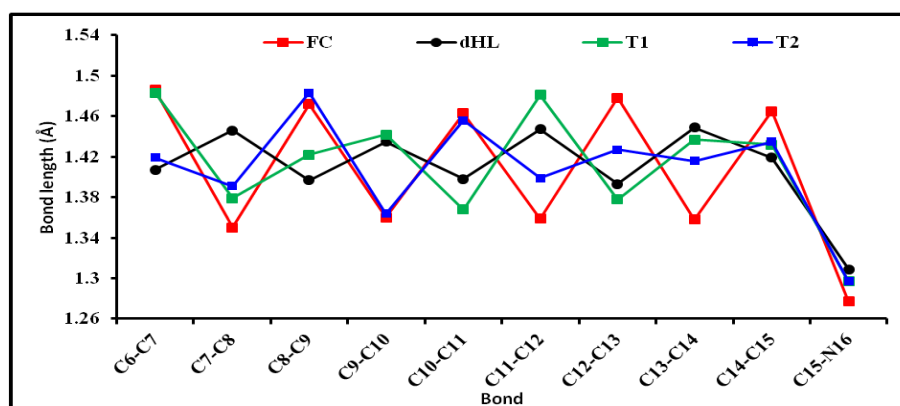


Figure 9-7. A comparison among the geometrical parameters of FC, dHL, T_1 and T_2 optimized geometries.

9.3.1.3 Spin Orbital coupling

As depicted in **Figure 9-6**, in the FC region, the bright excited state is S_1 , with two other triplet states (T_3 and T_4) close to it (1-5kcal/mol energy gaps). The spin orbit coupling (SOC) between S_1 and these two states is 0.17 and 2.41 cm^{-1} for T_3 and T_4 , respectively. While the latter is quite large, a singlet/triplet transition is unlikely to occur on this region, given its unstable nature. On the other hand, at dHL minimum, the SOC of the degenerate singlet dHL and the triplet T_2 states is very small (0.04 cm^{-1}). Therefore, the $S_1 \rightarrow T_2$ ISC, if occurring at this point, is expected to involve a slow process ($>ns$). Assuming this process occurs and T_2 gets populated, relaxation on the T_2 state leads to a minimum where the degeneracy with the dHL state is lost. More precisely, T_2 becomes well separated from any other singlet states (**Figure 9-6**). At this minimum, SOC calculations between T_2 and dHL (CASSCF S_1), $n \rightarrow L$ (CASSCF S_3) and HL (CASSCF S_7) lead to the values of 0.06, 9.59 and 3.20 cm^{-1} , respectively. Despite the large SOC values found in the latter two cases, the big energy gap between the singlet and triplet states makes back intersystem crossing very unlikely. Assuming a possible $T_2 \rightarrow T_1$ transition, relaxation on the T_1 state leads to a minimum (**T1** structure) where a large energy gap exists between T_1 and S_0 (ca. 16 kcal/mol). The SOC computed at this point between T_1 and GS (S_0), HL (CASSCF S_7), dHL (CASSCF S_1) and $n \rightarrow L$ (CASSCF S_3) is 0.32, 0.44, 15.20 and 0.29 cm^{-1} , respectively. Here again, even if the values of SOC may be high, the states are well separated in energy and ISCs are unlikely (see **Figure 9-6**).

9.3.1.4 Isomerization Energy Profiles of T_2 and T_1 Triplet States.

The $C_{11}-C_{12}$ bond length is 1.40 Å at the T_2 minimum (see **Figure 9-6**), so one should expect a PES that displays a high energy barrier for photoisomerization around this bond, as indeed it is shown in **Figure 9-8**, that is obtained by means of a constrained relaxed scan on the T_2 PES. More generally, there is a substantial barrier along any torsional coordinate (47.7 kcal/mol), thereby inhibiting an ultrafast/efficient isomerization (and decay) through this channel. The wave functions of all points along the scan display the same characters for both T_1 and T_2 except at 90° , where T_2 appears to be a mix between $^3H-1 \rightarrow L$ and $^3H \rightarrow L$, rather than between $^3H-1 \rightarrow L$ and $^3H \rightarrow L+1$, while T_1 has mainly $^3H \rightarrow L$ configuration instead of the mixed $^3H \rightarrow L$, $^3H \rightarrow L+1$ (**Table 9-2**). The different wave function characters at 90° may explain the high energies associated with this point. The split between T_1 and T_2 is big (13-15 kcal/mol) and remains nearly constant along the scan until 80° then increases abruptly to 30 kcal/mol at 90° , moreover the CI is located at high energy and associated with other geometrical deformations; therefore, the isomerization around $C_{11}-C_{12}$ bond is not efficient and fast. Since both C_8-C_9 and $C_{10}-C_{11}$ adopt a clear single bond (1.48 and 1.46 Å) character on T_2 minimum, we have also studied the possible isomerization around these torsional coordinates. The profiles obtained by scanning around those two torsional coordinates are depicted in **Figure 9-9** and **Figure 9-10** for C_8-C_9 and $C_{10}-C_{11}$, respectively. However, for both bonds the barrier height increases; a high lying sloped CI is found in both cases and appears earlier for scan around $C_{10}-C_{11}$. The higher energy barrier for rotation around C_8-C_9 and $C_{10}-C_{11}$ rule them out as a possible efficient deactivation path.

In contrast to T_2 minimum, T_1 displays more twisted geometry (-36° for $C_{10}-C_{11}-C_{12}-C_{13}$) and elongated $C_{11}-C_{12}$ (1.48 \AA); as a consequence the torsion around $C_{11}-C_{12}$ appears to be preferred. Indeed, along the torsional coordinate ($C_{11}-C_{12}$), the T_1 state shows only a small barrier (6 kcal/mol), (see **Figure 9-11**). On the other hand, the gap between T_1 and T_2 is very huge (44-53 kcal/mol) and increases gradually along the scan. A crossing with the ground-state is encountered for the scan at 90° ; consequently, this path could be a preferable decay channel to the GS if T_1 may be accessed from the higher initially populated excited states. However, this seems to be unlikely since the large energy separation always found between T_1 and all the other higher lying excited states, both in the singlet and triplet manifold (see **Figure 9-12**).

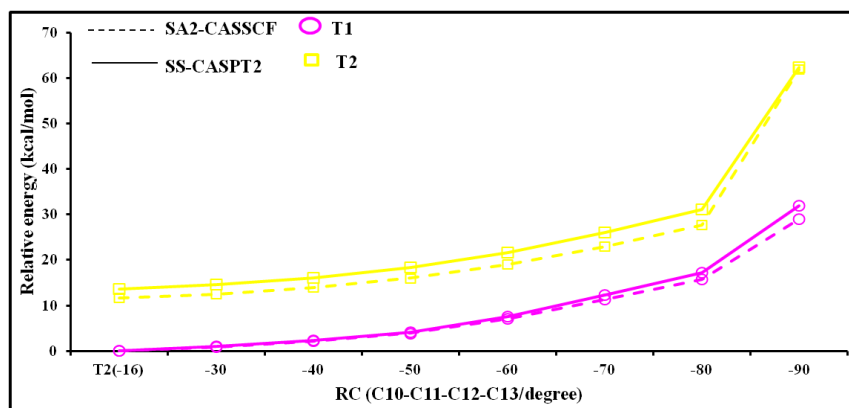


Figure 9-8. SA2-CASSCF and SS-CASPT2 energy profiles along the torsion angle $C_{10}-C_{11}-C_{12}-C_{13}$ obtained from relaxed scan of the second triplet state T_2 .

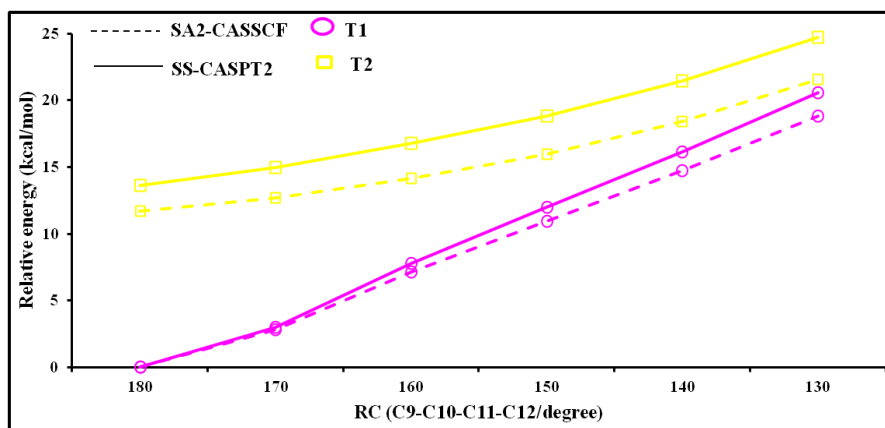


Figure 9-9. SA2-CASSCF and SS-CASPT2 energy profiles along the torsion angle ($C_9-C_{10}-C_{11}-C_{12}$) obtained from relaxed scan of the second triplet state T_2 .

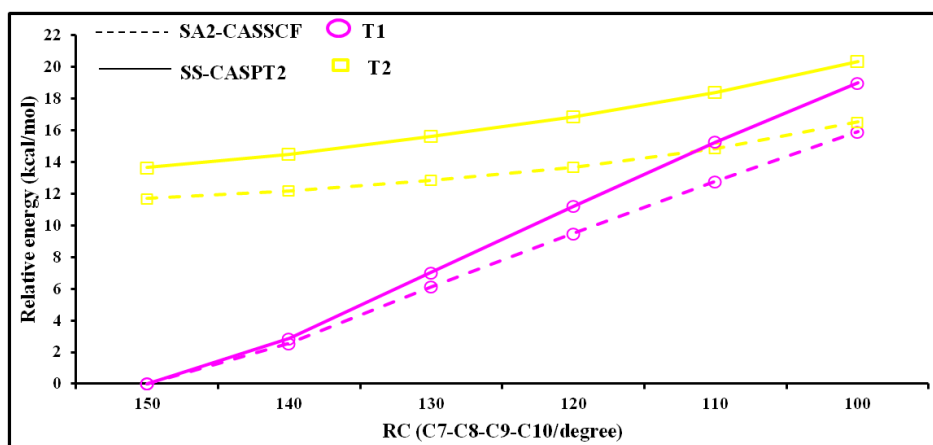


Figure 9-10. SA2-CASSCF and SS-CASPT2 energy profiles along the torsion angle ($C_7-C_8-C_9-C_{10}$) obtained from relaxed scan of the second triplet state T_2 .

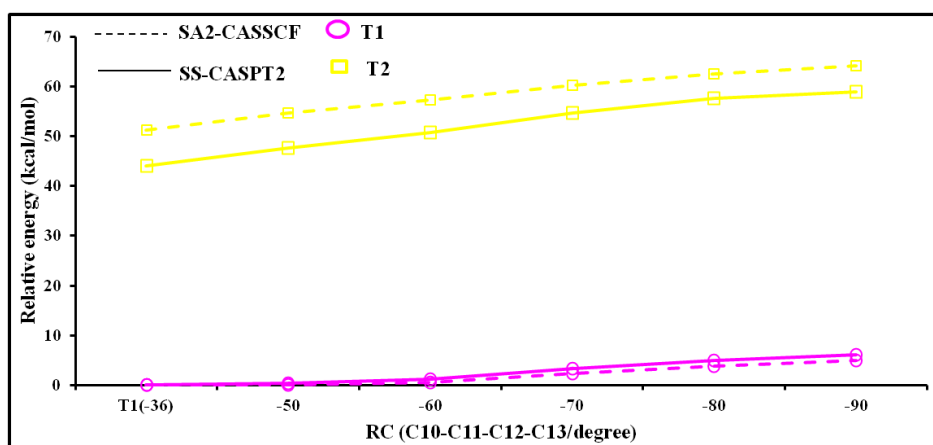


Figure 9-11. SA2-CASSCF and SS-CASPT2 energy profiles along the torsion angle ($C_{10}-C_{11}-C_{12}-C_{13}$) obtained from relaxed scan of the first triplet state T_1 .

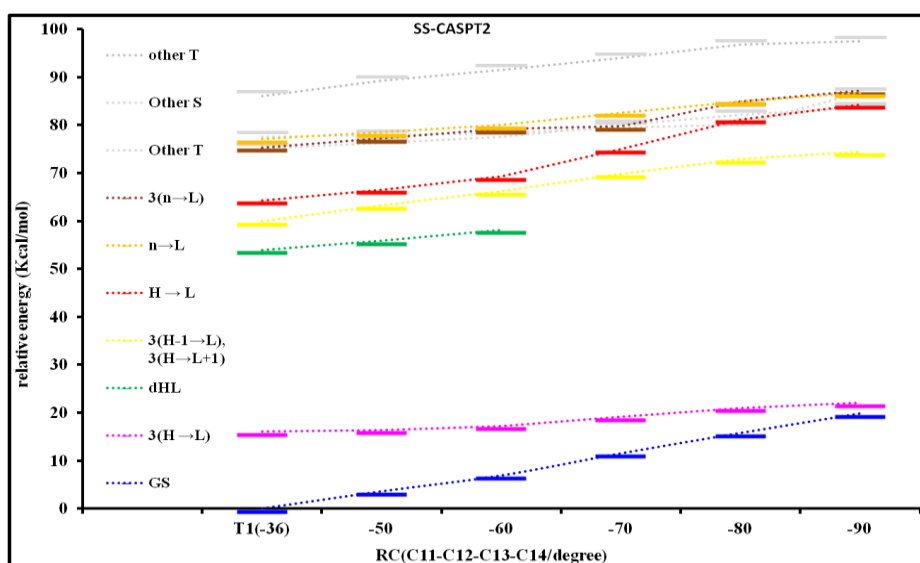


Figure 9-12. Evolution of the excited state manifold spectroscopic states along the T_1 scan. The energies were calculated at SS-CASPT2/CASSCF using in case singlet states SA8 and SA5 singlet and triplet states, respectively. The active space was expanded to (14,13) to locate the $n \rightarrow \pi$ transitions. The order of the states at $T_1(-36)$ geometry is the same as they appear in the legend of the Figure.

Table 9-1. The characteristic wave functions and their weights along the constrained scan on T₁ and T₂ PESs around C₁₀-C₁₁-C₁₂-C₁₃ torsion angle.

dh	Wave functions (weight) along T1		Wave functions (weight) along T2	
	T ₁	T ₂	T ₁	T ₂
-16			³ H→L (50), ³ H-1→L+1 (14)	³ H-1→L (33), ³ H→L+1 (30)
-30			³ H→L (50), ³ H-1→L+1 (14)	³ H-1→L (33), ³ H→L+1 (31)
-36/-40	³ H→L (69)	³ H-1→L (31), ³ H→L+1 (23)	³ H→L (50), ³ H-1→L+1 (14)	³ H-1→L (33), ³ H→L+1 (31)
-50	³ H→L (69)	³ H-1→L (30), ³ H→L+1 (21)	³ H→L (50), ³ H-1→L+1 (14)	³ H-1→L (33), ³ H→L+1 (31)
-60	³ H→L (70)	³ H-1→L (30), ³ H→L+1 (17)	³ H→L (49), ³ H-1→L+1 (14)	³ H-1→L (32), ³ H→L+1 (31)
-70	³ H→L (70)	³ H-1→L (31), ³ H→L+1 (13), ³ H→L, L+1 (12)	³ H→L (48), ³ H-1→L+1 (13)	³ H-1→L (31), ³ H→L+1 (30)
-80	³ H→L (70)	³ H-1→L (32), ³ H→L+1 (17)	³ H→L (48), ³ H-1→L+1 (12)	³ H-1→L (30), ³ H→L+1 (30)
-90	³ H→L (70)	³ H-1→L (35), ³ H→L+1 (22)	³ H→L (64)	³ H-1→L (36), ³ H→L, L+1 (27)

9.3.2 Photoinduced Proton Transfer (a comparison between models I & II)

Model I was build using a homology modeling[35] based on the bovine rhodopsin crystal structure resolved at 2.2 Å including the crystal water molecules[260]. However, because a better agreement between the experimental and calculated vertical excitation was found employing a model without water molecules H-bonded to the SB, a UV-pigment model without water molecules in contact with the SB was preferentially selected [35]. On the other hand, in rhodopsin two water molecules are existing in the binding pocket, one of them stabilizing (through H-bonds) the negatively charged counterion E113, also playing a role in the stabilization of the protonated form of the retinal chromophore [35,267,268]. Moreover, equilibrium between the protonated and unprotonated retinal chromophore was established in the photocycle of SHUV pigments by means of time-Resolved absorbance measurements [32]. Furthermore, the coexistence of the two forms was verified by UV-vis spectrum for the F86Y mutant of mouse UV pigment [269]. Therefore, one cannot rule out the possibility of a proton-transfer in the early stages of the photoisomerization process. In this respect, one may expect an important role played by water molecules in promoting a photoinduced proton transfer in SHUV. To inspect this assumption, we tested several positions for a water molecule nearby the Schiff base and the protonated counterion E113. Different orientations for both the water and the carboxyl group of E113, representing different H-bonding network, were used as starting geometries. The initial geometries were optimized in two steps using HML2 and HML2 schemes, respectively. The starting geometries as well as the optimized ones by HML2 and HML3 schemes are shown in **Figure 9-13**.

Table 9-2 reports a comparative analysis for the different structures of model II in terms of the absolute QM/MM energies as well as the vertical absorption spectra. As shown in **Table 9-2**, a comparison among the different geometries reveals that the calculated absorption maximum for model II_D (346 nm) is in good agreement with the reported experimental value (359 nm) [35,187]. Model II_A does also show a reasonable agreement (340 nm); in both models (II_A and II_D) the water molecules are oriented in a way easily to stabilize the carboxyl residue upon possible proton transfer to the Schiff base. Thermodynamically, Model II_D (hereafter we will refer to it as model II) is the most stable one, and has suitable orientation for proton transfer; we have selected this model to study the proton transfer process in comparison with model I. Therefore we modified model I by putting one water molecule in a similar way as in model II. The resulting model shows vertical excitation which is blue shifted by 17 nm from the previous reported results for the same model [35,187]. Both models display very similar ground state geometries (see **Table 9-3**). The only difference is related to the positions of the E113 and the water molecule in the active site (**Figure 9-13**): in model II the water molecule is much closer to E113; moreover, E113 is far away from the SB in model I than in model II. As consequence, the lone pair of the SB is more stabilized in model II than in model I by the proton of the carboxyl group of E113, which accounts for the blue shift shown in model I if we consider that the bright HL state has a partial CT character, i.e. the nitrogen holds more electron density in the HL state.

Table 9-2. QM/MM absolute energies and vertical excitations for the different structures of model II.

	relative QM/MM total energy (kcal/mol)	λ_{HL} (nm)	λ_{dHL} (nm)	ΔE_{HL} (eV)	ΔE_{dHL} (eV)
SA5-CASSCF					
II_A	2.2	201	261	6.16	4.75
II_B	5.1	198	256	6.27	4.84
II_C	7.5	198	256	6.26	4.84
II_D	0.0	204	264	6.09	4.70
SS-CASPT2					
II_A	2.9	340	302	3.64	4.10
II_B	6.0	334	295	3.71	4.20
II_C	8.3	335	296	3.70	4.19
II_D	0.0	346	306	3.59	4.05
MS-5-CASPT2					
II_A	3.1	361	279	3.43	4.44
II_B	7.8	355	277	3.49	4.48
II_C	8.7	358	278	3.47	4.45
II_D	0.0	371	283	3.34	4.37

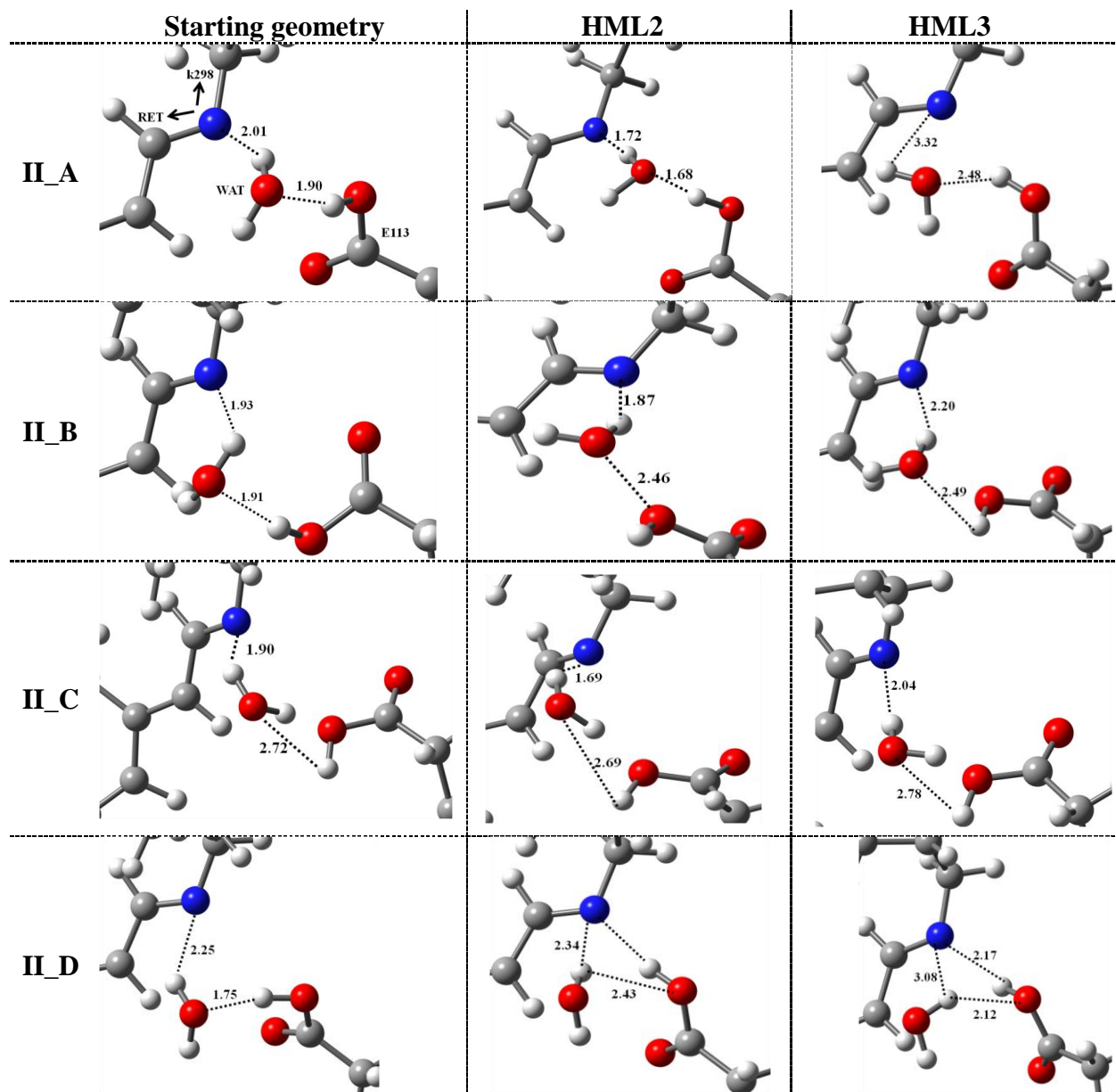


Figure 9-13. The active sites of different starting geometries of model II (left column) and optimized geometries employing HML2 (medal column) and HML3 (left column) schemes.

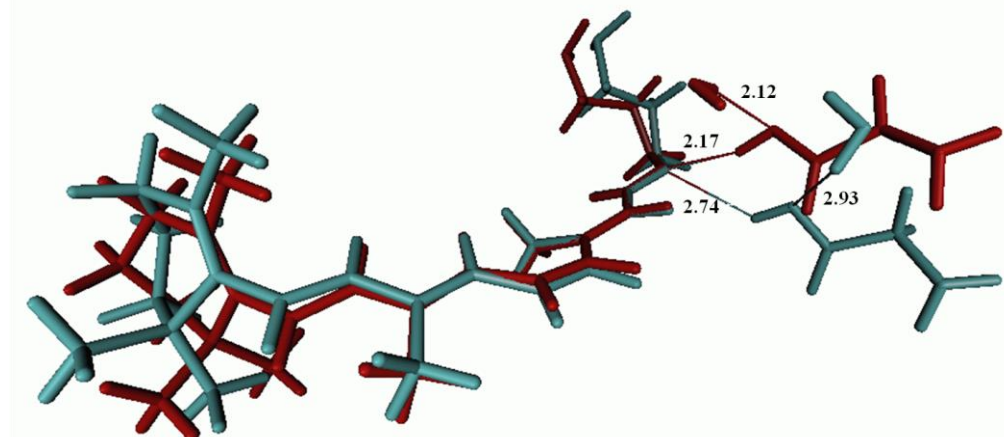


Figure 9-14. Superimposed of the ground state geometries of model I (pale blue) and II (brown), the distance values shown are in Å.

9.3.2.1 Thermodynamics of Photoinduced Proton Transfer Process

To investigate the possibility of a proton transfer process, we used the HML3 scheme to compute the absolute energies for both unprotonated (SHUV-USB) [RET + WAT + E113] and the protonated (SHUV-PSB) [RET(+H)⁺ + WAT + E113(-H)⁻] systems of each model at GS, HL and dHL minima. The energy profiles comparing the HL and dHL excited-state relaxation pathways calculated at SS-CASPT2/CASSCF and MS-CASPT2 levels for SHUV-USB and SHUV-PSB are shown in **Figure 9-14**. **Table 9-4** compares the relative stability calculated at the CASPT2/CASSCF level for each state of both SHUV-USB and SHUV-PSB at specific relaxed geometries, thus accessing the thermodynamical viability of the proton transfer path ($E_{\text{SHUV-PSB}} - E_{\text{SHUV-USB}}$). Both models show that the proton transfer from the E113 to the N atom of the USB in the UV-pigment ground state is an unflavored process (by +18.2 and 8.7 kcal/mol for model I and II, respectively). The destabilization energy associated with proton transfer in model I is consistent with the recently report value [187]. The huge energy difference suggests that the SHUV-USB is very stable in the ground state and the proton transfer is unlikely to occur at room temperature. As the chromophore becomes protonated, its absorption maximum is shifted to longer wavelength (only the USB visual pigments absorb in the UV; all the other visual pigments are protonated and absorb in the visible). Experimentally, the SHUV-USB absorbs in the UV (at 359 nm) while the SHUV-PSB absorbs in visible violet (at 425 nm) [32]; the corresponding calculated values are 323/395 nm and 346/359 nm at the CASPT2/CASSCF level for model I and II, respectively. Model I underestimates the experimental values with ~30 nm off for both SHUV-USB and SHUV-PSB; on the other hand, model II well predict the experimental value for SHUV-USB within only 13 nm, while it under estimates the corresponding experimental value of SHUV-PSB by ~ 60 nm, the reason behind that being the high mixing between the double excited and charge transfer states shown by the S_1 and S_2 CASSCF wave function. Both S_1 and S_2 display some charge transfer characters with an oscillator strength values of 0.27 and 0.65 and wave function characters H→L(21)/dH→L(17) and H→L(39)/dHL(16), for S_1 and S_2 , respectively, (the values in brackets give the corresponding weight). Moreover, the transition assigned as dHL shows $\lambda_{\text{MAX}}=410$ nm. On the other, the use of a multistate MS-CASPT2 treatment gives an overestimated value for H→L ($\lambda_{\text{MAX}}=473$ nm).

At the FC region, the SHUV-USB is found to be only slightly more stable than the RPSB in the HL excited state, with stabilization energy of 2.0 and 5.6 kcal/mol for model I and II, respectively. While the dHL excited state is destabilized slightly by protonation (3 kcal/mol) in case of model I, model II on the other hand shows a big stabilization for the SHUV-PSB by ca. 15 kcal/mol, this large value again is due to the mixed wave function observed with the HL state. It is worth noting that in the HL excited state the destabilization of the SHUV-PSB in the excited state (HL) decreases compared to the ground state decreases. This is consistent with the fact that HL involves an intramolecular charge transfer along the conjugated π system from SB to the β -ionone side: as a result, the SB nitrogen becomes more basic and can better accept proton compared to the covalent ground and dHL states. Since SHUV-USB is only slightly more stable than SHUV-PSB in the FC region of the bright HL state, this

suggests that a photoinduced proton transfer may actually occur when the systems relax on their respective excited state minima. This hypothesis is investigated below.

Once the systems have been relaxed to the HL minima, the relative stability of all states is changed abruptly and, most remarkably, the relative stability of the two (protonated vs unprotonated) forms swaps (see **Table 9-4**), with the HL minimum of the RPSB becoming more stable than the HL minimum of the USB for both model I and II (-1.5 and -2.7 kcal/mol, respectively). Notably, this suggests that an exothermic proton-transfer may actually occur already in the bright HL excited state. [32,269]. Another very interesting result that is shown by model II is that the HL excited-state minimum of the protonated SHUV-PSB form is the most stable minimum on the S_1 state (e.g., more stable than the S_1 (dHL) energy minimum (dHL minimum) of the unprotonated SHUV-USB form), further supporting the possibility of a proton transfer in the S_1 excited state. This S_1 process would then generate the protonated Schiff base form from the unprotonated one. Assuming this process happens in the excited S_1 state, we computed the photoisomerization profile for model II SHUV-PSB by means of relaxed scans in the CT (HL) S_1 state for rotation around the central C_{11} - C_{12} bond (**Figure 9-15**).

Table 9-3. The geometrical parameters of the optimized minima.

Model	model I								model II							
	Unprotonated				protonated				unprotonated				protonated			
	GS (11cis)	HL	dHL	GS (Alltrans)												
C5-C6	1.354	1.369	1.456	1.354	1.355	1.363	1.461	1.355	1.353	1.358	1.355	1.352	1.353	1.358	1.354	1.352
C6-C7	1.488	1.453	1.386	1.485	1.489	1.466	1.387	1.485	1.495	1.477	1.486	1.486	1.496	1.478	1.487	1.485
C7-C8	1.351	1.380	1.441	1.347	1.354	1.374	1.442	1.350	1.349	1.369	1.425	1.341	1.350	1.385	1.415	1.342
C8-C9	1.475	1.423	1.406	1.461	1.477	1.432	1.410	1.464	1.475	1.430	1.392	1.455	1.473	1.420	1.396	1.454
C9-C10	1.362	1.408	1.429	1.356	1.364	1.405	1.432	1.360	1.360	1.406	1.456	1.356	1.365	1.417	1.455	1.357
C10-C11	1.467	1.404	1.397	1.449	1.467	1.408	1.398	1.449	1.467	1.395	1.396	1.438	1.455	1.407	1.382	1.436
C11-C12	1.360	1.408	1.449	1.354	1.365	1.419	1.453	1.357	1.359	1.421	1.442	1.353	1.368	1.417	1.456	1.354
C12-C13	1.478	1.415	1.393	1.463	1.473	1.413	1.393	1.465	1.479	1.405	1.398	1.459	1.460	1.418	1.376	1.453
C13-C14	1.359	1.400	1.438	1.359	1.368	1.434	1.435	1.366	1.362	1.428	1.463	1.359	1.377	1.429	1.471	1.363
C14-C15	1.467	1.431	1.426	1.477	1.446	1.392	1.421	1.449	1.460	1.400	1.401	1.457	1.425	1.396	1.386	1.432
C15-N	1.280	1.299	1.305	1.278	1.292	1.360	1.305	1.297	1.287	1.332	1.330	1.287	1.293	1.352	1.327	1.296
N-H	2.737	2.668	2.681	2.753	1.027	1.005	1.026	1.004	2.169	2.002	2.136	2.014	1.047	1.019	1.039	1.028
C5-C6-C7-C8	-62	-44	-20	-59	-60	-50	-19	-55	-62	-56	-63	-63	-67	-59	-66	-63
C6-C7-C8-C9	-177	-177	173	-179	-178	-178	172	-179	178	179	176	-178	177	178	175	-179
C7-C8-C9-C10	-180	167	159	-176	180	171	159	-177	177	168	173	174	177	170	175	174
C8-C9-C10-C11	178	176	177	179	179	177	178	-179	179	178	175	179	178	177	171	179
C9-C10-C11-C12	173	174	169	-177	174	174	169	180	161	168	170	169	168	167	174	169
C10-C11-C12-C13	-9	-9	-9	172	-7	-7	-7	-179	-7	-7	-7	163	-6	-6	-6	162
C11-C12-C13-C14	159	161	162	178	163	164	166	171	161	164	165	175	161	163	165	176
C12-C13-C14-C15	175	176	177	169	-180	-174	-177	-180	-176	-176	-173	173	-175	-174	-169	170
C13-C14-C15-N	179	178	177	161	-177	-178	180	167	176	176	177	-166	174	180	176	-167
H-C11-C12-H	-2	-12	-21	-180	-2	-10	-17	-180	-3	-14	-17	175	-4	-12	-19	175

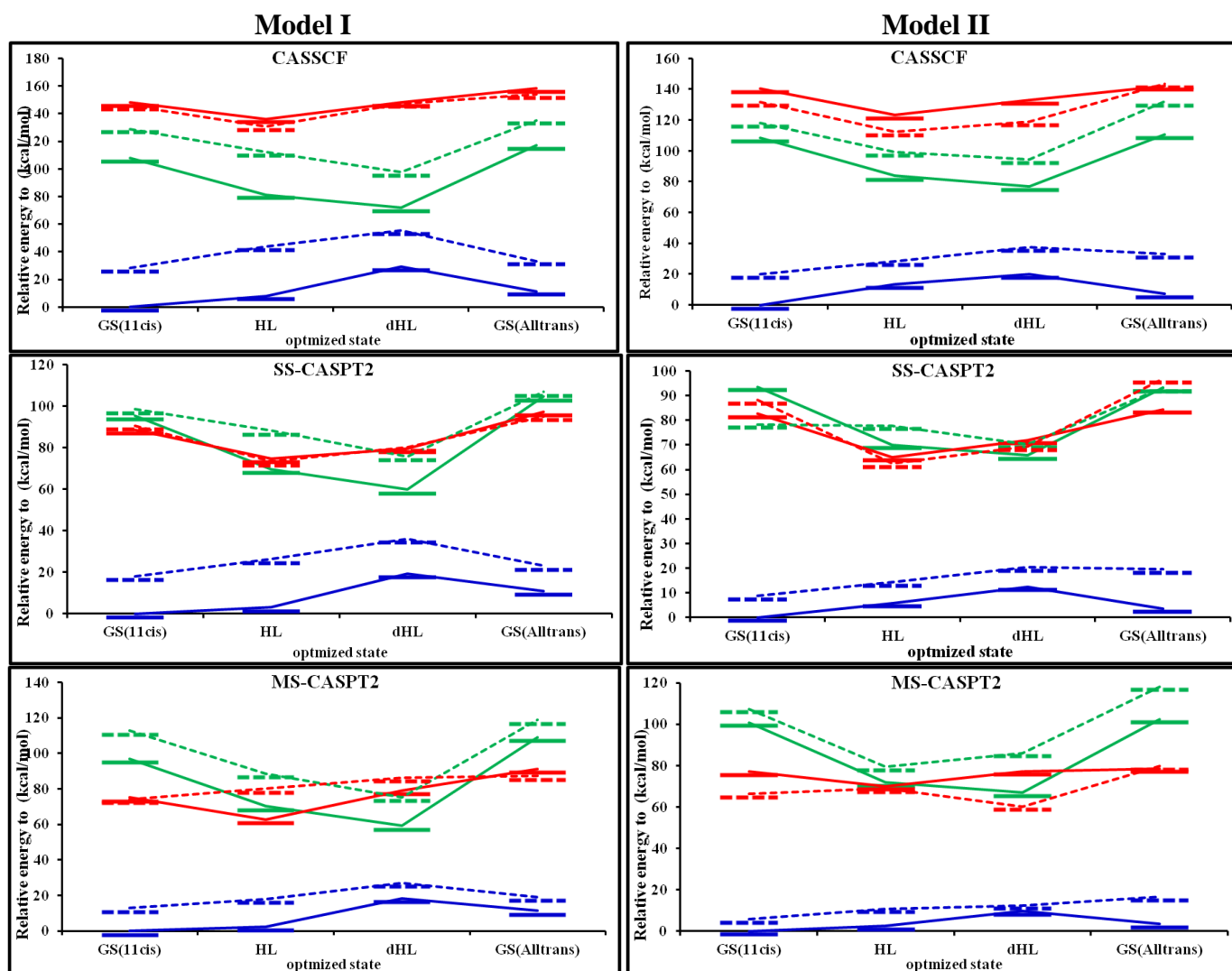


Figure 9-15. CASSCF, SS-CASPT2 and MS-CASPT2 (SA₈ and SA₅ were used for model I and II, respectively) energy profiles comparing the GS, HL, and dHL states (shown in blue, red and green colours, respectively) of SHUV-PSB (dotted lines) and SHUV-USB (solid lines) species at different minima for models I and II. The dihedral angle (C₁₀-C₁₁-C₁₂-C₁₃) was frozen during the optimization of HL and dHL to the values of their ground state minima (see **Table 9-3**).

Table 9-4. The relative stability of each state calculated at CASPT2/CASSCF, SA₈ and SA₅ were used for model I and II, respectively.

Model	I			II		
	GS	HL	dHL	GS	HL	dHL
Minimum						
GS(11cis)	+18.2	+2.0	+3.1	+8.7	+5.6	-15.1
HL	+20.1	-1.5	+18.6	+8.6	-2.7	+7.8
dHL	+16.8	+0.7	+15.9	+7.8	-2.6	+4.5
GS(Alltrans)	+12.1	-2.3	+2.2	+16	+12.4	0.0

Table 9-5. The relative energies of S₀, S₁ and S₃ states of SHUV-USB and SHUV-PSB calculated at CASPT2/CASSCF, SA8 and SA5 were used for model I and II, respectively.

Model	State	I			II		
		S ₀	S ₁	S ₂	S ₀	S ₁	S ₂
Minimum							
SHUV-USB							
GS(11cis)		0.0	89.6	95.4	0.0	93.6	82.7
HL		3.1	69.6	749	5.8	70.1	65.1
dHL		19.3	59.9	79.6	12.5	72.0	65.8
GS(Alltrans)		11.0	97.5	104.7	3.6	93.2	84.5
SHUV-PSB							
GS(11cis)		18.2	90.6	98.5	8.7	88.3	78.4
HL		26.3	73.4	88.1	14.3	77.9	62.4
dHL		36.1	75.8	80.3	20.3	70.4	69.4
GS(Alltrans)		23.1	95.1	106.9	19.6	96.9	93.2

The values of S₁ and S₂ reported in gray background cells associated with HL configuration while the others associated with dHL configuration.

9.3.2.2 Photoisomerization Energy Profile for model II SHUV-PSB.

In the FC region, as discussed before, the CT state of the SHUV-PSB is heavily mixed with the covalent ES making a clear assignment uncertain at the CASSCF level. The S₁/S₂ state mixing is reflected in their dipole moments (**Figure 9-16**) which are nearly identical. CASSCF optimizations were carried out (using SA3 for -10, -20 and 30° and SA2 for the other points) with an active space of 12 π -orbitals and 12 π -electrons only, and relaxing the third state (root 3). This leads to a planar minimum on S₁ with covalent character and equalized bond lengths. A similar situation has been reported due to the effect of a nearby counterion in RPSB chromophore models[22,165] or, analogously, under the effect of homogenous electric field [270]. The initial bond relaxation from FC to the free twisted HL minimum (free optimization of HL resulted in 18° of C₁₁–C₁₂ torsion angle) leads to an energy stabilization of ~25 kcal/mol for the ionic state (HL) while the covalent excited state (dHL) remains almost undisturbed. Along the torsional coordinate around the C₁₁–C₁₂ bond, the S₁ state shows a flat PES with a small barrier (1.6 kcal/mol) to escape the initially accessed S₁ minimum of covalent character, the energy profile becoming progressively steeper along the path while the S₁ state turns into a CT state and the covalent ground and excited states increase substantially in energy, thereby showing similar slopes. A CI with the ground-state is eventually accessed along the torsional coordinate already at 80°. In conclusion, the relaxed scan around the C₁₁–C₁₂ bond demonstrates that photoisomerization in the SHUV retinal chromophore becomes possible and favored as soon as it becomes protonated, opening up an ultrafast photoisomerization and deactivation route.

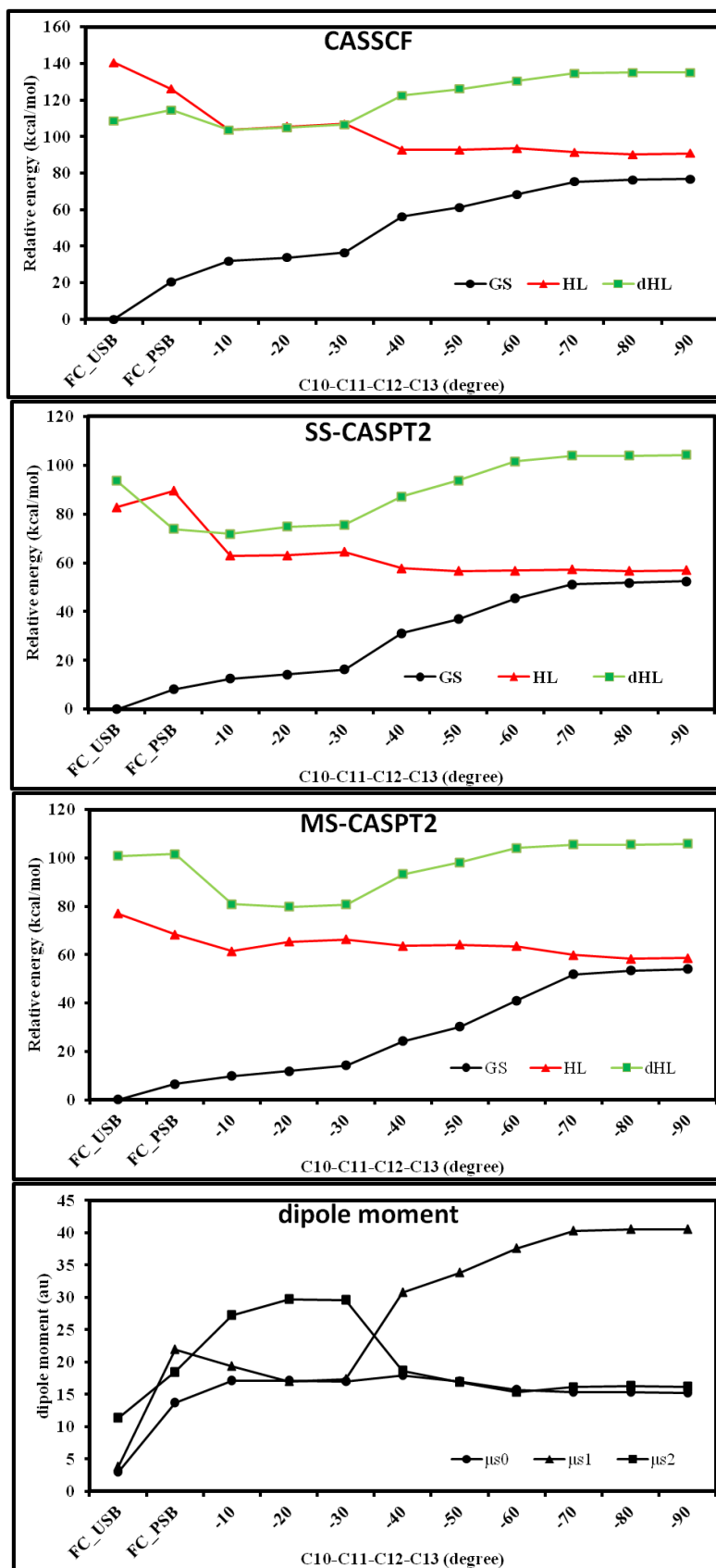


Figure 9-16. CASSCF, SS-CASPT2 and MS-CASPT2 energy profiles along the torsion angle around bonds C₁₀-C₁₁-C₁₂-C₁₃ of the SHUV-PSB of model II obtained from relaxed scans (relaxing the CT ES).

Table 9-6. The geometrical parameters of the SHUV-PSB model II for the scan around C₁₁-C₁₂ torsion bond.

	FC	-10	-20	-30	-40	-50	-60	-70	-80	-90
C5-C6	1.353	1.359	1.358	1.359	1.361	1.361	1.359	1.359	1.359	1.359
C6-C7	1.496	1.476	1.476	1.476	1.469	1.469	1.472	1.472	1.473	1.473
C7-C8	1.350	1.386	1.385	1.389	1.383	1.381	1.376	1.372	1.371	1.370
C8-C9	1.473	1.419	1.420	1.419	1.410	1.413	1.419	1.423	1.425	1.425
C9-C10	1.365	1.417	1.413	1.414	1.446	1.442	1.435	1.425	1.423	1.422
C10-C11	1.455	1.408	1.411	1.414	1.359	1.361	1.366	1.371	1.371	1.369
C11-C12	1.368	1.416	1.412	1.408	1.492	1.490	1.486	1.478	1.475	1.474
C12-C13	1.460	1.420	1.423	1.430	1.357	1.359	1.362	1.364	1.363	1.362
C13-C14	1.377	1.426	1.422	1.413	1.471	1.463	1.455	1.450	1.450	1.450
C14-C15	1.425	1.397	1.398	1.402	1.368	1.368	1.366	1.361	1.360	1.360
C15-N	1.293	1.352	1.350	1.348	1.362	1.362	1.365	1.372	1.375	1.374
N-H	1.047	1.019	1.017	1.021	1.016	1.016	1.014	1.012	1.012	1.012
C5-C6-C7-C8	-66.6	-57.0	-58.1	-56.8	-50.8	-49.6	-49.7	-48.4	-48.2	-48.0
C6-C7-C8-C9	176.8	178.5	178.7	177.1	179.4	179.9	-178.7	-176.6	-174.5	-172.4
C7-C8-C9-C10	177.3	168.7	169.1	168.8	169.1	169.7	170.4	170.4	169.6	168.5
C8-C9-C10-C11	178.0	178.2	180.0	-176.2	-167.9	-162.5	-157.2	-153.6	-152.0	-150.8
C9-C10-C11-C12	168.1	167.2	172.2	175.3	166.7	166.5	167.0	168.0	170.5	173.1
C10-C11-C12-C13	-6.1	-10.0	-20.0	-30.0	-40.0	-50.0	-60.0	-70.0	-80.0	-90.0
C11-C12-C13-C14	161.4	164.8	167.6	169.3	172.7	173.7	173.8	175.4	179.3	-176.3
C12-C13-C14-C15	-175.3	-174.2	-170.1	-170.5	-169.1	-168.3	-167.4	-167.7	-164.7	-161.1
C13-C14-C15-N	174.3	-180.0	-178.6	-174.8	-178.9	-177.8	-176.3	-173.9	-174.2	-176.0
H-C11-C12-H	-3.8	-12.6	-12.4	-14.1	-56.9	-69.6	-84.4	-95.6	-91.4	-82.6

9.4 Conclusion

We have investigated the possible photoisomerization mechanisms of the Siberian hamster ultraviolet visual pigment, containing an UV-active unprotonated retinal Schiff base chromophore, using multiconfigurational and multireference perturbative methods within a hybrid QM/MM scheme based on a previously reported homology model of the pigment.

Although a S_1/S_2 excited-state surface crossing is found during the initial skeletal relaxation on the S_1 potential energy surface, allowing to populate adiabatically a spectroscopically dark region on the S_1 surface with covalent character after photo-exciting the bright charge transfer transition in the Franck Condon region, it is revealed that this intermediate of covalent nature is unlikely to provide an efficient reactive channel in SHUV-USB since a sloped conical intersection with the ground state is located along the torsional coordinate high in energy. The $n\pi^*$ state can be excluded as well as a possible reactive channel as it remains located high in energy and appears insensitive to the skeletal deformations along the relaxational deformations in the spectroscopically accessible S_1 state.

The spin-orbit coupling calculation between singlet/triplet states at different minima, providing information about the probability and efficiency of inter-system crossings, discards its involvement due to negligible coupling rates. Nevertheless, the photoisomerization

reaction paths on the first and second triplet states (T_1 and T_2) along the C_8-C_9 and $C_{10}-C_{11}$ and $C_{11}-C_{12}$ torsion coordinates were explicitly computed. Such scans show high lying CI and large energy separation between T_1 and T_2 along the whole scan path, thus corroborating the view of inert triplet channels two different models were employed to investigate the effect of the water molecules in immediate vicinity of the chromophore on the spectroscopic properties. The resulting transition energies are in good agreement with the experimental values, thus suggesting that the presence of water molecules which form H-bonds with the retinal Schiff base does not contradict the experimentally observed blue-shift of the absorption energy. The presence of a water molecule close to the N-head of the retinal Schiff base offers the possibility for the formation of a protonated SHUV-PSB form in the ES shown to be the most stable conformation on the S_1 state which strongly supports the possibility of a proton transfer in the S_1 excited state. Under this condition, photoexcitation would catalyze the protonated Schiff base formation. By computing the photoisomerization profile for this model by means of relaxed scans in the CT (HL) S_1 state for rotation around the central $C_{11}-C_{12}$ bond it was demonstrated that the protonated form can reach a low lying and accessible CI seam with the GS. The relaxed scan demonstrates that photoisomerization in the SHUV retinal chromophore becomes possible and favored as soon as it becomes protonated, opening up an ultrafast photoisomerization and deactivation route.

Summary and Conclusions

Modeling spectral tunability and photoisomerization mechanisms in natural and artificial retinal systems was the focus of this PhD work. The photoinduced ultrafast isomerizations of the retinal chromophore in visual rhodopsins are characterized by high speed (ultrafast sub picosecond timescale processes) and efficiency (high quantum yields). It has been shown that this is due to a conical intersection between the excited and ground electronic states that drives its efficient internal conversion. The retinal chromophore displays also a cationic structure and the charge transfer character of its lowest excited bright state makes it sensitive to the environment, namely to the presence of an external electric field. This is in turn able to tune its absorption energy in order to cover the whole visible range (thus enabling color vision, for instance). All these properties call for the retinal chromophore as an ideal candidate for the design of fast, efficient and spectrally tunable molecular machines that work via reversible and controlled photo-induced reactions. The aim of this thesis is to investigate the mechanisms driving these reactions in different natural and artificial environments using high-level *ab initio* calculations, based on complete active space self-consistent field (CASSCF) and multiconfigurational second-order perturbation (CASPT2) theory, and hybrid quantum mechanics / molecular mechanics methods. Eventually, the aim is to understand how these systems work and provide guidelines for the design of artificial photoactive retinal inspired systems. The work throughout this thesis may be summarized into four main sections:

In the first part, the effect of a homogeneous electric field on the spectral tunability, photoisomerization efficiency and selectivity, of the native all-trans retinal protonated Schiff-base (RPSB) chromophore was investigated using CASPT2/CASSCF methodology. The analysis of the absorption energy dependence, charge distribution, and PES profiles along the torsional angles, as well as the electronic structure, energetics, and topography of the CI seam in the presence of strong positive and negative electric fields reveals the existence of qualitatively/fundamentally different photophysics and photochemistry with respect to the unperturbed (i.e., absence of an electric field) chromophore. Where a systematic linear shift of the absorption energy throughout the whole visible spectrum as a function of the field strength is observed, moreover, the photoisomerization paths revealed clear trends in the topography of the ES energy profiles that can be related to the interplay of the ionic and covalent configurations and their response to the geometrical deformations (bond relaxation and

torsion) in the conjugated system. Interestingly, a simple tentative proportional correlation between the absorption energy and the corresponding of the ES lifetime is found based on our calculations and further supported by time-resolved data recorded for native and mutated retinal proteins. Not only the isomerization rate but also its selectivity seems to be largely affected by the electric field, thereby making it possible to conceive controlling schemes involving switching between isomerization channels. Our study reveals that many of the characteristics encountered in the reference system exposed to an external field are also transferrable to other functionalized RPSBs.

In the second part, the outcomes of the study described above pushed us to take the first step towards applications. Thus, a large variety of functionalized RPSB chromophores were studied, in order to scrutinize the correlation between homogeneous external fields and local fields created through functional groups. Again, fine-tuning of the absorption energy over the whole visible region is achieved by modification of the parent compound with one or more chemical groups. The shift in absorption energy depends on two factors: the electronic nature of the functional groups and their positions in RPSB system. Namely, functional groups that cause blue shifts destabilize the ionic S_1 state and stabilize the covalent (S_0 and S_2) states. As the CT absorption blue shifts, the covalent states red-shifts, consequently the ionic and covalent become close to each other and do mix in the FC region. On the other hand, red-shifted functional groups stabilize the ionic S_1 state toward the covalent S_0 state, again inducing state mixing in the FC region. Therefore, strong red- or blue-shifts can be achieved by following different routes: through (i) charged groups, (ii) a combination of two or more additive functional group effects, and (iii) electron rich heterocyclic rings such as pyridine. Beyond this, we demonstrate that for a variety of compounds there is a correlation between the absorption energy and the topology of the ES profile, which can be employed to synthesize systems with desired photophysical and photochemical properties. Using a modified all-trans RPSB, we showed how the photo-isomerization can be selectively switched on/off by combining judicious substitutions and weak external electric fields. This marks a promising step toward the design of bio-inspired photo-controlled molecular devices.

The third part of this thesis deals with modeling the isomerization mechanisms of human melanopsin and invertebrate and vertebrate rhodopsins, and the prediction of the photoisomerization rates and quantum yields by means of semiclassical non-adiabatic

molecular dynamics at the quantum mechanics (CASSCF)/molecular mechanics (QM/MM) level. Our results show that the Landau–Zener rule does not apply for visual pigments. The reason behind that, speed is not the only control knob of the pigments' photosensitivity, i.e. a faster decay to the GS does not necessarily mean more efficient product formation. In fact phase–matching between the reactive torsional coordinate CCCC and the driving hydrogen out-of-plane mode HCCH is a major requirement. If the CCCC cannot follow fast enough the HCCH, a pronounced mismatch of the momenta is observed that inevitably reduces the QY. The WF character in the GS is another important parameter, which affects the decision taking, sometimes tens of fs after the hop to S_0 has occurred. This parameter is found to modulate non–uniformly the QY within 10% with respect to the predictions made at hopping time. Finally, higher momentum accumulated in the leading modes increases the number of random events. The nevertheless nearly perfect agreement between observed and predicted QY indicates that these random events lead to a 50/50 population distribution between trans and 11–cis. Based on these findings, we expect to find a reduced QY for pigments which decay to the GS on a time–scale below 60–65 fs for two reasons: a) HCCH/CCCC phase mismatch; b) an increase of random events in the GS. On the contrary, it would be intriguing to investigate the efficiency of slower isomerizer (with ES lifetimes around and beyond 100 fs). Rh has taught us that when the hydrogen out-of-plane mode *does not* acquire large momentum (which could be accomplished for example through weaker steric repulsion in the backbone or through H–bonds to nearby residues from the cavity), CCCC and HCCH are likely to be still in phase when the CI seam is reached, thus leading to higher QY.

In the last part, we shed some lights on the photoisomerization mechanism of the Siberian hamster ultraviolet (SHUV) visual pigment, which incorporates an unprotonated Schiff-base (USB) retinyl chromophore in the dark state, which becomes protonated after photoexcitation during the early stages of the photobleaching cycle. In such pigment, the photochemical relaxation processes is still unclear. We have investigated most of the possible decay channels. We have shown that a S_1/S_2 excited-state surface crossing occurs during the initial skeletal relaxation out of the FC region of the bright S_1 state, eventually leading to internal conversion into a dark excited state. However, our calculations reveal that this state is unlikely to be an efficient deactivation channel for SHUV-USB since a sloped conical intersection with the ground state is located high in energy. This also holds for the $n\pi^*$ state that is located high in energy and almost unperturbed by the skeletal deformations along the S_1 relaxation pathway. Involvement of the triplet states via singlet to triplet intersystem crossing processes

was also investigated. To this aim spin orbit couplings were computed between singlet/triplet states at different minima. While population of the triplet T_2 state cannot be ruled out, the results show that an efficient and fast photoisomerization decay process is unlikely to occur on the triplet states: photoisomerization reaction paths were mapped on the first and second triplet states (T_1 and T_2) about the C_{11} - C_{12} torsional coordinate, showing both not negligible isomerization barriers and high energy lying T_2/T_1 CI. We have thus investigated different molecular models with waters nearby the Schiff base, showing that we can both improve the agreement between the computed and observed absorption energy of the pigment and support a photoinduced proton transfer in the excited state, eventually leading to the formation of the retinal protonated Schiff base on its bright photoreactive S_1 state. Indeed, our results show that the protonated SHUV-PSB form is the most stable minimum on the S_1 state. Once formed, our calculations show that the photoisomerization around the central C_{11} - C_{12} bond and the internal conversion to the ground state become possible and favored (a barrierless C_{11} - C_{12} photoisomerization path leading to a twisted S_1/S_0 CI was found). In conclusions, this study demonstrates that photoisomerization of the SHUV retinal chromophore is triggered once it becomes protonated, opening up an ultrafast photoisomerization and deactivation route.

List of Abbreviations

- Atomic Unit (au)
- Born-Oppenheimer (BO)
- Charge Transfer (CT)
- CI with Singles (CIS)
- CI with Singles and Doubles (CISD)
- Complete Active Space Self-Consistent Field (CASSCF)
- Computational Bridge between Ab-initio and Molecular mechanic (COBRAMM)
- Configuration-Interaction (CI)
- Conical Intersection (CI)
- Coupled-Perturbed MCSCF(CPMCSCF)
- Excited State (ES)
- Franck-Condon (FC)
- Ground State (GS)
- Hartree-Fock(HF)
- High (H)
- Highest Occupied Molecular Orbital (HOMO)
- HOMO→LUMO (HL)
- HOMO2→LUMO2, (DHL)
- Hydrogen Out-Of-Plane (HOOP)
- Initial Relaxation Direction (IRD)
- Intramolecular Charge Transfer (ICT)
- Intrinsic Reaction Coordinate (IRC)
- Intrinsically Photosensitive Retinal Ganglion Cells (ipRGCs)
- Linear Absorption (LA)
- Linear Combination of Atomic Orbitals (LCAO)
- Low (L).
- Lowest Unoccupied Molecular Orbital (LUMO)
- Medium (M)
- Melanopsin (hMeRh)
- Minimum Energy Paths (MEP)
- Molecular Mechanics (MM)
- Molecular Orbitals (MO)
- Moller-Plesset (MP2)
- Multi-Reference-CI (MRCI)
- Multistate (MS)
- Potential Energy Surface (PES)
- Protonated Schiff-Base (PSB)
- Protonated Schiff Base (PSB)
- Quantum Mechanics (QM)
- Quantum Mechanics /Molecular Mechanics (QM/MM)
- Quantum Yield (QY)
- Restricted-Active-Space-Self-Consistent-Field (RASSCF)
- Retinal Protonated Schiff Base (RPSB)
- Rhodopsin (Rh)
- Second Order Perturbation Correction (CASPT2)
- Self-Consistent Field (SCF)
- Self-Consistent-Field (SCF)
- Short Wavelength Sensitive1 (SWS1)
- Short Wavelength Sensitive2 (SWS2)
- Siberian Hamster Ultraviolet (SHUV)
- Single-State (SS)
- Single-State CASPT2 (SS-CASPT2)
- Single-State CASSCF (SS-CASSCF)
- Spin Orbit Coupling (SOC)
- Squid Rhodopsin (sqRh)
- State-Average CASSCF (SA-CASSCF)
- Time-Dependent Electronic Schrödinger Equation (TDSE)
- Time-Dependent Density Functional Theory (TDDFT)
- Trajectory Surface Hopping (TSH)
- Transition Dipole Moment (TDM)
- Tully's Fewest Switches Surface Hopping (FSSH)
- Twisted Intramolecular Charge Transfer (TICT)
- Ultraviolet (UV)
- Unprotonated Schiff-Base (USB)
- Visible (Vis)
- Wave Function (WF)
- Woodward-Hoffmann (WH)
- Zero-Point Energy (ZPE)

List of Figures

Figure 1-1. Visual rhodopsin (top). Mechanism of spectral tuning and conical intersection suppression in retinal.....	3
Figure 1-2. Proposals of retinal variants with potential electrochromic behavior.....	3
Figure 2-1. Schematic representation of the hybrid QM/MM approach.	17
Figure 2-2. Boundary region crossing a covalent bond.....	17
Figure 2-3. The atom-link approach implies a change in the original charges (pod) of the MM region to be introduced in the QM calculation, according to the electrostatic embedding scheme. The procedure to obtain the new set of charges (emb) is described in the text.....	18
Figure 2-4. QM/MM implementation flowchart.....	19
Figure 3-1. (a) Two dimensional minimum. (b) Two dimensional transition state.....	21
Figure 3-2. Double cone representation of a symmetric conical intersection within two-dimensional, which lifts the energetic degeneracy between the ground state (blue) and the excited state (red).....	24
Figure 3-3. Schematic behavior of a thermal reaction. (b) Schematic behavior of a photochemical reaction.	25
Figure 5-1. Retinal protonated Schiff base in an electric field.	36
Figure 5-2. The complete active space molecular orbitals for the ground state optimized geometry of the RPSB chromophore calculated at CASSCF(12,12)/6-31G* level of theory in absence of the electric field.	37
Figure 5-3. The geometry parameters of the ground state of the RPSB chromophore in electric field calculated at CASSCF(12,12) using 6-31G* (solid lines) and ANO-L (dashed lines) levels of theory.	39
Figure 5-4. Dependence of a) the absorption energy; b) total Mulliken charge on the iminium moiety containing atoms C ₁₂ through C ₁₅ and the nitrogen (defined in the inset); c) TDM magnitude; on the electric field strength in the range -0.005 to +0.004 au. The dominant electronic configuration for each ES wave function is labeled through a coloured shape; in case of configuration mixing the second dominant configuration defines the inner colour of the shape. The strength of the external electric field is compared to the strength of an electric field created through a pair of point charges (shown in magenta for -0.005 au and +0.004 au field strengths), placed in 3 Å distance to both ends of retinal chromophore, reminiscent for the situation in the reactive pocket of opsins.....	40
Figure 5-5. Dependence of a) the absorption energy; b) total Mulliken charge on the iminium moiety containing atoms C ₁₂ through C ₁₅ and the nitrogen (defined in the inset); c) TDM magnitude; on the electric field strength in the range -0.005 to +0.004 au. The calculation based on CASSCF(12,12)/ANO-L level of theory. The dominant electronic configuration for each ES wave function is labeled through a coloured shape; in case of configuration mixing the second dominant configuration defines the inner colour of the shape.....	41

Figure 5-6. Profiles of RPSB along three torsion angles (around bonds C ₉ -C ₁₀ , C ₁₁ -C ₁₂ and C ₁₃ -C ₁₄) obtained from relaxed scans (relaxing the CT ES) in the presence of an electric field with strength -0.003 au (left column) and +0.003 au (right column). The profiles in the absence of an electric field are provided as a reference (middle column). The colour background denotes the character of the first ES along the optimized path being either covalent (red), CT (green), or mixed.	42
Figure 5-7. The bond lengths of optimized CT geometries of the RPSB for -0.003, 0.000 and +0.003 au versus the GS ones for 0.000 au.	43
Figure 5-8. Mulliken charges (left column, N-head and C-tail refer to the charges for the right and left moieties from the central of rotating bond, respectively) and permanent dipole moments (right column) of RPSB chromophore for the relaxed scans around C ₉ -C ₁₀ , C ₁₁ -C ₁₂ and C ₁₃ -C ₁₄ in the presence of electric field with strength +0.003 au, calculated at SA3-CASSCF(12/12)/6-31G* level of theory.	45
Figure 5-9. MS-3-CASPT2(12,12)/6-31G* on top of a SA-3-CASSCF computed adiabatic profiles of RPSB along three torsion angles (around bonds C ₉ -C ₁₀ , C ₁₁ -C ₁₂ and C ₁₃ -C ₁₄) obtained from relaxed scans (relaxing the CT excited state) in the presence of electric field with strength -0.003 au (left column) and +0.003 au (right column). The profiles in the absence of electric field a provided as a reference (middle column).	46
Figure 5-10. Structure of the RPSB chromophore functionalized with a -N(CH ₃) ₃ +group at the ionone ring, which shows a blue-shifted linear absorption spectrum.	47
Figure 5-11. SA3-CASSCF(12,12)/6-31G* (top) and SS-CASPT2 (middle) and MS-3-CASPT2 on the top of CASSCF (bottom) adiabatic profiles of the blue shifted RPSB (Figure 5-10) along three torsion angles (around bonds C ₉ -C ₁₀ , C ₁₁ -C ₁₂ and C ₁₃ -C ₁₄) obtained from relaxed scans (relaxing the CT excited state) in the absence of electric field.	47
Figure 5-12. Mulliken charges (left column, N-head and C-tail refer to the charges for the right and left moieties from the central of rotating bond, respectively) and permanent dipole moments (right column) of the blue shifted RPSB (Figure 5-10) along C ₉ -C ₁₀ , C ₁₁ -C ₁₂ and C ₁₃ -C ₁₄ for the absence of electric field, calculated at SA3-CASSCF(12,12)/6-31G* level of theory.	48
Figure 5-13. Profiles of RPSB along three torsion angles (around bonds C ₈ -C ₉ , C ₁₀ -C ₁₁ and C ₁₂ -C ₁₃) obtained from relaxed scans (relaxing the CT ES) in the presence of an electric field with strength -0.003 au.	51
Figure 5-14. Two-electron / two-orbital model, introduced via a correlation diagram for the π^2 , $\pi\pi^*$, and π^{*2} configurations for the torsional deformation along a double bond. In the region around 90° a noninteracting (not sharing common atomic centers) orbital basis (A,B) provides a more comprehensive description of the emerging covalent ($ A \bullet B \bullet\rangle$) and zwitterionic ($ A2 \rangle, B2 \rangle$) configurations. Absent or symmetric functionalization at both sides of the twisted double bond implies equivalence of the noninteracting orbitals A and B, a constellation known as a homosy-mmetric biradical.	52
Figure 5-15. a-C) Asymmetric geometrical or electronic (functionalization / substitution) deformation alters the electron affinity on both sides of the	

twisted double bond; depending on the strength of the deformation the systems can be categorized as weak (a), critical (b), and strong (c) heterosymmetric biradicaloids. An external electric field can alter the nature of the biradicaloid. Frontier orbitals and electronic structure of the GS and first ES resulting from occupying these orbitals at the geometry twisted by 90° around the C ₁₁ –C ₁₂ (d-f) and C ₁₂ –C ₁₃ (g-h) bonds of a minimal RPSB model consisting of two double bonds under the influence of a uniform external electric field.....	53
Figure 5-16. a)–C) Sketches of the potential energy surfaces of the ground (red), first (green), and second (blue) adiabatic ESs in the subspace of stretching and torsion for different electric field strengths; d)–f) sketches of the potential energy surfaces of the ground, first, and second ESs representing the relative position of the reactive coordinate (yellow) and the CI seam (magenta) for different electric field strengths. Dashed lines follow the diabatic character (covalent or ionic).....	54
Figure 5-17. CIs of RPSB for torsional angle 90° for negative (left) and positive (right) electric field of strength 0.003 au, as well as the CI for 50° torsion in the absence of electric field (middle). The bonds around which the torsion occurs, as well as the additional deformations, necessary to reach the CI are highlighted.	56
Figure 5-18. Mulliken charges (left column, N-head and C-tail refer to the charges for the right and left moieties from the central of rotating bond, respectively) and permanent dipole moments (right column) of RPSB chromophore for the relaxed scans around C ₉ –C ₁₀ , C ₁₁ –C ₁₂ and C ₁₃ –C ₁₄ in the presence of electric field with strength -0.003 au, calculated at SA3–CASSCF(12/12)/6-31G* level of theory.....	57
Figure 5-19. Mulliken charges (left column, N-head and C-tail refer to the charges for the right and left moieties from the central of rotating bond, respectively) and permanent dipole moments (right column) of RPSB chromophore for the relaxed scans around C ₈ –C ₉ , C ₁₀ –C ₁₁ and C ₁₂ –C ₁₃ in the presence of electric field with strength -0.003 au, calculated at SA3–CASSCF(12/12)/6-31G* level of theory.....	58
Figure 5-20. Mulliken charges (left column, N-head and C-tail refer to the charges for the right and left moieties from the central of rotating bond, respectively) and permanent dipole moments (right column) of RPSB chromophore for the relaxed scans around C ₉ –C ₁₀ , C ₁₁ –C ₁₂ and C ₁₃ –C ₁₄ in the absence of electric field, calculated at SA3–CASSCF(12/12)/6-31G* level of theory.....	58
Figure 5-21. (A) Bond lengths at the equilibrated ES geometry of the parent molecule for different strengths of the electric field (between -0.0018 au and -0.0033 au). (B) SS–CASPT2 S ₁ energy profiles obtained through linear interpolation between both minima coexisting in the electric field range -0.0018 au : -0.0032 au at the SA-2–CASSCF level. Profiles for three electric field strengths, -0.0018, -0.0025 and -0.0032 au, are shown. (C) Bond length alternation (BLA = $i = 7,9,11,13dC_i - C_{i+1} - i = 8,10,12,14dC_i - C_{i+1}$, d is the bond length) of both minima at different strengths of the electric field shown in part A.	60
Figure 5-22. CASSCF and MS–CASPT2 S ₁ energy profiles of the RPSB chromophore obtained through linear interpolation between both minima	

co-existing in the electric field range -0.0018 au : -0.0032 au at SA-2-CASSCF level. Profile for three electric field strengths, -0.0018, -0.0025 and -0.0032 au, are shown.....	60
Figure 5-23. Profiles of red-shifted (left) and blue-shifted (right) RPSB derivatives along the torsion angle $C_{11}-C_{12}$ obtained from relaxed scans (relaxing the CT ES) in the absence of an electric field. The colour background denotes the character of the first ES along the optimized path being either covalent (red), CT (green) or mixed.	62
Figure 5-24. SA3-CASSCF(12,12/6-31G* (top), MS-3-CASPT2(12,12/6-31G* on the top of CASSCF calculations (middle) and CASSCF permanent dipole moments (down) profiles of the blue-shifted RPSB (Figure 5-23 , right) (right column) and red-shifted RPSB (Figure 5-23 , left) (left column) along the torsion around $C_{11}-C_{12}$ bond calculated from relaxed scans (relaxing the CT excited state) in the absence of electric field at CASSCF(12,12)/6-31G* level of theory.....	62
Figure 6-1. Dependence of the absorption energy on the electronic natures and positions of the functional groups along the backbone of the RPSB. The vertical green line shows the shift in absorption energy by applying electric field of +0.004 and -0.005 au.	68
Figure 6-2. Functionalized retinal protonated Schiff bases ($R_{1 \rightarrow 44}$). The numeration is shown in R_{30} , the same descending order, starts at protonated SB which takes the number (16), will be used for the other systems.	69
Figure 6-3. The most important mesomeric structures in ground and excited state of RPSBs.	70
Figure 6-4. Correlation between the absorption energy and BLA of the relaxed geometries. Where $BLA = i = 714dCi - Ci + 1 - 1.41/8$, with $dCi - Ci + 1$ the bond length between carbon atoms I and i+1 from the conjugated chain labeling according to Figure 6-2 R_{30} , C_5-C_6 and C_6-C_7 are excluded for better comparison with systems without β -ionone ring.	72
Figure 6-5. Molecular structures of R_7 and R_{19}	74
Figure 6-6. CASSPT2/SA2-CASSCF/(12,12/6-31G* profile along relaxed scans (relaxing the CT excited state) around C_9-C_{10} torsion bond of R_{19} calculated in the absence (top) and in presence of EF of -0.001 au (bottom).....	74
Figure 6-7. CASSPT2/SA2-CASSCF/(12,12/6-31G* profile along relaxed scans (relaxing the CT excited state) around C_9-C_{10} torsion bond of R_7 calculated in EF of -0.003 au (top), 0.000 (middle) +0.001 au (bottom).....	75
Figure 7-1. Bovine rhodopsin structure resolved at 2.2 Å of resolution (pdb code 1U19). a) The tertiary structure of the protein where the seven transmembrane α -helices are highlighted with different colours. b) A magnification of the binding pocket around the chromophore (RET, in dark gray) showing the link of Schiff base with a Lys296 through the $C_{15} N$ bond.....	79
Figure 7-2. Diagram of the photoisomerization process of 11-Cis-Retinal to form all-trans-Retinal Schiff base (the double bond $C_{15}-N$ is protonated). The Greek letters refer to the nomenclature of the carbon atoms of the lysine residue 296 belonging to the protein.	79

Figure 7-3. Tertiary structure of the UV-pigment. To the left is shown the overall structure of the protein, and are highlighted with different colours the seven transmembrane α -helices. Zoom into the right focus the area around the chromophore (note the deprotonated Schiff base).	83
Figure 8-1. Comparative model (violet) of hMeOp superimposed on top of sqRh crystallographic structure used as template (green), this Figure taken from ref [12]......	87
Figure 8-2. Schematic representation for high and medium layers, the green dashed line show the cut between the H and M layers. The atoms in ball and stick are belonging to QM region while atoms represented in tube belong to medium layer. The low layer includes the rest of the protein not shown in the Figure.	88
Figure 8-3. The molecular orbitals comprising the full active space CAS(12,12). Highlighted in gray is the pair of bonding and anti-bonding orbitals resulting in the reduced CAS(10,10) which best reproduces the energy profiles and the structural features obtained using the full- π active space.	89
Figure 8-4. Overlay of S_1 and S_0 and total energies in pigment trajectories computed with CAS(10,10) and CAS(12,12) active spaces shown in red and blue colours, respectively. The overlays show, that CAS space and time step have virtually no influence on the excited state dynamics.....	90
Figure 8-5. Overlays of C_{11} - C_{12} bond length, C_{10} - C_{11} - C_{12} - C_{13} and H - C_{11} - C_{12} - H dihedrals in 0K trajectories computed with CAS(10,10) (red colours) and CAS(12,12) (blue colours) active spaces.	91
Figure 8-6. Linear fit of relative energies (referred to the ground-state minimum) calculated at CASPT2 and CASSCF level of theory along the computed CASSCF reaction path.	93
Figure 8-7. LA of the three pigments obtained from averaging over 60 calculated corrected with SS-CASPT2 (left) and MS-CASPT2(right) after SA3-CASSCF(12, 12) calculations.....	97
Figure 8-8. CASPT2//SA2-CASSCF(12,12)/6-31G*/AMBER energy profiles along the torsion angle C_{10} - C_{11} - C_{12} - C_{13} obtained from constrained relaxed scan with 10° increment.	98
Figure 8-9. Population transfer dynamics for the three pigments, quantum mechanical and classical quantities are shown in solid and dashed lines, respectively. Hopping zones highlighted in gray.	99
Figure 8-10: Distribution of hopping events as a function of the S_1 lifetimes for hMeOp (top), sqRh (middle) and Rh (bottom). The height of the bar graphs corresponds to the number of trans (nofill) and cis (gray) photoproducts of individual trajectories.....	100
Figure 8-11. Characteristic geometrical parameters in the three pigments and their temporal evolution.	101
Figure 8-12. Distribution of the hopping events in the space of the HCCH and CCCC coordinates.	102
Figure 8-13. Temporal evolution of CCCC and HCCH the 0K trajectories.....	103
Figure 8-14. Distribution of the "switching to a biradical WF" events in the space of the HCCH and CCCC coordinates.....	104

Figure 8-15. Distribution of hopping events as a function of the CASSCF energy differences $\Delta E(S_1-S_0)$ for hMeOp (top), sqRh (middle) and Rh (bottom). The height of the bar graphs corresponds to the number of trans (nofill) and cis (gray) photoproducts of individual trajectories.	104
Figure 8-16. Distribution of hopping events as a function of the torsion $C_{10}-C_{11}=C_{12}-C_{13}$ for hMeOp (top), sqRh (middle) and Rh (bottom). The height of the bar graphs corresponds to the number of trans (nofill) and cis (gray) photoproducts of individual trajectories.....	105
Figure 9-1. Schematic representation of the 11-Cis protonated (PSB) and unprotonated (USB) Schiff bases found in the dark state of (a) rhodopsin and (b) Siberian hamster UV pigment. Early photointermediates detected experimentally in (c) rhodopsin (batho and BSI) and (d) UV pigment (Batho-like and BSI) showing the preservation of the RPSB in rhodopsin and the multiple changes of the protonation state in the UV pigment. The photorhodopsin intermediate in rhodopsin is omitted for clarity. Absorption λ_{MAX} reported in parentheses are taken from Refs.[32,264].....	111
Figure 9-2: Superimposed of the initial geometries of model I (pale blue) and II (brown) showing the retinal chromophore, E113 and water molecules, only few water molecules of model I are shown. The distance values shown are in Å.....	114
Figure 9-3. Schematic representation for high and medium layers for (a) HML1 (b) HML2 (c) HML2 schemes, the green dashed line show the cut between the H and M layers. The atoms in ball and stick are belonging to QM region while atoms represented in tube belong to medium layer. The low layer includes the rest of the protein and is not shown in the Figures.	115
Figure 9-4. Evolution of energy levels of the low laying singlet and triplet excited states of the SHUV-USB along at FC, HL and dHL minima calculated at CASPT2/SA5-CASSCF(12,12)/6-31G* level, the active space was extend to (14,13) to locate the $n \rightarrow L$ state, the Figure modified from ref [187].	117
Figure 9-5. Evolution of the most important singlet and triplet states along the constrained scan on dHL state at different selected geometries (FC, dHL, dh(-60) and dh(-90)). The energies were calculated at SA10-CASSCF(12,12)/6-31G*, then corrected with SS-CASPT2 and MS-CASPT2. The active space was extend to (14,13) to locate the $n \rightarrow \pi$ transitions. For triplet state only SA5 was used, the order of the states at FC geometries is the same as they appear in the legend of each Figure.....	118
Figure 9-6. Evolution of the excited state manifold spectroscopic states on FC, HL, dHL, T_1 and T_2 regions. The energies were calculated at SS-CASPT2/CASSCF using in case singlet states SA10, SA8 and SA9 for FC and dHL, T_1 and T_2 minima, respectively, for the triplet states SA6 was used for T_1 minumim while SA5 was used for the other geometries. The active space was expanded to (14,13) to locate the $n \rightarrow \pi$ transitions. The order of the states at FC geometryis the same as they appear in the legend of the Figure.	119
Figure 9-7. A comparison among the geometrical parameters of FC, dHL, T_1 and T_2 optimized geometries.	119
Figure 9-8. SA2-CASSF and SS-CASPT2 energy profiles along the torsion angle $C_{10}-C_{11}-C_{12}-C_{13}$ obtained from relaxed scan of the second triplet state T_2	121

Figure 9-9. SA2-CASSF and SS-CASPT2 energy profiles along the torsion angle (C ₉ -C ₁₀ -C ₁₁ -C ₁₂) obtained from relaxed scan of the second triplet state T ₂	121
Figure 9-10. SA2-CASSF and SS-CASPT2 energy profiles along the torsion angle (C ₇ -C ₈ -C ₉ -C ₁₀) obtained from relaxed scan of the second triplet state T ₂	122
Figure 9-11. SA2-CASSF and SS-CASPT2 energy profiles along the torsion angle (C ₁₀ -C ₁₁ -C ₁₂ -C ₁₃) obtained from relaxed scan of the first triplet state T ₁	122
Figure 9-12. Evolution of the excited state manifold spectroscopic states along the T ₁ scan. The energies were calculated at SS-CASPT2/CASSCF using in case singlet states SA8 and SA5 singlet and triplet states, respectively. The active space was expanded to (14,13) to locate the $n \rightarrow \pi$ transitions. The order of the states at T ₁ (-36) geometry is the same as they appear in the legend of the Figure.	122
Figure 9-13. The active sites of different starting geometries of model II (left column) and optimized geometries employing HML2 (medal column) and HML3 (left column) schemes.	125
Figure 9-14. Superimposed of the ground state geometries of model I (pale blue) and II (brown), the distance values shown are in Å.....	125
Figure 9-15. CASSCF, SS-CASPT2 and MS-CASPT2 (SA ₈ and SA ₅ were used for model I and II, respectively) energy profiles comparing the GS, HL, and dHL states (shown in blue, red and green colours, respectively) of SHUV-PSB (dotted lines) and SHUV-USB (solid lines) species at different minima for models I and II. The dihedral angle (C ₁₀ -C ₁₁ -C ₁₂ -C ₁₃) was frozen during the optimization of HL and dHL to the values of their ground state minima (see Table 9-3).	128
Figure 9-16. CASSCF, SS-CASPT2 and MS-CASPT2 energy profiles along the torsion angle around bonds C ₁₀ -C ₁₁ -C ₁₂ -C ₁₃ of the SHUV-PSB of model II obtained from relaxed scans (relaxing the CT ES).....	130

List of Tables

Table 6-1. Bond length lengths for S_0 and S_1 states of R_9 and R_7 in electric field of 0.000, -0.001 and + 0.001 au strengths.	73
Table 8-1. α values according the linear fitting between CASSCF and CASPT2 of S_0 , S_1 and ΔE energies	93
Table 8-2. The ground state geometrical parameters optimized using CAS(12,12) and CAS(10,10)	95
Table 8-3. SS-CASPT2 and MS-CASPT2//CASSCF(12,12) and (10,10)/6-31G*/AMBER, NRoot=3, State-Averaged (weights: 1/3, 1/3, 1/3) absorption maxima (λ_{max} , nm) and the corresponding oscillator strengths f , calculated on the top of the corresponding S_0 minima employing.....	95
Table 8-4. SS-CASPT2 and MS-CASPT2//CASSCF(12,12)/6-31G*/AMBER, NRoot=3, State-Averaged (weights: 1/3, 1/3, 1/3) calculation of the averaged absorption maxima (λ_{max} , nm), vertical excitation energies ΔE (kcal/mol), oscillator strength f , over all the 60 starting geometries of each pigment ensemble.....	96
Table 8-5. The observed quantum yield vs. the predicted ones based on the HCCH direction at both the hopping decision times.....	102
Table 8-6. The averaged geometry parameters of the three pigments at hopping point.....	105
Table 8-7. Statistical of the individual trajectories of Rh shown the hopping and decision time, the photoproduct distribution and the mode govern the reaction.....	106
Table 8-8. Statistical of the individual trajectories of sqRh shown the hopping and decision time, the photoproduct distribution and the mode govern the reaction.....	107
Table 8-9. Statistical of the individual trajectories of hMeOp shown the hopping and decision time, the photoproduct distribution and the mode govern the reaction.....	108
Table 9-1. The characteristic wave functions and their weights along the constrained scan on T_1 and T_2 PESs around $C_{10}-C_{11}-C_{12}-C_{13}$ torsion angle.....	123
Table 9-2. QM/MM absolute energies and vertical excitations for the different structures of model II.	124
Table 9-3. The geometrical parameters of the optimized minima.	127
Table 9-4. The relative stability of each state calculated at CASPT2/CASSCF, SA_8 and SA_5 were used for model I and II, respectively.....	128
Table 9-5. The relative energies of S_0 , S_1 and S_3 states of SHUV-USB and SHUV-PSB calculated at CASPT2/CASSCF, SA_8 and SA_5 were used for model I and II, respectively.	129
Table 9-6. The geometrical parameters of the SHUV-PSB model II for the scan around $C_{11}-C_{12}$ torsion bond.....	131

References

- [1] Griesbeck, A. G. Book Review: Electronic Aspects of Organic Photochemistry. By J. Michl and V. Bonačić-Koutecký. *Angewandte Chemie International Edition in English* **1992**, *31*, 242-242.
- [2] Snow, T.; Brownsberger, K. *Universe: Origins and Evolution*; Wadsworth Publishing Company, 1997.
- [3] Polli, D.; Altoe, P.; Weingart, O.; Spillane, K. M.; Manzoni, C.; Brida, D.; Tomasello, G.; Orlandi, G.; Kukura, P.; Mathies, R. A.; Garavelli, M.; Cerullo, G. Conical Intersection Dynamics of the Primary Photoisomerization Event in Vision. *Nature* **2010**, *467*, 440-443.
- [4] Wald, G.; Brown, P. K. Human Rhodopsin. *Science* **1958**, *127*, 222-249.
- [5] Schoenlein, R. W.; Peteanu, L. A.; Mathies, R. A.; Shank, C. V. The First Step in Vision: Femtosecond Isomerization of Rhodopsin. *Science* **1991**, *254*, 412-415.
- [6] Warshel, A. Bicycle-Pedal Model for the First Step in the Vision Process. *Nature* **1976**, *260*, 679-683.
- [7] Lok, C. Vision Science: Seeing without Seeing. *Nature* **2011**, *469*, 284-285.
- [8] Garavelli, M.; Celani, P.; Bernardi, F.; Robb, M. A.; Olivucci, M. The C₅H₆NH₂⁺ Protonated Schiff Base: An Ab Initio Minimal Model for Retinal Photoisomerization. *J. Am. Chem. Soc.* **1997**, *119*, 6891-6901.
- [9] González-Luque, R.; Garavelli, M.; Bernardi, F.; Merchán, M.; Robb, M. A.; Olivucci, M. Computational Evidence in Favor of a Two-State, Two-Mode Model of the Retinal Chromophore Photoisomerization. *Proc. Natl. Acad. Sci. U. S. A.* **2000**, *97*, 9379-9384.
- [10] Serrano-Andrés, L.; Merchán, M.; Lindh, R. Computation of Conical Intersections by Using Perturbation Techniques. *J. Chem. Phys.* **2005**, *122*, 104107.
- [11] Grotendorst, J. *Modern Methods and Algorithms of Quantum Chemistry: Proceedings*; John-von-Neumann-Inst. for Computing, 2000.
- [12] Rinaldi, S.; Melaccio, F.; Gozem, S.; Fanelli, F.; Olivucci, M. Comparison of the Isomerization Mechanisms of Human Melanopsin and Invertebrate and Vertebrate Rhodopsins. *Proceedings of the National Academy of Sciences* **2014**, *111*, 1714-1719.
- [13] Rivalta, I.; Nenov, A.; Garavelli, M. Modelling Retinal Chromophores Photoisomerization: From Minimal Models in Vacuo to Ultimate Bidimensional Spectroscopy in Rhodopsins. *PCCP* **2014**, *16*, 16865-16879.
- [14] Punwong, C.; Owens, J.; Martínez, T. J. Direct Qm/Mm Excited-State Dynamics of Retinal Protonated Schiff Base in Isolation and Methanol Solution. *J. Phys. Chem. B* **2015**, *119*, 704-714.
- [15] A. Stuart, J.; R. Birge, R. In *Biomembranes: A Multi-Volume Treatise*; Lee, A. G., Ed.; JAI: 1996; Vol. Volume 2, p 33-139.
- [16] Palczewski, K. G Protein-Coupled Receptor Rhodopsin. *Annu. Rev. Biochem* **2006**, *75*, 743-767.
- [17] Hubbell, W. L.; Altenbach, C.; Hubbell, C. M.; Khorana, H. G. Rhodopsin Structure, Dynamics, and Activation: A Perspective from Crystallography, Site-Directed Spin Labeling, Sulfhydryl Reactivity, and Disulfide Cross-Linking. *Adv. Protein Chem.* **2003**, *63*, 243-290.

- [18] Sakmar, T. P.; Menon, S. T.; Marin, E. P.; Awad, E. S. Rhodopsin: Insights from Recent Structural Studies. *Annu. Rev. Biophys. Biomol. Struct.* **2002**, *31*, 443-484.
- [19] Ebrey, T.; Koutalos, Y. Vertebrate Photoreceptors. *Prog Retin Eye Res* **2001**, *20*, 49-94.
- [20] Zhou, X.; Sundholm, D.; Wesolowski, T. A.; Kaila, V. R. Spectral Tuning of Rhodopsin and Visual Cone Pigments. *J Am Chem Soc* **2014**, *136*, 2723-2726.
- [21] Andruniów, T.; Ferré, N.; Olivucci, M. Structure, Initial Excited-State Relaxation, and Energy Storage of Rhodopsin Resolved at the Multiconfigurational Perturbation Theory Level. *Proceedings of the National Academy of Sciences* **2004**, *101*, 17908-17913.
- [22] Cembran, A.; Bernardi, F.; Olivucci, M.; Garavelli, M. The Retinal Chromophore/Chloride Ion Pair: Structure of the Photoisomerization Path and Interplay of Charge Transfer and Covalent States. *Proc. Natl. Acad. Sci. U. S. A.* **2005**, *102*, 6255-6260.
- [23] Zen, A.; Coccia, E.; Gozem, S.; Olivucci, M.; Guidoni, L. Quantum Monte Carlo Treatment of the Charge Transfer and Diradical Electronic Character in a Retinal Chromophore Minimal Model. *J. Chem. Theory Comput.* **2015**, *11*, 992-1005.
- [24] Demoulin, B.; El-Tahawy, M. M. T.; Nenov, A.; Garavelli, M.; Le Bahers, T. Intramolecular Photo-Induced Charge Transfer in Visual Retinal Chromophore Mimics: Electron Density-Based Indices at the Td-Dft and Post-Hf Levels. *Theor. Chem. Acc.* **2016**, *135*, 1-10.
- [25] Polli, D.; Rivalta, I.; Nenov, A.; Weingart, O.; Garavelli, M.; Cerullo, G. Tracking the Primary Photoconversion Events in Rhodopsins by Ultrafast Optical Spectroscopy. *Photochem. Photobiol. Sci.* **2015**, *14*, 213-228.
- [26] Guler, A. D.; Ecker, J. L.; Lall, G. S.; Haq, S.; Altimus, C. M.; Liao, H. W.; Barnard, A. R.; Cahill, H.; Badea, T. C.; Zhao, H.; Hankins, M. W.; Berson, D. M.; Lucas, R. J.; Yau, K. W.; Hattar, S. Melanopsin Cells Are the Principal Conduits for Rod-Cone Input to Non-Image-Forming Vision. *Nature* **2008**, *453*, 102-105.
- [27] Ruby, N. F.; Brennan, T. J.; Xie, X.; Cao, V.; Franken, P.; Heller, H. C.; O'Hara, B. F. Role of Melanopsin in Circadian Responses to Light. *Science* **2002**, *298*, 2211-2213.
- [28] Hattar, S.; Liao, H. W.; Takao, M.; Berson, D. M.; Yau, K. W. Melanopsin-Containing Retinal Ganglion Cells: Architecture, Projections, and Intrinsic Photosensitivity. *Science* **2002**, *295*, 1065-1070.
- [29] Sekharan, S.; Altun, A.; Morokuma, K. Photochemistry of Visual Pigment in a Gq Protein-Coupled Receptor (Gpcr)—Insights from Structural and Spectral Tuning Studies on Squid Rhodopsin. *Chemistry – A European Journal* **2010**, *16*, 1744-1749.
- [30] Sekharan, S.; Morokuma, K. Drawing the Retinal out of Its Comfort Zone: An Oniom(Qm/Mm) Study of Mutant Squid Rhodopsin. *The Journal of Physical Chemistry Letters* **2010**, *1*, 668-672.
- [31] Matsuyama, T.; Yamashita, T.; Imamoto, Y.; Shichida, Y. Photochemical Properties of Mammalian Melanopsin. *Biochemistry* **2012**, *51*, 5454-5462.
- [32] Mooney, V. L.; Szundi, I.; Lewis, J. W.; Yan, E. C. Y.; Kliger, D. S. Schiff Base Protonation Changes in Siberian Hamster Ultraviolet Cone Pigment Photointermediates. *Biochemistry* **2012**, *51*, 2630-2637.
- [33] Hunt, D. M.; Wilkie, S. E.; Bowmaker, J. K.; Poopalasundaram, S. Vision in the Ultraviolet. *Cellular and Molecular Life Sciences CMLS* **2001**, *58*, 1583-1598.

- [34] Mooney, V.; Sekharan, S.; Liu, J.; Guo, Y.; Batista, V. S.; Yan, E. C. Y. Kinetics of Thermal Activation of an Ultraviolet Cone Pigment. *J. Am. Chem. Soc.* **2015**, *137*, 307-313.
- [35] Sekharan, S.; Mooney, V. L.; Rivalta, I.; Kazmi, M. A.; Neitz, M.; Neitz, J.; Sakmar, T. P.; Yan, E. C. Y.; Batista, V. S. Spectral Tuning of Ultraviolet Cone Pigments: An Interhelical Lock Mechanism. *J. Am. Chem. Soc.* **2013**, *135*, 19064-19067.
- [36] Young, D. C. In *Computational Chemistry*; John Wiley & Sons, Inc.: 2002, p 5-18.
- [37] Turro, N. J. *Principles of Molecular Photochemistry : An Introduction*; University Science Books: Sausalito, Calif., 2009.
- [38] Schrödinger, E. An Undulatory Theory of the Mechanics of Atoms and Molecules. *Physical Review* **1926**, *28*, 1049-1070.
- [39] Born, M.; Oppenheimer, R. Zur Quantentheorie Der Molekeln. *Annalen der Physik* **1927**, *389*, 457-484.
- [40] Cramer, C. J. *Essentials of Computational Chemistry: Theories and Models*; Wiley, 2005.
- [41] Levine, I. N. *Quantum Chemistry* Prentice Hall: Englewood Cliffs, 1991.
- [42] Griffiths, D. J. *Introduction to Quantum Mechanics*; Upper Saddle River: New Jersey: Prentice Hall, 1995.
- [43] Sakurai, J. J. *Modern Quantum Mechanics (Revised Ed.)*. Addison-Wesley: Tuan, San Fu, 1994.
- [44] Kutzelnigg, W. Friedrich Hund and Chemistry. *Angewandte Chemie International Edition in English* **1996**, *35*, 572-586.
- [45] Robert, S. Mulliken's Nobel Lecture. *Science* **1966**, *157*, no. 3784, 13 - 24.
- [46] Slater, J. C. Note on Hartree's Method. *Physical Review* **1930**, *35*, 210-211.
- [47] Hartree, D. R. "The Wave Mechanics of an Atom with a Non-Coulomb Central Field. Part I. Theory and Methods. *Mathematical Proceedings of the Cambridge Philosophical Society* **1928**, *24*, 89-110.
- [48] Fock, V. Näherungsmethode Zur Lösung Des Quantenmechanischen Mehrkörperproblems. *Zeitschrift für Physik* **1930**, *61*, 126-148.
- [49] Hall, G. G. Applications of Quantum Mechanics in Theoretical Chemistry. *Rep. Prog. Phys.* **1959**, *22*, 1.
- [50] Schäfer, L. *In Search of Divine Reality: Science as a Source of Inspiration*; University of Arkansas Press, 1997.
- [51] Atkins, P. W. *Molecular Quantum Mechanics Parts I and II: An Introduction to Quantum Chemistry* Oxford University Press: Oxford 1977; Vol. 1.
- [52] Roothaan, C. C. J. New Developments in Molecular Orbital Theory. *Reviews of Modern Physics* **1951**, *23*, 69-89.
- [53] Kato, S. Perspective on "a Molecular Orbital Theory of Reactivity in Aromatic Hydrocarbons". *Theor. Chem. Acc.* **2000**, *103*, 219-220.
- [54] Roos, B.; Taylor, P. R.; Siegbahn, P. E. M. A Complete Active Space Scf Method (Casscf) Using a Density Matrix Formulated Super-Ci Approach. *Chem. Phys.* **1980**, *48*, 157-173.
- [55] Hartree, D. R.; Hartree, W.; Swirles, B. Self-Consistent Field, Including Exchange and Superposition of Configurations, with Some Results for Oxygen. *Philosophical*

Transactions of the Royal Society of London. Series A, Mathematical and Physical Sciences **1939**, 238, 229.

- [56] Szabo, A.; Ostlund, N. S. *Modern Quantum Chemistry Introduction to Advanced Electronic Structure Theory* Attila Szabo, Neil S. Ostlund.; Mineola, N.Y Dover Publications, 1996.
- [57] Szalay, P. G.; Müller, T.; Gidofalvi, G.; Lischka, H.; Shepard, R. Multiconfiguration Self-Consistent Field and Multireference Configuration Interaction Methods and Applications. *Chem. Rev.* **2012**, 112, 108-181.
- [58] Dreuw, A.; Head-Gordon, M. Single-Reference Ab Initio Methods for the Calculation of Excited States of Large Molecules. *Chem. Rev.* **2005**, 105, 4009-4037.
- [59] Sherrill, C. D. The Multiconfigurational Self-Consistent-Field Method. **2004**.
- [60] Malmqvist, P. A.; Rendell, A.; Roos, B. O. The Restricted Active Space Self-Consistent-Field Method, Implemented with a Split Graph Unitary Group Approach. *J. Phys. Chem.* **1990**, 94, 5477-5482.
- [61] Dykstra, C.; Frenking, G.; Kim, K.; Scuseria, G. *Theory and Applications of Computational Chemistry: The First Forty Years*; Elsevier, 2011.
- [62] Hirao, K. Multireference Møller—Plesset Method. *Chem. Phys. Lett.* **1992**, 190, 374-380.
- [63] Hirao, K. Multireference Møller—Plesset Perturbation Theory for High-Spin Open-Shell Systems. *Chem. Phys. Lett.* **1992**, 196, 397-403.
- [64] Hirao, K. State-Specific Multireference Møller—Plesset Perturbation Treatment for Singlet and Triplet Excited States, Ionized States and Electron Attached States of H₂O. *Chem. Phys. Lett.* **1993**, 201, 59-66.
- [65] Nakano, H. Mscsf Reference Quasidegenerate Perturbation Theory with Epstein—Nesbet Partitioning. *Chem. Phys. Lett.* **1993**, 207, 372-378.
- [66] Andersson, K.; Malmqvist, P. A.; Roos, B. O.; Sadlej, A. J.; Wolinski, K. Second-Order Perturbation Theory with a Casscf Reference Function. *J. Phys. Chem.* **1990**, 94, 5483-5488.
- [67] James Finley, M., O. Roosa, Luis; Finley, J.; Malmqvist, P.-Å.; Roos, B. O.; Serrano-Andrés, L. The Multi-State Caspt2 Method. *Chem. Phys. Lett.* **1998**, 288, 299-306.
- [68] Gundertofte, K.; Liljefors, T.; Norrby, P.-o.; Pettersson, I. A Comparison of Conformational Energies Calculated by Several Molecular Mechanics Methods. *J. Comput. Chem.* **1996**, 17, 429-449.
- [69] Jensen, F. *Introduction to Computational Chemistry*; John Wiley & Sons, 2001.
- [70] Li, T. Computational Methods for Protein Folding, Advances in Chemical Physics Series, Vol. 120. *Pharm. Res.* **2002**, 19, 1078.
- [71] Lipkowitz, K. B.; Boyd, D. B. *Reviews in Computational Chemistry: * Volume 13*; Wiley Online Library, 2000.
- [72] Jorgensen, W. L.; Tirado-Rives, J. The Opls [Optimized Potentials for Liquid Simulations] Potential Functions for Proteins, Energy Minimizations for Crystals of Cyclic Peptides and Crambin. *J. Am. Chem. Soc.* **1988**, 110, 1657-1666.
- [73] Sekharan, S.; Altun, A.; Morokuma, K. Qm/Mm Study of Dehydro and Dihydro B-Ionone Retinal Analogues in Squid and Bovine Rhodopsins: Implications for Vision in Salamander Rhodopsin. *J. Am. Chem. Soc.* **2010**, 132, 15856-15859.
- [74] Senn, H. M.; Thiel, W. Qm/Mm Methods for Biomolecular Systems. *Angew Chem Int Ed Engl* **2009**, 48, 1198-1229.

- [75] Senn, H. M.; Thiel, W. Qm/Mm Methods for Biomolecular Systems. *Angew. Chem. Int. Ed.* **2009**, *48*, 1198-1229.
- [76] Lin, H.; Truhlar, D. G. Qm/Mm: What Have We Learned, Where Are We, and Where Do We Go from Here? *Theor. Chem. Acc.* **2007**, *117*, 185.
- [77] Altoè, P.; Stenta, M.; Bottoni, A.; Garavelli, M. A Tunable Qm/Mm Approach to Chemical Reactivity, Structure and Physico-Chemical Properties Prediction. *Theor. Chem. Acc.* **2007**, *118*, 219-240.
- [78] Gao, J.; Amara, P.; Alhambra, C.; Field, M. J. A Generalized Hybrid Orbital (Gho) Method for the Treatment of Boundary Atoms in Combined Qm/Mm Calculations. *J. Phys. Chem. A* **1998**, *102*, 4714-4721.
- [79] Warshel, A.; Levitt, M. Theoretical Studies of Enzymic Reactions: Dielectric, Electrostatic and Steric Stabilization of the Carbonium Ion in the Reaction of Lysozyme. *J. Mol. Biol.* **1976**, *103*, 227-249.
- [80] Washel, A.; Levitt, M. Theoretical Studies of Enzymatic Reactions: Dielectric, Electrostatic and Steric Stabilization of the Carbonium Ion in the Reaction of Lysozyme. *J. Mol. Biol.* **1976**, *103*, 227-249.
- [81] McCammon, J. A.; Gelin, B. R.; Karplus, M.; WOLYNES, P. G. The Hinge-Bending Mode in Lysozyme. **1976**.
- [82] Shoemaker, J. R.; Burggraf, L. W.; Gordon, M. S. Simomm: An Integrated Molecular Orbital/Molecular Mechanics Optimization Scheme for Surfaces. *J. Phys. Chem. A* **1999**, *103*, 3245-3251.
- [83] Svensson, M.; Humbel, S.; Froese, R. D.; Matsubara, T.; Sieber, S.; Morokuma, K. Oniom: A Multilayered Integrated Mo+ Mm Method for Geometry Optimizations and Single Point Energy Predictions. A Test for Diels– Alder Reactions and Pt (P (T-Bu) 3) 2+ H2 Oxidative Addition. *J. Phys. Chem.* **1996**, *100*, 19357-19363.
- [84] Groenhof, G. Introduction to Qm/Mm Simulations. *Biomolecular simulations: methods and protocols* **2013**, 43-66.
- [85] Sherwood, P. Hybrid Quantum Mechanics/Molecular Mechanics Approaches. *Modern methods and algorithms of quantum chemistry* **2000**, *3*, 285-305.
- [86] Peng, C.; Ayala, P. Y.; Schlegel, H. B.; Frisch, M. J. Using Redundant Internal Coordinates to Optimize Equilibrium Geometries and Transition States. *Journal of Computational Chemistry* **1996**, *17*, 49-56.
- [87] Field, M. J.; Bash, P. A.; Karplus, M. A Combined Quantum Mechanical and Molecular Mechanical Potential for Molecular Dynamics Simulations. *J. Comput. Chem.* **1990**, *11*, 700-733.
- [88] Singh, U. C.; Kollman, P. A. A Combined Ab Initio Quantum Mechanical and Molecular Mechanical Method for Carrying out Simulations on Complex Molecular Systems: Applications to the Ch3cl+ Cl- Exchange Reaction and Gas Phase Protonation of Polyethers. *J. Comput. Chem.* **1986**, *7*, 718-730.
- [89] Ferré, N.; Olivucci, M. The Amide Bond: Pitfalls and Drawbacks of the Link Atom Scheme. *Journal of Molecular Structure: THEOCHEM* **2003**, *632*, 71-82.
- [90] Pu, J.; Gao, J.; Truhlar, D. G. Generalized Hybrid Orbital (Gho) Method for Combining Ab Initio Hartree– Fock Wave Functions with Molecular Mechanics. *J. Phys. Chem. A* **2004**, *108*, 632-650.

- [91] Théry, V.; Rinaldi, D.; Rivail, J. L.; Maignet, B.; Ferenczy, G. G. Quantum Mechanical Computations on Very Large Molecular Systems: The Local Self-Consistent Field Method. *J. Comput. Chem.* **1994**, *15*, 269-282.
- [92] Aquilante, F.; Autschbach, J.; Carlson, R. K.; Chibotaru, L. F.; Delcey, M. G.; De Vico, L.; Fdez. Galván, I.; Ferré, N.; Frutos, L. M.; Gagliardi, L.; Garavelli, M.; Giussani, A.; Hoyer, C. E.; Li Manni, G.; Lischka, H.; Ma, D.; Malmqvist, P. Å.; Müller, T.; Nenov, A.; Olivucci, M.; Pedersen, T. B.; Peng, D.; Plasser, F.; Pritchard, B.; Reiher, M.; Rivalta, I.; Schapiro, I.; Segarra-Martí, J.; Stenrup, M.; Truhlar, D. G.; Ungur, L.; Valentini, A.; Vancoillie, S.; Veryazov, V.; Vysotskiy, V. P.; Weingart, O.; Zapata, F.; Lindh, R. Molcas 8: New Capabilities for Multiconfigurational Quantum Chemical Calculations across the Periodic Table. *J. Comput. Chem.* **2016**, *37*, 506-541.
- [93] Frisch, M. J.; Trucks, G. W.; Schlegel, H. B.; Scuseria, G. E.; Robb, M. A.; Cheeseman, J. R.; Scalmani, G.; Barone, V.; Mennucci, B.; Petersson, G. A.; Nakatsuji, H.; Caricato, M.; Li, X.; Hratchian, H. P.; Izmaylov, A. F.; Bloino, J.; Zheng, G.; Sonnenberg, J. L.; Hada, M.; Ehara, M.; Toyota, K.; Fukuda, R.; Hasegawa, J.; Ishida, M.; Nakajima, T.; Honda, Y.; Kitao, O.; Nakai, H.; Vreven, T.; Montgomery Jr., J. A.; Peralta, J. E.; Ogliaro, F.; Bearpark, M. J.; Heyd, J.; Brothers, E. N.; Kudin, K. N.; Staroverov, V. N.; Kobayashi, R.; Normand, J.; Raghavachari, K.; Rendell, A. P.; Burant, J. C.; Iyengar, S. S.; Tomasi, J.; Cossi, M.; Rega, N.; Millam, N. J.; Klene, M.; Knox, J. E.; Cross, J. B.; Bakken, V.; Adamo, C.; Jaramillo, J.; Gomperts, R.; Stratmann, R. E.; Yazyev, O.; Austin, A. J.; Cammi, R.; Pomelli, C.; Ochterski, J. W.; Martin, R. L.; Morokuma, K.; Zakrzewski, V. G.; Voth, G. A.; Salvador, P.; Dannenberg, J. J.; Dapprich, S.; Daniels, A. D.; Farkas, Ö.; Foresman, J. B.; Ortiz, J. V.; Cioslowski, J.; Fox, D. J.; Gaussian, Inc.: Wallingford, CT, USA, 2009.
- [94] Werner, H.-J.; Knowles, P.; Lindh, R.; Manby, F. R.; Schütz, M.; Celani, P.; Korona, T.; Rauhut, G.; Amos, R.; Bernhardsson, A. Molpro, Version 2010.1, a Package of Ab Initio Programs. See <http://www.molpro.net> **2010**.
- [95] Hornak, V.; Abel, R.; Okur, A.; Strockbine, B.; Roitberg, A.; Simmerling, C. Comparison of Multiple Amber Force Fields and Development of Improved Protein Backbone Parameters. *Proteins: Struct., Funct., Bioinf.* **2006**, *65*, 712-725.
- [96] Case, D. A.; Cheatham, T. E.; Darden, T.; Gohlke, H.; Luo, R.; Merz, K. M.; Onufriev, A.; Simmerling, C.; Wang, B.; Woods, R. J. The Amber Biomolecular Simulation Programs. *J. Comput. Chem.* **2005**, *26*, 1668-1688.
- [97] Dudek, M. J.; Ponder, J. W. Accurate Modeling of the Intramolecular Electrostatic Energy of Proteins. *J. Comput. Chem.* **1995**, *16*, 791-816.
- [98] Sutcliffe, B. T. The Idea of a Potential Energy Surface. *Mol. Phys.* **2006**, *104*, 715-722.
- [99] Shaik, S. S.; Schlegel, H. B.; Wolfe, S. *Theoretical Aspects of Physical Organic Chemistry*; Wiley, 1992.
- [100] Marcus, R. Skiing the Reaction Rate Slopes. *Science* **1992**, *256*, 1523-1525.
- [101] Steinfeld, J. I.; Francisco, J. S.; Hase, W. L. *Chemical Kinetics and Dynamics*; Prentice Hall Englewood Cliffs (New Jersey), 1989; Vol. 3.
- [102] Hratchian, H. P.; Schlegel, H. B. Finding Minima, Transition States, and Following Reaction Pathways on Ab Initio Potential Energy Surfaces. *Theory and applications of computational chemistry: The first* **2005**, *40*, 195-249.
- [103] Carr, J. M.; Trygubenko, S. A.; Wales, D. J. Finding Pathways between Distant Local Minima. *J. Chem. Phys.* **2005**, *122*, 234903.

- [104] Boggio-Pasqua, M.; Ravaglia, M.; Bearpark, M. J.; Garavelli, M.; Robb, M. A. Can Diarylethene Photochromism Be Explained by a Reaction Path Alone? A Cascf Study with Model Mmvd Dynamics. *J. Phys. Chem. A* **2003**, *107*, 11139-11152.
- [105] Neumann, J. v.; Wigner, E. Über Das Verhalten Von Eigenwerten Bei Adiabatischen Prozessen. *J-Stage* **1929**, *3*, 239-242.
- [106] Katz, J. R. X-Ray Spectrography of Polymers and in Particular Those Having a Rubber-Like Extensibility. *Transactions of the Faraday Society* **1936**, *32*, 77-94.
- [107] Teller, E. The Crossing of Potential Surfaces. *J. Phys. Chem.* **1937**, *41*, 109-116.
- [108] Robb, M. A.; Garavelli, M.; Olivucci, M.; Bernardi, F. A Computational Strategy for Organic Photochemistry. *Rev. Comput. Chem.* **2000**, *15*, 87-146.
- [109] Domcke, W.; Yarkony, D. R.; Horst, K. *Conical Intersections: Electronic Structure, Dynamics and Spectroscopy*; World Scientific, 2004; Vol. 15.
- [110] Desouter-Lecomte, M.; Lorquet, J.-C. Nonadiabatic Interactions in Unimolecular Decay. Iv. Transition Probability as a Function of the Massey Parameter. *J. Chem. Phys.* **1979**, *71*, 4391-4403.
- [111] Yarkony, D. R. On the Characterization of Regions of Avoided Surface Crossings Using an Analytic Gradient Based Method. *J. Chem. Phys.* **1990**, *92*, 2457-2463.
- [112] Dallos, M.; Lischka, H.; Shepard, R.; Yarkony, D. R.; Szalay, P. G. Analytic Evaluation of Nonadiabatic Coupling Terms at the Mr-Ci Level. Ii. Minima on the Crossing Seam: Formaldehyde and the Photodimerization of Ethylene. *J. Chem. Phys.* **2004**, *120*, 7330-7339.
- [113] Ragazos, I. N.; Robb, M. A.; Bernardi, F.; Olivucci, M. Optimization and Characterization of the Lowest Energy Point on a Conical Intersection Using an Mc-Scf Lagrangian. *Chem. Phys. Lett.* **1992**, *197*, 217-223.
- [114] Chachiyo, T.; Rodriguez, J. H. A Direct Method for Locating Minimum-Energy Crossing Points (Mecps) in Spin-Forbidden Transitions and Nonadiabatic Reactions. *J. Chem. Phys.* **2005**, *123*, 094711.
- [115] Yamazaki, S.; Kato, S. Locating the Lowest Free-Energy Point on Conical Intersection in Polar Solvent: Reference Interaction Site Model Self-Consistent Field Study of Ethylene and Ch 2 Nh 2+. *J. Chem. Phys.* **2005**, *123*, 114510.
- [116] Page, C. S.; Olivucci, M. Ground and Excited State Caspt2 Geometry Optimizations of Small Organic Molecules. *J. Comput. Chem.* **2003**, *24*, 298-309.
- [117] Manaa, M. R.; Yarkony, D. R. On the Intersection of Two Potential Energy Surfaces of the Same Symmetry. Systematic Characterization Using a Lagrange Multiplier Constrained Procedure. *J. Chem. Phys.* **1993**, *99*, 5251-5256.
- [118] Keal, T. W.; Koslowski, A.; Thiel, W. Comparison of Algorithms for Conical Intersection Optimisation Using Semiempirical Methods. *Theoretical Chemistry Accounts: Theory, Computation, and Modeling (Theoretica Chimica Acta)* **2007**, *118*, 837-844.
- [119] De Vico, L.; Olivucci, M.; Lindh, R. New General Tools for Constrained Geometry Optimizations. *J. Chem. Theory Comput.* **2005**, *1*, 1029-1037.
- [120] Yarkony, D. R. Marching Along Ridges. Efficient Location of Energy-Minimized Conical Intersections of Two States Using Extrapolatable Functions. *J. Phys. Chem. A* **2004**, *108*, 3200-3205.
- [121] Nocedal, J.; Overton, M. L. Projected Hessian Updating Algorithms for Nonlinearly Constrained Optimization. *SIAM Journal on Numerical Analysis* **1985**, *22*, 821-850.

- [122] Atchity, G. J.; Xantheas, S. S.; Ruedenberg, K. Potential Energy Surfaces near Intersections. *J. Chem. Phys.* **1991**, *95*, 1862-1876.
- [123] Bearpark, M. J.; Robb, M. A.; Bernhard Schlegel, H. A Direct Method for the Location of the Lowest Energy Point on a Potential Surface Crossing. *Chem. Phys. Lett.* **1994**, *223*, 269-274.
- [124] Logunov, S. L.; Volkov, V. V.; Braun, M.; El-Sayed, M. A. The Relaxation Dynamics of the Excited Electronic States of Retinal in Bacteriorhodopsin by Two-Pump-Probe Femtosecond Studies. *Proceedings of the National Academy of Sciences* **2001**, *98*, 8475-8479.
- [125] Ballhausen, C. J.; Hansen, A. E. Electronic Spectra. *Annual Review of Physical Chemistry* **1972**, *23*, 15-38.
- [126] Cederbaum, L. S. In *Conical Intersections: Electronic Structure, Dynamics & Spectroscopy*, World Scientific, Singapore; WORLD SCIENTIFIC: 2004; Vol. 15, p 3-40.
- [127] Avouris, P.; Gelbart, W. M.; El-Sayed, M. A. Nonradiative Electronic Relaxation under Collision-Free Conditions. *Chem. Rev.* **1977**, *77*, 793-833.
- [128] May, V.; Kühn, O. In *Charge and Energy Transfer Dynamics in Molecular Systems*; Wiley-VCH Verlag GmbH: 2007, p 227-284.
- [129] Runge, E.; Gross, E. K. U. Density-Functional Theory for Time-Dependent Systems. *Phys. Rev. Lett.* **1984**, *52*, 997-1000.
- [130] Appel, H.; Gross, E. K. U.; Burke, K. Excitations in Time-Dependent Density-Functional Theory. *Phys. Rev. Lett.* **2003**, *90*, 043005.
- [131] SAHNI, V. In *Recent Advances in Density Functional Methods*; WORLD SCIENTIFIC: 2011, p 79-128.
- [132] Roos, B. O. In *Adv. Chem. Phys.*; John Wiley & Sons, Inc.: 2007, p 399-445.
- [133] Tully, J. C.; Preston, R. K. Trajectory Surface Hopping Approach to Nonadiabatic Molecular Collisions: The Reaction of H⁺ with D₂. *J. Chem. Phys.* **1971**, *55*, 562-572.
- [134] Tully, J. C. Molecular Dynamics with Electronic Transitions. *J. Chem. Phys.* **1990**, *93*, 1061-1071.
- [135] Nielsen, S.; Kapral, R.; Ciccotti, G. Mixed Quantum-Classical Surface Hopping Dynamics. *J. Chem. Phys.* **2000**, *112*, 6543-6553.
- [136] Bonella, S.; Coker, D. F. Land-Map, a Linearized Approach to Nonadiabatic Dynamics Using the Mapping Formalism. *J. Chem. Phys.* **2005**, *122*, 194102.
- [137] McEniry, E. J.; Wang, Y.; Dundas, D.; Todorov, T. N.; Stella, L.; Miranda, R. P.; Fisher, A. J.; Horsfield, A. P.; Race, C. P.; Mason, D. R.; Foulkes, W. M. C.; Sutton, A. P. Modelling Non-Adiabatic Processes Using Correlated Electron-Ion Dynamics. *The European Physical Journal B* **2010**, *77*, 305-329.
- [138] Donoso, A.; Martens, C. C. Simulation of Coherent Nonadiabatic Dynamics Using Classical Trajectories. *J. Phys. Chem. A* **1998**, *102*, 4291-4300.
- [139] Horenko, I.; Salzmann, C.; Schmidt, B.; Schütte, C. Quantum-Classical Liouville Approach to Molecular Dynamics: Surface Hopping Gaussian Phase-Space Packets. *J. Chem. Phys.* **2002**, *117*, 11075-11088.
- [140] Burghardt, I.; Cederbaum, L. S. Hydrodynamic Equations for Mixed Quantum States. II. Coupled Electronic States. *J. Chem. Phys.* **2001**, *115*, 10312-10322.
- [141] Curchod, B. F.; Tavernelli, I. On Trajectory-Based Nonadiabatic Dynamics: Bohmian Dynamics Versus Trajectory Surface Hopping. *J. Chem. Phys.* **2013**, *138*, 184112.

- [142] Richings, G. W.; Polyak, I.; Spinlove, K. E.; Worth, G. A.; Burghardt, I.; Lasorne, B. Quantum Dynamics Simulations Using Gaussian Wavepackets: The Vmcg Method. *Int. Rev. Phys. Chem.* **2015**, *34*, 269-308.
- [143] Tapavicza, E.; Bellchambers, G. D.; Vincent, J. C.; Furche, F. Ab Initio Non-Adiabatic Molecular Dynamics. *PCCP* **2013**, *15*, 18336-18348.
- [144] Born, M. *Kopplung Der Elektronen- Und Kernbewegung in Molekeln Und Kristallen*, Von M. Born; Vandenhoeck und Ruprecht, 1951.
- [145] Born, M.; Huang, K. *Dynamical Theory of Crystal Lattices*; Clarendon Press: Oxford, UK, 1954
- [146] de Carvalho, F. F.; Bouduban, M. E.; Curchod, B. F.; Tavernelli, I. Nonadiabatic Molecular Dynamics Based on Trajectories. *Entropy* **2013**, *16*, 62-85.
- [147] Serrano-Andrés, L.; Merchán, M. Are the Five Natural DNA/Rna Base Monomers a Good Choice from Natural Selection?: A Photochemical Perspective. *Journal of Photochemistry and Photobiology C: Photochemistry Reviews* **2009**, *10*, 21-32.
- [148] Landau, L. On the Theory of Transfer of Energy at Collisions II. *Phys. Z. Sowjetunion* **1932**, *2*, 7.
- [149] Zener, C. Non-Adiabatic Crossing of Energy Levels. *Proceedings of the Royal Society of London. Series A* **1932**, *137*, 696-702.
- [150] Landry, B. R.; Falk, M. J.; Subotnik, J. E. Communication: The Correct Interpretation of Surface Hopping Trajectories: How to Calculate Electronic Properties. *J. Chem. Phys.* **2013**, *139*, 211101.
- [151] Nenov, A., lmu, 2012.
- [152] Coker, D. F.; Xiao, L. Methods for Molecular Dynamics with Nonadiabatic Transitions. *J. Chem. Phys.* **1995**, *102*, 496-510.
- [153] Jasper, A. W.; Stechmann, S. N.; Truhlar, D. G. Fewest-Switches with Time Uncertainty: A Modified Trajectory Surface-Hopping Algorithm with Better Accuracy for Classically Forbidden Electronic Transitions. *J. Chem. Phys.* **2002**, *116*, 5424-5431.
- [154] Swope, W. C.; Andersen, H. C.; Berens, P. H.; Wilson, K. R. A Computer Simulation Method for the Calculation of Equilibrium Constants for the Formation of Physical Clusters of Molecules: Application to Small Water Clusters. *J. Chem. Phys.* **1982**, *76*, 637-649.
- [155] Barbatti, M.; Sen, K. Effects of Different Initial Condition Samplings on Photodynamics and Spectrum of Pyrrole. *Int. J. Quantum Chem* **2016**, *116*, 762-771.
- [156] Wigner, E. On the Quantum Correction for Thermodynamic Equilibrium. *Physical Review* **1932**, *40*, 749-759.
- [157] Klaffki, N.; Weingart, O.; Garavelli, M.; Spohr, E. Sampling Excited State Dynamics: Influence of Hoop Mode Excitations in a Retinal Model. *PCCP* **2012**, *14*, 14299-14305.
- [158] Palings, I.; Pardo, J. A.; Van den Berg, E.; Winkel, C.; Lugtenburg, J.; Mathies, R. A. Assignment of Fingerprint Vibrations in the Resonance Raman Spectra of Rhodopsin, Isorhodopsin, and Bathorhodopsin: Implications for Chromophore Structure and Environment. *Biochemistry* **1987**, *26*, 2544-2556.
- [159] Yoshizawa, T.; Wald, G. Pre-Lumirhodopsin and the Bleaching of Visual Pigments. *Nature* **1963**, *197*, 1279-1286.
- [160] McBee, J. K.; Palczewski, K.; Baehr, W.; Pepperberg, D. R. Confronting Complexity: The Interlink of Phototransduction and Retinoid Metabolism in the Vertebrate Retina. *Prog. Retin. Eye Res.* **2001**, *20*, 469-529.

- [161] Wang, W.; Nossoni, Z.; Berbasova, T.; Watson, C. T.; Yapici, I.; Lee, K. S. S.; Vasileiou, C.; Geiger, J. H.; Borhan, B. Tuning the Electronic Absorption of Protein-Embedded All-Trans-Retinal. *Science* **2012**, *338*, 1340-1343.
- [162] Song, L.; El-Sayed, M. A.; Lanyi, J. K. Protein Catalysis of the Retinal Subpicosecond Photoisomerization in the Primary Process of Bacteriorhodopsin Photosynthesis. *Science* **1993**, *261*, 891-894.
- [163] Logunov, S. L.; El-Sayed, M. A.; Song, L.; Lanyi, J. K. Photoisomerization Quantum Yield and Apparent Energy Content of the K Intermediate in the Photocycles of Bacteriorhodopsin, Its Mutants D85n, R82q, and D212n, and Deionized Blue Bacteriorhodopsin. *J. Phys. Chem.* **1996**, *100*, 2391-2398.
- [164] Ernst, O. P.; Lodowski, D. T.; Elstner, M.; Hegemann, P.; Brown, L. S.; Kandori, H. Microbial and Animal Rhodopsins: Structures, Functions, and Molecular Mechanisms. *Chem. Rev.* **2014**, *114*, 126-163.
- [165] Cembran, A.; Bernardi, F.; Olivucci, M.; Garavelli, M. Counterion Controlled Photoisomerization of Retinal Chromophore Models: A Computational Investigation. *J. Am. Chem. Soc.* **2004**, *126*, 16018-16037.
- [166] Muñoz-Losa, A.; Fdez. Galván, I.; Aguilar, M. A.; Martín, M. E. Simultaneous Solvent and Counterion Effects on the Absorption Properties of a Model of the Rhodopsin Chromophore. *J. Chem. Theory Comput.* **2013**, *9*, 1548-1556.
- [167] Mori, T.; Nakano, K.; Kato, S. Conical Intersections of Free Energy Surfaces in Solution: Effect of Electron Correlation on a Protonated Schiff Base in Methanol Solution. *J. Chem. Phys.* **2010**, *133*, 064107.
- [168] Zhou, X.; Sundholm, D.; Woźniowski, T. A.; Kaila, V. R. I. Spectral Tuning of Rhodopsin and Visual Cone Pigments. *J. Am. Chem. Soc.* **2014**, *136*, 2723-2726.
- [169] Cheng, C.; Kamiya, M.; Uchida, Y.; Hayashi, S. Molecular Mechanism of Wide Photoabsorption Spectral Shifts of Color Variants of Human Cellular Retinol Binding Protein II. *J. Am. Chem. Soc.* **2015**, *137*, 13362-13370.
- [170] Kaila, V. R. I.; Send, R.; Sundholm, D. The Effect of Protein Environment on Photoexcitation Properties of Retinal. *J. Phys. Chem. B* **2012**, *116*, 2249-2258.
- [171] Hamm, P.; Zurek, M.; Röschinger, T.; Patzelt, H.; Oesterhelt, D.; Zinth, W. Femtosecond Spectroscopy of the Photoisomerisation of the Protonated Schiff Base of All-Trans Retinal. *Chem. Phys. Lett.* **1996**, *263*, 613-621.
- [172] Logunov, S. L.; Song, L.; El-Sayed, M. A. Excited-State Dynamics of a Protonated Retinal Schiff Base in Solution. *J. Phys. Chem.* **1996**, *100*, 18586-18591.
- [173] Wang, Q.; Schoenlein, R.; Peteanu, L.; Mathies, R.; Shank, C. Vibrationally Coherent Photochemistry in the Femtosecond Primary Event of Vision. *Science* **1994**, *266*, 422-424.
- [174] Zgrablić, G.; Voitchovsky, K.; Kindermann, M.; Haacke, S.; Chergui, M. Ultrafast Excited State Dynamics of the Protonated Schiff Base of All-Trans Retinal in Solvents. *Biophys. J.* **2005**, *88*, 2779-2788.
- [175] Zgrablić, G.; Haacke, S.; Chergui, M. Heterogeneity and Relaxation Dynamics of the Photoexcited Retinal Schiff Base Cation in Solution. *J. Phys. Chem. B* **2009**, *113*, 4384-4393.
- [176] Zgrablić, G.; Haacke, S.; Chergui, M. Vibrational Coherences of the Protonated Schiff Base of All-Trans Retinal in Solution. *Chem. Phys.* **2007**, *338*, 168-174.

- [177] Ruckebauer, M.; Barbatti, M.; Müller, T.; Lischka, H. Nonadiabatic Photodynamics of a Retinal Model in Polar and Nonpolar Environment. *J. Phys. Chem. A* **2013**, *117*, 2790-2799.
- [178] Bassolino, G.; Sovdat, T.; Soares Duarte, A.; Lim, J. M.; Schnedermann, C.; Liebel, M.; Odell, B.; Claridge, T. D.; Fletcher, S. P.; Kukura, P. Barrierless Photoisomerization of 11-Cis Retinal Protonated Schiff Base in Solution. *J. Am. Chem. Soc.* **2015**, *137*, 12434-12437.
- [179] Sovdat, T.; Bassolino, G.; Liebel, M.; Schnedermann, C.; Fletcher, S. P.; Kukura, P. Backbone Modification of Retinal Induces Protein-Like Excited State Dynamics in Solution. *J. Am. Chem. Soc.* **2012**, *134*, 8318-8320.
- [180] Bassolino, G.; Sovdat, T.; Liebel, M.; Schnedermann, C.; Odell, B.; Claridge, T. D. W.; Kukura, P.; Fletcher, S. P. Synthetic Control of Retinal Photochemistry and Photophysics in Solution. *J. Am. Chem. Soc.* **2014**, *136*, 2650-2658.
- [181] Nenov, A.; de Vivie-Riedle, R. Conical Intersection Seams in Polyenes Derived from Their Chemical Composition. *J. Chem. Phys.* **2013**, *137*, 074101.
- [182] Nenov, A.; de Vivie-Riedle, R. Geometrical and Substituent Effects in Conical Intersections: Linking Chemical Structure and Photoreactivity in Polyenes. *J. Chem. Phys.* **2011**, *135*, 034304.
- [183] Hariharan, P. C.; Pople, J. A. The Influence of Polarization Functions on Molecular Orbital Hydrogenation Energies. *Theor. Chim. Acta* **1973**, *28*, 213-222.
- [184] Pierloot, K.; Dumez, B.; Widmark, P.-O.; Roos, B. O. Density Matrix Averaged Atomic Natural Orbital (Ano) Basis Sets for Correlated Molecular Wave Functions. *Theor. Chim. Acta* **1995**, *90*, 87-114.
- [185] Forsberg, N.; Malmqvist, P.-Å. Multiconfiguration Perturbation Theory with Imaginary Level Shift. *Chem. Phys. Lett.* **1997**, *274*, 196-204.
- [186] Ghigo, G.; Roos, B. O.; Malmqvist, P.-Å. A Modified Definition of the Zeroth-Order Hamiltonian in Multiconfigurational Perturbation Theory (Caspt2). *Chem. Phys. Lett.* **2004**, *396*, 142-149.
- [187] Bonvicini, A.; Demoulin, B.; Altavilla, S. F.; Nenov, A.; El-Tahawy, M. M. T.; Segarra-Martí, J.; Giussani, A.; Batista, V. S.; Garavelli, M.; Rivalta, I. Ultraviolet Vision: Photophysical Properties of the Unprotonated Retinyl Schiff Base in the Siberian Hamster Cone Pigment. *Theor. Chem. Acc.* **2016**, *135*, 1-10.
- [188] Cembran, A.; Gonzalez-Luque, R.; Altoe, P.; Merchan, M.; Bernardi, F.; Olivucci, M.; Garavelli, M. Structure, Spectroscopy, and Spectral Tuning of the Gas-Phase Retinal Chromophore: The Beta-Ionone "Handle" and Alkyl Group Effect. *J. Phys. Chem. A* **2005**, *109*, 6597-6605.
- [189] Rivalta, I.; Nenov, A.; Weingart, O.; Cerullo, G.; Garavelli, M.; Mukamel, S. Modelling Time-Resolved Two-Dimensional Electronic Spectroscopy of the Primary Photoisomerization Event in Rhodopsin. *J. Phys. Chem. B* **2014**, *118*, 8396-8405.
- [190] Aquilante, F.; De Vico, L.; Ferré, N.; Ghigo, G.; Malmqvist, P.-Å.; Neogrády, P.; Pedersen, T. B.; Pitoňák, M.; Reiher, M.; Roos, B. O.; Serrano-Andrés, L.; Urban, M.; Veryazov, V.; Lindh, R. Molcas 7: The Next Generation. *J. Comput. Chem.* **2009**, *31*, 224-247.
- [191] Honig, B.; Nicholls, A. Classical Electrostatics in Biology and Chemistry. *Science* **1995**, *268*, 1144-1149.

- [192] Suydam, I. T.; Snow, C. D.; Pande, V. S.; Boxer, S. G. Electric Fields at the Active Site of an Enzyme: Direct Comparison of Experiment with Theory. *Science* **2006**, *313*, 200-204.
- [193] Dokukina, I.; Weingart, O. Spectral Properties and Isomerisation Path of Retinal in C1c2 Channelrhodopsin. *PCCP* **2015**, *17*, 25142-25150.
- [194] Gozem, S.; Huntress, M.; Schapiro, I.; Lindh, R.; Granovsky, A. A.; Angeli, C.; Olivucci, M. Dynamic Electron Correlation Effects on the Ground State Potential Energy Surface of a Retinal Chromophore Model. *J. Chem. Theory Comput.* **2012**, *8*, 4069-4080.
- [195] Laricheva, E. N.; Gozem, S.; Rinaldi, S.; Melaccio, F.; Valentini, A.; Olivucci, M. Origin of Fluorescence in 11-Cis Locked Bovine Rhodopsin. *J. Chem. Theory Comput.* **2012**, *8*, 2559-2563.
- [196] El-Sayed, M. A.; Griffiths, J. A.; Song, L.; Zhang, N. On the Molecular Mechanisms of the Rapid and Slow Solar-to-Electric Energy Storage Processes by the Other Natural Photosynthetic System, Bacteriorhodopsin. *Pure Appl. Chem.* **1995**, *67*, 149-155.
- [197] Julien, B.; Jérémie, L.; Stefan, H. Ultrafast Photo-Induced Reaction Dynamics in Bacteriorhodopsin and Its Trp Mutants. *J. Opt.* **2010**, *12*, 084004.
- [198] Janke, C.; Scholz, F.; Becker-Baldus, J.; Glaubitz, C.; Wood, P. G.; Bamberg, E.; Wachtveitl, J.; Bamann, C. Photocycle and Vectorial Proton Transfer in a Rhodopsin from the Eukaryote *Oxyrrhis Marina*. *Biochemistry* **2013**, *52*, 2750-2763.
- [199] Verhoeven, M.-K.; Neumann, K.; Weber, I.; Glaubitz, C.; Wachtveitl, J. Primary Reaction Dynamics of Proteorhodopsin Mutant D97n Observed by Femtosecond Infrared and Visible Spectroscopy. *Photochem. Photobiol.* **2009**, *85*, 540-546.
- [200] Lenz, M. O.; Huber, R.; Schmidt, B.; Gilch, P.; Kalmbach, R.; Engelhard, M.; Wachtveitl, J. First Steps of Retinal Photoisomerization in Proteorhodopsin. *Biophys. J.* **2006**, *91*, 255-262.
- [201] Scholz, F.; Bamberg, E.; Bamann, C.; Wachtveitl, J. Tuning the Primary Reaction of Channelrhodopsin-2 by Imidazole, Ph, and Site-Specific Mutations. *Biophys. J.* **2012**, *102*, 2649-2657.
- [202] Muñoz-Losa, A.; Martin, M. E.; Galván, I. F.; Sánchez, M. L.; Aguilar, M. A. Solvent Effects on the Radiative and Nonradiative Decay of a Model of the Rhodopsin Chromophore. *J. Chem. Theory Comput.* **2011**, *7*, 4050-4059.
- [203] Hou, B.; Friedman, N.; Ruhman, S.; Sheves, M.; Ottolenghi, M. Ultrafast Spectroscopy of the Protonated Schiff Bases of Free and C13c14 Locked Retinals. *J. Phys. Chem. B* **2001**, *105*, 7042-7048.
- [204] Michl, J.; Bonacic-Koutecky, V. *Electronic Aspects of Organic Photochemistry*; Wiley New York, 1990, 447.
- [205] Tomasello, G.; Bearpark, M. J.; Robb, M. A.; Orlandi, G.; Garavelli, M. Significance of a Zwitterionic State for Fulgide Photochromism: Implications for the Design of Mimics. *Angew. Chem. Int. Ed. Engl.* **2010**, *49*, 2913-2916.
- [206] Dartnall, H. J. A.; Lythgoe, J. N. The Spectral Clustering of Visual Pigments. *Vision Res.* **1965**, *5*, 81-100.
- [207] Hárosi, F. I.; MacNichol, E. F. Visual Pigments of Goldfish Cones: Spectral Properties and Dichroism. *J. Gen. Physiol.* **1974**, *63*, 279-304.
- [208] Suzuki, T.; Makino-Tasaka, M.; Eguchi, E. 3-Dehydroretinal (Vitamin A2 Aldehyde) in Crayfish Eye. *Vision Res.* **1984**, *24*, 783-787.

- [209] Lythgoe, J. N.; Partridge, J. C. Visual Pigments and the Acquisition of Visual Information. *J. Exp. Biol.* **1989**, *146*, 1-20.
- [210] Conti, I.; Bernardi, F.; Orlandi, G.; Garavelli, M. Substituent Controlled Spectroscopy and Excited State Topography of Retinal Chromophore Models: Fluorinated and Methoxy-Substituted Protonated Schiff Bases. *Mol. Phys.* **2006**, *104*, 915-924.
- [211] Conti, I.; Garavelli, M. Substituent-Controlled Photoisomerization in Retinal Chromophore Models: Fluorinated and Methoxy-Substituted Protonated Schiff Bases. *Journal of Photochemistry and Photobiology A: Chemistry* **2007**, *190*, 258-273.
- [212] Jacquemin, D.; Perpète, E. A.; Ciofini, I.; Adamo, C. Accurate Simulation of Optical Properties in Dyes. *Accounts of Chemical Research* **2009**, *42*, 326-334.
- [213] Valsson, O.; Filippi, C.; Casida, M. E. Regarding the Use and Misuse of Retinal Protonated Schiff Base Photochemistry as a Test Case for Time-Dependent Density-Functional Theory. *The Journal of Chemical Physics* **2015**, *142*, 144104.
- [214] Kochendoerfer, G. G.; Lin, S. W.; Sakmar, T. P.; Mathies, R. A. How Color Visual Pigments Are Tuned. *Trends in Biochemical Sciences* **1999**, *24*, 300-305.
- [215] Nielsen, M. B. Model Systems for Understanding Absorption Tuning by Opsin Proteins. *Chemical Society Reviews* **2009**, *38*, 913-924.
- [216] Wanko, M.; Hoffmann, M.; Strodel, P.; Koslowski, A.; Thiel, W.; Neese, F.; Frauenheim, T.; Elstner, M. Calculating Absorption Shifts for Retinal Proteins: Computational Challenges. *The Journal of Physical Chemistry B* **2005**, *109*, 3606-3615.
- [217] Ebrey, T.; Koutalos, Y. Vertebrate Photoreceptors. *Prog. Retin. Eye Res.* **2001**, *20*, 49-94.
- [218] Berson, D. M.; Dunn, F. A.; Takao, M. Phototransduction by Retinal Ganglion Cells That Set the Circadian Clock. *Science* **2002**, *295*, 1070-1073.
- [219] Provencio, I.; Rodriguez, I. R.; Jiang, G.; Hayes, W. P.; Moreira, E. F.; Rollag, M. D. A Novel Human Opsin in the Inner Retina. *J. Neurosci.* **2000**, *20*, 600-605.
- [220] Provencio, I.; Jiang, G.; De Grip, W. J.; Hayes, W. P.; Rollag, M. D. Melanopsin: An Opsin in Melanophores, Brain, and Eye. *Proc. Natl. Acad. Sci. U. S. A.* **1998**, *95*, 340-345.
- [221] Applebury, M. L.; Hargrave, P. A. Molecular Biology of the Visual Pigments. *Vision Res.* **1986**, *26*, 1881-1895.
- [222] Fryxel, K. J.; Meyerowitz, E. M. The Evolution of Rhodopsins and Neurotransmitter Receptors. *J. Mol. Evol.* **1991**, *33*, 367-378.
- [223] Yokoyama, S. Gene Duplications and Evolution of the Short Wavelength-Sensitive Visual Pigments in Vertebrates. *Mol. Biol. Evol.* **1994**, *11*, 32-39.
- [224] Lythgoe, J. N.; Partridge, J. C. Visual Pigments and the Acquisition of Visual Information. *J. Exp. Biol.* **1989**, *146*, 1-20.
- [225] Oseroff, A. R.; Callender, R. H. Resonance Raman Spectroscopy of Rhodopsin in Retinal Disk Membranes. *Biochemistry* **1974**, *13*, 4243-4248.
- [226] Siebert, F.; MÄNtele, W.; Gerwert, K. Fourier-Transform Infrared Spectroscopy Applied to Rhodopsin. *Eur. J. Biochem.* **1983**, *136*, 119-127.
- [227] Bagley, K. A.; Balogh-Nair, V.; Croteau, A. A.; Dollinger, G.; Ebrey, T. G.; Eisenstein, L.; Hong, M. K.; Nakanishi, K.; Vittitow, J. Fourier-Transform Infrared Difference Spectroscopy of Rhodopsin and Its Photoproducts at Low Temperature. *Biochemistry* **1985**, *24*, 6055-6071.

- [228] Honig, B.; Dinur, U.; Nakanishi, K.; Balogh-Nair, V.; Gawinowicz, M. A.; Arnaboldi, M.; Motto, M. G. An External Point-Charge Model for Wavelength Regulation in Visual Pigments. *J. Am. Chem. Soc.* **1979**, *101*, 7084-7086.
- [229] Hauser, F. E.; van Hazel, I.; Chang, B. S. Spectral Tuning in Vertebrate Short Wavelength-Sensitive 1 (Sws1) Visual Pigments: Can Wavelength Sensitivity Be Inferred from Sequence Data? *J Exp Zool B Mol Dev Evol* **2014**, *322*, 529-539.
- [230] Arendt, D. Evolution of Eyes and Photoreceptor Cell Types. *Int J Dev Biol* **2003**, *47*, 563-571.
- [231] Terakita, A.; Kawano-Yamashita, E.; Koyanagi, M. Evolution and Diversity of Opsins. *Wiley Interdisciplinary Reviews: Membrane Transport and Signaling* **2012**, *1*, 104-111.
- [232] Mure, L. S.; Cornut, P.-L.; Rieux, C.; Drouyer, E.; Denis, P.; Gronfier, C.; Cooper, H. M. Melanopsin Bistability: A Fly's Eye Technology in the Human Retina. *PLoS One* **2009**, *4*, e5991.
- [233] Berson, D. M. Phototransduction in Ganglion-Cell Photoreceptors. *Pflugers Arch* **2007**, *454*, 849-855.
- [234] Peirson, S. N.; Halford, S.; Foster, R. G. The Evolution of Irradiance Detection: Melanopsin and the Non-Visual Opsins. *Philosophical Transactions of the Royal Society B: Biological Sciences* **2009**, *364*, 2849-2865.
- [235] Parker, R. O.; Crouch, R. K. Retinol Dehydrogenases (Rdhs) in the Visual Cycle. *Exp. Eye Res.* **2010**, *91*, 788-792.
- [236] Altimus, C. M.; Guler, A. D.; Villa, K. L.; McNeill, D. S.; Legates, T. A.; Hattar, S. Rods-Cones and Melanopsin Detect Light and Dark to Modulate Sleep Independent of Image Formation. *Proc. Natl. Acad. Sci. U. S. A.* **2008**, *105*, 19998-20003.
- [237] Lupi, D.; Oster, H.; Thompson, S.; Foster, R. G. The Acute Light-Induction of Sleep Is Mediated by Opn4-Based Photoreception. *Nat. Neurosci.* **2008**, *11*, 1068-1073.
- [238] Do, M. T. H.; Kang, S. H.; Xue, T.; Zhong, H.; Liao, H.-W.; Bergles, D. E.; Yau, K.-W. Photon Capture and Signalling by Melanopsin Retinal Ganglion Cells. *Nature* **2009**, *457*, 281-287.
- [239] Kandori, H.; Shichida, Y.; Yoshizawa, T. Photoisomerization in Rhodopsin. *Biochemistry (Mosc)* **2001**, *66*, 1197-1209.
- [240] Kukura, P.; McCamant, D. W.; Yoon, S.; Wandschneider, D. B.; Mathies, R. A. Structural Observation of the Primary Isomerization in Vision with Femtosecond-Stimulated Raman. *Science* **2005**, *310*, 1006-1009.
- [241] Frutos, L. M.; Andruniow, T.; Santoro, F.; Ferre, N.; Olivucci, M. Tracking the Excited-State Time Evolution of the Visual Pigment with Multiconfigurational Quantum Chemistry. *Proc. Natl. Acad. Sci. U. S. A.* **2007**, *104*, 7764-7769.
- [242] Gozem, S.; Schapiro, I.; Ferré, N.; Olivucci, M. The Molecular Mechanism of Thermal Noise in Rod Photoreceptors. *Science* **2012**, *337*, 1225-1228.
- [243] Harosi, F. I. An Analysis of Two Spectral Properties of Vertebrate Visual Pigments. *Vision Res.* **1994**, *34*, 1359-1367.
- [244] Birge, R. R. Photophysics and Molecular Electronic Applications of the Rhodopsins. *Annual Review of Physical Chemistry* **1990**, *41*, 683-733.
- [245] Briand, J.; Bram, O.; Rehault, J.; Leonard, J.; Cannizzo, A.; Chergui, M.; Zanirato, V.; Olivucci, M.; Helbing, J.; Haacke, S. Coherent Ultrafast Torsional Motion and Isomerization of a Biomimetic Dipolar Photoswitch. *PCCP* **2010**, *12*, 3178-3187.

- [246] Lumento, F.; Zanirato, V.; Fusi, S.; Busi, E.; Latterini, L.; Elisei, F.; Sinicropi, A.; Andruniów, T.; Ferré, N.; Basosi, R.; Olivucci, M. Quantum Chemical Modeling and Preparation of a Biomimetic Photochemical Switch. *Angew. Chem. Int. Ed.* **2007**, *46*, 414-420.
- [247] Sinicropi, A.; Martin, E.; Ryazantsev, M.; Helbing, J.; Briand, J.; Sharma, D.; Léonard, J.; Haacke, S.; Cannizzo, A.; Chergui, M.; Zanirato, V.; Fusi, S.; Santoro, F.; Basosi, R.; Ferré, N.; Olivucci, M. An Artificial Molecular Switch That Mimics the Visual Pigment and Completes Its Photocycle in Picoseconds. *Proceedings of the National Academy of Sciences* **2008**, *105*, 17642-17647.
- [248] Weingart, O.; Garavelli, M. Modelling Vibrational Coherence in the Primary Rhodopsin Photoproduct. *J. Chem. Phys.* **2012**, *137*, 22A523.
- [249] Kandori, H.; Sasabe, H.; Nakanishi, K.; Yoshizawa, T.; Mizukami, T.; Shichida, Y. Real-Time Detection of 60-Fs Isomerization in a Rhodopsin Analog Containing Eight-Membered-Ring Retinal. *J. Am. Chem. Soc.* **1996**, *118*, 1002-1005.
- [250] Mathies, R. A.; Cruz, C. B.; PoLARD, W. T. Cis-Trans Isomerization in Bacteriorhodopsin. **1988**.
- [251] Kandori, H.; Katsuta, Y.; Ito, M.; Sasabe, H. Femtosecond Fluorescence Study of the Rhodopsin Chromophore in Solution. *J. Am. Chem. Soc.* **1995**, *117*, 2669-2670.
- [252] Weiss, R.; Warshel, A. A New View of the Dynamics of Singlet Cis-Trans Photoisomerization. *J. Am. Chem. Soc.* **1979**, *101*, 6131-6133.
- [253] Hurley, J. B.; Ebrey, T. G.; Honig, B.; Ottolenghi, M. Temperature and Wavelength Effects on the Photochemistry of Rhodopsin, Isorhodopsin, Bacteriorhodopsin and Their Photoproducts. *Nature* **1977**, *270*, 540-542.
- [254] Rajput, J.; Rahbek, D. B.; Andersen, L. H.; Hirshfeld, A.; Sheves, M.; Altoè, P.; Orlandi, G.; Garavelli, M. Probing and Modeling the Absorption of Retinal Protein Chromophores in Vacuo. *Angew. Chem. Int. Ed.* **2010**, *49*, 1790-1793.
- [255] Cembran, A.; González-Luque, R.; Serrano-Andrés, L.; Merchán, M.; Garavelli, M. About the Intrinsic Photochemical Properties of the 11-Cis Retinal Chromophore: Computational Clues for a Trap State and a Lever Effect in Rhodopsin Catalysis. *Theoretical Chemistry Accounts: Theory, Computation, and Modeling (Theoretica Chimica Acta)* **2007**, *118*, 173-183.
- [256] Fan, J.; Rohrer, B.; Moiseyev, G.; Ma, J.-x.; Crouch, R. K. Isorhodopsin Rather Than Rhodopsin Mediates Rod Function in Rpe65 Knock-out Mice. *Proceedings of the National Academy of Sciences* **2003**, *100*, 13662-13667.
- [257] Weingart, O.; Altoe, P.; Stenta, M.; Bottoni, A.; Orlandi, G.; Garavelli, M. Product Formation in Rhodopsin by Fast Hydrogen Motions. *PCCP* **2011**, *13*, 3645-3648.
- [258] Schapiro, I.; Ryazantsev, M. N.; Frutos, L. M.; Ferré, N.; Lindh, R.; Olivucci, M. The Ultrafast Photoisomerizations of Rhodopsin and Bathorhodopsin Are Modulated by Bond Length Alternation and Hoop Driven Electronic Effects. *J. Am. Chem. Soc.* **2011**, *133*, 3354-3364.
- [259] Murakami, M.; Kouyama, T. Crystal Structure of Squid Rhodopsin. *Nature* **2008**, *453*, 363-367.
- [260] Okada, T.; Sugihara, M.; Bondar, A.-N.; Elstner, M.; Entel, P.; Buss, V. The Retinal Conformation and Its Environment in Rhodopsin in Light of a New 2.2 Å Crystal Structure†. *J. Mol. Biol.* **2004**, *342*, 571-583.

- [261] Ferré, N.; Olivucci, M. Probing the Rhodopsin Cavity with Reduced Retinal Models at the Caspt2//Casscf/Amber Level of Theory. *J. Am. Chem. Soc.* **2003**, *125*, 6868-6869.
- [262] Ferré, N.; Cembran, A.; Garavelli, M.; Olivucci, M. Complete-Active-Space Self-Consistent-Field/Amber Parameterization of the Lys296–Retinal–Glu113 Rhodopsin Chromophore-Counterion System. *Theor. Chem. Acc.* **2004**, *112*, 335-341.
- [263] Granucci, G.; Persico, M. Critical Appraisal of the Fewest Switches Algorithm for Surface Hopping. *J. Chem. Phys.* **2007**, *126*, 134114.
- [264] Ahuja, S.; Smith, S. O. Multiple Switches in G Protein-Coupled Receptor Activation. *Trends Pharmacol. Sci.* **2009**, *30*, 494-502.
- [265] Karlström, G.; Lindh, R.; Malmqvist, P.-Å.; Roos, B. O.; Ryde, U.; Veryazov, V.; Widmark, P.-O.; Cossi, M.; Schimmelpfennig, B.; Neogrady, P.; Seijo, L. Molcas: A Program Package for Computational Chemistry. *Computational Materials Science* **2003**, *28*, 222-239.
- [266] Aquilante, F.; De Vico, L.; Ferré, N.; Ghigo, G.; Malmqvist, P.-å.; Neogrady, P.; Pedersen, T. B.; Pitoňák, M.; Reiher, M.; Roos, B. O.; Serrano-Andrés, L.; Urban, M.; Veryazov, V.; Lindh, R. Molcas 7: The Next Generation. *J. Comput. Chem.* **2010**, *31*, 224-247.
- [267] Okada, T.; Fujiyoshi, Y.; Silow, M.; Navarro, J.; Landau, E. M.; Shichida, Y. Functional Role of Internal Water Molecules in Rhodopsin Revealed by X-Ray Crystallography. *Proceedings of the National Academy of Sciences* **2002**, *99*, 5982-5987.
- [268] Katayama, K.; Furutani, Y.; Imai, H.; Kandori, H. An Ftir Study of Monkey Green- and Red-Sensitive Visual Pigments. *Angew. Chem. Int. Ed.* **2010**, *49*, 891-894.
- [269] Fasick, J. I.; Applebury, M. L.; Oprian, D. D. Spectral Tuning in the Mammalian Short-Wavelength Sensitive Cone Pigments. *Biochemistry* **2002**, *41*, 6860-6865.
- [270] El-Tahawy, M. M. T.; Nenov, A.; Garavelli, M. Photoelectrochromism in the Retinal Protonated Schiff Base Chromophore: Photoisomerization Speed and Selectivity under a Homogeneous Electric Field at Different Operational Regimes. *J. Chem. Theory Comput.* **2016**, *12*, 4460-4475.